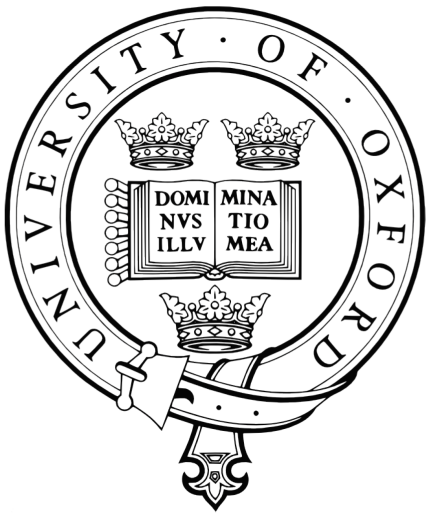
Passive Acoustic Mapping for Vascular Permeability Assessment



Catherine Mary Paverd

St John's College

University of Oxford

Supervisor: Constantin-Cassios Coussios

Thesis submitted for the degree of

Doctor of Philosophy

Trinity 2019

Copyright © 2019 Catherine Paverd

To my parents,

Kathleen & Graham,

for giving me the greatest gift of all – love.

Abstract

Despite significant research efforts, cancer remains one of the leading causes of death globally, and relative survival rates have not improved significantly over the past 40 years. Larger therapeutic agents rely on a high degree of vascular permeability for delivery and are increasingly being used for treatment, making permeability one of the most important biomarkers in tumour assessment. In this thesis, Passive Acoustic Mapping (PAM) of acoustic cavitation arising from nanoscale cavitation agents is explored in order to assess tumour permeability to molecules of a similar size to the latest therapeutics.

In vitro experiments using a dual High Intensity Focussed Ultrasound (HIFU) and dual linear array setup demonstrate that cavitation nuclei can be extravasated from a flow channel into a tissue mimicking phantom under ultrasound-enhanced delivery, and can then be re-excited using ultrasound and spatially mapped with PAM. *In vivo* experiments in a bilateral murine model following a similar process yield surprising results, namely that when a tumour on one side of the animal is exposed to ultrasound at a 5% duty cycle, the level of cavitation on the contralateral side tumour is increased relative to the treated side tumour and relative to tumours in animals that were treated with different acoustic parameters. It is hypothesised that this is due to a combination of biological and acoustic factors.

Further experiments to assess passive accumulation of nanoscale cavitation nuclei at different developmental stages within a single tumour line, as

well as between tumour lines with different stromal composition, demonstrate that passive accumulation occurs to varying degrees depending on developmental stage and tumour type. Micro-CT assessment of tumour vessel structure using radiopaque resin perfusions does not show clear structural differences in tumours with different levels of passive accumulation. This implies that ultrasound and nanoscale cavitation agents could be used to assess passive accumulation of large molecules, even in tumours with similar vessel structures. Finally, it is not always possible to use high resolution dual array PAM in a clinical setting due to geometric constraints. Therefore a new passive acoustic source localisation approach is proposed that relies on Blind Source Separation (BSS) and Acoustic Source Localisation (ASL). Mixed cavitation signals arising from individual sources are first separated using a BSS technique, before the time delays for each separated signal are determined on a linear array and used to estimate individual source position. Simulation results for this approach show good performance, and enable the localisation of multiple sources which, crucially, cannot be identified as separate sources using single array PAM, even with the most advanced algorithms currently available.

Overall, the combination of the proposed source localisation technique, with the assessment of passively accumulated and actively extravasated cavitation nuclei, could eventually be used to provide critical information to clinicians about tumour vasculature permeability.

Statement of Originality

I hereby declare that this submission is my own work and, to the best of my knowledge, it contains no materials previously published or written by another person, or substantial proportions of material which have been accepted for the award of any other degree of diploma at the University of Oxford or any other educational institution, except where due acknowledgement is made in the thesis.



Catherine Paverd

October 2019

Research Dissemination

Papers

1. **Paverd, C.**, Lyka, E., Elbes, D., and Coussios, C-C., **Passive Acoustic Mapping of Extravasation Following Ultrasound-Enhanced Drug Delivery**, *Physics in Medicine and Biology*, January 2019

2. Lyka, E., Coviello, C., **Paverd, C.**, Gray, M., Coussios, C.-C., **Passive Acoustic Mapping using Data-Adaptive Beamforming Based on Higher-Order Statistics**, *IEEE Trans. on Medical Imaging*, June 2018

Conferences

1. **Poster**: **Paverd, C.**, Lyka, E., and Coussios, C-C., **Multi-Source Passive Acoustic Source Localisation for Diagnostic and Therapeutic Applications**, *European Symposium on Ultrasound Contrast Imaging*, 16 - 17 Jan. 2019, Rotterdam, NL

2. **Presentation**: **Paverd, C.**, Lyka, E., and Coussios, C.-C., **Multi-Source Passive Acoustic Source Localisation**, *Acoustical Society of America*, 5 - 9 Nov. 2018, Victoria, CA

3. **Presentation**: **Paverd, C.**, Lyka, E., Elbes, D. and Coussios, C.-C., **Passive Acoustic Mapping of Extravasation for Vascular Permeability Assessment**, *Acoustical Society of America*, 25 - 29 June 2017, Boston, MA, USA

4. **Poster**: **Paverd, C.**, Elbes, D., Coussios, C-C., **Dual Array Passive Acoustic Mapping**, *International Cancer Imaging Society*, Oct. 2016, London, UK

Acknowledgements

This DPhil would not have been possible without the support of my supervisor, Professor Constantin-C. Coussios. I am honoured to have had the opportunity to learn from someone as passionate, intelligent, and motivated as Constantin, and I am grateful to him for taking me on as a student. I thank him for his patience and encouragement throughout the DPhil, and for taking the time to share his vast knowledge in all aspects of academia and entrepreneurship. It is rare that someone so accomplished still so genuinely cares about the best interests of his students, and I thank him for the opportunities he has given me, and for his mentorship.

My DPhil was financially supported by the Commonwealth Scholarship and the Oppenheimer Fund, and I am extremely grateful to them for their generosity.

I thank Professor Robert Carlisle for his advice on the design of *in vivo* experiments, and I am grateful to the many postdoctoral researchers in the lab, especially Dr Delphine Elbes, Dr Luca Baù, Dr Christophoros Mannaris, and Dr Shamit Shrivastava, for their wise advice, practical assistance, and enlightening discussions.

I had the pleasure of collaborating with two fellow lab members and friends, to whom I am not only immensely grateful, but also deeply indebted. I doubt I would have been able to complete this thesis without their encouragement during difficult times, and their practical and moral support in experiments and in life more generally. I therefore thank Dr Erasmia Lyka, whose expert advice, sound guidance, and continual encouragement has been invaluable, and Alexander Martin, whose advice, company, and willingness to work at all hours of the day saved me on many occasions.

I am also grateful to every member of the Biomedical Ultrasonics, Biotherapy, and Biopharmaceuticals Laboratory (BUBBL) for their help, advice, kindness, and company. I thank Sheena Wallington for her practical assistance, enthusiasm, and

endless patience when training me on *in vivo* techniques, and Jim Fisk and Dave Salisbury for their incredible workmanship and positivity.

My experience would not have been anywhere near as enjoyable without the friendship and camaraderie of so many people in BUBBL. I am especially grateful to Tammy Clark for her humour, honesty, and support; Jamie Wallis for his kind-hearted banter; and Joe Blackmore and Kya Shoar for the countless captivating discussions and unforgettable adventures.

I am honoured to have had the opportunity to work as part of the Merton College Welfare team. I thank all members of the team, especially the Rev'd Canon Dr Simon Jones, Jenny Barrett, and Seb Wylie, for their advice, understanding, and flexibility.

My Oxford experience was also significantly enhanced by the stimulating and fun environment of the St John's College MCR and Boat Club, and I thank my friends there for the fantastic socials and for their enthusiastic support.

I am grateful to those who, although not directly involved in this work, laid the academic foundation for it. In particular, I thank Professors David Rubin, Ian Jandrell, and Alan Clark at the University of the Witwatersrand, Johannesburg, for instilling in me a passion for engineering, and for supporting my ambition for further study.

On a personal note, I am incredibly grateful to my family for their love and support. I remember Sylvia Paverd, who gave so much of her life for others. I thank my aunts, Delia Brady and Mary Brady, for their exceptional kindness, generosity, and care. I am grateful to my brother, Dr Andrew Paverd, for always leading by example, and for his practical support and advice at every stage of my life.

Finally, I thank my parents, Kathleen and Graham Paverd. I would not be here today without the sacrifices they have made to give me every opportunity in life; this achievement is theirs as well. They have demonstrated that *what is essential is invisible to the eye*, and I am immensely grateful to them for the kindness, care, and encouragement they have given me throughout my life. Ultimately, I thank them for their unfailing support and, above all, for their absolute love.

Contents

1 Introduction **1**

1.1 Cancer Tumour Structure 5

1.1.1 Healthy Tissue 5

1.1.2 Tumour Vasculature 6

1.1.3 Enhanced Permeability and Retention 7

1.2 Cancer Imaging Techniques 8

1.2.1 Magnetic Resonance Imaging (MRI) 8

1.2.2 X-Ray Computed Tomography (CT) 9

1.2.3 Single-Photon Emission Computed Tomography (SPECT) . . 10

1.2.4 Positron Emission Technology (PET) 11

1.2.5 Optical Imaging 12

1.2.6 Photoacoustic Imaging 12

1.2.7 Ultrasound (US) 12

1.3 Cavitation-Based Tissue Imaging 15

1.3.1 Regimes of Cavitation 15

1.3.2 Non-Inertial Cavitation Applications 17

1.3.3 Inertial Cavitation Applications 18

1.3.4 Passive Acoustic Mapping (PAM) 20

1.3.5 Cavitation Nuclei 22

1.3.6 Nanocups 23

1.4 Summary 25

2 Passive Acoustic Mapping of Extravasated Particles *In Vitro* 26

2.1 Experiment Materials and Methods 27

2.1.1 Experimental Procedure 27

2.1.2 Phantom Design 28

2.1.3 Cavitation Nuclei 30

2.1.4 Acoustic Setup 31

2.1.5 Experiment Parameters 35

2.2 Image Processing Methods 36

2.2.1 Image Acquisition 36

2.2.2 Image Processing Procedure 38

2.2.3 PAM Processing 39

2.2.4 PAM Threshold Optimisation 40

2.3 Results 41

2.3.1 Qualitative Results 41

2.3.2 Quantitative Results 46

2.4 Discussion 48

2.4.1 Beamformer and Array Configuration 52

2.4.2 Tradeoffs And Limitations 53

2.5 Conclusion 54

3 *In Vivo* Passive Acoustic Mapping of Extravasated Particles 56

3.1 Introduction 56

3.2 Experimental Methods 59

3.2.1 Ultrasound Setup 59

3.2.2 Nanoscale Cavitation Nuclei 63

3.2.3 Tumour Implantation 64

3.2.4 Procedures Under Anaesthetic 64

3.2.5 Terminal Procedures 65

3.2.6 Resin Perfusion 65

3.3 Experiment 1: Assessment of Cavitation from Extravasated Particles *In Vivo* 66
3.3.1 Experimental Procedure 66
3.3.2 Results and Discussion 68
3.4 Experiment 2: Assessment of Vascular Integrity Following Cavitation in Tumours 77
3.4.1 Experimental Procedure 78
3.4.2 Results and Discussion 79
3.5 Experiment 3: Assessment of Cavitation in Tumours of Different Stages and Types 87
3.5.1 Experimental Procedure 88
3.5.2 Results and Discussion 89
3.6 Conclusion 96

4 Localisation of Cavitation by a combined Blind Source Separation and Acoustic Source Localisation Method 109
4.1 Introduction 109
4.2 Model Description 112
4.3 Passive Acoustic Source Localisation 115
4.3.1 Direct Method - Steered Beamformer 116
4.3.2 Direct Method - Subspace-Based Approaches 118
4.3.3 Indirect Method - Time Sum and Difference of Arrival 119
4.4 Source Separation 121
4.4.1 BSS by Second Order Statistics (SOS) Methods 123
4.4.2 BSS by Higher Order Statistics (HOS) Methods 124
4.4.3 Other BSS Methods 125
4.4.4 Non-negative Matrix Factorisation 126
4.5 Proposed Approach to Multi-source Cavitation Localisation 126
4.5.1 Step 1: Initial Estimate of Number of Sources 127

4.5.2 Step 2: Blind Source Separation by ICA 129
4.5.3 Step 3: Compensating for Ambiguities arising from ICA . . . 133
4.5.4 Step 4: Position Estimation using TDOA 134
4.5.5 Step 5: Application of Error Tolerances 137
4.6 Simulation Results 138
4.6.1 Simulation Parameters 138
4.6.2 Single Source 140
4.6.3 Multiple Sources 141
4.7 Experimental Results 154
4.8 Discussion 160
4.8.1 Limitations 163
4.8.1.1 Choice of ICA Approach 163
4.8.1.2 Performance in Variable Speed of Sound Conditions . 164
4.8.1.3 Required Level of Independence 165
4.8.1.4 Geometric Limitations 166
4.8.2 Other Algorithm Improvements 166
4.8.2.1 Determination of the Time Delays 166
4.8.2.2 Selection and Weighting of Received Signals 167
4.8.3 Applications 167
4.9 Conclusion 168

5 Conclusions and Future Work **169**
5.1 Future Work 175

A Full *In Vitro* Experimental Results **A.0-1**

List of Figures

2.1 *In vitro* experimental setup, top and side view 29
2.2 Images of *in vitro* experimental setup 29
2.3 Dynamic Light Scattering measurement of nanocup size 31
2.4 A TEM image of fabricated nanocups showing the characteristic cup deformation 32
2.5 Scans of the focal regions of the dual HIFU transducer setup 33
2.6 Calibration at 0.5 MHz for a single HIFU transducer, and for both HIFU transducers together. 34
2.7 Example of the PAM image obtained from the initial and second sonications for a single experiment. 37
2.8 Example of each stage of the image processing process for a single experiment. 42
2.9 Presentation of the optimal dB contour for PAM thresholding. 42
2.10 Three representative fused images created using the dual array configuration and the RLPB beamformer. 43
2.11 Fused images for both the single and dual array configurations for three beamformers. 44
2.12 Quantification of PAM energy, distance of fluorescent particle and clustering metric for overlay images 45

3.1 Block diagram of the *in vivo* acoustic setup. 61
3.2 *In vivo* setup images showing an animal on the custom holder, and an image of two animals being perfused. 62

3.3 Cavitation level for initial sonication for Assessment of Cavitation from Extravasated Particles experiment 70
3.4 Cavitation level during second sonication for 5% duty cycle group in Assessment of Cavitation from Extravasated Particles experiment . . 71
3.5 Cavitation level during second sonication for 1% duty cycle group in Assessment of Cavitation from Extravasated Particles experiment . . 72
3.6 Probability of cavitation during second sonication for 5% duty cycle group in the Assessment of Cavitation experiment 76
3.7 Cavitation level during initial sonication for three experimental groups in the Assessment of Vascular Integrity Experiment 81
3.8 Cavitation level during second sonication for 5% duty cycle group in the Assessment of Vascular Integrity experiment 82
3.9 Cavitation level during second sonication for 1% duty cycle group in the Assessment of Vascular Integrity experiment 82
3.10 Cavitation level during second sonication for 0.01% duty cycle group in the Assessment of Vascular Integrity experiment 83
3.11 Example of images acquired using the IVIS imaging system in conjunction with a long circulating small molecule (AngioSense 680 EX) . . . 84
3.12 Quantitative assessment of AngioSense fluorescence following treatment with 5%, 1% and 0.01% duty cycle on one side tumour. 86
3.13 Comparison of passive accumulation cavitation for CT-26 tumours grouped by weight 90
3.14 Comparison of passive accumulation cavitation level in different tumour lines 91
3.15 Cavitation to assess passive accumulation in individual tumours . . . 93
3.16 CT of three different tumours with different levels of cavitation 94
3.17 CT scan of a resin perfused tumour, showing different angles of view . 97
3.18 CT of tumour showing measurement planes for slices used in B-Mode and PAM overlay 98

3.19 CT scan of tumour showing a single slice for comparison with B-Mode and PAM 99
3.20 Overall B-Mode and PAM overlays for passive accumulation mapping 100
3.21 Overlay of CT, B-Mode and PAM for Layer 1 and 2 of tumour 101
3.22 Overlay of CT, B-Mode and PAM for Layer 3 and 4 of tumour 102
3.23 Overlay of CT, B-Mode and PAM for Layer 5 and 6 of tumour 103
3.24 Overlay of CT, B-Mode and PAM for Layer 7 and 8 of tumour 104
3.25 Overlay of CT, B-Mode and PAM for Layer 9 and 10 of tumour . . . 105
3.26 Overlay of CT, B-Mode and PAM for Layer 11 and 12 of tumour . . 106

4.1 Overall process of mapping cavitation activity on an array 128
4.2 Flowchart of the proposed new beamforming algorithm. 129
4.3 Setup for bubble simulations used in the assessment of the BSS-ASL algorithm 138
4.4 Comparison of BSS-ASL algorithm for single simulated source in noiseless case - Array 1 142
4.5 Comparison of BSS-ASL algorithm for single simulated source in noiseless case - Array 2 143
4.6 Comparison of BSS-ASL algorithm for single simulated source with added noise - Array 1 144
4.7 Comparison of BSS-ASL algorithm for single simulated source with added noise - Array 2 145
4.8 Comparison of BSS-ASL algorithm for three simulated sources in noiseless case - Array 1 146
4.9 Comparison of BSS-ASL algorithm for three simulated sources in noiseless case - Array 2 147
4.10 Comparison of BSS-ASL algorithm for three simulated sources with added noise - Array 1 149

4.11 Comparison of BSS-ASL algorithm for three simulated sources with added noise - Array 2 150
4.12 Output for each stage of the BSS-ASL algorithm for three bubbles with no noise. 151
4.13 Output for each stage of the BSS-ASL algorithm for three bubbles with noise. 153
4.14 BSS-ASL output for three bubbles showing effect of error removal . . 154
4.15 Representative TDOA curves for select ranges of elements 155
4.16 Three simulated bubbles with unconstrained error in BSS-ASL output 156
4.17 Sets 1 - 5 (of 10 total) of BSS-ASL output for 100 iterations of randomly positioned bubbles. 157
4.18 Sets 6 - 10 (of 10 total) of BSS-ASL output for 100 iterations of randomly positioned bubbles. 158
4.19 Experimental setup used to evaluate BSS-ASL algorithm 160
4.20 Experiment showing one distinct cavitation region as output of BSS-ASL, as confirmed by dual array PAM. 161
4.21 Experiment showing three distinct cavitation regions as output of BSS-ASL, as confirmed by dual array PAM. 162

A.1 Full results for *in vitro* flow channel experiment (1 of 10) A.0-2
A.2 Full results for *in vitro* flow channel experiment (2 of 10) A.0-3
A.3 Full results for *in vitro* flow channel experiment (3 of 10) A.0-4
A.4 Full results for *in vitro* flow channel experiment (4 of 10) A.0-5
A.5 Full results for *in vitro* flow channel experiment (5 of 10) A.0-6
A.6 Full results for *in vitro* flow channel experiment (6 of 10) A.0-7
A.7 Full results for *in vitro* flow channel experiment (7 of 10) A.0-8
A.8 Full results for *in vitro* flow channel experiment (8 of 10) A.0-9
A.9 Full results for *in vitro* flow channel experiment (9 of 10) A.0-10
A.10 Full results for *in vitro* flow channel experiment (10 of 10) A.0-11

List of Tables

3.1 Known pore sizes of tumour vasculature for various tumour cell lines 57

3.2 Known perfusion of tumours for various tumour cell lines. 58

3.3 Acoustic parameters for the extravasation and re-excitation of nanocups in the Assessment of Cavitation from Extravasated Particles Study . 68

3.4 Number of animals and animal tumour volume for the Assessment of Cavitation from Extravasated Particles Study 69

3.5 Acoustic parameters for the Assessment of Vascular Integrity Study . 80

3.6 Number of animals and tumour volume for the Assessment of Vascular Integrity Study 80

4.1 Bubble simulation parameters 139

4.2 Quantification of multi-bubble simulation results 159

List of Abbreviations

AMUSE	Algorithm for Multiple Unknown Signal Extraction
ANOVA	Analysis of Variance
ASL	Acoustic Source Localisation
AWSALM	Acoustic Wave Sparsely Activated Localization Microscopy
BBB	Blood Brain Barrier
BSS	Blind Source Separation
CLT	Central Limit Theorem
CT	Computed Tomography
DCE	Dynamic Contrast Enhanced
DC	Duty Cycle
DLS	Dynamic Light Scattering
DUET	Degenerate Unmixing Estimation Technique
ECM	Extracellular Matrix
EPR	Enhanced Permeability and Retention
ESPRIT	Estimation of Signal Parameters by Rotational Invariant Techniques
EVD	Eigenvalue Decomposition
FUS	Focussed Ultrasound
FWHM	Full Width Half Maximum
HIFU	High Intensity Focussed Ultrasound
HOS	Higher Order Statistics
HSD	Honestly Significant Difference
ICA	Independent Component Analysis
IC	Independent Component
IFP	Interstitial Fluid Pressure
IVIS	In Vivo Imaging System

MDL	Minimum Description Length
MIP	Maximum Intensity Projection
MI	Mechanical Index
MRI	Magnetic Resonance Imaging
MUSIC	Multiple Signal Classification
NIR	Near-Infrared
NMF	Non-negative Matrix Factorisation
PAM	Passive Acoustic Mapping
PBS	Phosphate-Buffered Saline
PCF	Phase Coherence Factor
PCI	Passive Cavitation Imaging
PET	Positron Emission Technology
PI	Pulse Inversion
PMMA	Polymethyl Methacrylate
PRF	Pulse Repetition Frequency
PRP	Peak Rarefactional Pressure
PSF	Point Spread Function
PVDF	Polyvinylidene Difluoride
RCB	Robust Capon Beamformer
RF	Radio Frequency
RLPB	Robust Linear Programming Beamforming
RoI	Region of Interest
SCA	Sparse Component Analysis
SNR	Signal to Noise Ratio
SOS	Second Order Statistics
SPECT	Single-Photon Emission Computed Tomography
STFT	Short Time Fourier Transform
TDOA	Time Difference of Arrival
TEA	Time Exposure Acoustics
TEM	Transmission Electron Microscope
THI	Tissue Harmonic Imaging
TRITC	Tetramethylrhodamine Isothiocyanate

Chapter 1

Introduction

Cancer is the third leading cause of death globally, and despite significant funding and research efforts, the relative survival rate for the most deadly forms of cancer has not improved significantly over the past 40 years [1][2]. Furthermore, the absolute number of cancer cases is predicted to more than double worldwide over the next few decades due to a growing and ageing population [1]. This effect will be most pronounced in economically developing countries, where public health systems already suffer from significant financial challenges [3]. Hence the need to increase the effectiveness and decrease the cost of cancer treatment will be of critical importance in the coming years.

In order to achieve this, it is vital to have an understanding of tumour progression and knowledge of whether drugs will be effective in tumour treatment. In recent years, the drugs used to treat cancer have become progressively larger, as new therapeutic classes such as antibodies and oncolytic viruses are increasingly employed. A significant factor affecting the efficacy of these agents is the permeability of the endothelial barrier [4]. In healthy tissue this barrier tightly regulates the exchange of molecules between the vasculature and the tissue, however in tumours, immature vessel formation and lack of support cells leads to large gaps in the barrier [4]. These gaps increase vascular permeability, which directly affects physiological processes such as angiogenesis, immune response and extravasation of chemotherapeutic drugs and cells [4]. Tumour specific vascular permeability is therefore one of the most impor-

tant biomarkers in the evaluation of tumours, and knowledge thereof can be extremely helpful in determining which treatments may have the greatest effect on the tumour.

At present, vascular permeability is most commonly assessed by either Dynamic Contrast Enhanced Magnetic Resonance Imaging (DCE-MRI) or DCE Computed Tomography (DCE-CT) [5]. While these techniques are useful, both are expensive and suffer from several limitations [5]. For example, DCE-CT makes use of ionising radiation, and DCE-MRI depends heavily on tissue properties at the time of imaging and the method of data analysis used [5][6]. In addition, both methods assess permeability to very small contrast agents, approximately 10 nm in diameter [5], but cannot be used to assess permeability to the larger therapeutics (for example, 500 nm oncolytic viruses [7]) that are now increasingly used in first-line treatments.

Another type of imaging that is significantly cheaper and that does not use ionising radiation is ultrasound. At present, ultrasound is used to assess tumour microvasculature in terms of perfusion (distribution of blood to small vessels) using contrast agents and imaging techniques such as Tissue Harmonic Imaging (THI) and Pulse Inversion (PI) Imaging [8].

However, recent developments have produced a nanoscale structure (known as a 'nanocup') of tunable size [9] that has the potential to be actively transported through leaky endothelial barriers (with pore sizes that range between 200 - 700 nm) under ultrasound excitation. A nanocup consists of a cup shaped solid polymer base and a stabilised bubble, which has the potential to undergo rapid expansion and collapse due to an applied acoustic wave with a pressure amplitude achievable by diagnostic imaging systems.

'Cavitation' is a broad term that describes a range of phenomena relating to bubbles. The term encompasses both bubble formation (due to radiation absorption, changes in fluid pressure, or changes in heat), as well as bubble dynamics (such as bubble expansion and collapse) [10][11]. In this thesis, cavitation will normally be used to refer to the dynamic bubble response which occurs as the result of an externally applied acoustic pressure wave. Depending on the type of bubble dynamics,

cavitation is classified into different regimes, as discussed further in Section 1.3.

Cavitating bubbles produce acoustic emissions that can be used to determine the particle location using cavitation based imaging techniques [12][13][14]. One such technique recently developed for cavitation imaging in biomedical ultrasound applications is Passive Acoustic Mapping (PAM) [14]. PAM has the ability to detect acoustic emissions arising from the cavitation of bubbles that are nucleated from nanocups. This means that it is now theoretically possible to use nanocups and PAM to assess vascular permeability. In addition, the use of nanoscale contrast agents in a similar size range to new therapeutics may more accurately reflect relevant levels of permeability compared to DCE-MRI and DCE-CT, and may inform the selection of first-line therapeutics based on the level of permeability.

This research focusses on the use of nanoscale cavitation nuclei, in conjunction with PAM, to assess tumour vasculature. The leakage or movement of particles, including cavitation agents, from inside blood vessels out into surrounding tissue is known as 'extravasation'. Extravasation of nanoscale structures can be enhanced by the thermal and mechanical effects generated as a result of focussed ultrasound and cavitation (discussed further in Section 1.3). The use of ultrasound to assist extravasation is called ultrasound enhanced extravasation, and is a central concept throughout this thesis.

The overall goal of this work is as follows:

1. To assess whether solid polymer based nanoscale cavitation nuclei, after ultrasound enhanced extravasation, can be re-excited and mapped using ultrasound.

2. To determine whether the excitation of cavitation nuclei that have passively accumulated in a tumour, or that have been extravasated under ultrasound excitation, can be used to assess tumour vasculature permeability *in vivo* at different stages of tumour development.

3. To develop a passive acoustic source localisation technique that aims to accurately determine the location of individual cavitation sources. This differs from

the current goal of PAM, which is to create a map of all cavitation energy across an entire region of interest.

The thesis structure is as follows. Chapter 2 details an *in vitro* experiment designed to assess whether nanoscale cavitation nuclei, once extravasated under ultrasound excitation, can be re-excited using ultrasound. Prior to this work, the re-excitation of cavitation nuclei following ultrasound enhanced extravasation had not been evaluated, and thus the *in vitro* work presented in this chapter is used as proof of one of the key principles necessary for vascular permeability assessment. The processes used in this chapter form the foundations of the *in vivo* work presented in this thesis.

Chapter 3 then details the translation of the concepts proven *in vitro* to an *in vivo* setting. Specifically, the permeability of tumour vasculature to nanoscale contrast agents is assessed for both passive accumulation via the Enhanced Permeability and Retention (EPR) effect, and ultrasound enhanced extravasation. Tumour vasculature permeability is assessed according to stage of tumour development, and a further comparison is made between different tumour models with significantly different micro-environment characteristics. For the first time, this *in vivo* work demonstrates that nanoscale cavitation nuclei can be used to differentiate between different levels of permeability at different stages of development in cancer tumours non-invasively (based on cavitation level alone). This type of assessment may be used to inform clinicians about the tumour-specific level of permeability to contrast agents that are in the order of several hundreds of nanometres, before they select a first line therapy for the patient. Whilst vascular permeability to a specific molecule size is not the only deciding factor in the selection of therapeutics, it may still prove to be a useful indicator of how effective certain classes of large-molecule, non-targeted therapies could be.

The *in vivo* results presented in Chapter 3 are mostly presented on a global (per tumour) scale, rather than as a spatial assessment of the vasculature within

tumours. Specific, localised, intra-tumoural information regarding vasculature permeability may also prove useful to clinicians when assessing tumours, for example, by allowing clinicians to determine whether areas of necrosis are present in large tumours. At present however, even the most advanced PAM algorithms alone are not able to localise cavitation sources to the level required for the small size scales found *in vivo*. Furthermore, it will be seen in Chapter 2 that the high resolution PAM algorithms can only be achieved with a large aperture setup, which is not always practically possible in clinical settings. Thus the final research topic of this thesis presents the development and testing of a novel passive localisation algorithm which approaches passive cavitation imaging from a different perspective: one of individual source localisation, rather than the current methods of overall energy mapping.

In order to assist this discussion it is first necessary to understand tumour biology and current imaging methods, including cavitation based imaging, in more detail. Thus the remainder of this chapter will focus on the relevant theory and the current state of the art in these topics.

1.1 Cancer Tumour Structure

The tumour microenvironment and vascular permeability play a crucial role in tumour development. Therefore it is necessary to examine some of the properties of tumour tissue in comparison to healthy tissue, and what the differences in tissue properties mean for the imaging, treatment, and ongoing monitoring of cancer tumours.

1.1.1 Healthy Tissue

Healthy tissue is well organised, with tightly controlled vascular permeability and regular vessel spacing [15]. This structure enables the efficient transport of oxygen and other nutrients from the capillary beds to most cells in the body [15]. Normally, arterial blood flows from large blood vessels via successively smaller vessels into regularly spaced capillary beds [15]. Once in the capillary beds, nutrients move

into the Extracellular Matrix (ECM) via diffusion and convection, with the diffusion limit for oxygen being approximately 100 µm in humans [16]. The endothelial barrier (composed of endothelial cells, support cells known as pericytes, smooth muscle cells, and the basal membrane) ensures selective molecular exchange and maintains tissue homeostasis [4]. Nutrient and molecule exchange can occur either through blood vessel cells (transcellular transport for small molecules approximately 3 nm in size), or between the cells via adherance, tight, and gap junctions (paracellular transport for molecules greater than 3 nm) [4].

1.1.2 Tumour Vasculature

In contrast to healthy tissue, the solid tumour microenvironment is highly irregular in terms of vessel spacing, structure and number of cells [16]. This is due to the formation of tumour vasculature under excessive pro-angiogenic signalling, which leads to irregular vessel structure, and allows for large gaps in the endothelial barrier through which molecules can escape (known as 'extravasation') [17]. Due to the large spacing between vessels, the distance from some tumour cells to the nearest blood vessel is greater than the maximum oxygen diffusion distance [16]. This creates significant oxygen gradients within the tumour, with associated regions of normoxic cells near the blood vessels and hypoxic cells further from the vessels [16].

Compounding this effect is the ability of tumour cells to circumvent usual cell division controls [18]. This allows for rapid tumour expansion, usually faster than angiogenesis, and causes an increase in the size of hypoxic areas in the tumour [16]. In addition, hyperproliferation causes the compression of intratumoural lymphatics, thereby limiting the clearance of metabolic products such as lactic and carbonic acid and thus lowering the pH of the microenvironment [16].

Finally, the tumour and stromal cells also assemble the ECM, which has been shown to resist the flow of molecules in the tumour [19]. The suppressed lymphatic system, dense ECM structure, and irregular vasculature all contribute to a high Interstitial Fluid Pressure (IFP) within the tumour [16].

1.1.3 Enhanced Permeability and Retention

From the perspective of tumour vasculature imaging, and from the perspective of targeted drug delivery, one of the most important differences between healthy tissue and tumour tissue is the Enhanced Permeability and Retention (EPR) effect [20]. This effect describes the ability of molecules to pass from blood vessels into tumour tissue relatively easily and remain there for a significant period of time [20]. The effect is as a result of leaky vasculature coupled with the limited lymphatic clearance of tumours [21].

EPR forms the foundation of a large class of targeted drug delivery that is based on molecule size, and its discovery has motivated a significant amount of work in the field of nanomedicine [22]. However, the cost of developing targeted drugs is high, and their effectiveness among tumours is variable due to highly heterogeneous EPR effects between tumour types and locations [20][23].

Specifically, different tumours exhibit different pore sizes, which limits the maximum size of particle that can extravasate into the ECM. Variability in pore size is evidenced by the different maximum pore sizes reported by several studies (which range between 200 and 700 nm) [19][22][24][25][26]. Unfortunately, the size of new antineoplastic agents is relatively large (for example, gene targeting vectors and encapsulated carriers are now approximately 300 nm), and while larger, more complex particles may be more effective in treating cancer cells, they are more difficult to deliver to tumour tissue [25].

Therefore, knowledge not only of vascular permeability, but also of pore size, is of critical importance in selecting treatment drugs [23]. Unfortunately, current imaging techniques that measure vascular permeability cannot determine pore size beyond the size of the contrast agents used, as explained in the following section.

1.2 Cancer Imaging Techniques

At present there are several major imaging techniques used by clinicians to identify and stage human cancer tumours [27]. While some techniques are more suitable for imaging different locations and types of cancer, all have either technical or practical limitations that restrict their ability to image the tumour microenvironment [5] [27]. A brief discussion of each major technique follows, with specific reference to the ability of the technique to identify tumour microenvironment characteristics.

1.2.1 Magnetic Resonance Imaging (MRI)

MRI is a non-invasive imaging technique suitable for imaging almost all areas of the body [28]. MRI works by aligning atoms in the body using a strong magnetic field, exciting them with a Radio Frequency (RF) electromagnetic pulse, and detecting the RF energy emitted by atoms as they return from the excited (high energy) state to the ground state [29]. MRI Signal to Noise Ratio (SNR), and hence sensitivity, can be improved by increasing the magnetic field strength used. Most clinical scanners use fairly modest field strengths of 1.5 - 3 Tesla, and these scanners have a typical in-plane spatial resolution of $0.5\,\mathrm{x}\,0.5\,\mathrm{mm}^2$ [30]. Ultra high-field scanners, with field strengths of 7 Tesla and above, have vastly improved resolution. The strongest clinically approved MRI scanners have a field strength of 7 Tesla, and can achieve a spatial resolution of approximately $0.2\,\mathrm{x}\,0.2\,\mathrm{mm}^2$ [31]. Scanners of 9.4 Telsa approved for research use can further achieve an in-plane resolution of $0.13\,\mathrm{x}\,0.13\mathrm{mm}^2$ in humans, without motion correction techniques [32]. Although increasing the field strength improves spatial resolution, these higher field strengths also pose problems, such as increased tissue heating and the creation of standing waves [27]. A more practical approach to improve MRI image quality is to use contrast agents that affect the properties of water signals in the region of interest [6].

Various types of contrast agents are used, and more recently, contrast agents have been used in conjunction with magnetic biomarkers for molecular imaging (the vi-

sualisation and tracking of molecular processes) [33]. MRI contrast agents range in size, but are typically in the order of a few nanometres and hence can escape from the blood vessels into the tumour microenvironment via the EPR effect [6][34]. This means that these contrast agents are suitable for assessing the tumour microenvironment. As previously discussed, this is most commonly achieved through DCE-MRI, which involves taking a baseline measurement and re-imaging after an injection of contrast agent to observe excursions from the baseline [5].

Typically, two parameters are obtained from DCE-MRI [6]:

- Volume Transfer Constant, K_{Trans}, which indicates vascular permeability, and
- Extravascular and Extracellular Space (EES) volume fraction, v_e, which measures the interstitial volume in a 3D volume of tissue.

While this information is useful, DCE-MRI suffers from several limitations. Notably, the technique relies on changes that are not linearly related to the amount of contrast agent present, and therefore requires a model and specialised image analysis to extract information about tumour vasculature [5]. Variations in data interpretation between institutions can make standardisation and comparison of DCE-MRI data very difficult [5][6]. In addition, the K_{Trans} term is a combination of vascular permeability (dependent on number of pores and pore size), flow rate and surface area of vessels for a given imaging region or voxel [6]. Therefore an assessment of permeability to large size molecules is not obtained with this technique.

Other more practical considerations such as the large size of MRI machines and the high cost of scans can limit the use of this imaging modality. These factors become more significant under the consideration that the largest increase in number of cancer cases will occur in low- and medium-income countries [3].

1.2.2 X-Ray Computed Tomography (CT)

X-rays are often used for diagnosing bone cancer, and 3D X-Ray Computed Tomography (CT) scans can be used for non-invasive imaging of most areas in the body [27].

A CT scanner acquires images by first transmitting multiple x-ray scans through the body, and then constructing an image using backprojection [29]. The resolution of a typical CT scan is similar to that of an MRI, and CT image contrast can also be enhanced by the use of contrast agents during scan acquisition [27]. DCE-CT can obtain similar information to that obtained by DCE-MRI, and the relationship between the amount of contrast agent and the received signal is linear, thereby simplifying the image processing required [5].

As CT scans rely on changes in density, they are most effective at identifying cancer tumours where the density of the tumour is different to that of the surrounding tissue, or where the shape of the tumour indicates that the structure is anatomically anomalous. Where tumours are small and have similar structural characteristics to the surrounding tissue, CT scans can be used in conjunction with functional imaging techniques such as Single-Photon Emission Computed Tomography or Positron Emission Technology (discussed in greater detail in the following subsections) to assist in identifying tumours.

However, CT scans are generally avoided where possible in order to limit the level of ionising radiation received by a patient [35]. In addition, the use of contrast agent is restricted due to the high concentrations required [27]. Similar to MRI, other practical factors that may limit the use of CT scanners are machine size and cost.

1.2.3 Single-Photon Emission Computed Tomography (SPECT)

SPECT is a 3D non-invasive functional imaging technique that detects photons emitted from radioisotopes injected into a patient before imaging [27]. SPECT has the ability to image metabolic processes in the body with a resolution of approximately 10 mm [27]. With a size of approximately 1 nm, radioisotopes leak out of vasculature and accumulate in various tissues, thereby indicating the presence or absence of certain types of tissue in the body. For example, thyroid tissue readily absorbs iodine, and therefore SPECT with radioactive iodine can be used to detect whether a thyroid carcinoma has metastasised to other parts of the body [36]. Antibodies asso-

ciated with certain tissues or biological processes can also be linked to radioisotopes and used in SPECT imaging to indicate the presence or absence of these tissues or biological processes [37].

Although useful in detecting the presence or absence of certain types of tissue, SPECT requires the use of radioactive isotopes, and therefore is not suitable for certain patients. In addition, SPECT resolution can limit its usefulness in the exact localisation of small tumours, and due to the high attenuation of photon energies by human tissue, SPECT sensitivity is relatively low [27].

1.2.4 Positron Emission Technology (PET)

Positron Emission Tomography (PET) is a 3D non-invasive functional imaging technique for imaging metabolic processes [27]. Like SPECT, PET operates on the principle of Emission Tomography, however PET images the photons created during the annihilation of a positron and an electron, rather than the photons directly emitted from positrons [27]. As an annihilation event produces photons that travel in opposite directions, PET detects a signal on two opposite detectors and uses the difference in time-of-flight of each signal to localise the source [27]. PET therefore has a slightly better resolution than SPECT (approximately 8mm) [27]. PET scanning with the tracer fluorine-18 fluorodeoxyglucose (a glucose analog) is most often used for the detection of cancer metastases due to its high uptake by cancer cells [38]. PET also has the highest specificity for the detection of hypoxia in tumour tissues [38], and can be used in conjunction with CT scans to create a functional and structural 3D image of a patient.

However, as with SPECT, PET scans require the injection of positron emitting radionucleotides, which may limit its use [27]. In addition, PET isotopes are typically more expensive and less readily available than SPECT isotopes [27].

1.2.5 Optical Imaging

Optical Imaging describes the collection of imaging techniques that use visible, ultraviolet and infrared light for imaging purposes. Optical imaging techniques are compact, low cost, and can provide functional and molecular information [39]. The two major types of optical imaging operate on the basis that tissues either reflect or scatter light [27]. While optical imaging has extremely good spatial resolution (approximately 10 µm), optical penetrance is limited and hence optical techniques are restricted to use on tumours close to the imaging device [27].

1.2.6 Photoacoustic Imaging

Photoacoustics is the generation of acoustic waves from an object undergoing transient thermoelastic expansion following the absorption of pulsed or intensity modulated optical irradiation [40]. Photoacoustic imaging therefore combines optical excitation with acoustic emission detection in order to image various endogenous particles, including haemoglobin and melanin [41]. In addition, physiological properties such as haemoglobin oxygen saturation are closely linked to optical absorption, and can therefore also be distinguished [41]. The resolution of photoacoustic imaging is in the order of 5 - 800 µm, but since the excitation is still optical, the technique is limited to relatively shallow depths (0.7 - 50 µm) [41].

1.2.7 Ultrasound (US)

Ultrasound is a non-invasive imaging technique that utilises the propogation and reflection of sound waves in tissue in order to create images [8]. Ultrasound for therapeutic and diagnostic purposes has been used for several decades, but recent advances have enabled the use of ultrasound for blood flow analysis (with Doppler Imaging), tissue elastic properties (with Elastography), and volumetric imaging (with multiplane and 3D ultrasound) [42].

The advent of Contrast Enhanced Imaging using microbubbles has allowed for the imaging of the blood supply to tissues, a process known as perfusion imaging [42].

Microbubbles are strong reflectors of ultrasound and as such can be used to amplify signals from small vessels which would otherwise be below the noise floor [8]. In addition, microbubbles can be functionalised by adding ligands (small molecules that can bind to proteins) to their surface, in order to target important tumour biomarkers such as inflammation, angiogenesis and early tumour formation [8]. In this way, these targeted microbubbles can be used to assess certain biological and molecular processes involved in tumour growth. Under certain conditions, non-linear scattering from bubbles transfers energy from the fundamental frequency into higher harmonics [8]. Therefore, when contrast agents are present, images can be improved with imaging techniques that rely on signals from non-linear scatterers, for example Tissue Harmonic Imaging and Pulse Inversion Imaging (discussed further in Section 1.3.2).

The use of contrast-enhanced ultrasound for both perfusion imaging and to assess biological processes provides several advantages over other modalities. Most notably, it is low-cost, portable, and does not use ionising radiation, and therefore has very few patient restrictions. However, ultrasound imaging has limitations in terms of locations that can be imaged (for example, areas with acoustic impedance significantly different to that of soft tissue cause large reflections and are therefore difficult to image).

Another limitation is that the size of contrast agents (in the order of a few micrometers) prohibits their extravasation out of the vessels, meaning that ultrasound cannot be used for vascular permeability assessments [8].

To overcome the size limitation of microbubbles, recent work has focussed on the use of another type of contrast agent, known as a droplet. Droplets are typically made of a perfluorocarbon liquid, and exhibit some echogenicity, although they typically have substantially less contrast than microbubbles since they act as weak scatterers [43]. However, droplets do exhibit greater stability than microbubbles in circulation, and furthermore can be manufactured in the sub-micron range, which would allow them to be used to assess vasculature permeability [44]. To assist in allowing the droplets to be imaged with ultrasound, a type of droplet that has the ability to change phase from liquid to gas has been introduced. This ‘Phase Change

Contrast Agent' is typically made with liquids that have boiling points close to body temperature [45] and which can be tipped from a liquid into a gaseous state by the application of sufficient acoustic energy. Thus phase change contrast agents provide the benefit of being in the size range required for extravasation from vessels (100 - 500 nm), and also allow for highly echogenic contrast imaging once they have transitioned from a liquid droplet into a gaseous state [44].

Other recent advances using nanodroplets include functionalisation for targeting specific tumour biomarkers, and nanodroplet loading for delivery of therapeutic payloads [45][46][47]. Furthermore, significant advances in the imaging of droplets with ultrasound have been achieved through the use a super-resolution imaging technique combined with sparse activation of nanodroplets, called Acoustic Wave Sparsely Activated Localization Microscopy (AWSALM) [48].

Although there are several clear benefits of using nanodroplets for ultrasound contrast imaging, there are also several factors that have limited their widespread adoption. First, unlike microbubbles, low concentrations of nanodroplets cannot be imaged with ultrasound until they have undergone a phase transition, which limits the ability of a clinician to accurately assess when the particles have reached their target site [43]. Second, the threshold for activation of droplets can be variable due to the different sizes of droplets present in a population, and the manufacture of droplets with a tightly controlled size on a large scale is extremely challenging [46][49]. Finally, whilst the nanodroplets have better stability in comparison to microbubbles, their stability is still poor in comparison to that of solid particles [50].

In addition to microbubbles and nanodroplets, a new solid polymer nanoscale particle has been created for use in ultrasound applications [9]. This particle is small enough to extravasate into tumour tissue, and therefore may be used to evaluate vessel permeability. However, due to the small size of the particle, its location can only be determined using cavitation based imaging. Thus the following section will include a more detailed discussion of the regimes and effects of cavitation.

1.3 Cavitation-Based Tissue Imaging

The use of focussed ultrasound in conjunction with micro- and nanoscale cavitation nuclei, for both diagnostic and therapeutic applications, is rapidly increasing. Many of these applications rely primarily on the physical effects caused by inertially and non-inertially cavitating bubbles. The primary diagnostic application of cavitation nuclei is for improving the Signal to Noise ratio (SNR) in Contrast Enhanced Ultrasound and Doppler Imaging [51] [52]. Examples of therapeutic applications of Focussed Ultrasound (FUS) that rely on cavitation effects, both with and without added cavitation nuclei, include ultrasonic heating of tissue for ablation of cancer tumours [53], sonothrombolysis for the dissolution of blood clots [54], enhanced drug delivery to tumours [55], opening of the blood-brain barrier for drug transport [56], and transdermal sonophoresis [57].

Two key factors have enabled these applications. First, the introduction of cavitation nuclei at the target site has allowed for inertial and non-inertial cavitation to be caused at relatively low pressure amplitudes. This has been essential in ensuring targeted interventions with minimal off-target side effects. Second, the development of real-time, non-invasive monitoring strategies has contributed to the assessment of safety and efficacy in many of the aforementioned applications, and hence increased their adoption. In this section, cavitation activity will be examined first, along with the associated therapeutic and diagnostic applications, followed by a discussion on the formation of cavitation nuclei and the development of cavitation nuclei for *in vivo* use.

1.3.1 Regimes of Cavitation

Bubble cavitation is generally described as being either inertial or non-inertial [58]. The type of cavitation activity depends on bubble size, excitation frequency, pressure amplitude and the presence or absence of a coating surrounding the bubble [58][59]. In order for cavitation to occur, a cavitation nucleus must either be created in the

medium, or must be pre-existing in the medium. In particular, the nucleation threshold defines the minimum pressure at which a cavitation nucleus will be created. The nucleation threshold in a pure liquid without exogenous nuclei can be found using classical nucleation theory, and is directly related to the energy required to overcome the intermolecular bonds of the liquid (the tensile strength of the liquid) [11][60]. For water, this threshold is predicted by classical nucleation theory to be approximately -140 MPa [60]. However, when impurities exist in the liquid, the threshold for cavitation is much lower, since microscopic pockets of gas can be trapped on the surface of impurities and then act as cavitation nuclei [61]. When bubbles or pockets of gas exist in a fluid, the minimum applied acoustic pressure at which a bubble will grow is dependent on the bubble radius, the ambient pressure and the surface tension of the liquid, and is given by a static threshold known as the Blake Threshold [10]. Each type of cavitation activity yields different physical and acoustic effects, described in greater detail below.

Non-Inertial Cavitation

At low pressure amplitudes bubbles tend to act as harmonic oscillators, expanding and contracting about an equilibrium radius following the rarefactional and compressional cycles of an incident pressure wave. However, as the pressure increases, a non-inertially cavitating bubble will scatter sound with increasing nonlinearity [59], and hence energy will be transferred from the fundamental driving frequency into higher harmonics.

In this regime, effects such as microstreaming and particle translation are prevalent [58]. Microstreaming describes fluid motion (usually circular) created near a small bubble, and is caused by asymmetrical bubble oscillation. The movement of particles (including bubbles) in the fluid is caused by a time averaged net force on the particles, known as the Acoustic Radiation Force.

Inertial Cavitation

In certain cases, a bubble can undergo rapid expansion followed by violent collapse. This violent collapse phenomenon is termed 'inertial cavitation', and several definitions are used to define the point at which a cavitation event is considered 'inertial'. For example, a bubble radius of at least two times the original radius [62], a bubble collapse velocity equal to that of the speed of sound of the medium [10], and a bubble temperature of 5000 K [63] have all been proposed as threshold points. Regardless of the exact definition selected, the point at which the bubble exceeds the selected threshold is the point at which inertial cavitation is said to occur. In order for growth of an existing bubble to occur, the Blake threshold pressure must be exceeded. However, the Blake threshold does not contain any information about the bubble collapse, and thus simply exceeding the Blake threshold does not guarantee that the conditions for inertial cavitation will be met for all acoustic regimes [64]. Rather, a method of determining the maximum bubble radius or the maximum temperature reached is required in order to ascertain whether inertial cavitation occurs for a given set of acoustic parameters [64]. Details of one such model are proposed by Apfel and Holland [63], who gauge the likelihood of inertial cavitation occurring (for an optimally sized bubble) as a function of pressure and frequency.

Violently collapsing bubbles generate extremely high core temperatures and pressures, and they can therefore produce effects such as heat deposition, sonoluminescence (light production from sound), shockwave formation, microstreaming, microjetting (where a re-entry jet travels through the centre of the bubble), and chemical reactions [58].

1.3.2 Non-Inertial Cavitation Applications

Notable therapeutic applications associated with non-inertial cavitation include reversible Blood Brain Barrier (BBB) opening for the delivery of therapeutic drugs into the brain [65], sonoporation of cell membranes for delivery of large molecules into cells,

and heat deposition through viscous absorption at the bubble boundary [58]. Several mechanisms have been proposed to explain why BBB opening and sonoporation are enhanced in the presence of non-inertially cavitating microbubbles, including mechanical stretching of the vessel wall due to enlarged bubbles and opening of junctions due to the shear stress from microstreaming effects [65].

In addition to therapeutic applications, the nonlinearity associated with non-inertially cavitating bubbles is also used in diagnostic imaging to enhance the resulting image. Specifically, Tissue Harmonic Imaging (THI) and Pulse Inversion (PI) Imaging both rely on nonlinear scattering by bubbles [42]. In THI, images are created from the second harmonic, rather than the fundamental frequency [42]. Therefore, contributions from linear reflectors such as the body wall can be eliminated [42]. PI Imaging involves transmitting identical pulses of opposite amplitudes and summing the received echoes [42]. Components of the signal from linear reflectors are received with equal but opposite amplitude and hence cancel out, thereby leaving the nonlinear components that were created primarily from the contrast agents [42].

1.3.3 Inertial Cavitation Applications

The therapeutic effects of inertial cavitation stem from the mechanical and thermal effects of a cavitation event. One of the most notable applications is the enhancement of thermal ablation of tumour tissue during High Intensity Focussed Ultrasound (HIFU) treatment [58]. The broadband emissions from inertially cavitating bubbles contain high frequencies that are readily absorbed in tissue (as tissue absorption contains a frequency dependent term described by frequency raised to the power 1.1) [58]. In addition, it has been shown that cells next to an inertially cavitating bubble can be mechanically destroyed, and phenomena such as jetting and microstreaming can also be used to assist drug delivery into cells [58].

Some of the therapeutic applications of inertial cavitation have not been clinically realised due to the lack of a truly real time, non-invasive monitoring system with resolution suitable for clinical application [66]. In order to overcome this limitation,

Gyöngy *et al.* [66] developed Passive Acoustic Mapping (PAM), which directly maps sources of nonlinear acoustic emissions (including broadband emissions) and does not require any prior knowledge about the precise timing of cavitation events.

Due to the potentially damaging effects of inertial cavitation, it has typically been avoided as a method for diagnostic imaging, and careful attention must be paid to the safety of any technique relying on cavitation mechanisms. For example, in contrast enhanced blood flow imaging, microbubbles in a region are destroyed by low frequency, relatively high pressure 'diagnostic' pulses in order to then assess the time it takes for new microbubbles to flow into the region (reperfusion time). Different mechanisms of microbubble destruction have been described, including both bubble fragmentation and inertial cavitation, and the method of microbubble destruction in these studies will typically depend on the acoustic parameters used in the study as well as on the composition of the microbubble. Often a metric known as the Mechanical Index (MI) is used to determine the safety of diagnostic ultrasound imaging [63][67]. The MI was derived to demonstrate the minimum acoustic pressure required for a single cycle pulse at a given frequency to cause inertial cavitation (defined as the bubble temperature reaching 5000 K) in an optimally sized bubble [63]. The threshold does not take into account the increased likelihood of cavitation with multiple cycles. Furthermore it is not necessarily correlated with the onset of bioeffects [63]. However it is widely used by radiologists and displayed on clinical ultrasound scanners as a safety metric, and thus it is an important consideration in the proposal of any new imaging technique. MI is directly proportional to the applied pressure. The ability to cause controlled inertial cavitation in a target region at the lowest possible pressure amplitudes (for example, by using cavitation agents with a low inertial cavitation threshold), ensures that a relatively low MI can be used. The ability to use the lowest possible pressures overall will ultimately help to ensure that significant tissue damage to off-target regions (through heating or unintended cavitation of native cavitation nuclei) is minimised. Within the target region to be assessed, if the overall level of cavitation can be closely monitored and controlled, then it is possible to create a

level of cavitation that, although detectable, does not cause any large scale damage to the surrounding tissue (even though individual inertial cavitation events may have some thermal and mechanical effect on their immediate, local, surroundings). Such a regime, although not strictly diagnostic, could be used for ascertaining information without causing significant changes to the tissue being assessed. Before such a regime could be implemented however, an extensive study to assess morphological changes to cells, microvasculature and other tissue structures would need to be conducted[1]. In addition, further histological investigations and assessment of inflammation markers in the blood would also be required before the overall safety of the technique can be determined.

1.3.4 Passive Acoustic Mapping (PAM)

To visualise cavitation activity, a real-time monitoring technique is required. Several such techniques exist, such as interleaved B-Mode monitoring [68] and MRI [69], but these methods are either impractical or do not directly measure inertial cavitation in real time, and hence are not suitable for mapping extravasated nanoparticles. However other techniques for passive mapping of sound have also been developed. For example, passive sonar mapping with two or more receive elements has been in use since the early part of the twentieth century, and has been used in naval applications in particular [12]. Similarly, passive acoustic detection of cavitation, with a specific focus on cavitation that occurs in biological systems, has been in use since the 1980s [70]. Mapping of cavitation with diagnostic ultrasound systems was implemented by Farny [13][71] and further detailed by Gyöngy with the specific intent of overcoming the limitations of B-Mode and MRI based monitoring strategies [14]. Since then, multiple other implementations of PAM have been developed, and are discussed in more detail in Section 4.3.1. During PAM, acoustic signals from col-

[1]To date, unpublished work conducted by Prateek Katti, a DPhil student at the University of Oxford, in conjunction with Oxford Nanopore Imaging (ONI), have observed no visible damage in histological sections of murine colorectal cancer tumour tissue following a treatment involving significant levels of inertial cavitation caused by the nanoscale cavitation agents known as 'nanocups'.

lapsing bubbles are passively recorded on a set of receivers. The received signals are then filtered and combined using one of several beamforming techniques in order to generate an estimate of the power of wideband sources in a region, and hence to generate maps of the cavitation energy, and ultimately the spatial distribution, of sources in that area. If a source is located within the target region, then the time delayed signals will interfere constructively when the beamformer is steered to that pixel, and destructively when the beamformer is steered to another location [66]. PAM therefore does not require any information about the initial source excitation signal, and is capable of localising any source of nonlinear acoustic emissions provided that sufficient amplitude is received. In order to map an extended region of cavitation, a passive beamforming algorithm known as Time Exposure Acoustics (TEA) was implemented in [66], and was followed by several other implementations of passive mapping techniques [72][73][74][75][76][77][78]. A more detailed review and discussion of these techniques is given in Chapter 4 of this thesis, where a new passive source localisation algorithm is also proposed.

The resolution of PAM varies based on the type of beamformer used, and is further dependent on the diffraction pattern of the detector [59][79]. At present though, it is useful to state the theoretical axial and transverse resolution limit for a simple delay-and-sum PAM algorithm, TEA-PAM. The limit represents the minimum distance required between two point sources for them to be distinguishable in an image. The full derivation of the limits for axial and transverse resolution can be seen in [80]. The result presented here is taken directly from that work:

$$\Delta z_{Axial} = 6.95 \left(\frac{z}{D}\right)^2 \lambda \tag{1.1}$$

$$\Delta x_{Transverse} = 0.89 \left(\frac{z}{D}\right) \lambda \tag{1.2}$$

where D is the linear array aperture, z is the distance between the source and the array, and λ is the wavelength. As can be seen from the resolution equations,

increasing the array aperture can improve resolution, which is essential for mapping extravasated particles. This can be achieved by the use of multiple receive arrays, however the geometric space requirements for larger apertures may not always be practical, and thus these setups can have limited clinical applicability.

PAM can also be extended to 3D volumetric imaging by use of a 2D receiver array, as demonstrated by Coviello *et al.* [74]. In order to overcome the practical challenges of creating a full 2D receiver array, the authors created a sparse boundary array using Polyvinylidene Difluoride (PVDF) sensor technology, and used the concept of a co-array to synthesise a fully fledged 2D weighted aperture [74]. Results show that this system is able to correctly identify a cavitation region. However, in order to make the technology more clinically relevant, further work in array design (to improve resolution) and beamforming algorithms (to deal with partial array occlusions such as ribs) is necessary [74].

1.3.5 Cavitation Nuclei

The discussion up to this point has assumed that cavitation nuclei are present for all therapeutic and imaging applications. In reality however, cavitation nuclei in human tissue are not abundant in clinically relevant quantities and forms, and thus it is usually necessary to inject cavitation nuclei in order to utilise non-inertial and inertial cavitation phenomena.

One such cavitation agent consists of microbubbles, which as previously mentioned, are extremely useful as contrast agents. Whilst the use of these types of cavitation nuclei enable many treatments, there are two factors that limit their applicability. First, the large size of microbubbles relative to human vessel pore sizes confines these agents to act within blood vessels, and consequently their use in imaging regions outside of the vasculature (for example, the tumour microenvironment around a vessel), is limited [8]. This is true even in vessels with large pore sizes, such as those found in the leaky vasculature of cancer tumours, where pore sizes range from approximately 100 to 1200 nm [19] [22] [24] [25] [26]. Second, while some types

of microbubbles can be stable in circulation (for example, polymer-shelled microbubbles), others have limited stability [81] and are rapidly destroyed if inertial cavitation is initiated by Focussed Ultrasound (FUS). Rapid destruction of microbubbles due to cavitation allows for good SNR in cavitation based imaging, but also significantly reduces the population of nuclei left for imaging longer processes. Hence in some imaging scenarios, a cavitation agent with the ability to sustain cavitation over longer periods of time, either due to the number of cavitation nuclei or due to the ability of nuclei to re-stabilise gas particles, would be advantageous.

A recently introduced ultrasound responsive cup-shaped polymeric nanoparticle with trapped gas in its cavity (know as a 'nanocup') has been shown to successfully initiate and sustain exclusively inertial cavitation activity over prolonged periods of time when compared to commercially available micron-sized cavitation agents [82]. Due to its size and acoustic properties, it has exciting potential applications in diagnostic cavitation based imaging, and so is discussed in more detail in the next subsection.

1.3.6 Nanocups

A nanocup is a polystyrene based particle between 100 and 800 nm which contains a cavity in which an air bubble is stabilised. Nanocups are formed from a seeded polymerisation technique in which polystyrene beads are coated with a cross-linked polymethyl methacrylate (PMMA) polymer [9]. Polymer-polymer interactions between the core and the copolymer shell cause the core to expand, whilst osmotic forces deform the shell to form the depression characteristic of the cup shape [9]. Nanocups can also be fluorescently labelled during fabrication and, when dried, entrap an air bubble in the cup cavity.

The air bubble trapped in the nanoparticle cavity is the nucleation agent, and therefore the response of the nanocups to ultrasound is largely determined by the size of the air bubble and the contact angle between the air bubble and the solid nanoparticle cavity [9]. More specifically, the smaller the solid nanoparticle, the

smaller the bubble that will be entrapped in the particle depression. As predicted by the Rayleigh-Plesset Crevice Model, higher acoustic pressure at any given frequency is then required to achieve inertial cavitation of a small bubble compared to a large bubble [82].

Several properties of these nanoparticles make them preferable for use in a biomedical context over existing clinical microbubble agents. First, even though the particles are significantly smaller than clinically used microbubbles, the cavitation threshold of the particles is still situated at relatively low pressures (achievable by diagnostic ultrasound) [82]. Although theory predicts that the maximum bubble size should be dependent on the magnitude of the pressure used, Kwan *et al.* experimentally observed that after the inertial cavitation threshold has been reached, maximum bubble diameter does not increase significantly with increasing pressure [83]. Further work specifically focussed on nanobubble nucleation from a crevice model is needed to reconcile this theoretical and experimental difference. However, the experimental observation implies that reasonable pressure amplitudes can be used to create inertial cavitation without a substantial decrease in received SNR when compared to current microbubble agents.

Secondly, where the population of microbubbles is rapidly depleted due to bubble destruction as a result of inertial cavitation, a single injection of nanocups can continue cavitating for significantly longer periods of time [9], thereby eliminating the need for multiple injections or long infusions of microbubbles when ultrasound contrast is required *in vivo* for long periods of time.

Thirdly, due to their composition, the nanocups are non-toxic *in vivo*, and are cleared from the circulation by specialised phagocytotic cells (cells that ingest foreign particles in the body) known as Kupffer cells, which are situated in the liver [9][84]. Although still under investigation, this clearance mechanism has been verified through preliminary experiments which suggest that nanocups are primarily cleared from circulation within 90 minutes of administration (at human physiological flow rates), captured by Kupffer cells in the liver within 24 hours, and ultimately fully excreted

into the bile[2].

Finally, one of the most significant benefits of using nanoparticles as cavitation nucleation agents is that they are in the size range of the tumour pores. Recent work has demonstrated that nanocups, under ultrasound exposure, facilitate drug extravasation through the leaky tumour vasculature, thereby providing improved penetration and distribution of the drug into tumour tissue when compared to delivery of the drug alone [9]. Previous studies have also investigated the role of inertial and non-inertial cavitation both *in vitro* and *in vivo* [85][86]. These studies demonstrate drug delivery in the presence of nanocups, but have not investigated the potential for nanocups to be used as markers of tumour vasculature permeability, following either passive, or ultrasound-assisted active delivery through the leaky endothelium.

1.4 Summary

The discussion and review of the tumour micro-environment and imaging methods presented in this section demonstrates a need for new methods of vasculature assessment. Specifically, the use of nanoscale cavitation agents, in conjunction with passive acoustic mapping strategies, offers a promising approach to assessing vasculature permeability to compounds that are of a similar size to advanced, large-molecule cancer therapeutics. The next chapter will therefore aim to establish whether nanoscale cavitation nuclei, once extravasated under ultrasound excitation, are still acoustically active, and whether they can be non-invasively located in a tissue-mimicking phantom.

[2]The verification of the clearance mechanism described here was confirmed via histology from unpublished work performed at the Oxford based company, OxSonics Ltd

Chapter 2

Passive Acoustic Mapping of Extravasated Particles *In Vitro*

The literature review of the previous chapter has highlighted the significant therapeutic applications of both non-inertial and inertial cavitation, in conjunction with passive mapping techniques. One area of research that has not yet been evaluated is the use of extravasated cavitation nuclei for diagnostic purposes. Therefore the research goals addressed in this chapter are:

- First, to ascertain whether solid cavitation nuclei (nanocups), once extravasated under Focussed Ultrasound (FUS), can be re-excited using ultrasound.
- Second, to determine whether the localisation of extravasated nuclei can be achieved with clinically relevant spatial resolution.

This chapter focusses on *in vitro* work completed to answer these research questions and is divided into four sections: Background, Experimental Design, Results, and Discussion. The Background section describes the manufacture and properties of the cavitation nuclei used in this work, in addition to detailing the Passive Acoustic Mapping (PAM) techniques used. Other methods of passive localisation are discussed in Chapter 4.

The Experimental Design section then describes the design and implementation of an *in vitro* experiment for extravasation detection and mapping. The selection of

acoustic parameters and offline acoustic and image processing parameters are also presented.

The results of the experiment are then described and compared for a selection of beamformers. The chapter ends with a discussion of the performance benefits and drawbacks of different beamformers, with specific emphasis on clinical translation.

Some work in this chapter was completed as part of a collaboration with Dr Erasmia Lyka, a post-doctoral researcher within the Biomedical Ultrasonics Group at the University of Oxford. Specifically, the determination of the optimal PAM threshold presented in section 2.2.4, and the processing of the recorded data using a PAM beamformer known as the Robust Linear Programming Beamformer was preformed mainly by Dr Lyka. These sections of work are still presented in this chapter for completeness in the overall assessment of re-excitation and mapping of extravasated particles.

2.1 Experiment Materials and Methods

2.1.1 Experimental Procedure

A series of flow channel experiments were performed in a vertically oriented flow channel embedded in an agarose (agar) gel phantom, as shown in figures 2.1 and 2.2. The experimental procedure was as follows. First, nanocups were pumped through the flow channel at a constant rate of 0.3 ml/min using a syringe pump (Aladdin Single Syringe Pump, AL-1000, World Precision Instruments, Hertfordshire, UK). Initial ultrasound excitations were then performed using a dual HIFU transducer configuration with the aim of causing extravasation of the nanocups from the flow channel into the surrounding phantom material. The flow channel was then flushed for 30 minutes with ultrapure, degassed water. The flow of water was halted and a second sonication was performed at each target location, with the aim of re-exciting nanocups that had been embedded in the phantom material during the initial sonication. During both the initial and second sonications, acoustic emissions were recorded on two L11-

4 linear arrays using a Verasonics Vantage 256 channel research ultrasound system. Once the sonications were complete, the phantom was removed and cut transversely and in cross section in order to verify the location of extravasated particles using fluorescence microscopy with a Nikon TI Eclipse microscope.

From figure 2.1 it can be seen that the axial-transverse planes of both ultrasound transducers are perpendicular to the long axis of the flow channel. When cut transversely, a significant part of the long axis of the channel is visible on microscopy (with the edges of the channel appearing as two parallel lines), and the incident direction of the ultrasound is out of plane relative to the microscopy slide. When cut in cross section, the full circular border of the channel is visible, and the incident direction of the ultrasound is in plane with the microscopy slide.

In typical drug delivery applications, a cavitation agent is used in combination with a drug. However, in this experiment an additional drug is not added to the system, but rather the nanocups themselves are assumed to act as a model drug. This is because the nanocups have been designed to have a comparable overall size (300 - 500 nm) to many of the larger therapeutic agents for which they are meant to aid extravasation, including oncolytic viruses (100 - 300 nm), liposomes and polymerosomes (100 - 250 nm) and, to a lesser extent, therapeutic antibodies (10 - 30 nm). Only a subset of the nanocups are activated within any one acoustic pulse. Thus the remaining fluorescently labelled particles act as an adequate free drug model, since comparable transport length scales for nanocups and model or real co-administered drugs have been previously demonstrated [9][87].

2.1.2 Phantom Design

The available phantom materials are numerous, and many aim to emulate specific characteristics such as speed of sound, density and attenuation in soft tissue. Some common tissue mimicking materials include agar, gelatin, polyacrylamide gel, polyvinal alcohol gel, and silicone [88]. Of specific interest in this project is the pore size of the gel, which should be similar to that of a tumour vessel. Of the gels mentioned,

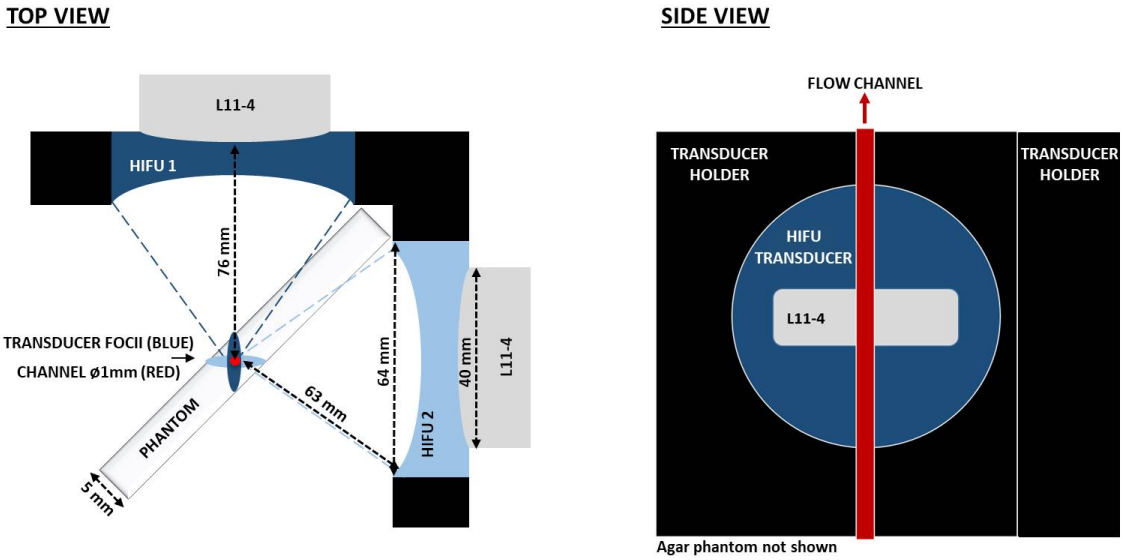


Figure 2.1: Left: Top view of the experiment setup showing two confocally aligned FUS transducers, with two L11-4 linear arrays coaxially aligned with each transducer. Right: Side view of the experiment setup showing the flow channel (red) at the focus of the FUS transducer and L11-4 array.

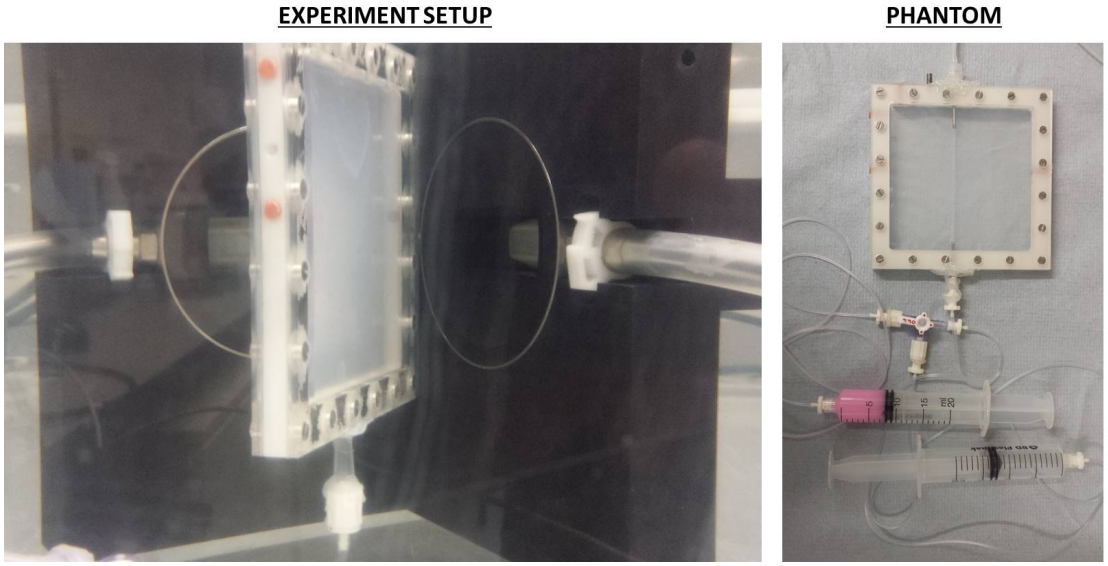


Figure 2.2: Left: The experiment setup showing an agar phantom with flow channel placed at the focus of two HIFU transducers and two L11-4 linear arrays. Right: The Phantom showing a flow channel in agar surrounded by a plastic frame, with flow channel tubing attachments on the top and bottom, and the syringes containing fluorescent nanocups (pink) and degassed water.

agar can exhibit pore sizes from lower than 100 nm up to 1200 nm [89], which makes it ideally suited to model tumour vessels. To prepare the phantom, a 1% by weight solution of Ultrapure Low Melting Point agar powder (ThermoFisher Scientific Inc., Waltham, MA) was mixed into filtered, de-ionised water and degassed for a minimum of 30 minutes, heated to 70 °C, poured into a phantom mould containing a 1 mm diameter stainless steel rod in the channel position, and then left overnight to set in a 4 °C fridge. Once set, the steel rod was removed, leaving an agar bounded flow channel.

2.1.3 Cavitation Nuclei

Currently, the three main options for cavitation nuclei are microbubbles, nanodroplets and nanocups. Of these, only nanodroplets and nanocups exhibit a size larger than that of healthy pores (in the order of tens of nanometres), and small enough that they can still be delivered through leaky tumour vessels (with pores of approximately 200 to 700 nm) using ultrasound [82][90]. In addition, both microbubbles and nanodroplets are rapidly depleted during inertial cavitation, however nanocups persist in cavitation for far longer timescales, mainly due to the large number of nuclei present in a sample [82][91]. In addition, because nanocups contain a solid nanoparticle, their post-extravasation location can be easily verified using fluorescence microscopy. Due to these characteristics, nanocups are ideally suited for use in these experiments.

The process for fabricating nanocups is briefly described in Section 1.3.6 and fully described in [9]. The cups used in these experiments are polystyrene based, cup shaped particles with a mean diameter of 420 nm, as measured by Dynamic Light Scattering (DLS) on a Zetasizer Nano (Malvern Panalytical Ltd, Malvern, UK), and shown in figure 2.3. The particles produced exhibit the characteristic 'cup' shape in which air can be entrapped during the process of re-suspension of dried cups in water. The shape was visually confirmed by viewing samples with a Transmission Electron Microscope (TEM) (located at Oxford Brookes University, Headington Campus, Headington Rd, Oxford, UK). In addition, the cups were fluorescently labelled

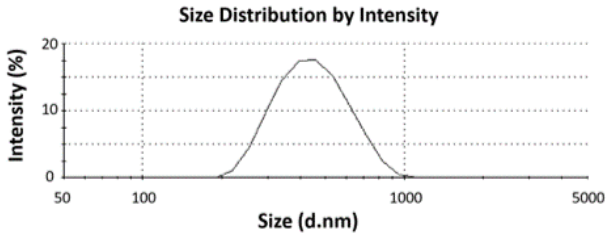


Figure 2.3: Dynamic Light Scattering measurement of nanocup size (Zetasizer Nano, Malvern Panalytical, Worcestershire, UK) indicating mean size of 420nm, with a Polydispersity Index of 0.08.

with Nile Red dye (Sigma-Aldrich Inc., Merck KGaA, Darmstadt, Germany) during fabrication.

Under ultrasound excitation, these nanocups exclusively exhibit inertial cavitation above a certain pressure threshold, and this cavitation threshold increases as the size of the entrapped gas bubble decreases. The entrapped gas bubble is assumed to have the same diameter as the cavity diameter (or inner diameter) of a nanocup. Kwan et al. demonstrate that for nanocup cavity diameters of 100 nm, the inertial cavitation threshold is approximately 2 MPa at 0.5 MHz, and decreases below 1 MPa peak rarefactional pressure for cavity diameters greater than 300 nm [82]. In this set of experiments, the smallest measured particle size was approximately 200 nm (as shown in figure 2.3). Thus the minimum cavity diameter is assumed to be between 100 and 200 nm. This minimum size range was used to determine the selection of acoustic pressures described in section 2.1.4.

2.1.4 Acoustic Setup

Focussed Ultrasound: Two 0.5 MHz confocal HIFU transducers (H107, outer diameter 64 mm, focal length 63.2 mm, Sonic Concepts, Bothell, WA) with Full Width Half Maximum (FWHM) focal width of 3 mm and FWHM focal depth of 21 mm were arranged as shown in figure 2.1. Each transducer has a 45 x 20 mm rectangular cutout, and is placed in a custom transducer holder such that the transducers remain perpendicular to each other. The dual transducer setup was used to increase spatial

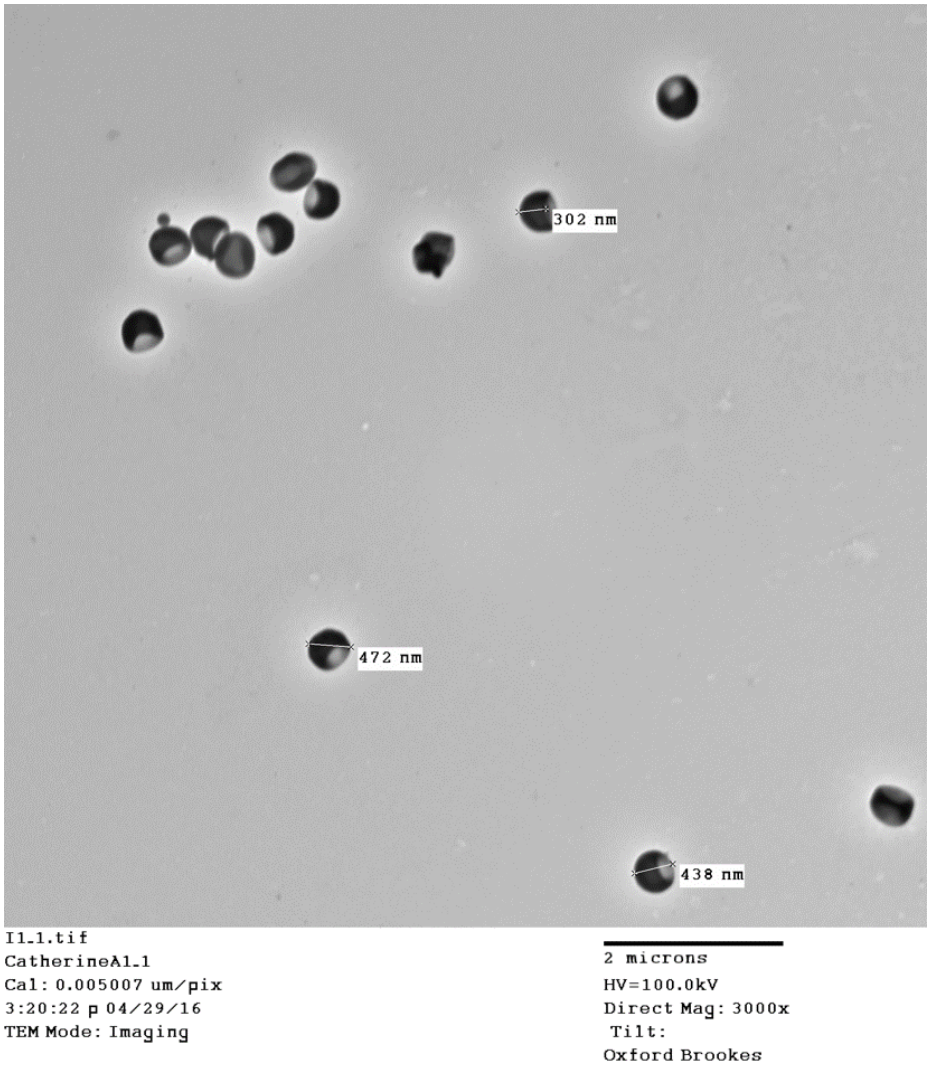


Figure 2.4: A TEM image of fabricated nanocups showing the characteristic cup deformation, and showing a diameter in the region of 400 nm.

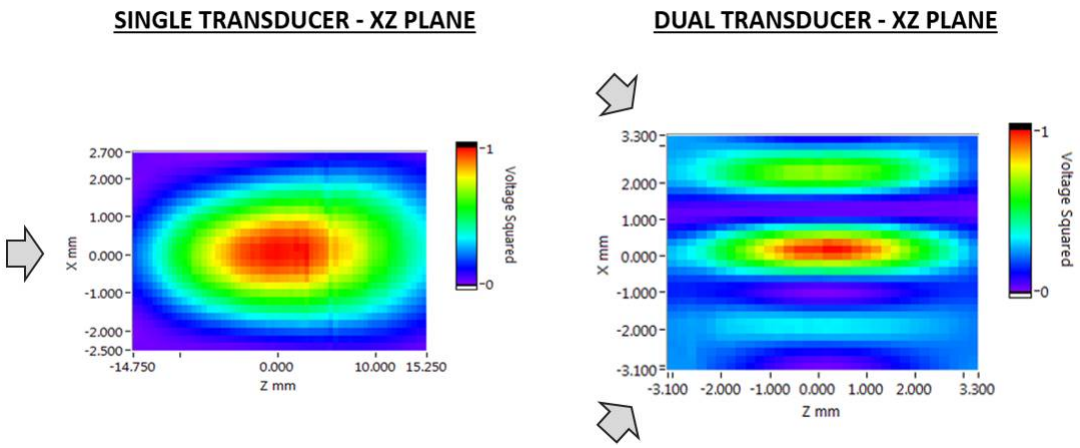


Figure 2.5: Scans of the focal region of the HIFU transducers, taken in the Axial - Transverse Plane at 0.5MHz. Grey arrows indicate the axial direction of each individual transducer in each scan. Left: The scan for a single H107 HIFU transducer located parallel to the X axis. The scan shows how the focal region is elongated in the axial (Z) direction relative to the transducer. Right: The scan for the dual HIFU transducer setup. The transducers are located perpendicularly to each other, and at a 45 degree offset relative to the X-Z axes shown in the scan.

targeting, resulting in a FWHM focal area of 1 x 6 mm, with reduced side lobes located approximately 1 mm away on either side of the focus, as shown in figure 2.5. The transducers have also been calibrated at the focus up to 1.75 MPa (at 0.5 MHz) using a 400 µm needle hydrophone (HNA400, Onda Corporation). Higher pressure values in the case of both transducers have been extrapolated using a 2nd order polynomial, as shown in figure 2.6.

PAM: Monitoring of cavitation activity was achieved by PAM using signals recorded on two L11-4 linear arrays (centre frequency 6.25 MHz, bandwidth 4 - 11 MHz, 128 elements, pitch 0.298 - 0.302 mm, Verasonics Inc., Redmond, WA). Each array was placed in a custom holder that was secured to the back of the holder of each HIFU transducer with three screws, such that the array was positioned in line with the rectangular cutout of the HIFU transducer. The holders ensured that the transducers could be assembled in an identical manner between experiments, and also ensured that there was no movement of transducers relative to each other during experiments. The perpendicular array arrangement increased the effective array aperture, and en-

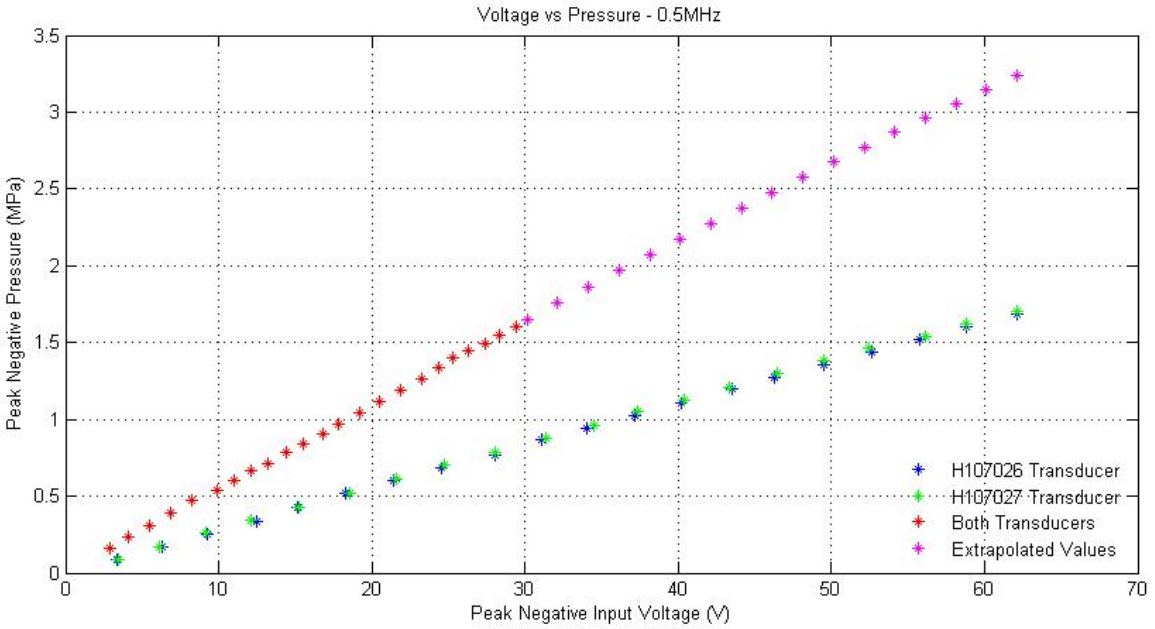


Figure 2.6: Calibration at 0.5 MHz for a single HIFU transducer, and for both HIFU transducers together. Calibrations were performed with a 400 µm Onda needle hydrophone placed at the centre of the focal region of a single transducer (green and blue datapoints), or at the centre of the focal region created when both transducers were driven simultaneously, in phase, and with the same acoustic parameters (red datapoints). Dual HIFU transducer focal pressure values were extrapolated to higher Peak Negative Input voltages using a 2^{nd} order polynomial (magenta datapoints).

abled the best possible resolution (ordinarily only in the transverse direction) in both the transverse and axial directions. The linear arrays were connected to a Verasonics Vantage ultrasound research system (Verasonics Inc., Redmond, WA) on which signals received by each element were recorded for use in offline PAM processing. When PAM reconstruction was completed with data from both linear arrays, it is referred to as a 'Dual Array' case in this chapter. If signals from one of the two arrays were used in PAM reconstruction, it is referred to as a 'Single Array' case.

2.1.5 Experiment Parameters

Acoustic parameters such as pressure, frequency, Duty Cycle (DC), Pulse Repetition Frequency (PRF) and total number of cycles have a significant impact on the probability and distance of nanocup extravasation. The selection of parameters is a balance between achieving accuracy with respect to the *in vivo* situation, and creating the desired effects in an experimental context to show proof of concept. The reasoning behind the selection of acoustic parameters is discussed in this section.

Two different types of acoustic exposure regimes were used in this experiment. In this thesis all pressures are reported as Peak Rarefactional Pressure (PRP) and pressures were measured using a 400 µm needle hydrophone calibrated at 0.5 MHz by the manufacturer (HNA Needle Hydrophone, Onda Corp., Sunnyvale, CA).

For the initial sonication, where the goal was to cause extravasation, a 5% duty cycle at a constant pressure of 1.6 MPa and PRF of 3 Hz was used. Previous work by Myers [91] has demonstrated that a DC below 2.5% and total number of cycles below 2.4 million significantly reduces extravasation distance, thus a 5% duty cycle and a total of 3.0 million cycles was selected to ensure that extravasation was readily achieved. Higher duty cycles were avoided in order to minimise thermal effects in the phantom. The 3 Hz PRF was selected to ensure sufficient time for data to be saved on the Verasonics. A pressure of 1.6 MPa was selected as it is the minimum pressure at which the probability of cavitation is 100% for the nanocups used. A flow rate of 0.3 ml/min was used to ensure that the nanocup solution was replaced at the focus

between each pulse.

In contrast, the second sonication (post-clearance) was designed to facilitate inertial cavitation of extravasated particles of all sizes, whilst minimising any further movement of these particles into the phantom. As smaller nanocups have slightly higher inertial cavitation thresholds, a pressure ramp was used on the second sonication in order to map as many extravasated nanocups as possible. The minimum PRP was the same as the pressure for the first sonication, 1.6 MPa. This pressure was then gradually increased to 2.1 MPa over the course of the second sonication. The maximum PRP of 2.1 MPa was selected as it is above the PRP cavitation threshold for the smallest size of nanocups used in this experiment, but is still below the PRP cavitation threshold of the phantom material (as evidenced by a lack of cavitation activity during controls at the same pressure). In addition, at the maximum PRP used, the PRP in parts of the sidelobes was also significant enough to exceed the PRP cavitation threshold for some of the larger nanocups, thereby allowing for post-extravasation mapping of nanocups in a larger region. To minimise further transport of the cavitation nuclei into the phantom, and to allow for sufficient time between pulses for the computation and display of real-time PAM images, the duty cycle and PRF were reduced to 0.05% and 1 Hz respectively.

A representative image of the PAM signal received during the initial and second sonications is shown in figure 2.7. Recorded PAM maps such as these are then processed and overlaid with microscopy, and described in the next section.

2.2 Image Processing Methods

2.2.1 Image Acquisition

Upon completion of the ultrasound exposures, the agar phantom was removed and imaged in transverse and cross section using a Nikon TI Eclipse microscope (Nikon Corp., Tokyo, Japan) with Tetramethylrhodamine Isothiocyanate (TRITC) filter under 4x magnification, to verify the location of extravasated cavitation nuclei. Areas of

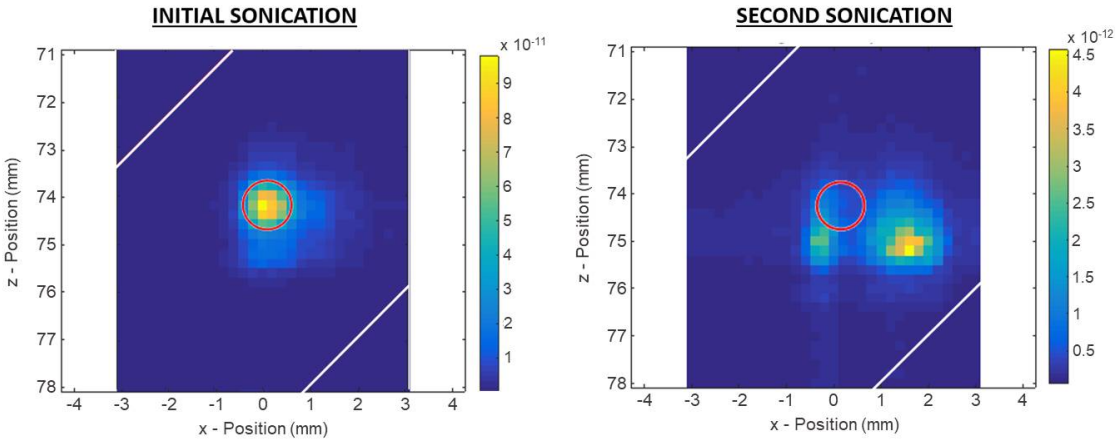


Figure 2.7: Example of the PAM image obtained from the initial (left) and second (right) sonications for a single experiment. The axes show distance (x-position and z-position), with the origin of the co-ordinate system taken as the centre of one of the L11-4 linear arrays. The red outline represents the position of a 1mm diameter, vertically oriented flow channel in an agar phantom, and the white lines show the outer boundary of the agar phantom. The colour scale represents the energy in a region in arbitrary units (proportional to energy in Joules). The PAM maps have been generated by beamforming the broadband acoustic signals received on an L11-4 linear array (Verasonics Inc.) using the Robust Capon Beamformer PAM algorithm. During the initial sonication, when cavitation agents are flowing through the channel, the corresponding cavitation energy is localised within the flow channel, as expected. On the second sonication, once the channel has been flushed with degassed water, the cavitation energy is localised outside of the flow channel, indicating that cavitation was generated from extravasated nuclei embedded within the agar gel.

fluorescence within the agar at the ultrasound target locations indicated the presence of extravasated nanocups.

2.2.2 Image Processing Procedure

After acquisition, offline processing of the PAM signal data and microscopy images was completed using Matlab (MathWorks Inc., Natick, MA) and ImageJ (National Institute of Health, Rockville, MD) as shown in figure 2.8.

Microscopy

The microscopy images from a cross-sectional segment of agar gel at the ultrasound focus were compressed into a single image using a Maximum Intensity Projection (MIP). This image was then loaded into Matlab and a set angle rotation of $135° \pm 5°$ was applied. This rotation was required because during the experiment, for ease and accuracy of microscopy, the cross sectional segments of the agar phantom were imaged at an angle that was different to their original setup orientation (such that a straight edge of the section of agar being imaged could be aligned with an axis of the microscopy movement stage). The PAM co-ordinate system was chosen as the reference co-ordinate system, and therefore the microscopy rotation was required in order to orient the microscopy image correctly. Although the microscopy images were obtained in such a manner as to minimise alignment error, we could not ensure that we had performed the alignment perfectly, or that the phantom was at exactly 45 degrees to the linear arrays. Thus we allowed for the rotation to vary by a small amount ($\pm 5°$) for each experiment. Once rotated, an automated circle detection algorithm in Matlab was used to identify the channel wall in the image. An iterative automated thresholding procedure using the IsoData method [92] was applied in order to automatically identify a microscopy Region of Interest (RoI).

PAM

The location of the channel relative to each linear array was identified using B-Mode data collected while the channel was filled with air, before the solution of nanocups was introduced. To ensure that the start of the flow did not disturb the channel, the identified location was confirmed using single array PAM maps from each linear array acquired during the initial sonication. Once the location of the channel relative to each probe was determined, the coordinates of the elements in one of the linear arrays were referenced to the other array, thereby creating a larger aperture array for PAM reconstruction in the dual array case. PAM reconstruction for each probe individually and for both probes together was performed using the three different beamformers, as described in section 2.2.3. For the second sonication, PAM maps displaying activity above baseline noise were identified and thresholded using the thresholds described in section 2.2.4. The resulting frames were added to form a composite PAM image, thereby encapsulating data from the entire exposure period. The composite PAM map was then upscaled to the same size as the microscopy image using bicubic interpolation and thresholded to remove values outside of the original PAM map range. The channel location previously identified was added to the composite image, allowing for an uncertainty of one B-Mode pixel (0.12 mm), which is the equivalent distance of half a PAM pixel.

Merging and Analysis

The composite PAM map and the binary microscopy image were then co-registered using the channel location, and the two images were fused to create the resulting images shown in figure 2.10 and 2.11. In addition, metrics that aim to quantify performance in relation to energy and pixel distance were calculated.

2.2.3 PAM Processing

The acoustic emissions recorded during the second sonication were filtered using a 4 - 10 MHz bandpass filter to isolate the broadband emissions due to inertial cavitation

within the bandwidth of the arrays. PAM maps of the sources of the filtered acoustic emissions were generated for both the single and dual array configurations using three different beamforming approaches: Time Exposure Acoustics (TEA) [14], Robust Capon Beamforming (RCB) [75], and Robust Linear Programming Beamforming (RLPB) [78]. TEA is a representative non-adaptive beamformer. It recreates the energy in a pixel of interest by time delaying the signals received on each array element by an appropriate amount before summing the signals using equal weights, thereby determining the total signal energy in a particular pixel. Other non-adaptive beamformers employ a similar strategy either in the time or frequency domain, and include Passive Cavitation Imaging (PCI) [73] and Angular Spectrum PAM (AS-PAM) [76]. Such non-adaptive approaches have very low computational cost, but result in low spatial resolution as the statistical characteristics of the recorded signals are not taken into consideration. In contrast to conventional beamformers, both RCB and RLPB are data-adaptive beamformers, since the calculation of the array element weights is the solution of an optimisation problem based on information from the recorded signals. Adaptive approaches provide improved resolution through better interference suppression, as well as by the mitigation of minor array calibration errors. While RCB assumes the signals follow a Gaussian distribution and attempts to minimise the variance of the array output, RLPB makes no prior assumptions on the signal distribution, and factors in the Higher Order Statistics of the signals by attempting to minimise the ℓ_∞-norm of the array output [93]. A more complete discussion of passive acoustic mapping is presented in Chapter 4 of this thesis.

2.2.4 PAM Threshold Optimisation

Accurate detection and localisation of regions of acoustic sources within a PAM map requires the application of a relevant threshold. To determine an optimal threshold, a series of numerical simulations were performed on 2D bubble clouds of various spatial distribution, bubble population and radius. In the simulations, when the bubble distribution was varied, the number of bubbles was held constant and conversely,

when the number of bubbles was varied, the distribution was held constant.

Both the single and dual array configurations were investigated, with the arrays situated 75 mm away from the bubble cloud, as in the *in vitro* experimental setup. Bubble oscillations due to an incident acoustic field identical to that used in the *in vitro* setup were modelled using the Keller-Miksis model under the assumption of an infinite medium of incompressible fluid [94] [95]. Pressure waves radiated from the excited bubbles were spherically propagated towards either one or two linear arrays, whose bandwidth and configuration matched that of a Verasonics L11-4 probe, and white Gaussian noise was added to the array to mimic noise due to electronics. The resulting acoustic signals were beamformed using RCB, and different thresholds were applied, which range between -20 dB and 0 dB with respect to the maximum PAM energy in the map. The application of a threshold yielded an RoI for the PAM map. Then, for each simulation, two measures of localisation were calculated: the percentage of bubbles located inside the RoI, and the percentage of the RoI covered by bubbles. The optimal threshold is defined as the best compromise between capturing all of the bubbles in a given area, and accurately representing only areas in which bubbles are present in a map. This optimal threshold is therefore represented by the intersection of the aforementioned two metrics, as shown in figure 2.9. The parameters tested in these numerical simulations result in a mean optimal threshold of -2.0 ± 0.58 dB for the single array configuration, and -5.3 ± 0.87 dB for the dual array configuration. These thresholds were used for the PAM reconstructions discussed throughout the remainder of this chapter.

2.3 Results

2.3.1 Qualitative Results

Ten experiments were conducted with the procedure described in section 2.1.1. Three representative fused images created using the dual array configuration and the RLPB beamformer are shown in figure 2.10, and the full set of resulting images can be seen

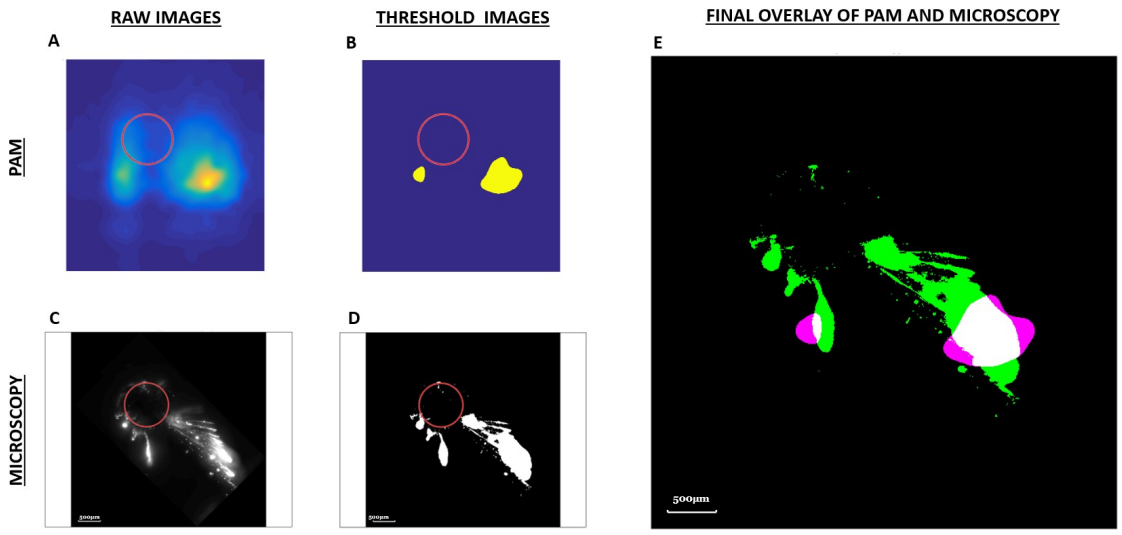


Figure 2.8: Example of each stage of the image processing process for a single experiment. A) The weighted total PAM map of all second sonication frames, upsampled to the same number of pixels as the microscopy image. Red circle represents channel location. B) Thresholded PAM image. C) Original fluorescent microscopy image of a cross-section of the channel (the channel therefore appears as a circle). D) Thresholded microscopy image (automated thresholding process). E) Overlay of thresholded images. Green represents microscopy, magenta represents PAM, and white represents areas of co-localisation.

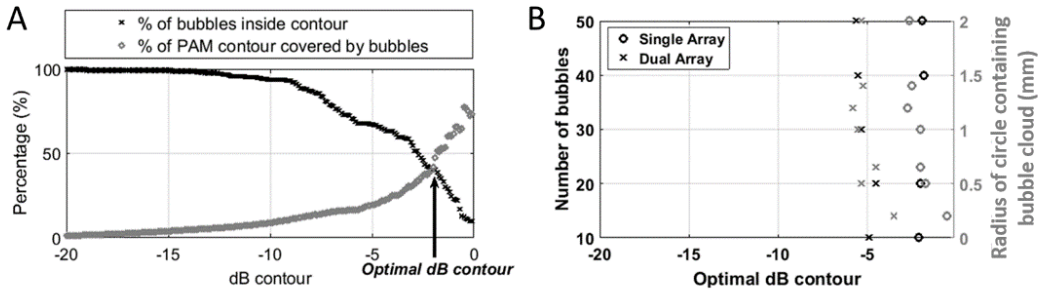


Figure 2.9: Figure created by Dr Erasmia Lyka and reproduced in this thesis with permission. A) Example of the calculation of the optimal dB contour for PAM thresholding. The optimal contour is taken as the intersection of two metrics. The first represents the percentage of bubbles inside each dB contour, and the second represents the percentage area of the dB contour covered by bubbles. B) The optimal dB threshold for single and dual arrays for a range of bubble populations and distributions. The left Y-Axis represents the number of bubbles and the right Y-Axis represents the radius of the circle containing the bubbles in the imaging plane of the linear arrays.

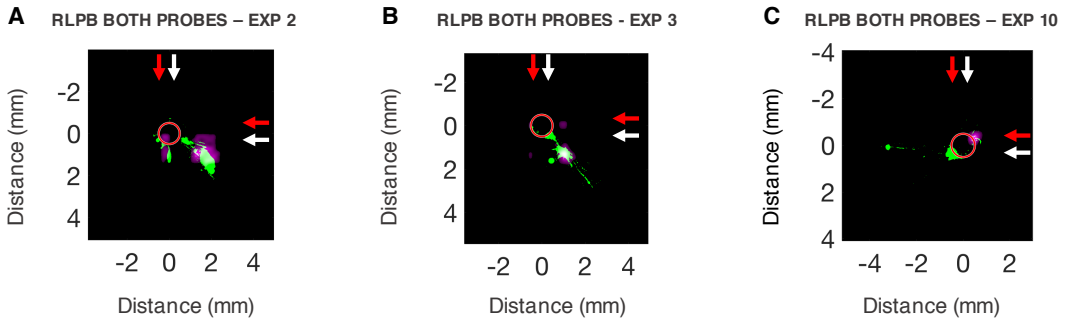


Figure 2.10: Three representative fused images created using the dual array configuration and the RLPB beamformer. Green represents the microscopy RoI (indicating the presence of extravasated fluorescent nanocups), magenta indicates the thresholded composite PAM image, white indicates areas of overlap between PAM and the microscopy RoI, the red circle shows the location of the channel, the red arrows indicate the direction of ultrasound, and the white arrows indicate the axial direction of view of the linear arrays used during the PAM reconstruction.

in Appendix A. In the images, green represents the microscopy RoI (indicating the presence of extravasated fluorescent nanocups), magenta indicates the thresholded composite PAM image, white indicates areas of overlap between PAM and the microscopy RoI, the red circle shows the location of the channel, the red arrows indicate the direction of ultrasound, and the white arrows indicate the axial direction of view of the linear arrays used during the PAM reconstruction.

Thus in the images presented, regions of white indicate 'on-target' PAM energy and regions of purple indicate 'off-target' PAM energy. Hence a high ratio of on-target to off-target PAM energy is indicative of good localisation performance, provided the off-target energy is still clustered in the general area of extravasated particles. Experiment 2 in figure 2.10A demonstrates average localisation performance, in which there is a relatively good ratio of on-target to off-target energy, and the off-target energy is still located in the immediate vicinity of extravasated particles. Experiment 3 in figure 2.10B demonstrates a high percentage of on-target energy, but also shows a small amount of off-target energy located slightly further away from the extravasated particles than in the previous case. Finally, Experiment 10 in figure 2.10C shows very little on-target energy, even though the signal is located in the correct region.

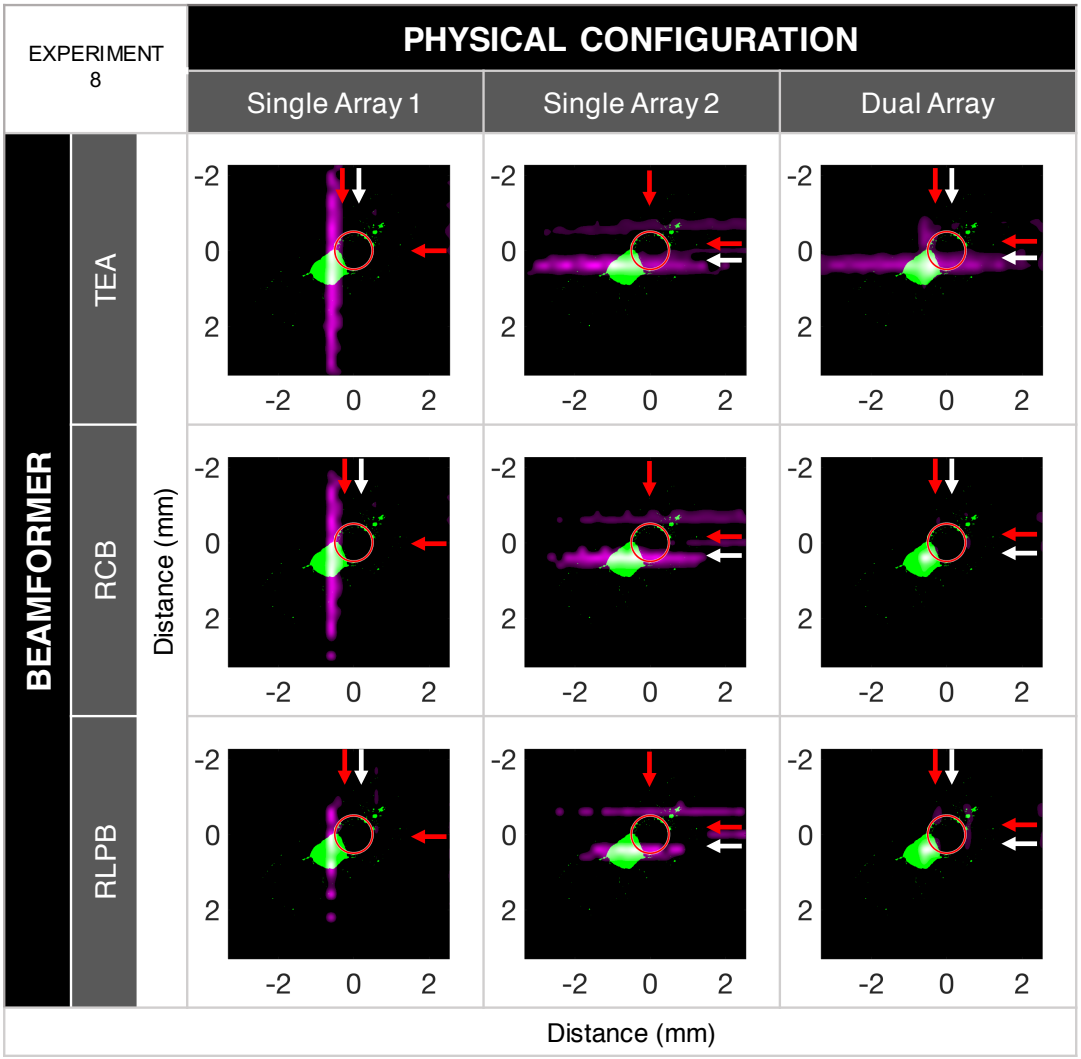


Figure 2.11: The fused images for both the single and dual array configurations for each of the three beamformers evaluated. Green represents the microscopy RoI (indicating the presence of extravasated fluorescent nanocups), magenta indicates the thresholded composite PAM image (generated from individual PAM frames collected during the second sonication), white indicates areas of overlap between PAM and the microscopy RoI, the red circle shows the location of the channel, the red arrows indicate the direction of ultrasound, and the white arrows indicate the axial direction of view of the linear arrays used during the PAM reconstruction.

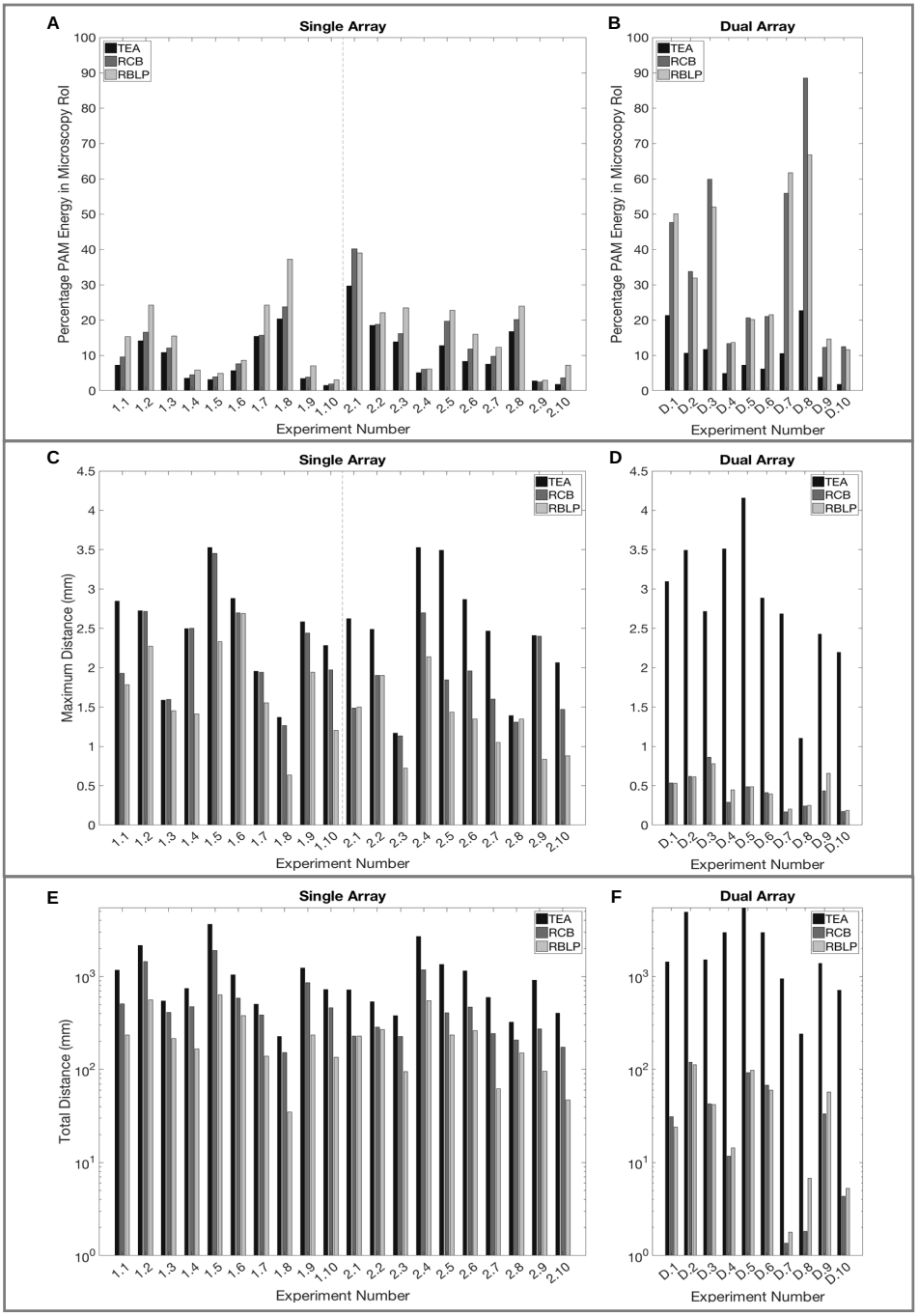


Figure 2.12: A & B) PAM energy within the microscopy RoI as a percentage of total PAM energy for all beamformers for (A) the single or (B) dual array case. C & D) The maximum euclidean distance of a PAM pixel to the nearest pixel inside the microscopy RoI, for (C) the single and (D) dual array case. E & F) The sum of the distance of every PAM pixel outside of the microscopy RoI to the nearest pixel inside the microscopy RoI. This metric represents the 'clustering' of PAM around extravasated particles for (E) the single and (F) dual array case.

In addition, in Experiment 10, there is a significant 'green-only' area, indicating that even though particles have extravasated to that area, they have not been re-excited during the second sonication. The reasons for this are discussed in section 2.4.

Similar to the examples shown in figure 2.10, in all of the other experiments performed, several PAM frames showing cavitation events which overlapped with extravasated particles were always recorded during the second sonication. On the second sonication, cavitation events were recorded at the minimum PRP of 1.6 MPa (the same PRP as used in the initial sonication), and also at greater pressures (up to the maximum PRP of 2.1 MPa). No such signal was recorded and no extravasation was evident in control experiments employing an identical experimental protocol and acoustic exposure parameters, but using fluorescent spheres of 300 nm in diameter instead of nanocups. This result indicates that nanocups, initially extravasated under ultrasound excitation, can be acoustically re-excited and localised using PAM.

To assess clinically relevant setups, the single array case was also evaluated. A representative qualitative result that illustrates both single and dual array cases is given in figure 2.11. A degradation in performance is shown by a larger region of PAM energy located further away from the extravasated particles, and is clearly evident in the axial direction of the single array case compared to the dual array case. In addition, the conventional TEA beamformer demonstrates greater spreading of the PAM energy over a region in comparison to the adaptive beamformers. Thus the single array cases using TEA demonstrate the worst localisation performance.

2.3.2 Quantitative Results

To quantify the performance change, three metrics are presented in figure A.10. The first metric, 'Percentage Energy', measures the percentage of PAM energy inside the microscopy RoI for all configurations as a percentage of total PAM energy (i.e. the white area divided by the total of the magenta and white areas). This metric therefore indicates how much of the total PAM energy originates from a region of extravasated particles. Therefore, in this graph, a higher percentage of energy is generally con-

sidered to indicate better performance. However, whilst a high percentage of energy may overlap with extravasated particles, it is also important to consider where the remainder of the energy is distributed. Thus we introduce a second metric, 'Maximum Distance', which displays the maximum distance of any PAM pixel to the nearest extravasated particle for the different setups and beamformers. Here, a greater distance is normally indicative of degraded performance. This is especially evident in the single array case where PAM energy is significantly elongated in the axial direction. Finally, a third 'Clustering' metric is used to evaluate both the number and distance of off-target pixels in order to ascertain how tightly clustered the PAM energy is around a region of extravasation. This metric is calculated as the summation of the distance of every PAM pixel that is outside of the microscopy RoI to the nearest pixel within the microscopy RoI. Thus a high value implies that the PAM energy is not clustered near to a region of extravsated particles. However this metric may still be biased by a significant number of 'off-target' PAM pixels, or the distant location of a small number of PAM pixels. Thus it is useful to examine information across all three metrics simultaneously when analysing performance.

For example, comparing Experiments 2 and 10 (shown in figure 2.10) according to the Energy metric, Experiment 2 has approximately three times the percentage of 'on-target' pixels than Experiment 10. However, from the Maximum Distance and Clustering metrics it can be seen that Experiment 2 has more PAM pixels located further away from extravasated particles, and hence Experiment 2 has a greater spread of energy around the extravasated particles. If the results are normalised to a single beamformer within each experiment and compared, statistically significant differences exist between every beamformer for the single array case, and between TEA and RCB, and TEA and RLPB for the dual array case (1-way ANOVA, $p < 0.05$). No statistically significant difference exists between RCB and RLPB for the dual array case for any metric. Overall the adaptive beamformers, when compared to TEA, reduce the maximum distance of PAM pixels to extravasated particles from an average of 2.4 ± 0.7 mm to 1.8 ± 0.6 mm in the single array case. The distance is further

reduced to 0.4 ± 0.2 mm using the dual array configuration. In terms of PAM energy co-localised with extravasated particles, this increases from an average of 10.1 ± 7.5 % to 14.2 ± 10.1 % with adaptive beamformers in the single array case, and further increases to 35.5 ± 23.0 % when using the dual array system geometry. Finally, on the Clustering metric, the mean total distance across experiments for TEA in the single array case is 1051 ± 861 mm, which reduces to 391 ± 379 mm with adaptive beamformers in the single array case, and further decreases to 41 ± 39 mm with dual array adaptive beamformers.

2.4 Discussion

From the qualitative results it is clear that nanocups can be re-excited, which may be possible for two reasons. First, during the initial sonication, it is likely that not all nanocups would have cavitated, but rather that some would have been forced into the agar gel as a result of the mechanical effects of neighbouring cavitating nanocups. These nanocups would then still contain their entrapped gas pocket, and hence would retain the ability to cavitate under ultrasound excitation. Second, it is possible that gas from collapsed bubbles reforms on the surface of the solid polymer cup base, and hence enables the nanocup to cavitate again during the second sonication. This is possible because the polymeric base of the nanocups is hydrophobic, and therefore forms an energetically attractive structure for the re-formation of a gas bubble. In reality it is likely to be a mixture of these two hypotheses, and further work is required to completely elucidate the underlying mechanisms.

The dual array transducer configuration increases the relative contribution of cavitation activity to particle extravasation versus the effect of radiation force in a single direction. By extension, the probability of extravasation occurring in only one single direction out of the channel is decreased relative to using only a single HIFU transducer.

From the qualitative results, extravasation is clearly evident in the experiments.

This extravasation occurs as a result of the mechanical effects arising from cavitation as described in Section 1.3. Specifically, the predominant form of cavitation in these experiments is inertial cavitation, since this is the main regime of cavitation exhibited by the nanocups used [9]. In an inertial cavitation regime, bubbles can exhibit non-spherical behaviour, which in turn leads to mechanical effects. Two effects that may play a role in extravasation are microstreaming (due to momentum transfer from an oscillating bubble into the surrounding liquid), and microjetting (the formation of a high velocity liquid jet that is propelled through the centre of an asymmetrically collapsing bubble). The exact contribution of different effects to extravasation would be extremely difficult to quantify due to the complex nature of the system. For example, the direction of a microject might typically be towards the solid polymer base of the nanocup in most cases, but could also change direction based on the proximity of other bubbles [83].

Although the effect of a strong, directional radiation force cannot be completely eliminated by this setup, previous work has demonstrated that an acoustic radiation force in the absence of cavitation nuclei does not have a significant effect on the transport of particles (in the order of hundreds of nanometers in size) when compared to cavitation-mediated delivery [96]. Furthermore, during the controls performed for this experiment (in which fluorescent polymeric spheres of similar size and density to the nanocups were used), the lack of significant extravasation projections indicates minimal transport due to acoustic radiation force. To verify the impact of DC, experiments with DCs below 2% with the same total number of cycles were also performed, and again, no extravasation projections were observed under microscopy. The ability of cavitation nuclei to extravasate in multiple directions around the channel is also evident from the results. For example, in Figure 2.10, extravasation towards one of the transducers is evident. This phenomenon has also been observed in similar experimental setups, especially at a 0.5 MHz sonication frequency compared to higher sonication frequencies [97]. At lower frequencies, lower pressure amplitudes can be used to generate cavitation, and ultimately cause extravasation in tissue mimicking

phantoms [91][97]. Due to the lower pressure, the acoustic radiation force on bubbles that have nucleated from nanocups is lower at lower frequencies, implying that bubbles will not necessarily be pushed to the distant wall of a flow channel at 0.5 MHz. Thus cavitation effects such as microstreaming and microjetting will still occur at the near wall of a flow channel. In addition, since agarose gels have a heterogeneous structure, a weak point in the gel may occur at any location around the channel wall. The reduced effect of acoustic radiation force at lower frequencies, combined with the heterogeneous nature of the agarose gel, means that the mechanical effects of cavitating bubbles may cause extravasation projections to occur in any direction around the channel, including on the side of the channel closest to the transducers.

It was also noted in the qualitative results section that in some cases, the PAM signal is not located in all regions in which extravasation is observed (which is indicated by a small region of white compared to the total green region). This may be due to several factors. First, relatively long extravasation projections may be formed in any direction around the channel during the initial sonication due to the unpredictable interactions between cavitation forces, acoustic radiation forces, microstreaming effects and the local structural properties of the agar gel. However, the focal region of the FUS setup is extremely small and highly targeted to the channel, so only the nanocups located in the focal region (or side lobes at high enough pressures) will cavitate. Therefore it is unlikely that extravasated nanocups in all areas of the phantom will be detected without steering the ultrasound focal area to cover the entire region. Second, although nanocups may have extravasated into a region that is still covered by the FUS focus, those extravasated nanocups may have lost their entrapped gas bubble during the initial sonication, and hence may have lost their ability to cavitate again during the second sonication, or the concentration of cavitating nanocups may be too low to produce detectable signals. Third, diffusion and convection of nanocups following a cavitation event may occur on length-scales that are large relative to the region of the cavitation event alone. It should be noted however, that the focus of the current work was not to localise all extravasated particles, but rather to show

that PAM signals received on the second sonication do originate from extravasated nuclei. Finally, since the dye used in these nanocups in not covalently bonded to the methacrylate base, but rather entrapped within the polymer shell, it is possible that some dye could have separated from the nanocups and created areas of fluorescence that are not true locations of nanocups. However, *in vitro* this is unlikely because the nanocup suspension is thoroughly washed by centrifugation three times during the manufacture process, and also because no other charged particles that may have an effect on the dye are co-injected with the nanocups. In addition, given the small size of dye molecules, free dye would easily seep out of the flow channel into the phantom thereby creating a uniform band of fluorescence around the flow channel, but this was not observed.

For a more complete mapping of all extravasated particles, it would be necessary to steer the FUS focus or move the phantom relative to the transducers in order to ensure that all regions of the phantom are exposed to sufficiently high pressure on the second sonication. In addition, higher concentrations of cavitation nuclei may be required to ensure sufficient cavitation signal can be recorded for all regions of extravasation on the second sonication.

Finally, variability within each metric, and especially within the PAM Energy metric, may also be due to several factors. First, in cases where there is a high level of cavitation, the PAM energy is spread out extensively due to the Point Spread Function (PSF) of the system. Therefore when a large cavitation event is detected, the PAM map will show the peak energy at the source of the cavitation event, but will also show energy 'smeared' around that location. However the PSF of PAM is significantly larger than that of microscopy for both the single and dual array cases. Thus the fluorescence microscopy image of the groups of sub-micron cavitation nuclei that cause these cavitation events will not be as 'smeared' and will thus indicate a smaller (and more accurate) representation of the true location of extravasated nuclei. This is the primary reason why a significant level of PAM energy does not coincide with extravasated nanocups, as shown in the representative images in figures 2.10 and 2.11.

It is further clarified by noting the extremely low values in the Clustering and Maximum Distance metrics in figure A.10 for the adaptive beamformers in the dual array case. The following subsection discusses variations between beamformers and array configurations in more detail. In addition, a low percentage energy may also be due in part to the loss of low fluorescence intensity areas of the microscopy images as a result of automated thresholding.

2.4.1 Beamformer and Array Configuration

For all beamformers, the choice of array configuration, and hence array aperture, has a direct impact on the spatial resolution of PAM, with a larger array aperture resulting in better resolution. In addition, the orthogonality of the arrays in the dual array case ensures that the resolution in both the transverse and axial directions is at least equivalent to the resolution in the transverse direction for a single array.

As can be seen in figure 2.11, adaptive beamformers have significantly smaller PSF and result in less spreading of the PAM energy. This performance improvement is due to the ability of adaptive beamformers to adjust signal weighting based on statistical characteristics of the received signals, as described by Coviello *et al.* [75]. Furthermore, in the case of the single array configuration, RLPB exhibited significantly better performance than RCB in terms of source localisation. Such behaviour illustrates the importance of considering not only the variance, but also the higher order statistics of the signals during beamforming for improved interference suppression, and ultimately, better source localisation. However in the dual array case, there is no significant difference between RCB and RLPB. This similarity in performance of the adaptive beamformers is most likely because the use of two arrays already significantly improves the PSF of the setup, and hence the reduction in PSF due to RLPB is less apparent.

In addition to the type of beamformer used, the physical array geometry has a significant impact on the system performance. The resolution of all of the beamformers used is dependent on array aperture. Therefore, by increasing the array aperture

the PAM resolution, and hence the particle localisation performance, is significantly improved.

2.4.2 Tradeoffs And Limitations

Although the dual array setup with an adaptive beamformer provides the best performance for mapping extravasated particles, the use of two orthogonal arrays presents practical geometric challenges, and hence may only be applicable in very limited clinical settings.

Thus it is important to examine the results of the single array case for clinical relevance. In this case, RLPB significantly outperforms TEA and RCB, and is therefore a promising candidate for adoption into a clinically relevant setup.

However the use of adaptive beamformers compared to conventional beamformers increases computational cost. Of the adaptive beamformers, RLPB requires significantly more computational time than RCB, as the beamformer is required to find the solution to a linear programming problem - an inherently iterative process that cannot be parallelised. In contrast, the most computationally expensive part of RCB is the eigenvalue decomposition of a covariance matrix. By comparison, for a typical map of 100 voxels and signals recorded for 120 µs at 25 MHz, an RCB map is generated approximately 200 times faster than the corresponding RLPB map. Thus using a 2.6 MHz Intel Xeon CPU (E5-2650v2, Intel Corp., Santa Clara, CA), the achievable RCB PAM frame rate is 0.86 Hz, while the corresponding RLPB frame rate would currently be 0.004 Hz.

These timings are based on implementation of both algorithms in MATLAB using the available built-in functions. Therefore whilst the current implementation of RLPB is not fast enough for real-time applications, it is likely that by using optimised commercially available software for solving linear programming problems, in conjunction with data reduction strategies that do not significantly compromise signal quality, RLPB can be performed on clinically relevant timescales.

Even if the processing time can be reduced, the resolution of PAM created with

a single array, particularly in the axial direction relative to the array, would not suffice in a clinical setting where sub-millimetre length scales are common. Thus further work is necessary to improve the resolution of these techniques for the single array case. A novel approach to source localisation is discussed more completely in Chapter 4 of this thesis.

2.5 Conclusion

This chapter has demonstrated *in vitro* that it is possible to re-excite cavitation nuclei embedded within a viscoelastic matrix after they have been extravasated under ultrasound (for the purpose of ultrasound-mediated drug delivery applications), and once they are no longer present in flow. The location and extent of nuclei extravasation can be determined by Passive Acoustic Mapping of sources of broadband acoustic emissions associated with cavitation activity from these sub-micron extravasated nuclei. There was evidence of relatively good co-location of PAM signal with optical imaging of extravasated nanocups, but only for the case of the dual array setup using adaptive beamformers. In this case the average maximum distance of a PAM pixel from an extravasated particle was $0.4 \pm 0.2\,\mathrm{mm}$. Although PAM energy is located within areas of extravasation shown by microscopy, PAM was not able to map all areas of extravasation. The spatial correlation between post-extravasation cavitation maps and extravasated nanocups depends significantly on the array aperture, and on the beamforming algorithms used.

Whilst the dual linear array configuration demonstrates the best performance for this application, geometric constraints limit the applicability of this setup. Therefore, a single array configuration has also been evaluated with the aforementioned beamformers, and in this case, the RLPB algorithm demonstrates the best performance in terms of source localisation, but still has a PSF that is prohibitively large to demonstrate co-localisation here. Further work is therefore required to ensure that adequate source localisation and time resolution can be achieved with a single lin-

ear array. Time resolution improvements may include the optimisation of the RLPB algorithm using commercially available purpose-built software and other data reduction strategies. For increased localisation performance in both the single and dual array configurations, image processing techniques such as attenuation and diffraction correction, and superresolution can be employed.

The results presented in this chapter for a dual array setup show promise in non-invasively localising extravasated cavitation nuclei of a similar size to therapeutic drugs. As discussed in the introduction to this chapter, the main purpose of the *in vitro* work presented here is as a proof of concept to assess whether this procedure could be used as a marker of tumour permeability *in vivo*. Thus this extravasation and re-excitation procedure is applied to *in vivo* models in the next chapter of this thesis.

Chapter 3

In Vivo Passive Acoustic Mapping of Extravasated Particles

Acknowledgements: The work in this chapter is my own, however I am grateful to the following people for their assistance. I thank Alexander Martin for his practical help with some in vivo experiments and, in particular, for his assistance during the resin perfusion procedures. I thank Sheena Wallington for performing some initial test perfusions (data not used in this thesis), and for training me to perform the in vivo techniques that I have used in this chapter. I thank Claudia Hill for providing the CAPAN-2 tumour-bearing animals used in the resin perfusion study, and I am grateful to Dr Luca Baù for suggesting the use of Pentobromophenyl Methacrylate as a radiopaque modifier for the perfusion resin.

3.1 Introduction

The overall effectiveness of cancer treatment depends not only on the selected therapeutic, but also on the ease with which the therapeutic can be delivered to cells. Specifically, the ability to deliver therapeutics depends on tumour microenvironment factors such as the level of vascularity in a tumour, permeability of tumour vessels, Interstitial Fluid Pressure (IFP), and organisation of the Extracellular Matrix (ECM) [16][98][99]. These factors are all interlinked, but vascularity in particular directly affects the initial delivery of therapeutics to the physical location of tumour cells, as well as the ability of tumours to grow beyond a certain critical size and to

metastasize to other organs. The level of vascularity is dependent on the type, size, and location of the tumour in the body, as well as the location within the tumour (peripheral or central)[25][100][101][102].

Tables 3.1 and 3.2 present examples of vascular properties of some common cell lines. The information in Table 3.1 is from the literature [24][25][101][103][104]. The information in Table 3.2 is from unpublished work currently under way at the University of Oxford[1]. In order to measure the pore size in tumour vasculature, long circulating fluorescent liposomes and latex beads of different sizes were used. An accumulation of liposomes or latex beads in the tumour region (assessed by intravital microscopy) at 24 hours after the initial injection, indicated that the pore sizes in the tumour vasculature were large enough to allow extravasation [25]. The final pore size for each cell line was taken as the maximum size liposome or latex bead that was able to extravasate [25].

Table 3.1: Known pore sizes of tumour vasculature for various cell lines, primarily obtained from [25].

Cell Line	**Species**	**Origin**	**Vessel Pore Size**
LS174T	Human	Colon	400 - 600 nm
MCa-IV	Murine	Breast	1200 - 2000 nm
Shionogi	Human	Breast	200 - 380 nm
HCa-I	Murine	Liver	380 - 550 nm
ST-8	Murine	Mesenchyme	550 - 780 nm

As can be seen from the tables, the type of tumour cell line plays a significant role in the properties of the tumour vasculature. In addition to tumour type, another significant consideration when assessing tumour vascularity in terms of perfusion and permeability is the stage of development of the tumour. In the case of table 3.1, pore sizes were measured when the tumours had a diameter of approximately 5 mm [25].

[1]Research performed as part of a Contrast Enhanced Ultrasound and MRI Perfusion Study, led by Sheena Wallington, and supported by researchers from the Oxford Institute for Radiation Oncology and from the Biomedical Ultrasonics, Biotherapy and Biopharmaceuticals Laboratory group.

Table 3.2: Known perfusion of tumours for various cell lines. Data in this table is from unpublished work using contrast enhanced ultrasound and MRI, led by Sheena Wallington at the Oxford Institute for Radiation Oncology.

Cell Line	**Species**	**Origin**	**Level of Vascularity**	**Vessel Distribution**
CT-26	Murine	Colon	High	Peripheral & Central
CAPAN-2	Human	Pancreatic	Low	Peripheral
MDA-MB-468	Human	Breast	Very Low	Peripheral
MDA-MB-435	Human	Skin	Medium	Peripheral & Central

Although not stated in the original paper, this is likely to equate to a tumour volume of approximately 50 - 100 mm^3. In the case of table 3.2, the tumours were also imaged at 50 - 100 mm^3. However, significant changes to the vasculature can occur after the tumour reaches a certain size, with rapidly growing tumours developing necrotic regions in the centre of the tumour due to poor vascularisation [105][106].

The experimental process and techniques discussed in the previous chapters have successfully allowed for the monitoring of extravasated particles *in vitro*. The aim of the work in this chapter is to adjust the *in vitro* procedure to an *in vivo* model, in order to determine whether any further information about tumour vasculature can be obtained non-invasively using focussed ultrasound and nanocups.

The first part of the chapter details the methods and experimental setup that is common across all experiments. The remainder of the chapter is then dedicated to detailing three main *in vivo* experiments that were completed, identifying any individual experiment specific procedural differences within each section.

The first experiment is a full investigative study into the cavitation mediated extravasation of sub-micron cavitation nuclei for different acoustic pressures. This experiment was completed in a tumour line frequently used in the field of immuno-oncology [107], and readily available within the Biomedical Ultrasonics group at the

University of Oxford (CT-26, murine colorectal carcinoma). The aim of the experiment was to investigate the ideal acoustic parameters for extravasation and re-excitation of nuclei.

Two follow-up experiments were then completed to investigate interesting results from the first experiment. First, the level of vasculature and permeability of the vasculature to a small molecule tracer was examined in order to assess whether the properties of the tumour vasculature were altered by the ultrasound treatment. The final experiment then proceeded to examine passive, rather than active accumulation of cavitation nuclei within the tumour region. In particular, this experiment focussed on the assessment of vasculature permeability at different stages of tumour development. In addition, a comparison of passive accumulation was made between the murine colorectal tumour line (CT-26) and a human pancreatic tumour line (CAPAN-2) in order to assess differences in passive accumulation across cell lines[2].

The chapter concludes with a discussion of the implications of non-invasive permeability assessment using ultrasound and nanocups, and also includes recommendations for future *in vivo* studies in this area.

3.2 Experimental Methods

3.2.1 Ultrasound Setup

The experimental setup is identical to the dual transducer setup described in the previous chapter. A block diagram of the setup is shown in figure 3.1, and pictures of the setup can be seen in figure 3.2 which shows a mouse attached to a custom holder for treatment, as well as the animal in the water bath, and finally, being perfused with a radiopaque resin.

The setup consists of two 0.5 MHz confocal HIFU transducers (H107, outer diameter 64 mm, focal length 63.2 mm, Sonic Concepts, Bothell, WA) with full width half maximum (FWHM) focal width of 3 mm and FWHM focal depth of 21 mm placed at

[2]I thank Claudia Hill for providing the CAPAN-2 tumour-bearing mice for this study.

90 degrees to each other as shown in figure 3.1. Each transducer has a 45 x 20 mm rectangular cutout, and is placed in a custom transducer holder such that the transducers remain perpendicular to each other. Two L11-4 linear arrays (centre frequency 6.25 MHz, bandwidth 4 - 11 MHz, 128 elements, pitch 0.298 - 0.302 mm, Verasonics Inc., Redmond, WA) are aligned with the HIFU transducer cutout and secured to the back of the HIFU transducer holders. In addition, in all experiments a heater is used to maintain the water bath containing the setup at 37 °C to ensure animals remain warm during the treatments.

A custom Matlab script provided by OxSonics Therapeutics (Oxford Science Park, Oxford, UK) was used for these experiments as it has been optimised in order to enable real-time acquisition of PAM and B-Mode images at frame rates in excess of 3 Hz. The realtime display of cavitation activity allows for dynamic adjustment of ultrasound exposure conditions in order to cause sustained cavitation activity during the therapy parts of the experiment. The code, implemented on the Verasonics Vantage 256 (Verasonics Inc., Redmond, WA), first acquires a B-Mode image for each individual L11-4 array connected to the system. The Verasonics then sends a low voltage signal to an Agilent 33210A function generator (Keysight Technologies, CA) to initiate a pulse. A Pulse Repetition Frequency (PRF) of 0.5 Hz is used in this experiment. Acoustic data is passively recorded on two L11-5v linear arrays (128 elements, pitch 0.298 - 0.302 mm, Verasonics Inc., Redmond, WA), and realtime RCB PAM processing is calculated for each image frame. PAM images are overlaid on the acquired B-Mode image on every pulse, and the maximum energy of the PAM map for each frame is plotted on a graph in custom 'Cavitation Level' units, reproduced in this thesis as Arbitrary Units (A.U.). The 'cavitation level' unit thus corresponds to the maximum energy from the PAM map generated for each ultrasound pulse, and is thus used as a surrogate measure of the maximum intensity of cavitation activity in a region. Therapy pulse settings are manually selected on the function generator before each treatment. B-Mode image data for each frame, as well as the first 100 µs raw signal data on each element, is recorded and saved for further off-line processing.

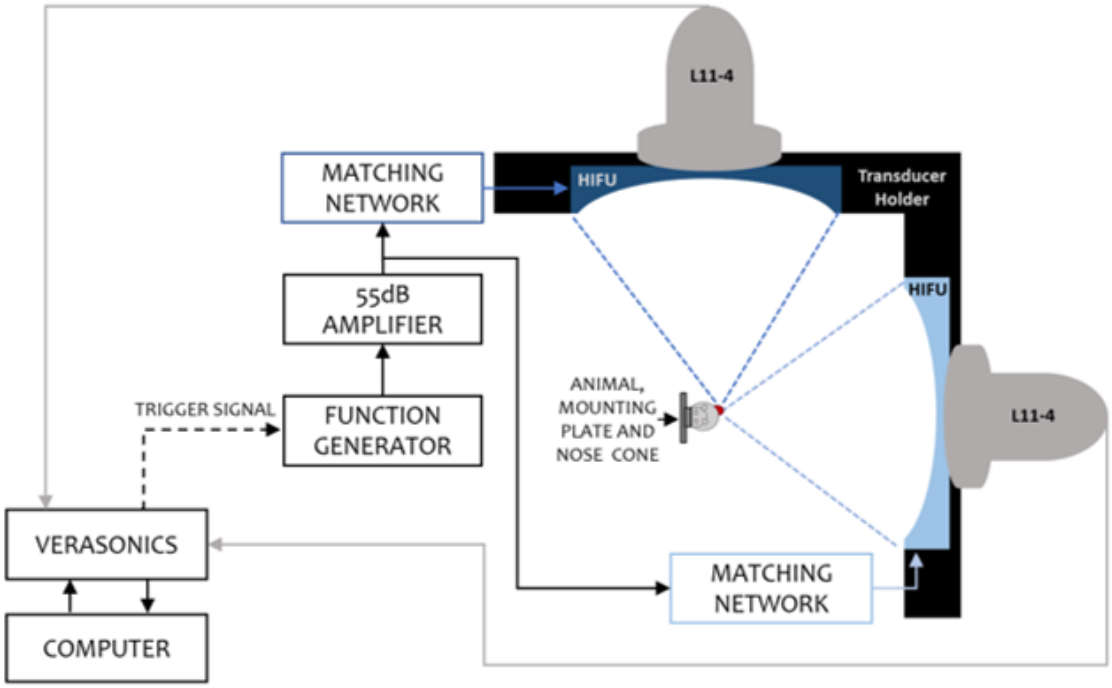


Figure 3.1: A block diagram of the *in vivo* acoustic setup. Custom Matlab code is run on the computer attached to the programmable Verasonics ultrasound research platform. During treatment, the Verasonics sends a low voltage trigger signal to a function generator to trigger the function generator to send a pulse. The output of the function generator is passed through a 55dB power amplifier before being connected to two 0.5 MHz HIFU transducers (Sonic Concepts, WA) via their matching networks. The animal is positioned at the focus of the two transducers on a mounting stage. Two Verasonics L11-4 linear arrays are used to provide B-Mode imaging throughout the treatment. Acoustic emissions from cavitation in the tumour region are also recorded on the linear arrays, which are directly connected to the Verasonics. Realtime B-Mode and PAM are computed during treatment and shown on the computer screen.

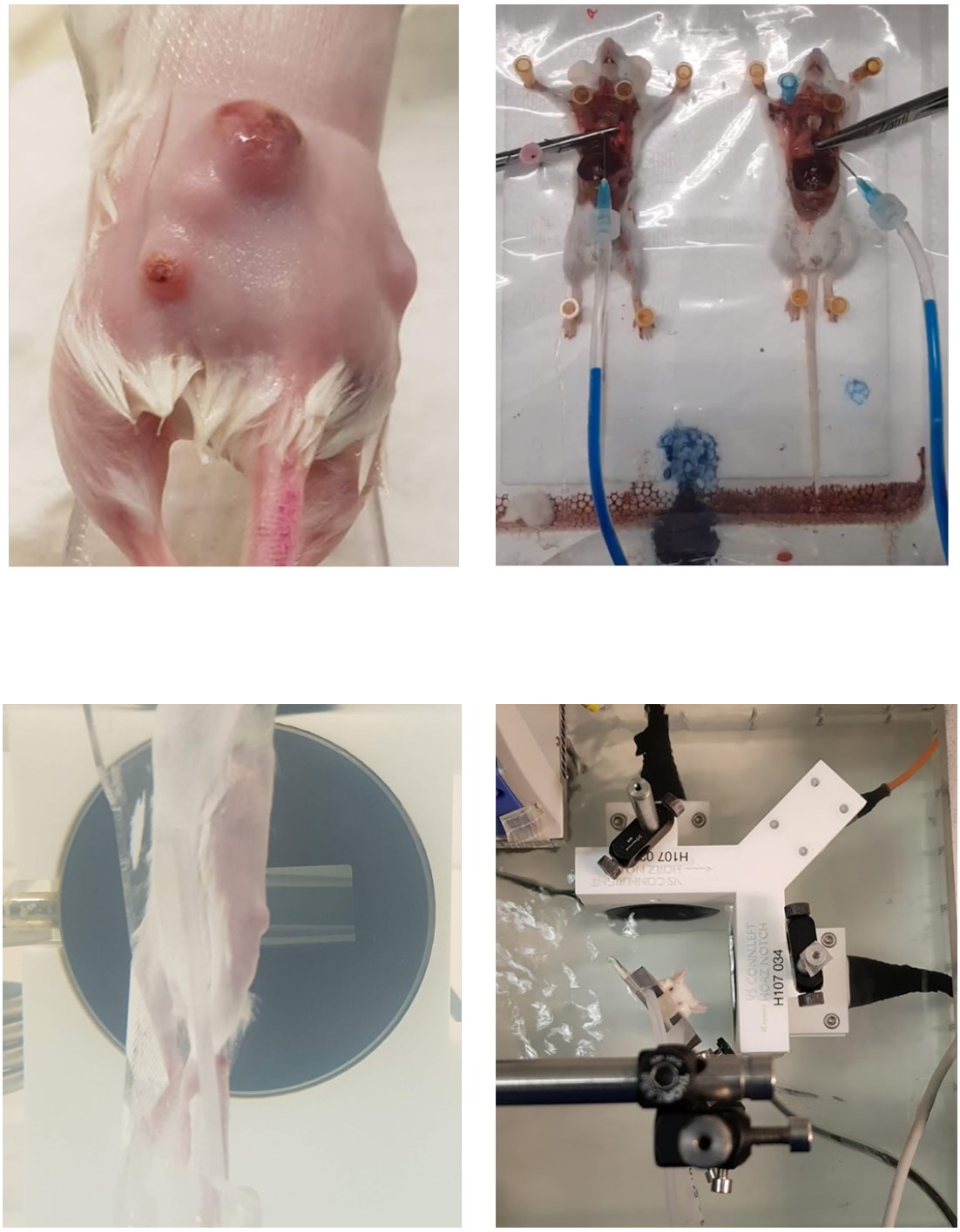


Figure 3.2: Pictures of the *in vivo* setup used in this experiment. Top Left: An animal attached to the custom holder, showing a late stage tumour. Top Right: Two animals being perfused with blue resin for visualisation of vasculature by micro-CT. Bottom: Front and top views of the dual transducer setup.

3.2.2 Nanoscale Cavitation Nuclei

Nanoscale cavitation nuclei ('nanocups') were fabricated in the laboratory, following a similar procedure to that described in sections 1.3.6 and 2.1.3. However two key modifications were made in the development of these nanocups compared to those used in the *in vitro* setup. First, the fluorescent dye was changed from Nile Red to a methacrylate based dye, Fluorescein O-Methacrylate (Sigma-Aldrich, green fluorescence, excitation 490 nm, emission 525 nm). This change ensured that the dye was covalently bound to the methacrylate monomer, rather than just being trapped inside the nanocup construct, thus minimising the ability of the dye to separate from the cup even in the presence of other charged particles and proteins *in vivo*. The drying process was also changed from air drying on a large surface (such as a petri-dish) to freeze drying in order to allow for easy resuspension of particles and to reduce large clumps in the dried cups. Flash freezing was completed in an acetone/ dry-ice cooling bath, and freeze-dryer shelf temperature was maintained at $-30\,^{\circ}\mathrm{C}$ under a vacuum. Dynamic Light Scattering was performed on these nanocups and showed a similar distribution to that of figure 2.3, but with a mean size of 495 nm and a polydispersity index of 0.1. As with the *in vitro* experiment, the size distribution of nanocups ranges from approximately 200 nm for the smaller particles up to 800 nm for the largest sizes. This size distribution is important to consider, given that the cavitation threshold of the nanocups is dependent on the cavity diameter of the nanocups. Cavity diameter is smaller than the mean overall particle size reported from DLS measurements, and therefore a 200 nm particle has a cavity diameter of approximately 100 nm, whilst an 800 nm particle will have a cavity diameter of approximately 600 nm [82]. Another important consideration is the clearance time of the nanocups. Previous work by Myers *et al.* in the supplementary material of [108] shows that cavitation activity from nanocups typically lasts less than 10 minutes in a murine model before the signal is no longer detectable by PAM. In addition, internal studies within the Biomedical Ultrasonics Group at the University of Oxford, and at OxSonics Therapeutics, have used

radiolabelled nanocups to assess their clearance and have demonstrated that the level of cavitation nuclei still in circulation at 20 minutes post injection is undetectable.

3.2.3 Tumour Implantation

CT-26 tumour cells were cultured in RPMI-1640 medium, and CAPAN-2 cells were cultured in McCoy's 5a modified medium, in accordance with ATCC guidelines. Five week old female BALB/c mice (for CT-26 tumours) or five week old female BALB/c nude mice (for CAPAN-2 tumours) were obtained from Charles River Laboratories (Oxford, UK), and left to acclimatise in the animal facility for a minimum of one week before tumour cell implantation. For bi-lateral CT-26 tumours, $5x10^5$ cells in 50 µl of Phosphate-Buffered Saline (PBS) were implanted subcutaneously on each hind limb. For unilateral CAPAN-2 tumours, $1x10^6$ cells in 100 µl PBS were implanted subcutaneously on the right hind limb.

3.2.4 Procedures Under Anaesthetic

Before anaesthesia, animals were placed in a hot box (maintained between 37 °C and 40 °C) for a minimum of five minutes prior to being anaesthetised. Animals were induced in a small induction chamber using 5% isofluorane gas for approximately 2 minutes. Once anaesthetised, animals were placed on a heating pad for cannulation, if required. Cannulations were performed with a 29 gauge needle inserted into a tail vein. Sufficient length of cannula was used to ensure that the syringe could be kept out of the water tank when the animal was positioned at the ultrasound focus. A custom holder designed to allow the animal to be placed on a flat surface whilst being kept under anaesthetic and immersed in the water tank was used, as shown in figure 3.2. For IVIS imaging, animals were placed on the IVIS stage which was pre-heated to 37 °C. Once treatments were complete, animals were recovered in hand until conscious, and then placed in a hot box for a minimum of 5 minutes, or until full recovery of normal movement was observed.

3.2.5 Terminal Procedures

All animals were sacrificed by Schedule 1 methods in accordance with UK Home Office guidelines. For studies that required resin perfusions, animals were sacrificed by overdose of Pentobarbitone (1 in 5 dilution, 200 µl intraperitoneal injection), and death was confirmed by cessation of circulation before the perfusions were performed[3].

3.2.6 Resin Perfusion

A resin perfusion procedure is used in the final experiment in this chapter to assess the true 3D location of tumour vessels. The perfusion method followed is the same as the perfusion technique for corrosion casting of vessels for Scanning Electron Microscope Imaging [109][110]. First, the animal is sacrificed using an overdose of anaesthetic (200 µl of a 1 in 5 dilution of Pentobarbitone, intraperitoneal injection), and death is confirmed by cessation of circulation. Immediately following confirmation of death, the animal is dissected along the midline, taking care to avoid major vessels. The animal is pinned at an angle to expose the heart. A 23 gauge needle is inserted into the left ventricle and clamped in place (as shown in figure 3.2), while the right atrium is lacerated to allow outflow of fluid. A preheated solution of heparinised Phosphate Buffered Saline (PBS) (500 I.U. heparin in 50 ml PBS) is perfused until the outflow of liquid becomes clear (approximately 20 - 30 ml solution is perfused at this stage). This is followed with a perfusion of 2.5% solution of gluteraldehyde in PBS, in order to fix the vessel walls in preparation for the viscous resin. Approximately 10 - 20 ml is used in this stage. Finally, a solution of modified Batson No. 17 Resin (Polysciences Europe GmbH) is prepared according to manufacturer's recommendations and perfused into the animal. The modification to the resin is to dilute the resin with a radiopaque methacrylate based compound, Pentobromophenyl Methacrylate, at 25% molarity, to enable visualisation of the resin on micro-CT[4]. Following the resin perfusion, the

[3]I thank Alexander Martin for his practical assistance during these experiments, in particular, for performing the intraperitoneal injections, as well as for assisting with the resin perfusion procedures.

[4]I thank Dr Luca Baù for suggesting Pentobromophenyl Methacrylate as a radiopaque modifier to the resin.

animal is left in place for 30 minutes, after which time it is placed in a container on ice overnight, before being fixed in a 10% buffered formaldehyde solution for 48 hours, before ultimately being stored in 70% ethanol. The entire animal is then scanned on a micro-CT (Rikagu, CT Lab, GX90, located at the Kennedy Institute of Rheumatology, Old Road Campus, Oxford, UK), before the tumour region is dissected out and scanned separately. A separate scan is required to enable the smallest field of view to be used (10 mm) which provides the best possible resolution (4 µm) for the scan.

3.3 Experiment 1: Assessment of Cavitation from Extravasated Particles *In Vivo*

In order to determine whether extravasated nuclei can be mapped *in vivo*, several factors need to be taken into account. Firstly, the acoustic parameters of the initial sonication should be carefully considered in order to ensure a balance between causing extravasation, and still leaving a sufficient number of activatable cavitation nuclei within the tumour region in order to allow for detection and mapping during the second (re-excitation) sonication. Furthermore, the selection of acoustic parameters on the second sonication should be selected so as not to cause further movement of extravasated particles, but rather to map the particles *in situ*. Overall, the aim of this experiment was to assess the energy and probability of cavitation of a treated side tumour against an untreated side tumour in bi-laterally implanted mice, with the outcome of determining whether cavitation on the second sonication was possible.

3.3.1 Experimental Procedure

Two groups of mice with bi-lateral tumours were used in order to assess whether it would be possible to re-excite extravasated nuclei given two different acoustic parameters for the initial sonication. In addition to the evaluation of cavitation in the second sonication between the treated and untreated side tumours, it is also important to assess the level of cavitation that occurs naturally in tumours at different pressures,

due to either pre-existing pockets of gas within the tumours, or due to small gas bubbles that may be trapped on the skin of the mouse. In this experiment, three animals only had a tumour on a single side, and were thus used as a reference group to assess the cavitation level in a tumour in the absence of injected cavitation nuclei. This reference group cannot therefore be considered a full control group for the study, but rather only as an indicator of the approximate level of cavitation in a tumour without injected nuclei for one of the experimental groups. Where the two treated groups received 50 µl of nanocups in 5% glucose, the reference group received 50 µl of 5% glucose solution only.

The variables in the acoustic parameters are pressure, Duty Cycle (DC), and Pulse Repetition Frequency (PRF). PRF was kept constant at 0.5 Hz as this is based on the physiological flow rate in mice, and allows for enough time for the replenishment of cavitation nuclei to the tumour region. In addition, the pressure in typical drug delivery studies within the Biomedical Ultrasonics Group is usually varied between a minimum and maximum pressure in real-time by the ultrasound operator during treatment in order to keep the overall output cavitation energy (and hence the total amount of cavitation delivered) as constant as possible. Thus DC was selected as the acoustic parameter to investigate.

A similar procedure to the *in vitro* procedure in the previous chapter was used. The tumour that was exposed to the first sonication is known as the 'Treated Side' tumour, whilst the other side tumour that did not receive the first sonication acts as an internal control, and is known as the 'Untreated Side' tumour. The step by step experimental procedure is as follows:

1. Intravenously inject fluorescent nanocups
2. 1st Sonication: Treat tumour on one side of bi-laterally implanted mice carrying CT-26 tumours
3. Vascular Clearance: Wait for a minimum of 25 minutes to allow for the nanocups to clear from circulation (length of time limited by animal licence)

4. 2nd Sonication: Expose tumours on both sides to second sonication with a pressure ramp

5. Sacrifice animals

The acoustic parameters for each sonication are given in table 3.3, and the tumour volumes and number of animals used are given in table 3.4. The total exposure time for the initial sonication was fixed at 5 minutes, however the pressure for the initial sonication was varied by the operator in real-time in order to maintain a constant level of cavitation activity. For the second sonication, a very low number of cycles was used in order to induce a detectable cavitation response without further transport of the cavitation nuclei. The pressure was increased through set pressure steps every 30 seconds in order to excite and map as many extravasated nanocups as possible.

Table 3.3: Acoustic parameters for the extravasation and re-excitation of nanocups in the Assessment of Cavitation from Extravasated Particles Study

Group	**1st Sonication**			**Second Sonication**		
	Pressure (MPa)	DC	No. Cycles	Pressure (MPa)	DC	No. Cycles
1 (Bi-lat, with nuclei)	Variable, 1.6 - 2.1	5%	50000	Ramp, 0.8 - 3.0	0.001%	10
2 (Bi-lat, with nuclei)	Variable, 1.6 - 2.1	1%	10000	Ramp, 0.8 - 3.0	0.001%	10
Ref (Uni-lat, no nuclei)	Variable, 1.6 - 2.1	5%	50000	Ramp, 0.8 - 3.0	0.001%	10

3.3.2 Results and Discussion

The cavitation levels recorded for all groups during the first and second sonications are shown in figures 3.3 to 3.5.

In figure 3.3, the total cavitation levels plotted correspond to the mean of the total cavitation level recorded for mice in each group. The total cavitation level recorded

Table 3.4: The number of animals and the tumour volume for the Assessment of Cavitation from Extravasated Particles Study

Group	DC, 1st Sonication	No. Animals	Average Treated Volume	Average Untreated Volume
1 (with nuclei)	5%	3	95	105
2 (with nuclei)	1%	3	117	126
Ref (no nuclei)	5%	3	186	93

for each animal is itself the sum of the maximum energy in each realtime PAM frame displayed during every pulse in the 5 minute treatment period.

Similarly, in figures 3.4 and 3.5, the total cavitation levels plotted refer to the mean total cavitation level for each pressure tested for each group of animals. The total amount of time spent at each pressure was held constant (30 seconds per pressure level).

Although PAM returns an estimate of the power of radiated broadband acoustic emissions in Joules, this unit is only strictly applicable for arrays that have been calibrated to account for sensitivity differences. In addition, another normalisation has been performed on the output energy in the processing stage in order to aid readability in real time. As the custom Matlab script used in these experiments is provided by an external company, OxSonics Therapeutics, the exact nature of this conversion is not disclosed, and thus the 'cavitation level' in Arbitrary Units is used. Although the normalisation factor is not available, the normalisation process is the same for all outputs from the system, and thus the cavitation levels between experiments using the same OxSonics code can be compared to one another. The Arbitrary Units effectively represent, to within a constant factor, a measure of the maximum acoustic energy in a region determined from the output of PAM. PAM itself is described in more detail in Chapter 4, but essentially estimates the source strength, and consequently acoustic power, of oscillating bubbles at different locations in order

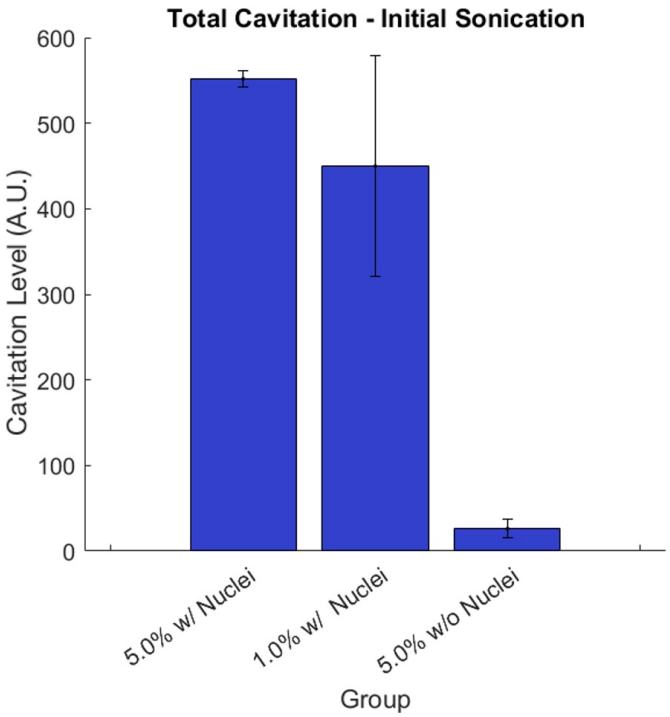


Figure 3.3: Mean of the 'Total Cavitation Level (A.U.)'. The total cavitation level is computed as the sum of the maximum energy values seen in the realtime PAM maps generated throughout the 5 minute sonication. This figure shows the average 'total cavitation level' for the three animals in each group. In the 5% and 1% DC groups, cavitation nuclei were injected intravenously, but for the 5% DC control group, no cavitation nuclei were injected. For each group, $n = 3$, and error bars represent the standard deviation.

to form an estimate of the acoustic energy in a region.

From figure 3.3, it is clear that there is a significant amount of cavitation activity in both the 5% and the 1% DC group, as expected for nanocups at this size and with the range of pressures used. It should be noted here that the graph shown is based on the recorded signal for the first 100 µs after the trigger pulse has been sent due to memory and time constraints. No correction has been applied to account for the fact that the pulse duration is five times longer at a 5% duty cycle (100 ms total) than at a 1% duty cycle (20 ms total) for the same PRF. Thus although the level of cavitation shown is similar between the two treatment groups, this may not be representative of the physical reality, since the difference in DC is not accounted for in this graph. Furthermore, the pressure during the initial sonication is typically varied between a

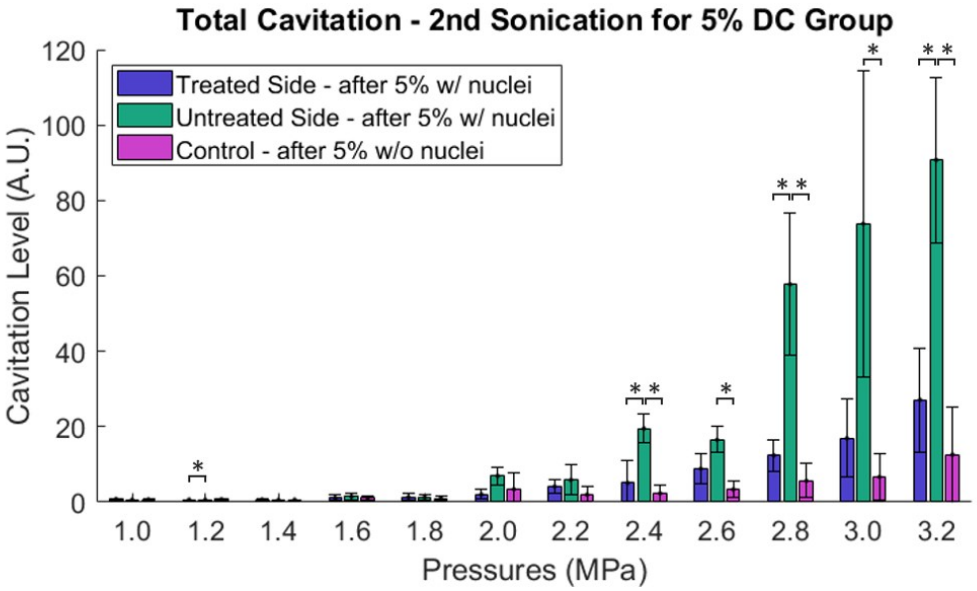


Figure 3.4: Mean of the 'Total Cavitation Level' recorded during second sonication for the 5% DC group for each tested pressure level for the treated and untreated sides. Each pressure level was tested for 30 seconds, and the mean and standard deviation were calculated at each pressure level using n = 3 animals. The same animals were used to test different pressure levels (a pressure ramp was performed for each animal on the second sonication). The level of cavitation in the treated side of the 5% DC control group is also presented to show baseline cavitation in a 5% treated side tumour without prior injection of cavitation nuclei. Asterisks indicate statistical significance within pressure groups (1-way ANOVA, $p < 0.05$).

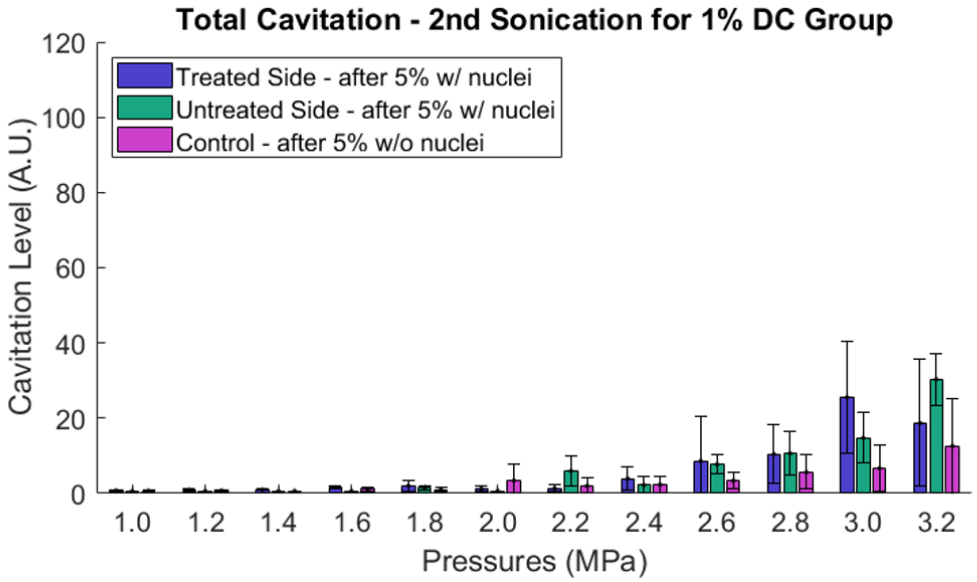


Figure 3.5: Mean of the 'Total Cavitation Level' recorded during second sonication for the 1% DC group for each tested pressure level for the treated and untreated sides. Each pressure level was tested for 30 seconds, and the mean and standard deviation were calculated at each pressure level using $n = 3$ animals. The same animals were used to test different pressure levels (a pressure ramp was performed for each animal on the second sonication). The level of cavitation in the treated side of the control group is also presented to show baseline cavitation in a treated side tumour without prior injection of cavitation nuclei. Note that the same normalisation was used for this figure as for Figure 3.4. No statistical significant differences are present within pressure groups.

minimum and maximum value in order to try and maintain cavitation level over the recorded signal period, which further serves to make the total recorded signal within the first section of the ultrasound exposure similar between the two treatment groups.

For the second sonications, statistically significant differences were assessed by using 1-way ANOVA, $p<0.05$, using Tukey's Honestly Significant Difference (HSD) Criterion as a post-hoc pair-wise comparison test, and are denoted by asterisks on figures 3.4 and 3.5.

Significant differences between the treated and untreated tumours were observed for some of the higher pressures (2.4 MPa, 2.8 MPa and 3.2 MPa) in the 5% DC group, but not in the 1% group. Surprisingly, in the 5% DC group it was the non-ultrasound treated tumour that exhibited the significant enhancement in cavitation activity during the second sonication.

In addition, the cavitation levels in the untreated side at the highest pressures of the 5% DC group were significantly higher than the cavitation levels in the untreated side of both the 1% DC group and reference group. This result strongly suggests that the passive accumulation of nanocups in the tumour cannot be held solely responsible for the increased cavitation activity on the untreated side.

This is an interesting result, and implies that the 5% DC may have an effect on the ability of nanocups to passively accumulate on the untreated side. Specifically, two possible explanations exist: either the 5% treatment has some mechanical effect on the cavitation nuclei that enables them to accumulate passively more effectively in the untreated tumour, or the effect is biological, with the treatment of one tumour resulting in greater vascular permeability in the other.

It is also possible that the treated area becomes less permeable to larger particles as a result of the treatment. However, since the second sonication in all groups used only 10 cycles, the cavitation levels in the untreated side of the 5% and the 1% should be directly comparable to each other. Thus whilst the lower permeability to large particles on the treated side would contribute to lower levels of cavitation in the treated side compared to the untreated side for each group, it cannot explain why

the cavitation in the untreated side of the 5% DC group is so much higher than the cavitation in the untreated side of the 1% DC group. It remains a possibility however, that reduced permeability to larger particles in the 5% DC group is a contributing factor to the overall effect.

Although the levels of cavitation in the treated side seemed to trend higher than the reference group, the differences were not statistically significant. It should also be emphasised here that the reference group was for a treated side tumour (5% DC group) only, and did not contain an untreated side for comparison, and therefore cannot be considered a full control for this experiment. There are two possible processes that may cause greater cavitation on the second sonication in both sides of the treatment group mice compared to the reference group mice: either there remains a low percentage of nanocups still in circulation at the time of the second sonication, or the effect is due to passive accumulation of nanocups in the tumour region. As discussed in Section 3.2.2, the circulation of nanocups at 25 minutes post injection is unlikely given their rapid clearance from the bloodstream. Therefore it is likely that the cavitation signal received on the second sonication is mostly due to cups that have passively accumulated in the tumour tissue which are then excited for the first time during the second sonication.

It is instructive in this case to examine the acoustic response data in more detail. Instead of looking at the cavitation level directly, the data presented in figure 3.4 has been re-plotted in terms of the probability of cavitation, where the cavitation threshold is defined as a PAM signal that is at least double that of the PAM signal from noise alone. The probability of cavitation is calculated as the number of PAM maps that contain a maximum PAM energy greater than the cavitation threshold, divided by the total number of PAM maps recorded, expressed as a percentage. The total number of PAM maps obtained at each pressure is equivalent for every mouse. The probability of cavitation is obtained for each pressure for every mouse. The mean and standard deviation plotted at each pressure represents the mean values for the probability of cavitation across all mice used in the group (in this case, $n = 3$).

Figure 3.6 evidences that the Probability of Cavitation for the 5% DC group is increasing with increasing excitation pressure. Overlaid as asterisks onto this figure are the results from Kwan *et al.* [82] showing the probability of cavitation at the same excitation frequency for different sizes of nanocups. Nanocups in the size range 300 - 800 nm are comparable to the size of those used in the present experiment, and are considered 'medium' nanocups. Their probability of cavitation is shown as pink asterisks. Nanocups in the range 100 - 300 nm are considered 'small', and their probability of cavitation is plotted as red asterisks in the figure. From the shape of the probability of cavitation curves, it appears as if the population present during the second sonication of this experiment is in the 100 - 300 nm range. This strongly suggests that only the smaller end of the available size distribution successfully extravasates into tumour tissue. The associated approximate cavity diameter for these size nanocups is in the order of 100 nm [82].

One possible explanation for the enhancement of cavitation activity is that the 5% duty cycle may cause the creation of other stabilised nanobubbles within the bloodstream that are then able to accumulate more easily in the untreated side tumour. Although extended sonication of the nanocups in vitro does not materially alter their size or size distribution [82], it is unclear what happens when this is repeated in the presence of plasma proteins, or in the proximity of tumours and other tissues. Future work could therefore involve a more advanced investigation and characterization of cups pre- and post- ultrasound exposure *in vitro* in the presence of blood and tumour tissue, both in terms of size and characterisation of cavitation activity. To investigate any possible biological mechanisms, a future study would need to include the monitoring of biological markers of inflammation and vascular response to assess systemic response, and well as full untreated controls in order to assess the effect of ultrasound alone on treated and untreated side tumours.

Another potential explanation for the low cavitation level on the second sonication on the treated side is that the initial 5% DC treatment could be causing structural damage to the vasculature of tumours. Such a structural change may limit the passive

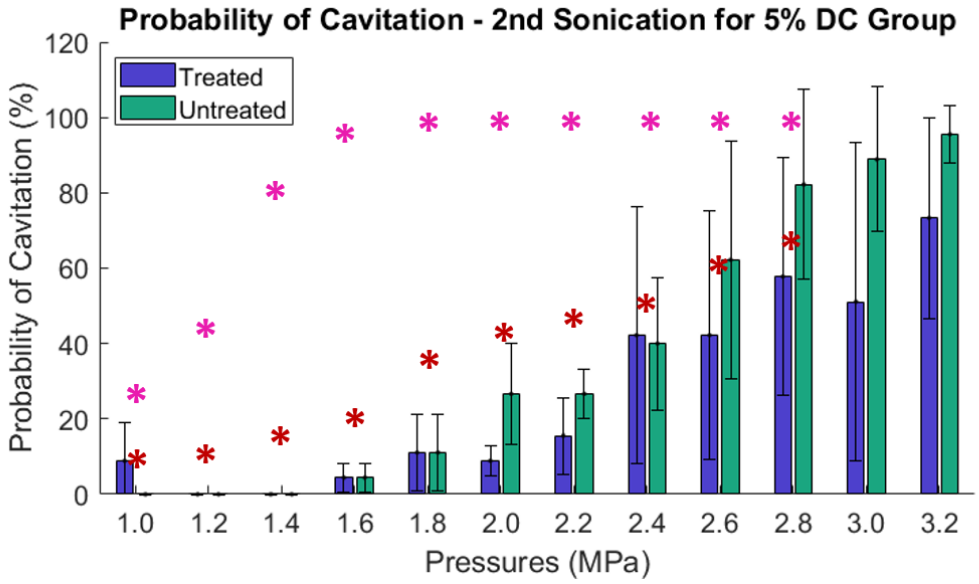


Figure 3.6: Mean 'Probability of Cavitation' for the 5% DC group. Asterisks denote data reproduced from Kwan [82] showing the probability of cavitation by pressure for medium size nanocups in the range of 300 - 600 nm (pink), and for small nanocups of less than 300 nm (red). Probability of cavitation is defined as the percentage of PAM frames in which the maximum cavitation energy shown is at least twice that of background noise energy (taken as a percentage of the total number of PAM frames created, which in this case is equivalent to the total number of pulses sent at each pressure step). Cavitation at different pressures was measured in the same animal (n = 3).

accumulation of nanocups during the treatment period, which ultimately would cause a decrease in cavitation signal on the treated side on the second sonication. In order to assess this effect, another experiment was designed that uses a fluorescent blood pool marker to assess vasculature structure and overall mass transport of a small molecule into the tumour. The results of this study are presented later in this chapter.

In summary, in this experiment, cavitation on the initial sonication was as expected for all groups.

Surprisingly however, on the second sonication, it was not the ultrasound-treated tumour but rather the contralateral side tumour that exhibited significantly enhanced cavitation response. This effect only occurred in the 5% DC group, but not in the 1% DC group. An investigation of the probability of cavitation as a function of pressure revealed that the population of particles cavitating during the second sonication are most likely drawn from the lower end (<300 nm particle size, approximately 100 nm cavity size) of the size distribution of the injected nuclei. This result suggests preferential extravasation of smaller particles.

3.4 Experiment 2: Assessment of Vascular Integrity Following Cavitation in Tumours

The results of figure 3.4 suggest that the cavitation response upon second exposure of the treated size is lower than for the untreated contralateral tumour.

The differences in the second sonication cavitation seen in the previous experiment show that exposure to ultrasound with a 5% DC appears to decrease the level of cavitation on the second sonication. As mentioned, this may be due to changes in vasculature as a result of the cavitation regime. For example, it is possible that the vasculature is altered temporarily as a result of the 5% DC treatment, thereby reducing the ability of nanocups to accumulate. To assess this hypothesis, the present experiment was designed to examine the influence of ultrasound treatment with different duty cycles on vasculature structure and permeability to a small molecule flu-

orescent marker known as AngioSense 680EX (PerkinElmer, Bukinghamshire, UK). AngioSense is a long circulating molecule that can be used to assess vessel structure when first injected, and can also be used to assess accumulation in a region 24 hours after the initial injection.

3.4.1 Experimental Procedure

A similar procedure to the previous experiment is followed, however there is an addition of AngioSense. AngioSense has an excitation wavelength of 680 nm - in the Near-Infrared (NIR) part of the spectrum. NIR imaging reduces the contribution of autofluorescence to the final image. Imaging can be further improved by placing the animals on a diet low in fluorescent components. Therefore the mice in this study were kept on an Alfalpha free diet (Teklad Global 19% Protein Extruded Diet, supplied by Envigo, UK) so as to reduce the contribution of autofluorescence from food in the red and NIR region of the spectrum.

The experimental procedure, performed on animals with bi-lateral CT-26 tumours, is as follows:

1. Anaesthetise animal and cannulate
2. Capture baseline IVIS
3. Recover animal fully
4. Re-anaesthetise and cannulate
5. Align animal in tank and inject 50 µl fluorescent nanocups
6. Treat one side tumour with utlrasound according to group sonication parameters
7. Wait 25 minutes for vasculature clearance
8. Expose treated side tumour to second sonication
9. Expose untreated side tumour to second sonication

10. Remove and recover animal fully
11. Re-anaesthetise animal and image with IVIS
12. Inject 25 µl AngioSense and IVIS
13. Recover animal fully
14. At 24 hours, re-anaesthetise and IVIS
15. Sacrifice animal and recover organs

The acoustic parameters for each sonication for this experiment are given in table 3.5, and the tumour volumes and number of animals used are given in table 3.6. In this case, the size of the study was expanded to three groups by the addition of a group with an even lower duty cycle. In part, this was because the previous study had shown an increase in cavitation on the second sonication on the untreated side for 5% DC, but no difference at 1% DC. Therefore it may be possible that a very low DC could improve permeability whilst also increasing the cavitation on the second sonication of the treated side tumour. If a very low DC treatment does increase permeability of tumour vessels, then drug delivery regimes may be assisted by using a two stage sonication approach to first increase vascular permeability with a low DC regime and then to push nanocups and drugs further into the tumour tissue with a higher DC sonication.

As before, the pressure for these sonications was varied by the operator in real-time, and the second sonication consisted of short pulses with increasing pressure at set intervals throughout the sonication. However given that very little interesting acoustic activity occurred below 2.0 MPa in the initial experiment, the pressure ramp for the second sonication was started at 2.2 MPa in this experiment.

3.4.2 Results and Discussion

The graphs of cavitation level on the initial and second sonications are shown in figures 3.7 to 3.10, and the quantification of the results of the IVIS imaging for each

Table 3.5: Acoustic parameters for the extravasation and re-excitation of nanocups in the Assessment of Vascular Integrity Study

Group	1st Sonication			Second Sonication		
	Pressure (MPa)	DC	No. Cycles	Pressure (MPa)	DC	No. Cycles
1	Variable, 1.6 - 2.1	5%	50000	Ramp, 2.2 - 3.2	0.001%	10
2	Variable, 1.6 - 2.1	1%	10000	Ramp, 2.2 - 3.2	0.001%	10
3	Variable, 1.6 - 2.1	0.01%	100	Ramp, 2.2 - 3.2	0.001%	10

Table 3.6: The number of animals and the tumour volume for the Assessment of Vascular Integrity

Group	**DC, 1st Sonication**	**No. Animals**	**Average Treated Volume**	**Average Untreated Volume**
1	5%	4	114	110
2	1%	4	109	97
3	0.01%	4	117	204

stage are given in figure 3.12. A representative IVIS image from each stage output of the experiment is shown in figure 3.11. As in the first experiment, the graphs shown in this experiment show the mean 'total cavitation levels' for each group of animals. In this experiment an n of four animals per group was used.

Once again, when looking at the second sonication data, the trend in cavitation energy for the 5% DC groups is that the untreated side shows higher levels of cavitation compared to the treated side. However when looking at the 1% and 0.01% DC groups, the cavitation energy in the treated side was not consistently significantly different from the untreated side. This confirms the cavitation response trends observed in the first experiment with an entirely new cohort of animals.

Although not significant in this cohort of animals, there also appears to be somewhat of a difference in cavitation levels on the untreated side of the tumour between

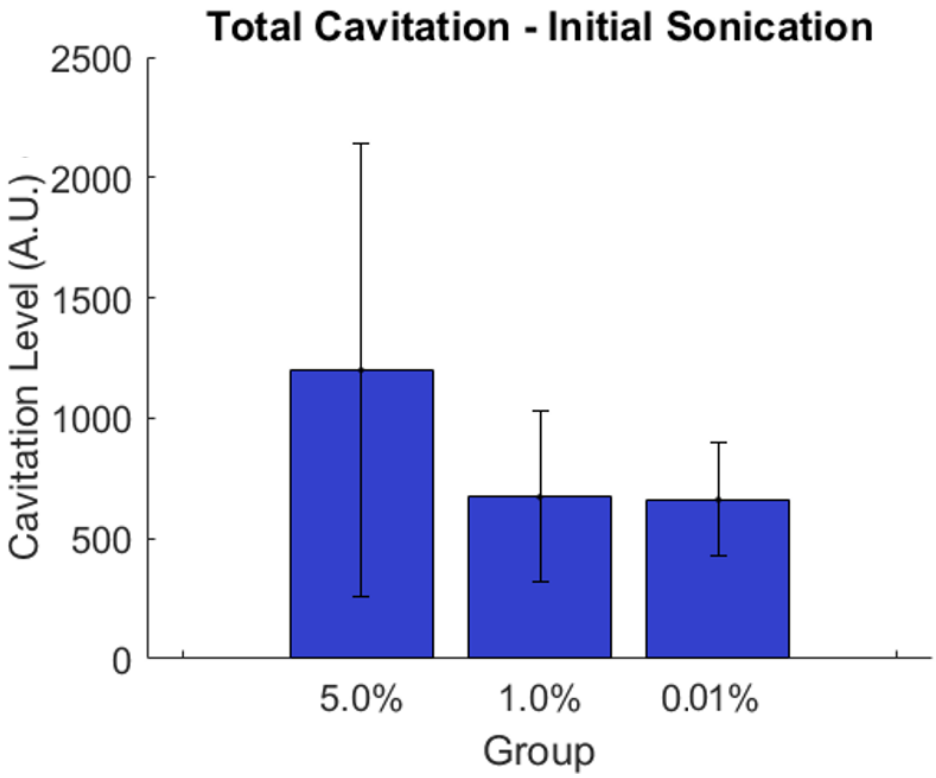


Figure 3.7: Average 'Total Cavitation Level' computed for each group (n = 4 animals, error bars represent standard deviation). 'Total Cavitation Level is the sum of the maximum energy of every PAM frame recorded during the 5 minute treatment time. The 5%, 1%, and 0.01% DC groups all had cavitation nuclei injected intravenously. No statistically significant difference exists between the groups, which is as expected.

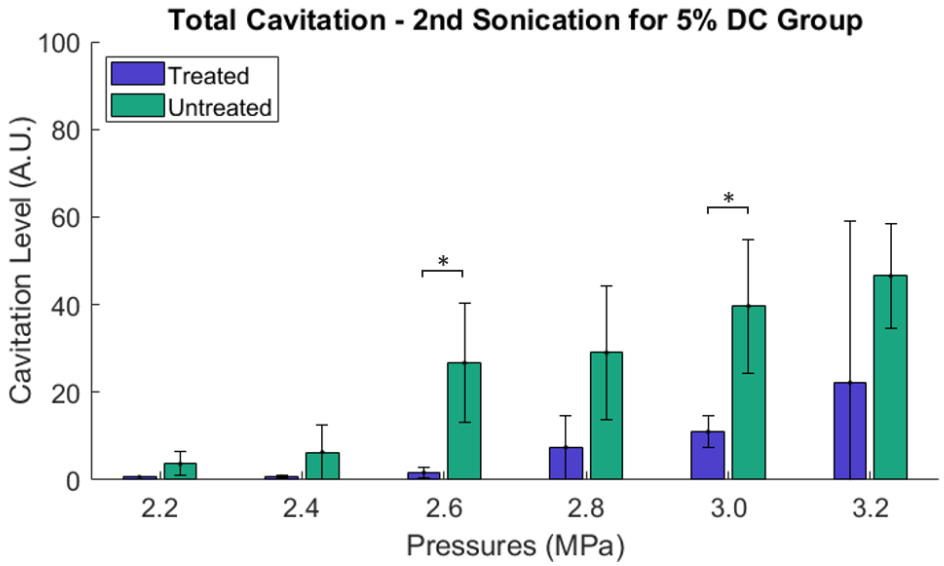


Figure 3.8: Mean of the 'Total Cavitation Level' recorded during second sonication for the 5% DC group for each tested pressure level for the treated and untreated sides. Each pressure level was tested for 30 seconds, and the mean and standard deviation were calculated at each pressure level using n = 4 animals. The same animals were used to test different pressure levels (a pressure ramp was performed for each animal on the second sonication). Asterisks indicate statistical significance within pressure groups (Independent t-test, $p < 0.05$).

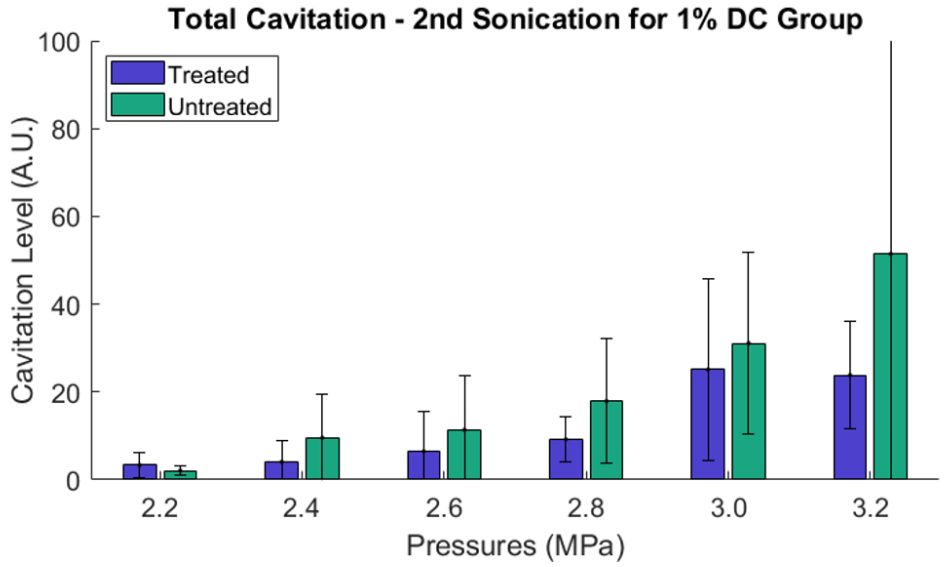


Figure 3.9: Mean of the 'Total Cavitation Level' recorded during second sonication for the 1% DC group for each tested pressure level for the treated and untreated sides. Each pressure level was tested for 30 seconds, and the mean and standard deviation were calculated at each pressure level using n = 4 animals. The same animals were used to test different pressure levels. No statistically significant differences were observed between groups.

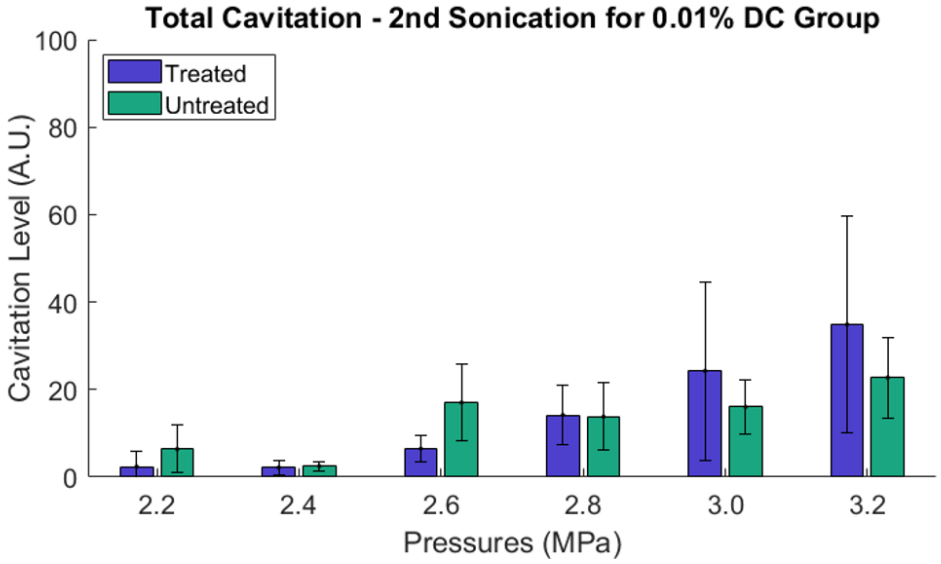


Figure 3.10: Mean of the 'Total Cavitation Level' recorded during second sonication for the 0.01% DC group for each tested pressure level for the treated and untreated sides. Each pressure level was tested for 30 seconds, and the mean and standard deviation were calculated at each pressure level using n = 4 animals. The same animals were used to test different pressure levels. No statistically significant differences were observed between groups.

different groups, especially at higher pressures. As with the previous experiment, this is a puzzling result, and further investigation is necessary to determine if a biological effect, or perhaps an acoustic effect that modifies the population of cavitation nuclei *in vivo* is responsible.

Quantitative AngioSense results are plotted in figure 3.11. Fluorescence is plotted as the Average Radiance Efficiency, which is a measure of the radiance of the animal in a given area, normalised to the illumination intensity over that area, and divided by the size of the area. Looking at the quantitative AngioSense results, although there are a few statistically significant results in the 'Immediately Post AngioSense (AS) Injection group', the significance does not continue into the 24 hour measurement. Therefore it can be seen that the overall mass transport of a small molecule into the tumour over time appears unaffected by exposure to ultrasound of different duty cycles. Thus exposure to an ultrasound treatment does not materially change the vasculature permeability negatively at 24 hours post sonication, and also does not

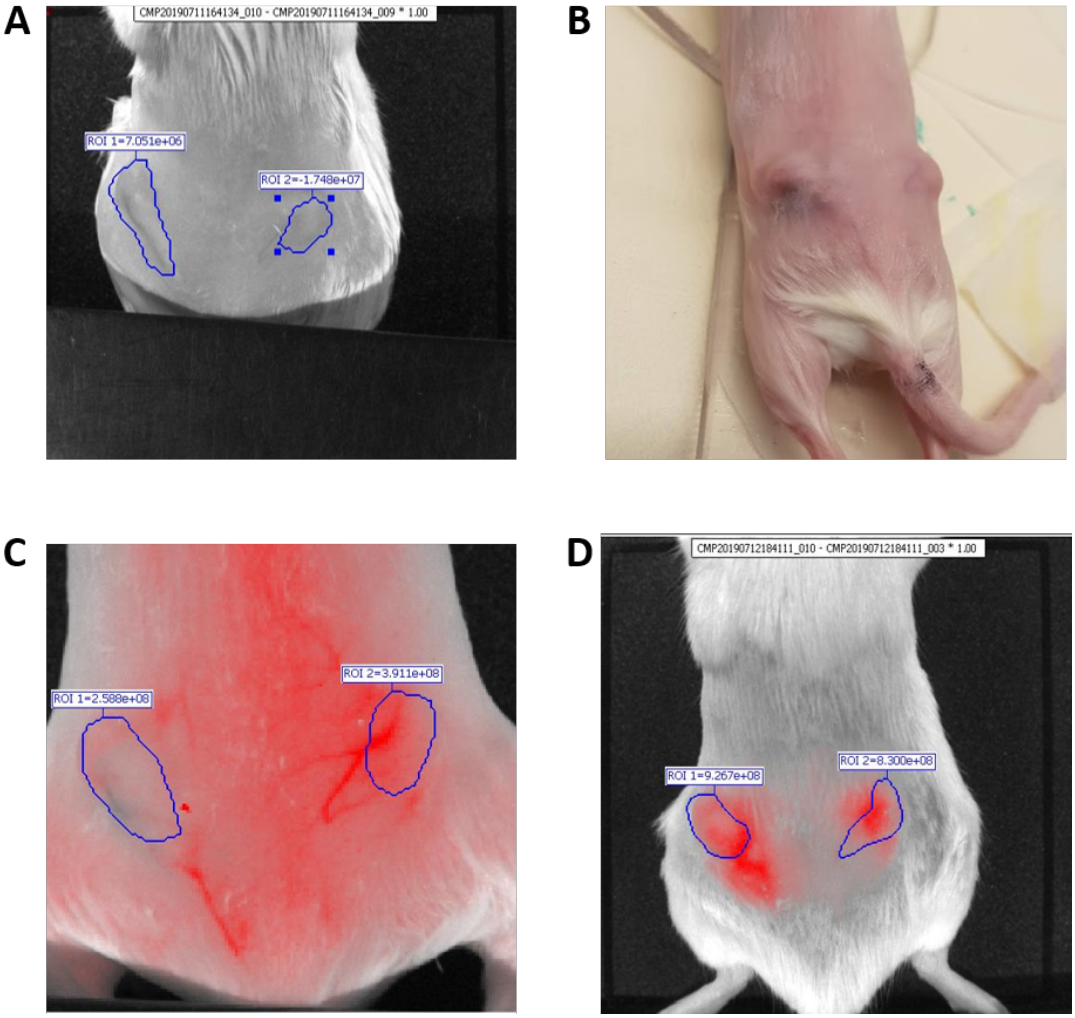


Figure 3.11: Representative images of the IVIS output for a single animal. A) IVIS image pre-treatment. B) Picture of the animal post treatment of the left hand side tumour with a 5% DC. C) IVIS image immediately post AngioSense injection. D) IVIS image at 24 hours post treatment.

appear to increase permeability to a small molecule, even for a 5% DC treatment.

No statistically significant differences exist between the treated and untreated side tumours in either the 5% or the 1% DC group. There is however a non-statistically significant decrease in the mean AngioSense levels. A possible explanation for this is shown in figure 3.11, where the AngioSense did not immediately flow into the tumour region via the most direct route. However this type of vasculature change did not occur on all animals within that group. In light of this observation and given that there was no statistically significant difference at 24 hours, it is unlikely that the vessel structure or the permeability of vessels to small molecules is changed significantly by any of the ultrasound treatments.

It should be noted however that although the permeability to small molecules is unchanged, this may not remain true for larger molecules. In order to assess that possibility, a larger long circulating molecule would need to be designed specifically for this purpose. Alternatively, another study using AngioSense might be designed with multiple injections of AngioSense, or the capture of IVIS images at closer time intervals to evaluate the timecourse of AngioSense accumulation in the tumour. In order to complete such a study however, the current Animal Licence under which this work is completed would need to be amended before work could commence.

The key acoustic results from this experiment have further served to highlight the changes in cavitation activity in a 5% DC treatment group, and again point to passive accumulation of cups in the size range 100 - 300 nm as the most likely underpinning mechanism. Again, passive accumulation alone cannot fully explain these results, as the accumulation of particles should occur in both the treated and untreated side tumours. Therefore in this case, as in previous cases, the results are likely due to a combination of factors. First, acoustic cavitation at high duty cycles could potentially create stabilised nanobubbles with a somewhat smaller size distribution (100 - 300 nm) that matches with the probability of cavitation data. In addition, other biological mechanisms, for example, systemic inflammation, could increase the permeability in the entire mouse. And a final contributing factor could be that the cavitation causes

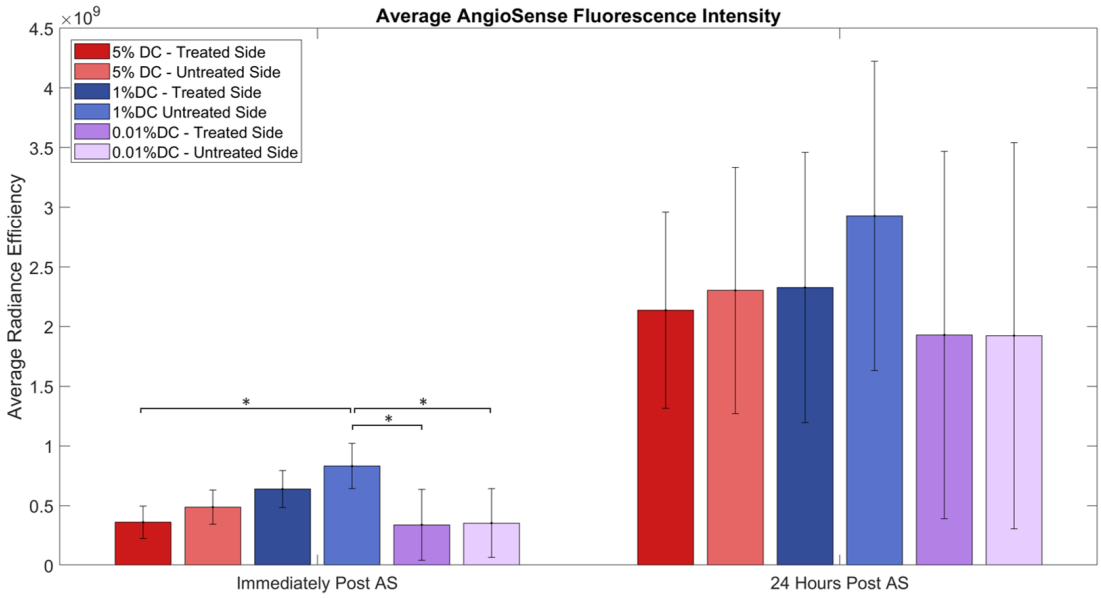


Figure 3.12: Quantitative assessment of AngioSense fluorescence immediately post injection, and at 24 hours post injection. Baseline AngioSense fluorescence signal (pre-treatment) has been subtracted for each animal. n = 4 for each of the groups (5%, 1%, and 0.01% Duty Cycle). Asterisks indicate statistical significance within each timepoint group (1-way ANOVA, $p < 0.05$).

a morphological change on the treated side that does not allow the flow or perfusion of the larger size nanocups.

In addition, the study of vasculature using a simple small molecule fluorescent marker has shown that changes in the accumulation of such molecules over time do not occur between different groups, even if some difference is observed immediately following treatment. As discussed, AngioSense is a useful marker, but due to its size it is likely to extravasate through minimally leaky vasculature, and therefore cannot necessarily be used as a surrogate marker for the likelihood of extravasation of larger molecules via active or passive extravasation. Another factor not yet discussed relates to a limitations of the IVIS imaging technique itself. Whilst the fluorescence images obtained immediately post AngioSense injection highlight the blood vessels well, the nature of the technique is that it is a 2D surface measurement, and therefore does not capture a full picture of tumour vasculature. In order to overcome these limitations,

a new 3D visualisation technique is employed in the final study of this chapter in order to ensure the visualisation of vessels in 3D.

3.5 Experiment 3: Assessment of Cavitation in Tumours of Different Stages and Types

As discussed in the outcomes of the first experiment presented in this chapter, passive accumulation appears to be a factor contributing to the increased cavitation levels observed on the second sonication. In addition, due to the small study sizes ($n = 3$, $n = 4$) used in the initial experiments, high variability within the groups may have contributed to the lack of statistical significance of the increased cavitation levels in the treated side compared to the reference group. Therefore, a study was designed to assess the passive accumulation alone (without the addition of active ultrasound extravasation), using a larger sample size. The aim of this experiment is to answer three key questions.

Firstly, does the level of passive accumulation differ by tumour stage? For example, due to their size, larger and more aggressive tumours tend to recruit new blood vessels at a much faster rate than their smaller counterparts. In doing so, the rapid growth rate of vessels means that the vessel wall is significantly underdeveloped, and thus very large endothelial gaps may result. This would be represented by an increase in 'leakiness'. Thus tumours at different stages of development were used to investigate this hypothesis.

Secondly, does the level of passive accumulation differ with tumour type? Two different tumour lines were used to investigate this outcome. The tumour lines selected are both adenocarcinomas, and have both been shown to be perfused via contrast enhanced ultrasound and DCE-MRI by Sheena Wallington as part of work completed for the Oxford Institute of Radiation Oncology. One significant mechanical difference between the tumour lines is found in the stromal content of each tumour line. Specifically, the human pancreatic model (CAPAN-2) has a very dense stroma, and excised

tumours feel hard on palpation. The murine colorectal model (CT-26) has a much less dense stroma, contains a significant number of leukocytes, and feel relatively soft when palpated (compared to the CAPAN-2 line). It is hypothesised that the dense stroma of the CAPAN-2 tumours may hinder the passive accumulation of nanoscale agents.

Thirdly, is the location of the PAM signal preferentially associated with tumour vasculature? This is investigated by comparing PAM data to a ground truth of vessel location. In order to accurately investigate the tumour vasculature pattern, and in order to assess the ground truth of where tumour vessels are located, a resin perfusion technique (based on previously established Corrosion Casting procedures) is implemented. This resin perfusion method provides a good way to assess vasculature heterogeneity *in vivo* in order to add information to a passive accumulation study. However, the procedure does not always succeed, and therefore AngioSense is employed in this experiment again as a secondary measure to visualise surface tumour vessels.

3.5.1 Experimental Procedure

The experimental procedure is thus as follows:

1. Anaesthetise animal and cannulate
2. Image baseline on IVIS
3. Inject 50 µl of fluorescent nanocups, and 20 µl of AngioSense and image
4. Recover animal fully
5. After a minimum of 35 minutes, re-anaesthetise animal
6. Position animal in water tank and exposure both side tumours to ultrasound, scanning layer by layer in the elevational direction
7. Remove and recover animal

8. At 2 hours after treatment, anaesthetise animal and image with IVIS

9. Immediately sacrifice animal by an overdose of anaesthetic and perform resin perfusions

10. Fix tissue and perform CT scans

Groups in this experiment are divided by stage of tumour development, and also by tumour line. The stage of development is initially categorised by tumour volume measurements, and later recategorised by tumour weight. The final groups are as follows: 'Early Stage' (0 to 25 mg), 'Mid Stage' (26 to 70 mg), 'Normal Stage' (71 to 250 mg), 'Late Stage' (greater than 250 mg). The full size distribution is given as part of the results in figure 3.15. Groups were selected based on usual treatment ranges for *in vitro* and *in vivo* studies performed within the Biomedical Ultrasonics group at the University of Oxford.

3.5.2 Results and Discussion

The cavitation results for the tumour development stage study (showing data by group), and for the comparison between tumour lines, are presented in figures 3.13 and 3.14. In this case the unit of measurement is still presented as Arbitrary Units (A.U.), however these are different to the units presented in the first two experiments of this chapter. This is because offline processing of PAM data, with a finer PAM grid, was performed, and results from figures 3.13 and 3.14 should not be compared to the figures presented earlier in this chapter (figures 3.3 to 3.10). This processing allowed for better localisation of cavitation activity, which ultimately enabled the co-localisation of PAM activity to vasculature in a large tumour. Graphs in this experiment are presented as the mean and standard deviation of the average of the 'maximum cavitation level' per PAM frame. The 'maximum cavitation level' represents the spatial maximum of the energy in a region determined using PAM. The average of the 'maximum cavitation level' is thus the total sum of the maximum cavitation levels divided by the length of sonication time. The length of sonication has

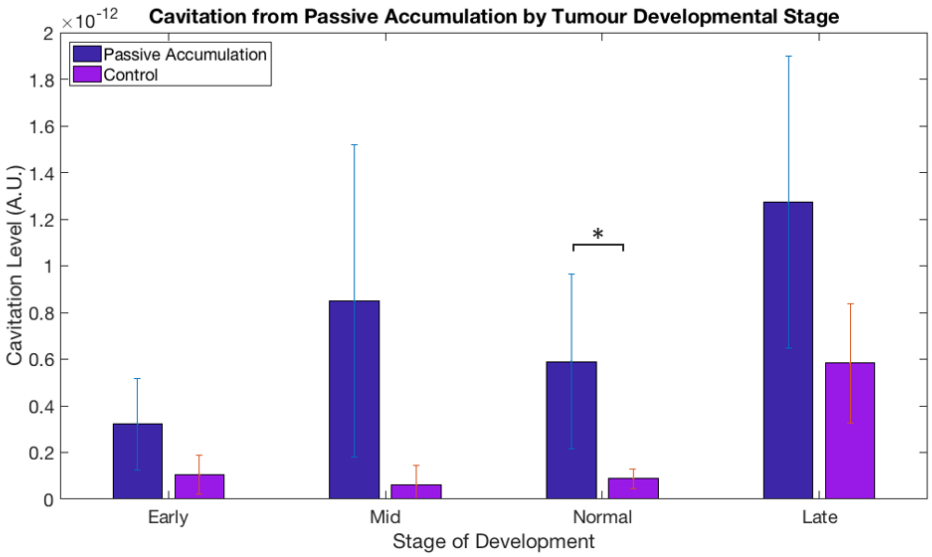


Figure 3.13: Cavitation level recorded due to passively accumulated particles compared to controls for CT-26 tumours grouped by weight into Early (0 - 25 mg tumour size, n = 10 treatment, n = 3 controls), Mid (26 - 70 mg tumour size, n = 10 treatment, n = 3 control), Normal (71 - 250 mg tumour size, n = 12 treatment, n = 3 control), and Late (larger than 250 mg tumour size, n = 11 treatment, n = 4 control) stage groups. Asterisks indicate statistical significance within each group (Independent t-test, p <0.05).

been chosen as the averaging factor rather than tumour weight in order to mitigate artificially high cavitation levels for extremely small (1 - 5 mg) tumours.

From figure 3.13 a significant difference in the level of cavitation in the CT-26 tumours compared to controls is evident for the 'normal' treatment size. This significance is not present at $p < 0.05$ in the earlier or later stage groups. A lack of strict significance in the early stage groups is expected, since passive accumulation may not yet be present in small tumours. In very late stage tumours, it is possible that they contain necrotic regions, and therefore normalising by treatment time tends to decrease the average cavitation level compared to controls. In addition, for the late stage group, controls show high levels of cavitation. This may be due to the fact that due to the size of late stage tumours, a significant amount of skin surface (which often contains entrapped gas bubbles) is also exposed to ultrasound, thereby increasing the total cavitation recorded compared to smaller tumours. Furthermore, the larger

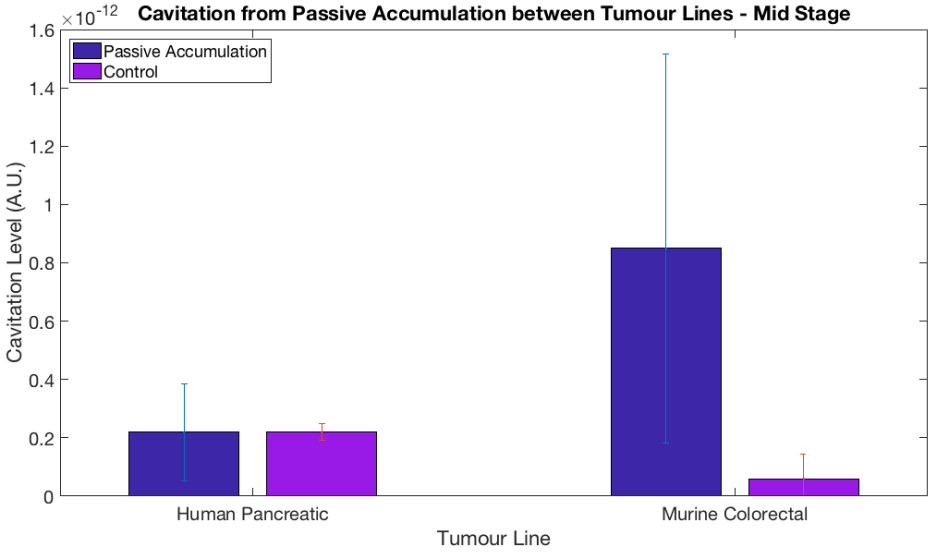


Figure 3.14: Cavitation level recorded due to passively accumulated particles compared to controls for the mid stage group for two different tumour lines, CT-26 (murine colorectal,n = 10 treatment, n = 3 control) and CAPAN-2 (human pancreatic, n = 3 treatment and control). No statistically significant differences are observed at the p <0.05 significance level.

tumours are often very irregularly shaped, which can also lead to larger entrapped gas bubbles which, if cavitated, may drastically increase the cavitation output level.

In the comparison between tumour lines given in figure 3.14, there is a clear difference between the level of cavitation in tumours in the medium size range compared to controls for the CT-26 compared to the CAPAN-2 cell line. The CT-26 group clearly shows higher cavitation overall compared to the controls, even though the difference is not statistically significant. However there is very little difference for the CAPAN-2 line, indicating that passive accumulation, if it does occur in CAPAN-2 at all, would be difficult to distinguish at this stage. While certainly not the only factor affecting passive accumulation, these results in part support the hypothesis that the density of the tumour stroma plays a role in determining the levels of passive accumulation of nanoscale cavitation nuclei.

Although there is a difference in the groups of CT-26 tumours, all of the groups showed high variability. In order to assess this, figure 3.15 shows the average 'max-

imum cavitation level' against the tumour weights. Here the reason for the large standard deviations in the grouped data is clear. In particular, the CT-26 data shows high variability in cavitation level for tumours between 300 and 500 mg. This is possibly because passive accumulation is not only a function of tumour size, but is also affected by vascular distribution, growth rate and other inflammatory markers.

In order to qualitatively assess whether any difference in tumour vasculature is immediately obvious between tumours with high and low cavitation, the CT scans of three tumours in the mid size range were examined. The CT scans of these tumours are shown in figure 3.16, in which the top row represents a CAPAN-2 tumour, the middle row represents a low cavitation CT-26 tumour, and the bottom row represents a high cavitation CT-26 tumour. In the CT images, vessels appear as lighter (white or cream coloured) than the surrounding soft tissue. Tumour tissue has a very similar radiopacity to soft tissue, and therefore both the tumour and any surrounding skin tissue appear brown in colour, with a grainy texture.

The tumours were selected based on their size and cavitation data, and individual values are indicated by a small red arrow on the corresponding data points in figure 3.15. All appear to contain some vessels surrounding the tumour, and some internal to the tumour. In addition, all tumours appear to have some sinusoidal, tortuous vessels common to all tumour types [111]. The largest feeding vessel is present in the tumour with the highest cavitation, and this tumour also appeared to have some larger diameter vessels on the perimeter of the tumour. However, no quantitative conclusions can be drawn from these tumours.

There are also some limitations in the use of this perfusion technique for vasculature assessment. Specifically, it is difficult to determine whether there are truly no large vessels in a region, or if the resin simply cannot perfuse through a certain size vessel. In addition, the minimum resolution of the CT scanner is 4.5 µm, which is not good enough to assess the smallest vessels present.

Nonetheless, CT imaging provides a useful starting point to assist in visualising vasculature. In order to elucidate some of the other possible passive accumulation

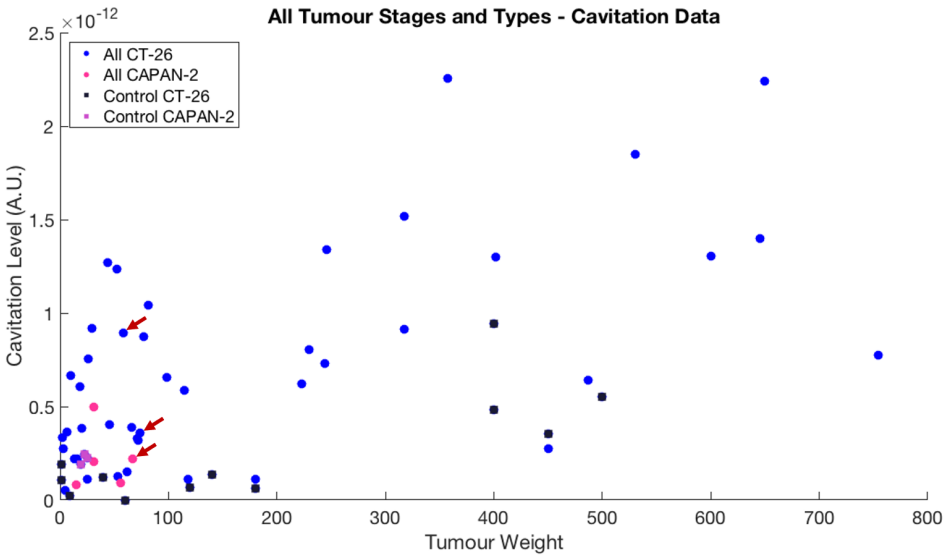


Figure 3.15: Cavitation level due to passively accumulated particles compared to controls for all tumours used, normalised by the length of the sonication and plotted against the final tumour weights. Red arrows indicate tumours with CT scans of vasculature shown in a subsequent figure in this section.

factors, a passive accumulation study that assesses not only cavitation by tumour size, but also by other biomarkers would be required. These may include endothelial growth factor markers, or may include other vasculature related markers such as haemostatic markers, as demonstrated by recent studies on the topic [112][113].

In order to address the third aim of this study - to determine whether passive accumulation can be meaningfully mapped using PAM - a sample tumour from the late stage group was selected for evaluation in comparison to B-Mode and PAM. Images of the micro-CT scan of the tumour are shown in figure 3.17. In the figure, different angles of view are shown, and the relative position of the B-Mode linear array is described in the caption. These images give an overview of the general positioning of vessels (for example, vessels closer to a given side of the tumour at different elevational planes).

The ultrasound data for this experiment was acquired by scanning the tumour layer by layer in the elevational dimension. During the experiment, elevational 'slices' were taken at 1 mm intervals. Specifically, the animal was attached to a manual

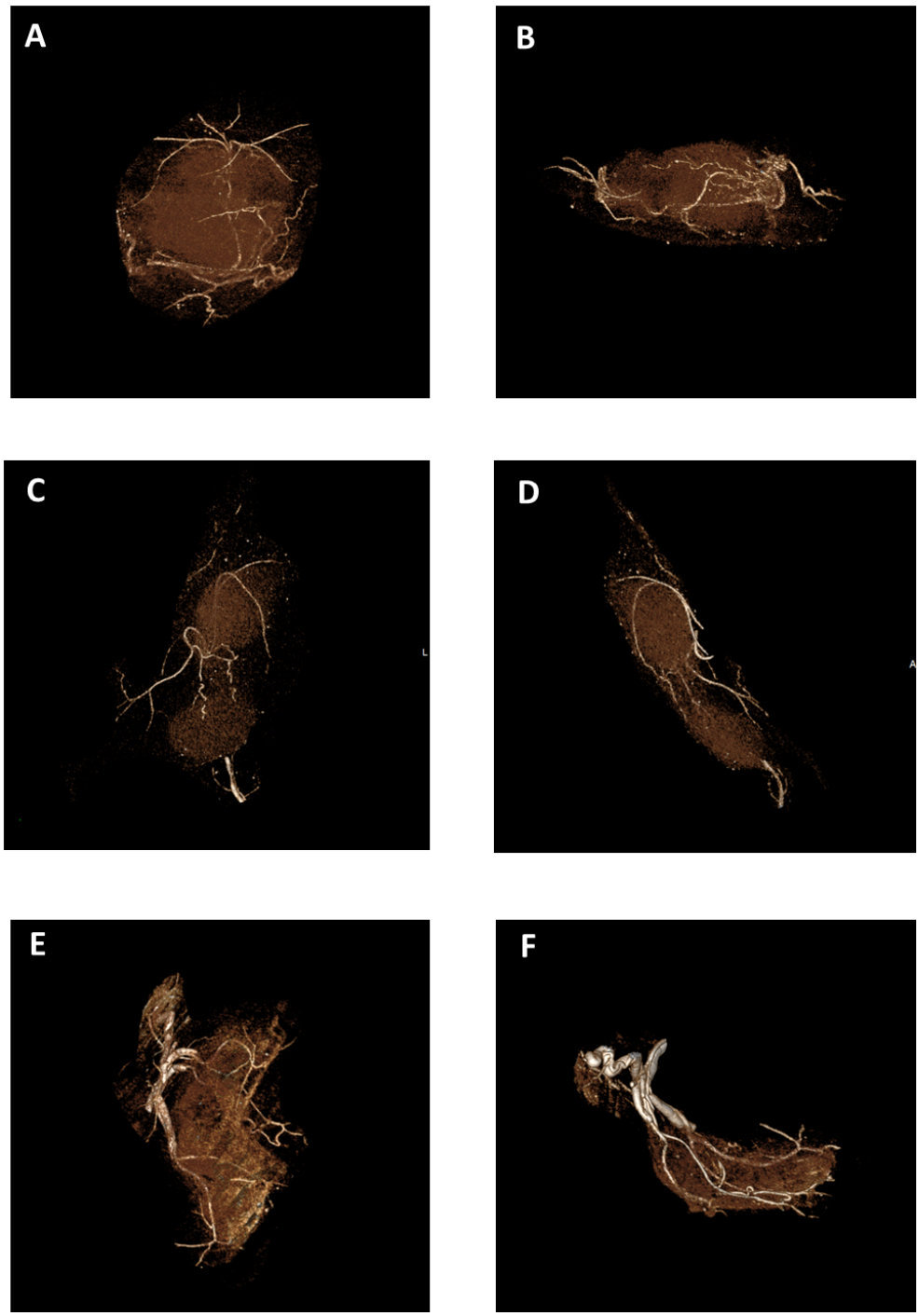


Figure 3.16: Micro-CT scans of three different tumours of a similar size, but with different cavitation levels. Vasculature appears lighter (more cream or white) than the tumour tissue, which appears as a brown colour with grainy texture. Tumours shown in this figure are also indicated by red arrows on the scatter plot of 'cavitation versus weight' presented earlier in this section. A and B) Front and side views of a CAPAN-2 (human pancreatic) tumour with low cavitation. C and D) Front and side views of a CT-2 (murine colorectal) tumour with low cavitation. E and F) Front and side views of a CT-2 (murine colorectal) tumour with high cavitation.

micrometer positioning stage in the experimental setup. Once the entire 2D tumour region in a single elevational plane had been exposed to ultrasound, the animal was moved down 1 mm and the 2D tumour region in the new plane was scanned, until this processes had been repeated for the entire length of the tumour.

Then, once the CT scan of the resin perfused tumour had been obtained, the orientation of the tumour was changed manually such that it matched the orientation of the tumour during the experiment as closely as possible. Measurement lines were then placed on the CT scan to delineate 1 mm thick elevational planes that correspond to the ultrasound elevational scanning planes. The 1 mm elevational sections are shown by the green lines in figure 3.18. In order to compare the ultrasound plane with the corresponding plane in the CT scan, the CT scan was digitally cropped such that only a single scanning plane was shown. This is demonstrated in figure 3.19, where the green lines indicating the other scanning planes have been left on the figure for clarity. Once digital sections had been created, the section was rotated to a 'top view' to match the B-Mode orientation of the tumour.

Figure 3.20 shows all layers of ultrasound performed, with the total PAM aligned and overlaid on top. As the mouse was moved relative to the transducers during treatment, an automated co-registration script relying on 2D cross correlation was developed in order to determine a global position for the PAM data for the entire layer, relative to the first B-Mode frame for that layer. These planes are then compared to the corresponding CT layer, which is manually oriented and overlaid on the B-Mode image. Manual placement is performed due to the complexity of automating the alignment of a system with multiple degrees of freedom in both the experimental setup and the CT scan image, combined with the difficulty of defining the tumour borders from a B-Mode image. The results of this alignment of PAM, B-Mode and CT data can be seen in figures 3.21 to 3.26. Insets of the CT slice in the correct orientation, and of the PAM data alone are also shown for clarity (insets not to scale).

Given that it is unlikely that nanocups were still circulating in large numbers at

the time of treatment, the PAM data is likely to be from cavitation nuclei that have leaked out near the vessels, or are lodged in the vessel wall. Thus the positioning of PAM near the site of tumour vessels makes sense. A good alignment between the PAM signal and tumour vessels can be seen in some of the final combination frames, for example in layers 1, 3, 9 and 11. Other layers however do not demonstrate good alignment, and further work on the technique is needed before a true 3D PAM image of passively extravasated particles can be obtained.

For full confirmation that nanocups have extravasated, and that the cavitation seen is not purely the result of a small number of nanocups circulating in the blood stream, the tumours will need to be sectioned and the fluorescent nanocups located under confocal microscopy. This confirmation will form part of future work on this topic.

3.6 Conclusion

In this chapter, an investigation into the *in vivo* vascularity and permeability of tumours was performed. Following on from promising *in vitro* results, a similar approach to active extravasation and re-excitement of cavitation nuclei was taken. Although the *in vivo* results did not match the *in vitro* results in terms of expected outcomes, the first study performed still showed two interesting results: passive accumulation may occur in some tumour types, and the interaction between ultrasound treatments and the vasculature could play a role in second sonication cavitation levels and requires further investigation.

Therefore, a further study was undertaken using a small fluorescent molecule in order to assess the effect on vasculature and vascular permeability following ultrasound treatments. In this case, quantitative assessment of fluorescence results indicated no significant difference in fluorescence at 24 hours post treatment. This lack of significant difference in accumulation of a small molecule over time implies that ultrasound treatment did not impact tumour permeability or cause vasculature dam-

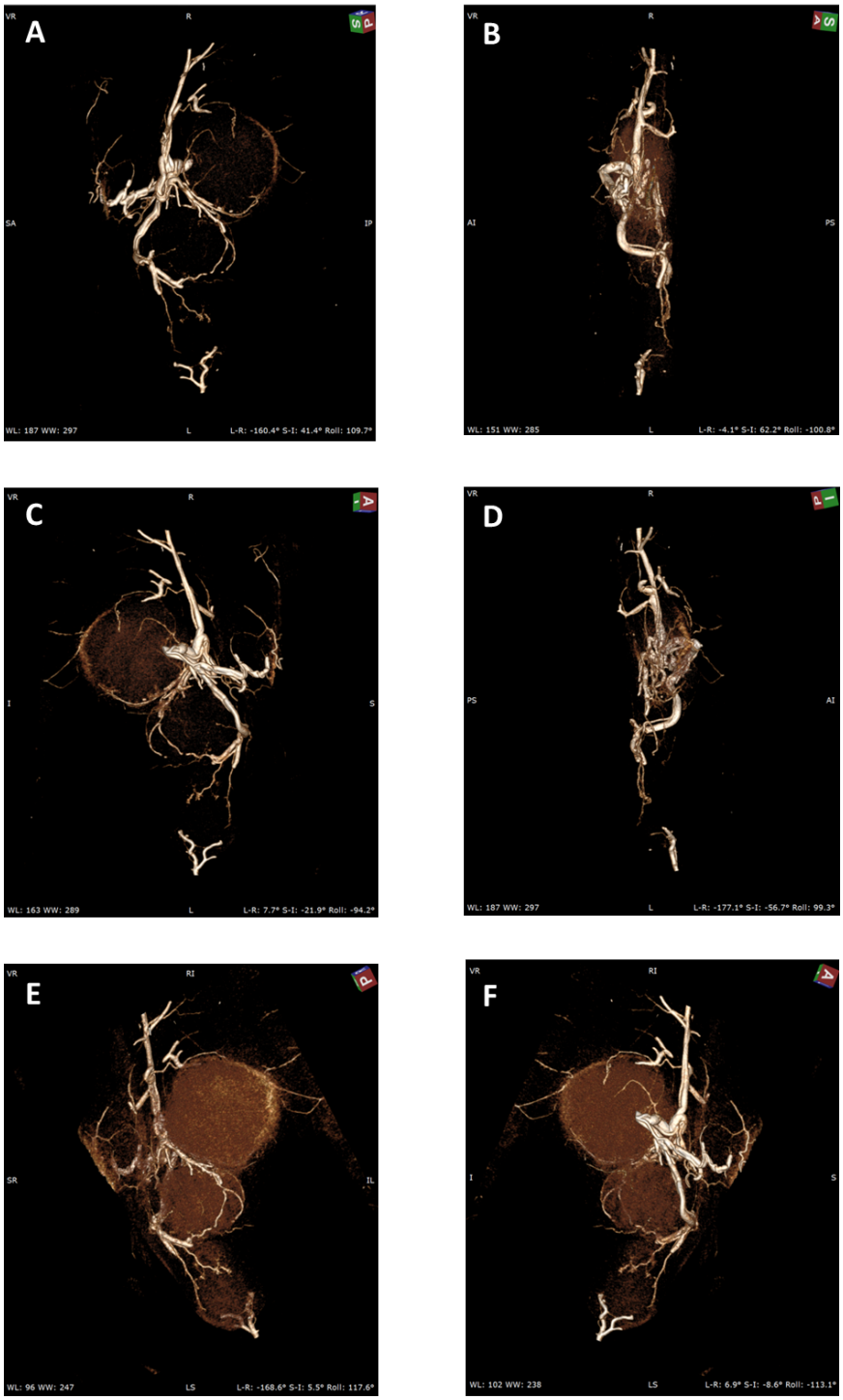


Figure 3.17: A micro-CT scan of a resin perfused tumour, showing different views. Vasculature appears lighter (more cream or white) than the tumour tissue, which appears as a brown colour with grainy texture. A) Side view, ultrasound array on right of frame. B) Back view, ultrasound array on the far side of the tumour. C) Side view, ultrasound array on left of frame. D) Front view, ultrasound array looking at tumour from the same position as the reader. E and F) Other orientations to aid 3D orientation of the tumour.

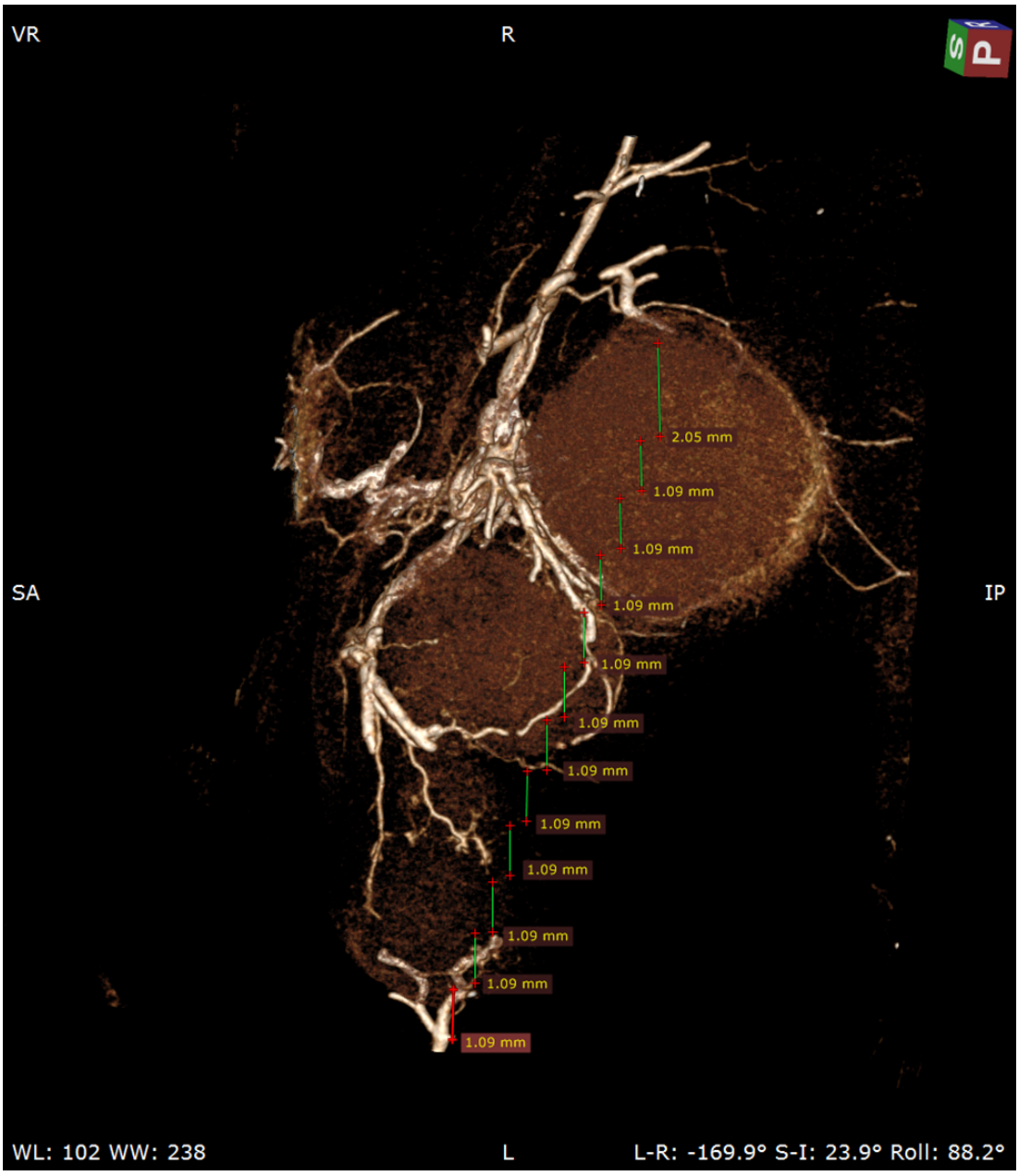


Figure 3.18: A micro-CT scan of a resin perfused tumour. PAM was used in this experiment to create a 3D map of regions in the tumour in which passive accumulation of particles had occurred. To achieve this, ultrasound excitation and PAM was performed in sequential elevational planes in the animal. In this CT image, the green lines indicate the regions that correspond to the elevational planes in which the ultrasound was performed. Vasculature appears lighter (more cream or white) than the tumour tissue, which appears as a brown colour with grainy texture.

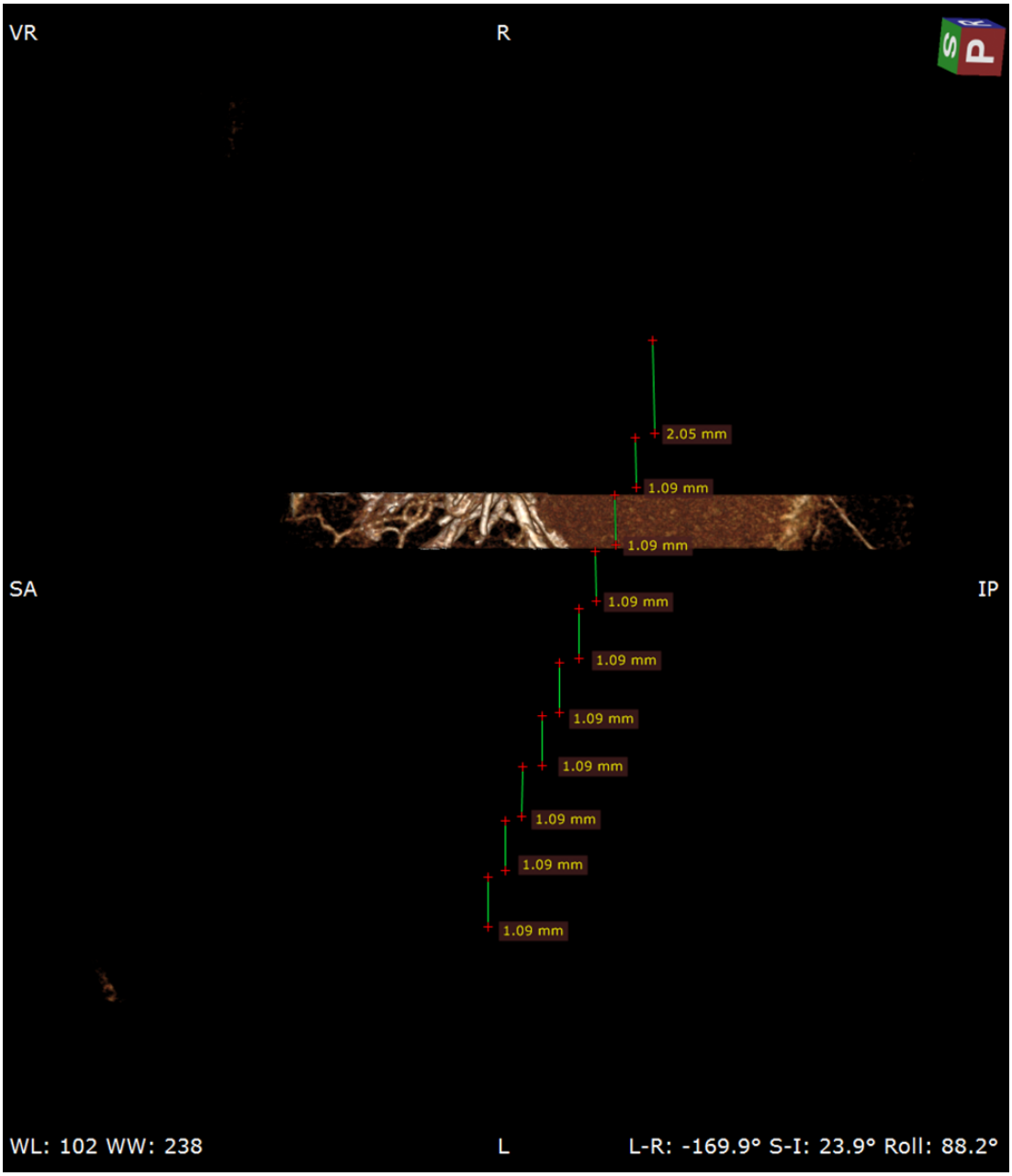


Figure 3.19: A section of the micro-CT image of a resin perfused tumour. In this image, the green lines indicate the regions of the tumour on the CT scan that correspond to the elevational planes in which ultrasound excitation and PAM were performed during the experiment. Here, a single plane has been 'cut' to demonstrate how it is possible to isolate separate levels of the tumour in the CT scan for comparison with the PAM maps that were obtained for each elevational plane during the experiment. The CT section shown is then rotated to match the orientation of the PAM map and B-Mode images (shown in subsequent figures).

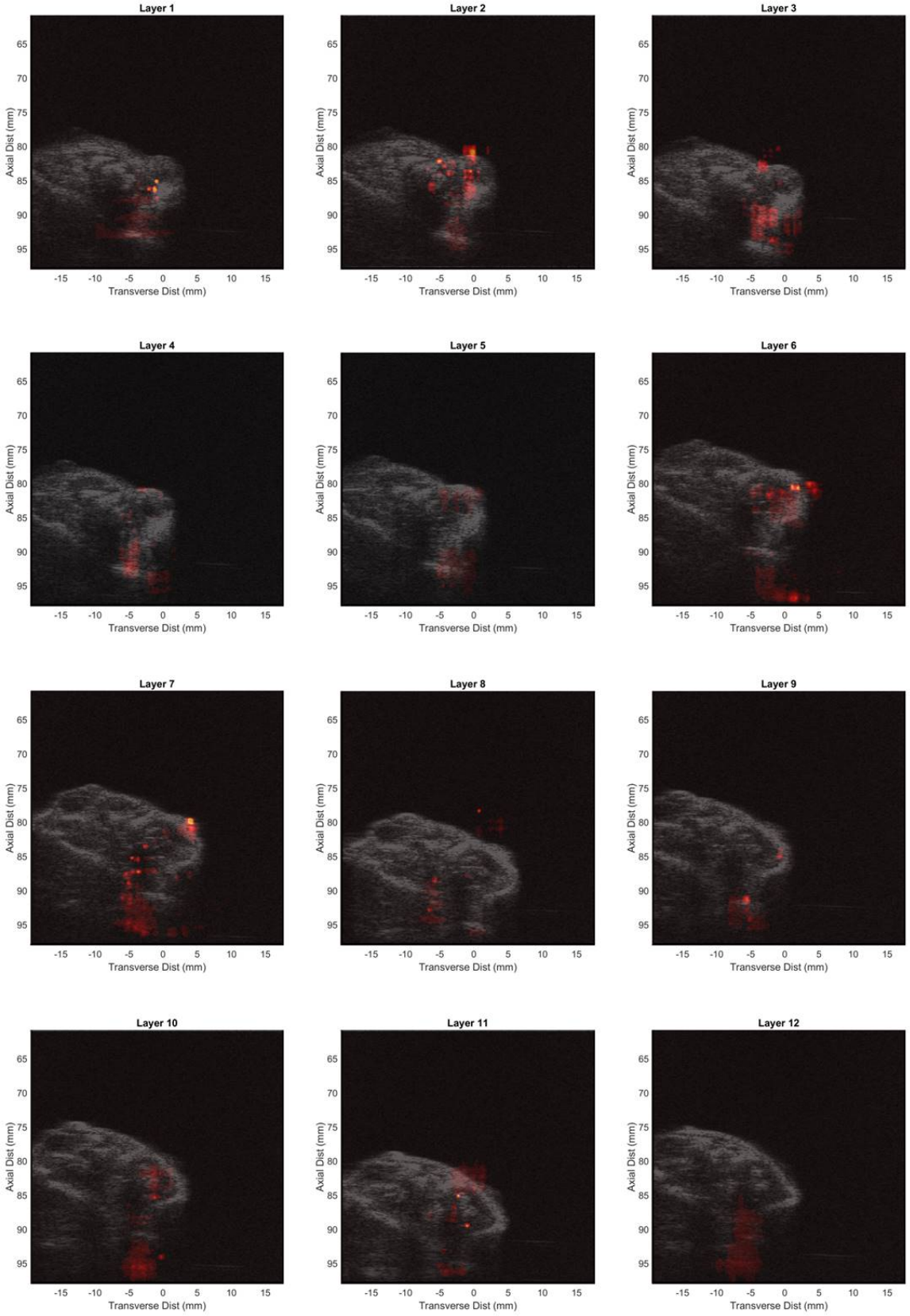


Figure 3.20: B-Mode images (gray) with overlaid PAM data (red) for each imaging layer.

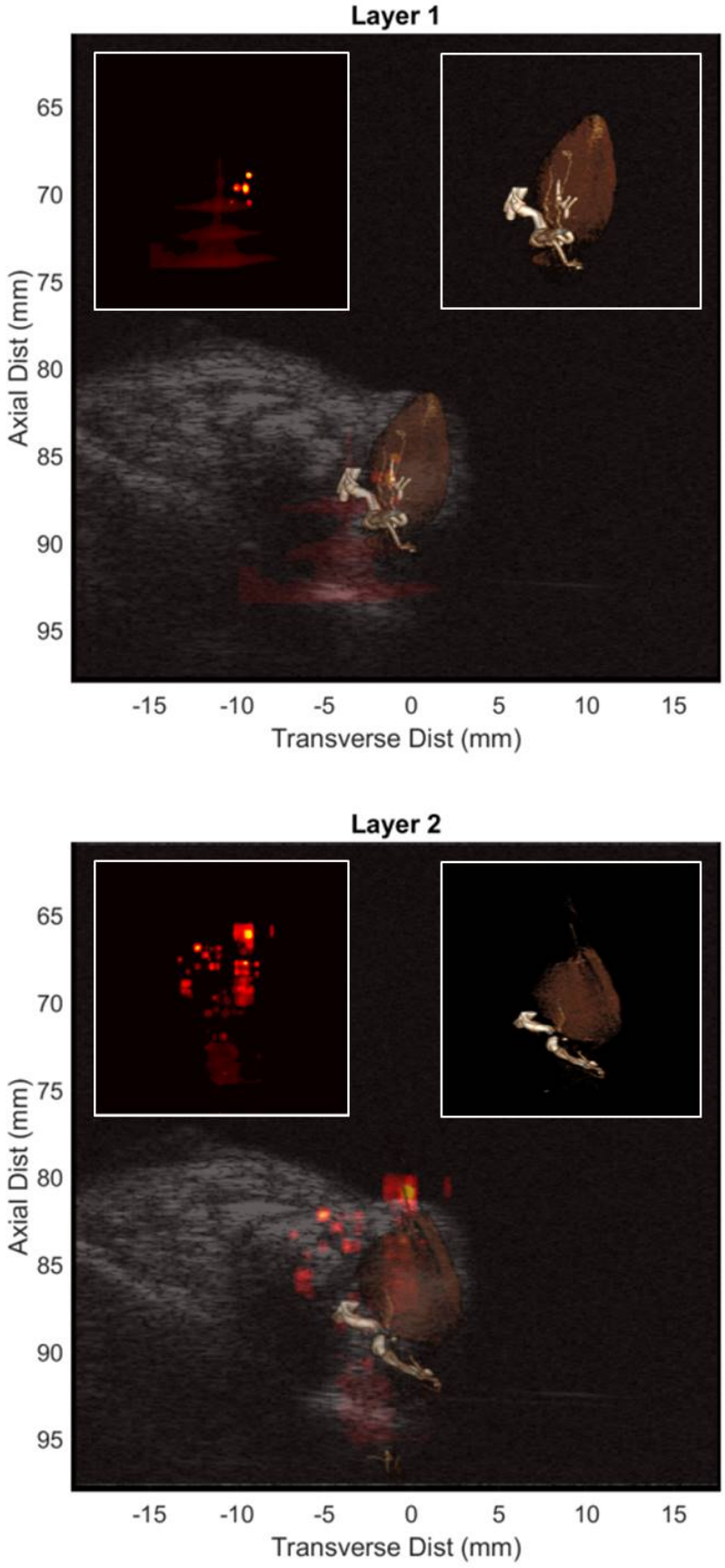


Figure 3.21: Layer 1 and 2 of overlay of B-Mode, PAM and CT data. Insets (not to scale): Left - PAM only data (red), Right - CT only data.

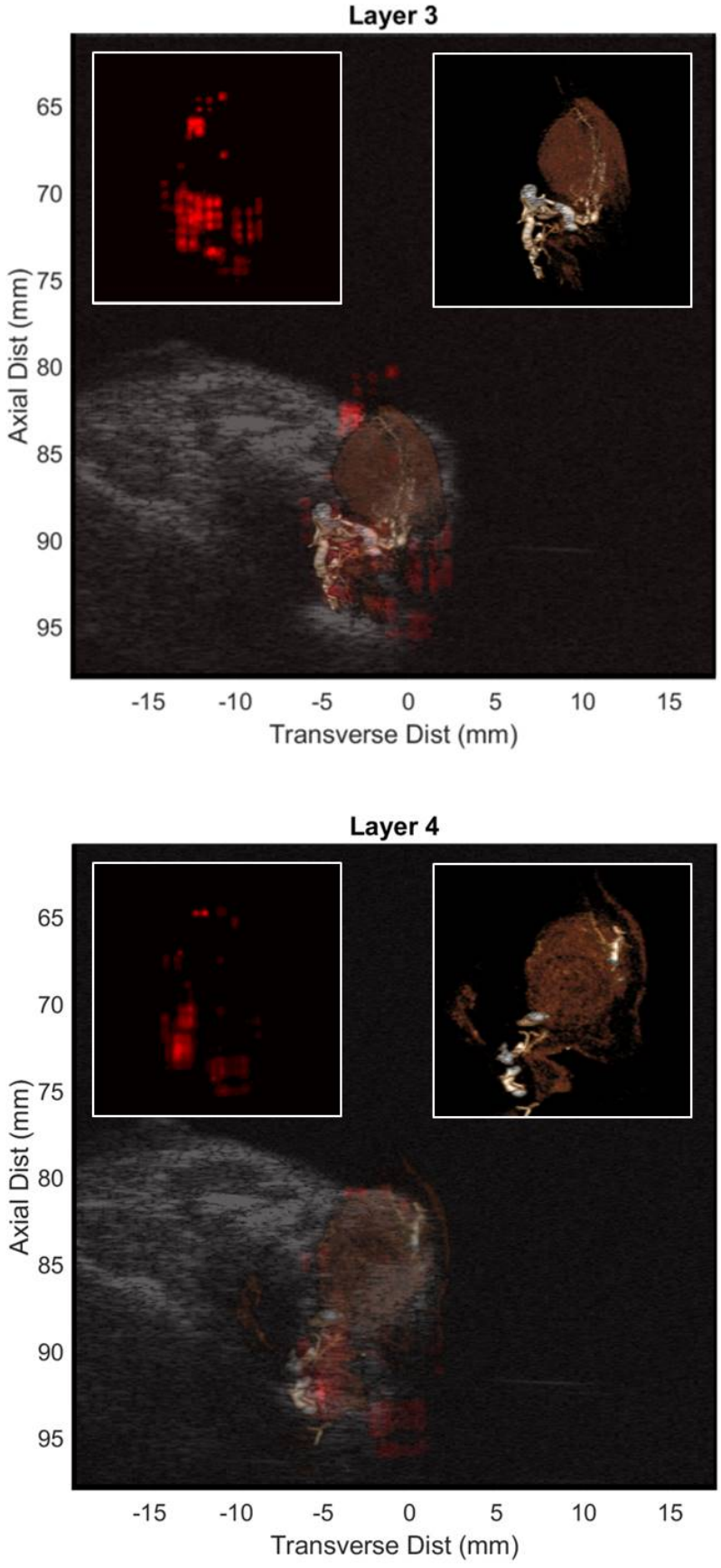


Figure 3.22: Layer 3 and 4 of overlay of B-Mode, PAM and CT data. Insets (not to scale): Left - PAM only data (red), Right - CT only data.

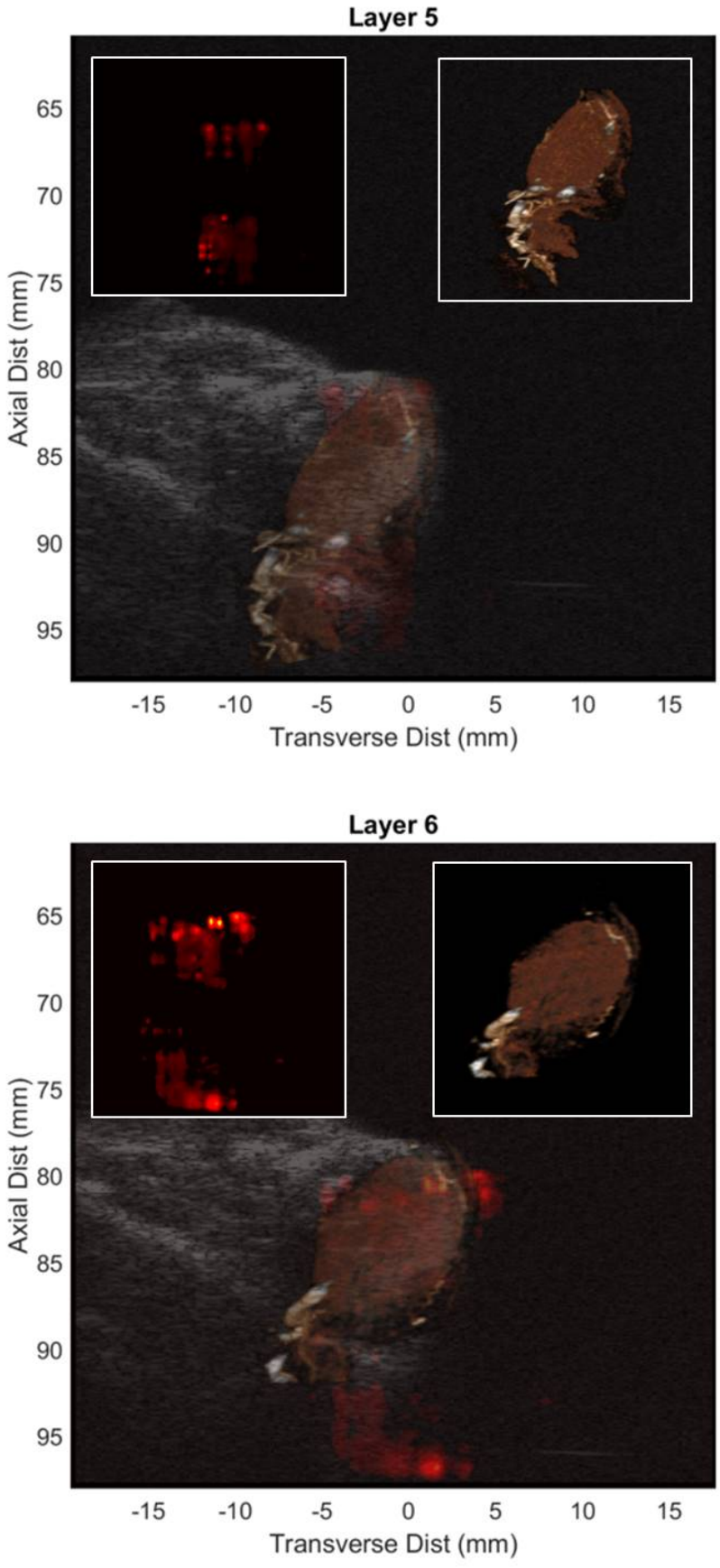


Figure 3.23: Layer 5 and 6 of overlay of B-Mode, PAM and CT data. Insets (not to scale): Left - PAM only data (red), Right - CT only data.

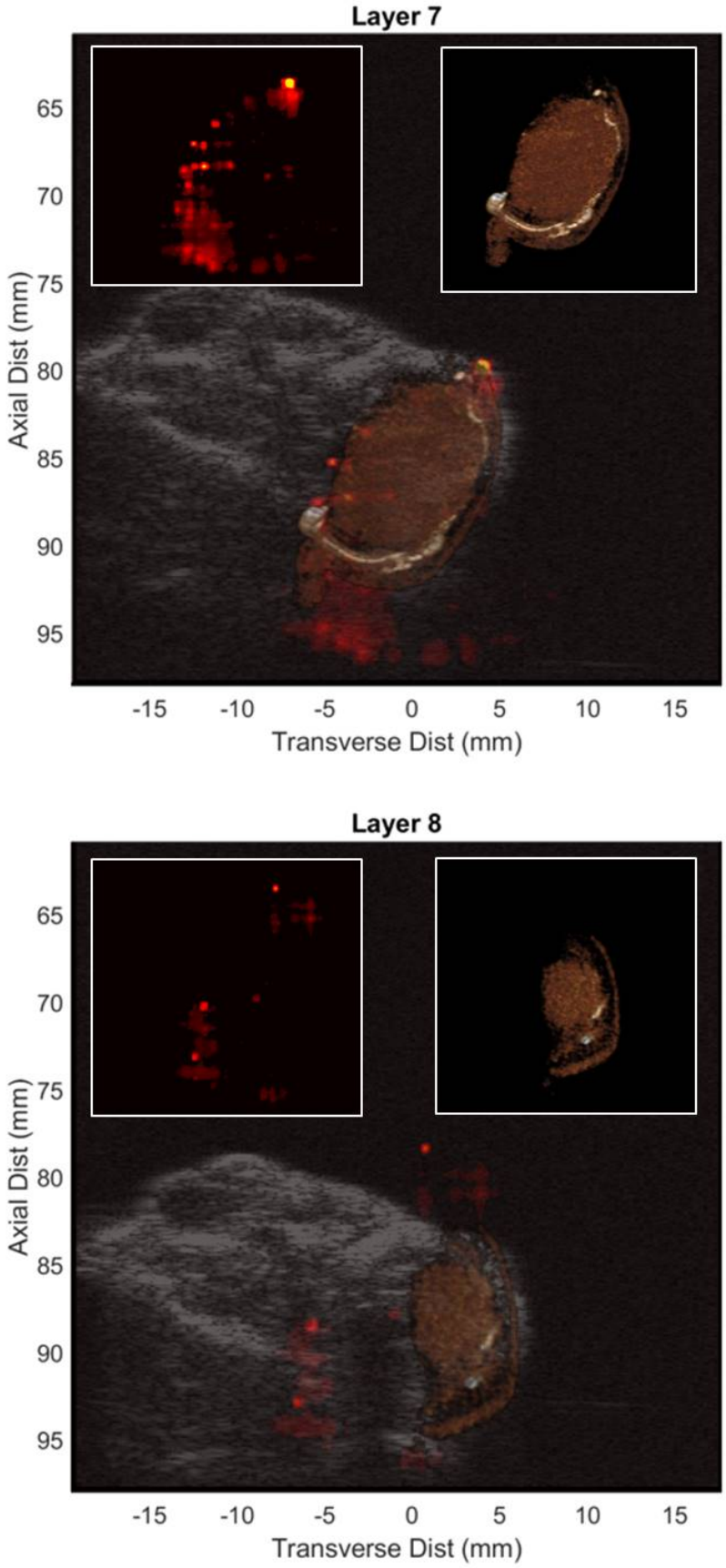


Figure 3.24: Layer 7 and 8 of overlay of B-Mode, PAM and CT data. Insets (not to scale): Left - PAM only data (red), Right - CT only data.

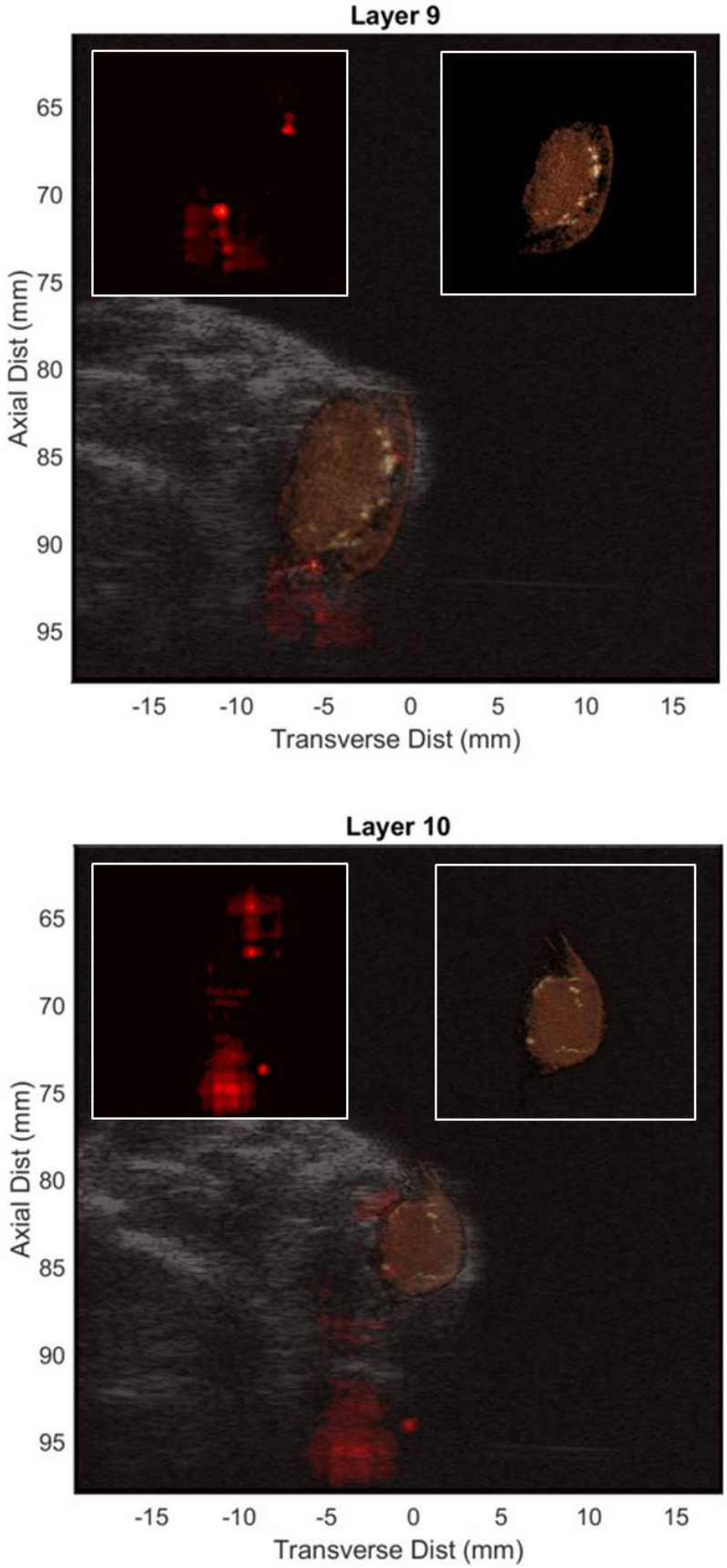


Figure 3.25: Layer 9 and 10 of overlay of B-Mode, PAM and CT data. Insets (not to scale): Left - PAM only data (red), Right - CT only data.

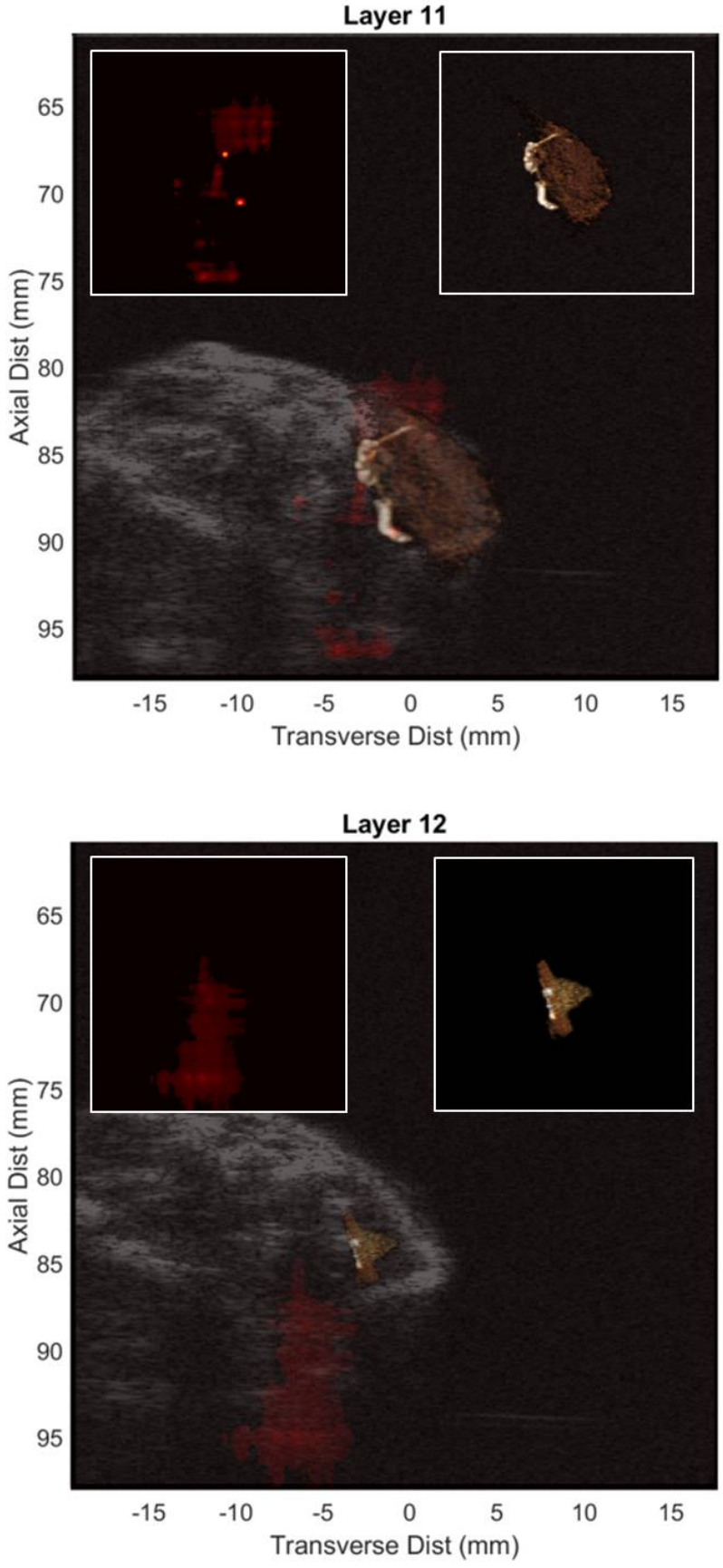


Figure 3.26: Layer 11 and 12 of overlay of B-Mode, PAM and CT data. Insets (not to scale): Left - PAM only data (red), Right - CT only data.

age to an extent that was detectable by quantifying small molecule accumulation in that region. However, the cavitation data from this experiment confirmed the trends observed in the cavitation data from the first experiment, and thus further supported the possibility that passive accumulation occurs.

Therefore a final study to investigate the passive accumulation of nanoscale cavitation nuclei by tumour development stage, as well as between two different tumour lines, was undertaken. The results of this study show that it may be possible to acoustically distinguish between leaky and non-leaky vasculature. However given that the extent of accumulation may vary significantly between different tumour lines, an individual assessment of each tumour line would need to be implemented before any distinction can be made. Furthermore, in some tumour lines, passive accumulation may not occur to an extent that is measurable by PAM, and therefore it may not be possible to use this approach to vasculature assessment in all tumour lines. Data based on tumour size alone was not able to fully explain the differences in passive accumulation, as indicated by recorded cavitation cavitation signal. Thus future work on this topic should include a study of passive accumulation that looks at a larger cohort, and assesses other tumour progression markers in addition to tumour size.

Finally, the passive cavitation data was analysed against the ground truth of vasculature location, obtained via a resin perfusion technique. Reasonably good co-location of PAM data and vessel position was observed in some parts of the tumour, supporting the hypothesis that the PAM data could be mapping nanoscale cavitation nuclei in or near to existing tumour vessels when those vessels are leaky.

If the location of extravasated nanocups can be confirmed using other microscopy techniques, then the evaluation of passive accumulation in tumours using PAM could prove useful in non-invasively determining both the permeability of certain types of tumours to large cancer therapeutics, as well as assessing whether regions of necrosis exist. This additional information about tumour vasculature could ultimately prove useful to clinicians when selecting first line therapies. However, in order to accurately map vessels on a smaller scale, a new approach to acoustic source localisation is

required. Rather than mapping the entire energy in a region, a new approach aims to localise individual sources using only a single linear array. The proposed approach is discussed in the next chapter of this thesis.

Chapter 4

Localisation of Cavitation by a combined Blind Source Separation and Acoustic Source Localisation Method

4.1 Introduction

The results from the *in vitro* and *in vivo* studies described in the previous chapters demonstrate that a region of extravasated particles can be mapped using PAM, and that the application of more advanced array geometries and beamforming techniques allows for more accurate localisation of extravasated particles. However this approach, whilst providing useful information about the region of extravasation and the level of cavitation activity, still leaves two significant challenges, namely:

1. In general, *in vivo* vessels and spatial scales are smaller than those used in the *in vitro* setup, and thus the application of PAM to assess the characteristics of tumour vasculature *in vivo* can only provide spatial information about vasculature in tumours that are significantly larger than the Point Spread Function (PSF) of the PAM system.

2. Although the dual array setup does manage to provide useful information in some cases, it is not always possible to use two perpendicular probes in an *in vivo* setting due to geometric constraints. Limiting PAM to only a single

probe setup increases the PSF of the system and thus reduces the ability of a user to accurately identify regions of cavitation, thereby further limiting the applicability of the use of PAM for vasculature assessment.

Thus for the proposed application of monitoring extravasated particles to gain information about the tumour vasculature, it may be more useful to examine methods for localising specific sources rather than relying on existing methods that completely map regions of cavitation activity. In this chapter, a method for determining the location of cavitating sources, rather than for mapping the energy of the sources, is presented.

In order to describe and compare the proposed algorithm with existing methods of cavitation mapping, the first part of this chapter lays out the mathematical foundation of small amplitude propagating waves, and defines a simple linear model to describe the signal recorded on a set of receivers due to the cavitation of multiple acoustic sources. Using the model, current approaches to Acoustic Source Localisation (ASL) are then evaluated in section 4.3. These approaches are classed as single step (direct) or two-step (indirect) approaches, and include popular cavitation mapping techniques such as Passive Acoustic Mapping (PAM). Improvements in source localisation by using super-resolution techniques are also discussed.

The performance of existing algorithms for source localisation, with specific focus on the case of multiple cavitating sources, is then highlighted. In particular, because the localisation performance of existing ASL algorithms significantly decreases when multiple sources are present, section 4.4 of this chapter introduces methods of recovering individual signals using only the information contained in a set of mixed recorded signals. This technique is known as Blind Source Separation, and has been shown to be extremely useful in environments where multiple sources are present, such as in the case of multiple cavitation sources.

A new approach to multi-source cavitation localisation is then introduced in section 4.5.2. The new approach uses two distinct techniques in order to localise multiple

cavitation sources with a high degree of accuracy. First, a Blind Source Separation (BSS) technique is applied to the signals recorded on a linear ultrasound array in order to separate and reconstruct signals arising from independent cavitation sources (for example, from individual bubbles). The BSS technique used is called Independent Component Analysis (ICA), and the mathematical basis for the technique is described in this section. Second, a cross-correlation approach is used to identify the time delays of individual signals arriving on different elements of a receive array, and the time delay information between different receiver pairs is used to generate a location estimate for each source using a hyperbolic position estimator.

To verify the proposed localisation technique, various cavitating bubble configurations are generated using the Keller-Miksis bubble simulation equations in section 4.6. These simulations are used to evaluate the localisation performance of the proposed algorithm for multiple cavitation sources at known locations. The limitations of the simulations will also be discussed, as well as the impact these limitations will have when applying the proposed algorithm to experimental, rather than simulation, data.

With the limitations in mind, section 4.7 shows the results of the proposed localisation algorithm applied to data collected from a simple *in vitro* experiment. To identify the true source location in the experimental setup, a high resolution, dual array PAM algorithm (as described in the previous chapters) is applied. The performance, limitations, and possible future improvements for the algorithm are also discussed in this section.

Ultimately, the contribution of the work discussed in this chapter is to propose a new method for passively localising multiple cavitation sources using only a single linear array, for use in situations where existing cavitation mapping algorithms are unable to localise individual sources.

4.2 Model Description

In the case of multiple cavitating sources, there are two useful ways to model the physical situation. First, the acoustic field can be described in terms of the source strength field [59], which is conceptually helpful when reconstructing energy over a given area. Second, the signal recorded from multiple acoustic sources can also be treated as point sources and ultimately described as a summation of the individual source signals.

Following the derivation by Gyöngy [59], source strength is considered the rate of change of mass outflow, $\dot{q}(t)$. The pressure, p, arising from a source at a distance r can then be expressed as:

$$p = \frac{1}{4\pi r}\dot{q}\left(t - \frac{r}{c}\right) \tag{4.1}$$

When describing the field in terms of field strength, it is useful to start first by summing the source strength estimates from equation 4.1 as follows:

$$\tilde{q}(\mathbf{r}, t) = \frac{1}{M}\sum_{i=1}^{M} w_i 4\pi|\mathbf{r_i} - \mathbf{r}|p_i\left(\mathbf{r_i}, t + \frac{|\mathbf{r_i} - \mathbf{r}|}{c}\right) \tag{4.2}$$

where $4\pi|\mathbf{r_i} - \mathbf{r}|$ is a correction factor for spherical spreading, $\mathbf{r_i}$ denotes the location of the i^{th} element of a receive array consisting of M receivers, p_i is the pressure recorded on each element, c is the speed of sound of propagation, and w_i represents a weighting factor.

The intensity and power are given by equations 4.3 and 4.4.

$$\mathrm{I}(\mathbf{r}, t) = \frac{p^2(\mathbf{r}, t)}{\rho_0 c} \tag{4.3}$$

$$\mathrm{P}(\mathbf{r}, t) = 4\pi|\mathbf{r_i} - \mathbf{r}|^2\mathrm{I}(\mathbf{r}, t) = \frac{1}{4\pi\rho_0 c}q^2\left(\mathbf{r}, t - \frac{|\mathbf{r_i} - \mathbf{r}|}{c}\right) \tag{4.4}$$

Integrating the power over time leads to an estimate of energy in a region, $\Psi(\mathbf{r})$:

$$\Psi(\mathbf{r}) = \frac{1}{4\pi\rho_0 c}\int_{t_0}^{t_0+T} \tilde{q}^2\left(\mathbf{r}, t - \frac{|\mathbf{r_i} - \mathbf{r}|}{c}\right) dt \tag{4.5}$$

By combining equation 4.2 with equation 4.5, an estimate of the source energy at a given location can be obtained. This is the fundamental process used in the PAM algorithms throughout this thesis.

An alternative, more general model, is to express the signals arriving at the receivers in terms of a summation of individual sources. In the most basic case, using the superposition principle of the linearised wave equation, the acoustic signals arising from N independent cavitation sources, received on M receivers, can be linearly mixed with an unknown mixing function. In this case, the signal, x, recorded on the i^{th} receiver is expressed by the following equation in the time domain as:

$$\begin{aligned}
x_1(t) &= a_{11}s_1(t) + a_{12}s_2(t) + \cdots + a_{1n}s_n(t) \\
x_2(t) &= a_{21}s_1(t) + a_{22}s_2(t) + \cdots + a_{2n}s_n(t) \\
&\vdots \\
x_i(t) &= a_{i1}s_1(t) + a_{i2}s_2(t) + \cdots + a_{in}s_n(t)
\end{aligned}$$

which can be compactly written as:

$$x_i(t) = \sum_{n=1}^{N} a_{in}s_n(t) + \eta_i(t) \tag{4.6}$$

where x_i is the recorded signal on receiver i, s_n is the signal produced by one of N statistically independent sources, and a is the mixing coefficient associated with a particular signal-receiver pair. In this simple model, time delays and noise are ignored. In most real-world environments, receiver noise is unavoidable. Therefore, rewriting the model in matrix format, with an added noise component to denote the noise present on the i^{th} receiver, $v_i(t)$, and dropping the time symbol for convenience, the equation becomes:

$$\mathbf{x} = \mathbf{As} + \mathbf{V} \tag{4.7}$$

where A is now an MxN matrix containing mixing coefficients.

Furthermore, in reality, signals are not only linearly mixed by an unknown mixing function, but often also experience propagation delays. Therefore, in a reverberation free environment, the model for mixed and delayed signals can be stated as:

$$x_i(t) = \sum_{n=1}^{N} a_{in} s_n(t - k_{in}) + \eta_i(t) \tag{4.8}$$

where k_{in} is the propagation delay between the n^{th} source and the i^{th} receiver.

Finally, sources may also experience multipath propagation due to reflections, and thus the model can be extended to include the summation not only of delayed sources, but also of multiple iterations of the same source with different delays. This is the most complex model, and is given as:

$$x_i(t) = \sum_{n=1}^{N} \sum_{k=0}^{K-1} a_{ink} s_n(t - k) + \eta_i(t) \tag{4.9}$$

where a_{ink} contains the filter coefficients of the k^{th} sample, and $\eta_i(t)$ is the noise component of the signal on receiver i.

Although the convolutive model presented best captures the complex real environment, for the purposes of the remainder of this chapter the simple linear model will be used in order to demonstrate proof of concept for the proposed algorithm. This simplification is recognised as a limitation of this work, and discussed further in Section 4.8.1.

In addition to the assumption of linear superposition, another key assumption that is made throughout this chapter is that the source signals are statistically independent, which implies that knowledge of the amplitude of the acoustic emission from a single source at time t does not provide any information about the amplitude of the acoustic emission arising from a different source at the same point in time.

Clearly this assumption will not hold in some cases in reality, especially where the concentration of bubbles is high, since bubbles cavitating in close proximity to one another will interact and therefore cannot be considered to be independent. The bubble-bubble interactions can be modelled as a function of the distance between the bubbles, the instantaneous bubble radii, and the first and second time derivative of the radii [114]. Although interactions between bubbles exist in some cases, this does not immediately imply that the source separation techniques discussed in this chapter will fail, since, in practice, the algorithms supply components that are as independent as possible and which may still be fairly accurate [115]. Thus the question of the exact level of independence of acoustic sources that is required for the proposed technique cannot be easily stated, and further work is required to fully define this limit.

The models and notation described in this section will be used throughout the remainder of the chapter for the description of existing algorithms and for the development of BSS and ASL algorithms.

4.3 Passive Acoustic Source Localisation

Current ASL methods can generally be classified as either a direct or an indirect technique [116]. Direct techniques include traditional beamforming approaches, as well as single step subspace based approaches. These methods search a predefined grid area for possible source locations, and then use the most probable location (based on the maximisation or minimisation of a cost function) as the source location. By contrast, two separate steps are necessary in indirect approaches. First, the time delays between the received signal recorded on different elements on a receive array are determined. Second, the source location is found through evaluating the half hyperboloids between receiver pairs. A brief review of some of the main classes of source localisation algorithms is given here. Particular focus is placed on the current method of ASL used in the context of cavitation monitoring.

4.3.1 Direct Method - Steered Beamformer

A beamformer applies delays and weights to received signals in order to improve signal to noise ratio for a specific spatial location. Beamformers have been used extensively in the field of radar, sonar, robotics and biomedical signal analysis. They are typically classed as either non-adaptive (conventional) or adaptive. Non-adaptive beamformers apply delays to signals for time alignment purposes, and apply the same importance, or weight, to signals received on different receivers. In contrast, adaptive beamformers apply individual weights to signals on different receivers in order to maximise or minimise a cost function based on the statistical properties of the received signals.

The general principle of a beamformer is as follows. First, a search grid of possible signal source locations is defined. Then, for each location on the search grid, the signals on each receiver are delayed in order to 'steer' the beamformer to 'look' at the pixel of interest. The idea is that if a source is located in the pixel of interest, the delayed signals will interfere constructively and the energy from that particular pixel will be high. The signals are then multiplied by a weighting factor, before being summed. In the case of non-adaptive beamformers this weighting factor is unity for all signals. In the case of adaptive beamformers, the weighting factor for each signal is different and is calculated using statistical information contained in the received signals. By calculating the weights in this manner, adaptive beamformers aim to suppress noise and amplify the signal of interest. Multiple adaptive beamformers were initially developed for the narrowband farfield case. Since then, several adaptive beamforming approaches have been developed specifically for wideband signals and the nearfield case. These include the Reference Signal-Based Beamformer, the Minimum Variance Distortionless Response (MVDR) Beamformer, and the Generalized Sidelobe Canceller [116]. In addition, some narrowband algorithms may be extended to the wideband case by coherent or incoherent (subband) algorithms [116][117].

In the context of passively mapping ultrasound induced cavitation, both adap-

tive and non-adaptive approaches have been considered and implemented in both the time [14][72][75] and frequency domains [73][76][118][119][120]. The first PAM beamformer utilised a technique known as Time Exposure Acoustics [59][121]. This is a non-adaptive beamformer and as such, demonstrated significant performance degradation in the presence of interference. The first adaptive beamformer applied to cavitation mapping was the Robust Capon Beamformer (RCB), implemented by Coviello *et. al* [75]. In the frequency domain, Angular Spectrum PAM [76] and a frequency domain implementation of RCB [73] have also been developed, in addition to using the Phase Coherence Factor (PCF) as a weighting metric in a method known as PAM-PCF [122]. All of these approaches have thus far assumed signals to be Gaussian, which is often an incorrect assumption in the context of HIFU induced cavitation. To utilise greater signal information, a Robust Linear Programming Beamforming approach that examines the Higher Order Statistics (HOS) of received signals was recently implemented by Lyka *et al.* [78]. In addition, improvements to compensate for array diffraction and attenuation have also been proposed [79] [123].

This steered beamformer approach creates a map of cavitation energy in a target region, as described by equation 4.5. This approach is useful in monitoring an entire region of cavitation. Visually, the 'location' of a source is often just considered an area of cavitation activity, and in many applications this type of area of activity is sufficient. However sometimes an actual source location is required rather than an evaluation of global cavitation energy. In fact, strictly speaking, mapping entire regions of cavitation is only the first step in true ASL, and a method to select the final source locations from the generated maps must then be implemented [116][124].

In the context of acoustic source localisation, there has been significant progress in applying super-resolution algorithms to ultrasound data in recent years [125][126][127]. More specifically, for the application of cavitation monitoring, superresolution has been applied in conjunction with a PAM algorithm [128]. However, this approach, in which the PSF of the imaging system is deconvolved with the image, is limited in two ways. First, this system can only be implemented if a single source is present,

which is not always the case in PAM. If a single source cannot be used (either in time or frequency domains), then the image must be discarded. Second, if adaptive beamformers are used, their PSF will not strictly be the same across every frame due to the variable weightings available. Furthermore, the PSF in adaptive beamformers can be spatially varying, as shown by [129], and degradation in performance is pronounced in the presence of sound speed errors. A spatially variant PSF implies that global Fourier methods cannot be used for deconvolutions, which in turn significantly increases computational cost and complexity, since local estimates of the PSF must be made at each position [130]. Generating the PSF for every location in every frame of PAM would likely be prohibitively complex for most applications. Even if a set of PSFs could possibly be pre-calculated, this process would decrease system flexibility as they would need to be recalculated when moving from for example, a 32 x 32 pixel map to a 64 x 64 pixel map. Thus in the case of ASL, a steered beamformer plus super-resolution approach, whilst possible, has significant drawbacks. These limitations are significant, especially if a single source cannot be guaranteed, for example in cases where the number of nucleation sites cannot be controlled.

4.3.2 Direct Method - Subspace-Based Approaches

Subspace-based approaches utilise the covariance matrix of the received signals, along with Eigenvalue Decomposition, to separate the eigenvectors of the Signal-plus-Noise subspace from eigenvectors of the Noise-only subspace [116]. Some popular algorithms in this field include MUltiple SIgnal Classification (MUSIC) [131] and Estimation of Signal Parameters by Rotational Invariant Techniques (ESPRIT) [132].

Like the steered beamformer approaches, subspace based approaches also define a search grid of possible locations, and then determine the maximum or minimum of a cost function based on second order signal statistics in order to define the most likely source positions. For example, in the case of MUSIC, considering the frequency domain model for multiple sources (for simplicity the frequency variable is not written):

$$\mathbf{X} = \mathbf{AS} + \mathbf{V} \tag{4.10}$$

Now assuming the noise is independent of the signals, and assuming that the variance of the noise is the same on each receiver, the spectral covariance matrix can be defined as:

$$\boldsymbol{Q_{xx}} = \mathrm{E}\{\mathbf{X}\mathbf{X}^{\mathrm{H}}\} = \mathbf{A}\boldsymbol{\Phi}_{\mathbf{ss}}\mathbf{A}^{\mathbf{H}} + Q_{vv}\mathbf{I} \tag{4.11}$$

where $\mathrm{E}\{\cdot\}$ denotes the expectation operator, H is the conjugate transpose of a matrix, and $\mathbf{I}$ denotes the identity matrix.

Then using an eigenvalue decomposition yields:

$$\boldsymbol{Q_{xx}} = \mathbf{U}(\mathbf{D} + Q_{vv}\mathbf{I})\mathbf{U}^{H} \tag{4.12}$$

Finally, the space of possible source locations, r can be defined by a steering vector $\mathbf{H}(\mathbf{r})$, and the spatial spectrum defined by:

$$\mathrm{S}_{\mathrm{MUSIC}}(\mathbf{r}) = \frac{1}{\mathbf{H}^{H}(\mathbf{r})\mathbf{U_v}\mathbf{U_v}^{H}\mathbf{H}(\mathbf{r})} \tag{4.13}$$

The maximisation of the spatial spectrum, $r_{s_n} = argmax\mathrm{S}_{\mathrm{MUSIC}}(\mathbf{r})$ yields the required source positions.

This type of subspace based approach was originally developed for narrowband source in the farfield [131], and in this case the algorithm is computationally efficient. Since then, MUSIC and other subspace based approaches have been extended to wideband sources [133][134], however these algorithms increase complexity and computational load.

4.3.3 Indirect Method - Time Sum and Difference of Arrival

In indirect ASL, two steps are required to localise signals. First, the Time Difference of Arrival (TDOA) of signals on each receiver is determined, then a position estimate is obtained.

TDOA Estimation

For a single source, the TDOA for each element can be computed by taking various weighted forms of cross correlation of the signal on receiver pairs. Several weighting approaches have been developed to improve the TDOA estimation using cross correlation for a single source on a pair of receivers [116], and have further been extended to the case of multiple pairs of receivers in a noisy environment [135][136]. Another approach to determining TDOA estimates is through adaptive eigenvalue decomposition, which was developed to handle reverberant environments, and which has also been extended to multiple channels [137]. Due to their low complexity, these TDOA estimation approaches have been used extensively in human speech localisation, for example, for tracking a speaker in teleconference systems.

Position Estimation

Once the time delays have been determined, one of several estimation algorithms is then used to determine the location that would give rise to those time delays, given the sensor positions. If the source is at position (x_s, y_s), and the sensors at positions (x_i, y_i), then:

$$\begin{aligned} r_i^2 &= (x_i - x_s)^2 + (y_i - y_s)^2 \\ &= x_i^2 + y_i^2 - 2x_i x_s - 2y_i y_s + x_s^2 + y_s^2, \;\; for\; i = 1, 2, \ldots, M \end{aligned} \tag{4.14}$$

Then a set of nonlinear equations that relate the source position, sensor positions, and relative time delays between elements to each other can be expressed as:

$$r_{i,1} = cd_{i,1} = r_i - r_1 \tag{4.15}$$

where $d_{i,1}$ is the time delay of sensor i relative to the first sensor on the array.

Several approaches to solve this series of non-linear equations exist, including first linearlising equation 4.15 and using a Taylor Series Expansion [138], or by transforming the equations and using a least squares or a maximum likelihood approach [139] [140] [141] [142].

All indirect source localisation methods discussed are typically applied to single source problems, and often suffer significant performance degradation in the presence of multiple sources [116]. However in cavitation monitoring, multiple sources are often present. Although some of the direct approaches can handle multiple sources, these approaches suffer from limitations in the type of signals they can localise, and can be computationally complex. In addition, their ability to localise individual sources is limited by the PSF of the imaging system, which in the case of a steered beamformer used on a linear ultrasound array can be fairly large.

Therefore, another approach to localising multiple sources is to first explicitly separate sources, before then applying an ASL algorithm. Some methods to separate signals are thus described in the subsequent section.

4.4 Source Separation

In the case of multiple cavitating bubbles, the only information about the sources available is the mixed signals recorded on each element of the array. As neither the source signals, nor the matrix describing the linear combination of the signals, is known, the problem is classified as a Blind Source Separation (BSS) problem. It is often useful to solve this in order to identify and separate out signals arising from different sources. For example, one classical problem in this area is known as the 'Cocktail Party Problem', and describes a situation where multiple people are speaking, and where it is necessary to focus on the voice of an individual person whilst suppressing other voices. Humans are good at solving this problem, however the processing mechanisms by which we isolate a single speaker's voice are not fully understood. Consequently it has been exceptionally difficult to replicate a similar type of signal separation and isolation computationally.

According to Jutten [143], work in this area started in the 1980s, when the focus of signal processing researchers up to that point had primarily been on separating uncorrelated sources using a process known as Blind Deconvolution. The focus on

Blind Deconvolution rather than on BSS was in part due to the prevailing assumption that signals had Gaussian distributions, and further due to the fact that Bienvenu and Kopp [144] had shown that eigenvectors of the spectral matrix could not be used to recover sources [115][144], hence signal separation and recovery did not seem possible at the time.

However a small amount of research on BSS did occur within the neural networks community by French researchers Herault, Jutten and Ans [143][145][146][147], who developed a feedback network in order to describe motion coding in muscle contraction. Cardoso [148] and Comon [149] followed with papers describing signal separation that relied on algebraic methods and was based on the properties of input cumulants respectively. The first BSS algorithm based on Higher Order Statistics (HOS) (i.e. using an independence criterion) was proposed by Lacoumbe in 1988 [150]. Other early neural network algorithms included an adaptive neural network developed by Burel [151] which used an iterative approach that produced first uncorrelated components and then, with enough iterations, independent components.

In the 1990's, Cichocki and Unbehauen proposed two robust, unsupervised, self-normalising neural networks for BSS [152][153]. In addition, another adaptive neural network algorithm developed by Bell and Sejnowski [154] demonstrated the ability to isolate independent components by using an information maximisation approach. The work of Cichocki, Unbehauen, Bell and Sejnowski popularised the idea of BSS, and further research focussed on increasing computational efficiency, improving algorithm stability, reducing the number of initial model assumptions, and solving output ambiguities [155][156].

Today, BSS algorithms typically use Second Order Statistics (SOS), Higher Order Statistics (HOS) [157], or other non-linear techniques to achieve separation, and these classes are briefly reviewed here. For a more complete discussion of the current BSS methods, the reader is directed to an excellent review by Pederson [157], and a resource with a specific focus on Higher Order Statistical methods of BSS can be found in [158].

4.4.1 BSS by Second Order Statistics (SOS) Methods

Second Order Statistics (SOS) use signal covariance, in conjunction with other known properties of the signals, in order to perform BSS. Knowledge of other signal properties is necessary with these methods since BSS cannot be achieved using SOS alone [157][159]. In come cases, methods using SOS are sometimes referred to as Blind Deconvolution methods rather than BSS methods [115]. Although assumptions about signal structure are required, SOS methods are still commonly used due to their ease of implementation and, in many cases, their ranked output structure [155][157].

Methods Relying on Non-Stationarity

Signals whose statistical properties vary with time are called non-stationary. Weinstein proposed the first algorithm to separate two sources using these temporal variations in the signal statistics [160], and was followed by Souloumiac [161] who separated a signal from noise using the same principle. These techniques were then extended to multiple convolutive sources in the frequency domain by Wu [162]. In general, this class of algorithms compute the eigenstructure of the signal covariance matrices taken at different frequencies and times, and iteratively minimise the cross-power spectrum across these matrices in order to determine a separation matrix [157].

Methods Relying on Cyclostationarity

Signals whose statistical properties vary cyclically with time are called cyclostationary, and if the SOS of the signal also vary cyclically with time then the signal is classified as wide-sense cyclostationary. This property can also provide enough information to separate signals using Maximum Likelihood and Common Factor Analysis approaches [157][163][164][165].

Methods Relying on Spatio-Temporal Characteristics

Signals that are stationary, but that have spatial, temporal, or spatiotemporal correlations can also be separated using only SOS [155]. For example, An Algorithm

for Multiple Unknown Signal Extraction (AMUSE) [166] exploits two Eigenvalue Decompositions (EVDs) in order to achieve separation, whilst Belouchrani improves on this technique through separating several covariance matrices simulataneously using a Joint Diagonalisation approach [167].

4.4.2 BSS by Higher Order Statistics (HOS) Methods

In order to recover the original signals without making assumptions on the signal's second order statistical properties, it is necessary to use information contained in the Higher Order Statistics (HOS) of the signal. In order to do so, sources must be non-Gaussian in order to ensure they contain useful information in their HOS. Approaches that utilise HOS typically assume signals are independent, and therefore are usually called Independent Component Analysis (ICA) algorithms. They are typically iterative, which means that if the system contains many more sensors than there are sources of interest, these approaches can be used to extract signals only down to a certain level of interest [155].

Methods Relying on Fourth Order Statistics

One measure of independence is Gaussianity, which can be seen from considering the Central Limit Theorem (CLT). The CLT states that the probability distribution of the sum of independent random variables will tend towards a Gaussian distribution, even if the distributions of the independent variables are not themselves Gaussian. This implies that the most statistically independent variables can be determined by maximising the non-Gaussianity of a mixture of signals. This is the central idea behind the ICA algorithm presented here. Gaussianity however cannot be directly measured easily, and thus a surrogate metric, Kurtosis, which is based on the fourth order cumulants of the signals, is often used. A more detailed description of an ICA method using fourth order statistics is given in Section 4.5.2.

Methods Relying on Information Theoretic Criteria

An alternative, and equally popular approach to ICA arises from separating sources based on the entropy (a surrogate measure of how 'random' a variable is) of each signal. For example, Gaussian signals have the greatest entropy. By using entropy as a metric to be minimised, the mutual information between signals can also be minimised, and the signals with the greatest independence can be found. This information theoretic approach requires the modelling of the probability density of the signals, and was first proposed by Bell and Sejnowski [154]. This approach to ICA was extended to use both parametric and non-parametric assumptions on the signal PDF, and has also been extended for use with convolutive mixtures.

4.4.3 Other BSS Methods

Other techniques for BSS have also been proposed, and rather than being based explicitly on SOS or HOS methods, these approaches use the sparseness of sources in order to separate them. The assumption with these techniques, classed as Sparse Component Analysis (SCA), is that only a single source will be active at a given time [168][169]. This simplifies the problem of the linear mixing system (equation 4.7) significantly, as it removes several elements of the mixing matrix, $\mathbf{A}$, such that the estimation of the mixing matrix required is simplified. For example,in the case of two sources, if only a single source is active at any given time, then the matrix to be estimated for a single component can be reduced from equation 4.16 to equation 4.17

$$\mathbf{A} = [a_{11}, a_{21}]^T \tag{4.16}$$

$$\mathbf{A} = \left[1, \frac{a_{21}}{a_{11}}\right]^T \tag{4.17}$$

Typical SCA algorithms involve pre-processing signals by representing them in the time-frequency domain, and then estimating the mixing matrix using a hierarchical clustering technique [170]. A popular SCA algorithm in use today is the Degenerate

Unmixing Estimation Technique (DUET) [171], which also demonstrates one of the greatest advantages of SCA: the model can be used to estimate the positions of more sources than there are receivers. Although SCA algorithms are incredibly powerful, they are also computationally complex, and furthermore they usually require some knowledge or assumptions about the points of a signal at which individual sources are active in isolation.

4.4.4 Non-negative Matrix Factorisation

The main principle of Non-negative Matrix Factorisation (NMF) is to factorise a matrix into another set of matrices such that all matrices do not contain negative elements [172]. Time domain audio signals contain negative values, and are therefore unsuited to this algorithm. However the magnitude of their spectrograms, determined from taking the Short Time Fourier Transform (STFT) of the time domain signal, contains only positive values and therefore can be used in NMF algorithms. NMF can be performed for each frequency bin and reconstructed, and phases can be recovered either by probabilistic interference, or by comparison with the original signal [173]. Other algorithms that utilise a Baysian Extension to NMF have also been applied to audio signals [174].

4.5 Proposed Approach to Multi-source Cavitation Localisation

In this section a new method of source localisation is proposed which combines the ideas discussed in the previous ASL and BSS sections. Figure 4.1 gives a schematic overview of the overall process. The proposed method consists of two main stages: BSS using a method based on fourth order statistics, and ASL using an indirect TDOA method.

A more detailed breakdown of the stages is shown in figure 4.2. First, a starting estimate of the number of sources is generated using an information theoretic criterion known as the Minimum Description Length. Then, an ICA algorithm proposed by

Hyvärinen *et al.* [175], known as *fastICA*, is implemented on the central 10 elements of a linear array. Output signals are assessed against each other in order to identify and remove any signals that are repeated, or that are purely noise. A least squares approach is then taken to solve the output scaling ambiguity. Once the correct scaling for each signal has been identified, the recovered 'Independent Components' (ICs) are remixed with known delays and compared to the original received signals by cross correlation. From this comparison, the time delays of each signal arriving on each receiver can be obtained, yielding a TDOA matrix for each IC. The estimated position of the source can then be determined using a hyperbolic estimation algorithm originally described by Chan and Ho [140].

The remainder of this section is used to describe the mathematical basis and practical implementation considerations of each stage of the proposed algorithm.

4.5.1 Step 1: Initial Estimate of Number of Sources

The BSS part of this algorithm assumes a linear instantaneous mixing model, as described by equation 4.7, and thus the input to the BSS algorithm will be the received signals on the central 10 elements of the array. This implies that the greatest number of ICs that can be estimated with this approach is 10. However not all 10 components need be estimated, and in fact, an initial approximation of the number of sources can greatly improve the quality of the BSS output.

Two options exist to estimate the initial number of signals. First, it is possible to use an eigenvalue decomposition and then select the minimum number of sources that capture a high enough percentage of the signal variance [176] to accurately represent the information contained in the signal. The challenge with this approach is deciding what percentage of the variance captures the required level of information in the signal. In order to overcome this challenge, the present work uses an information theoretic approach known as the Minimum Description Length (MDL) [177]. It is recounted here:

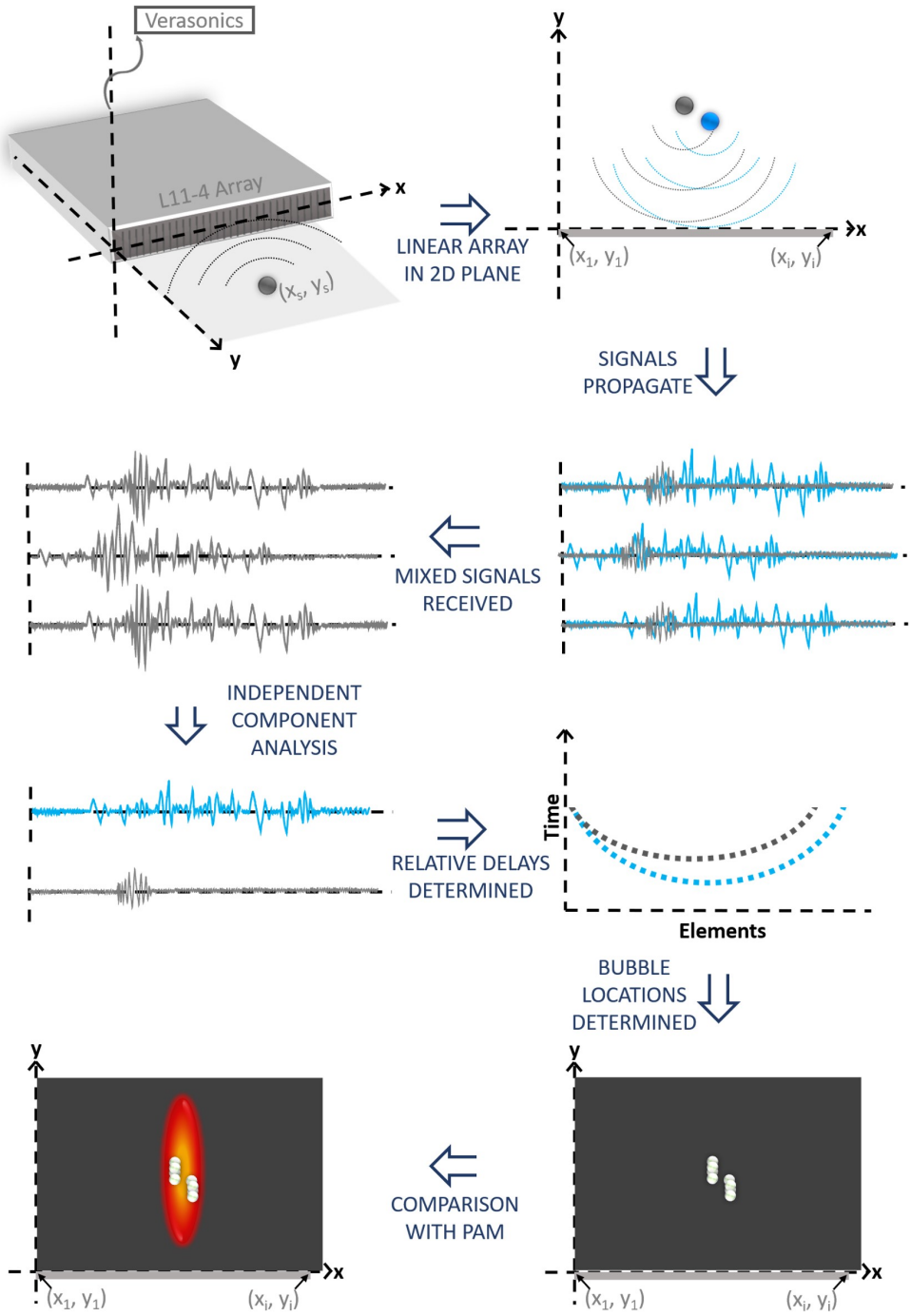


Figure 4.1: Overall process: Cavitating sources generate pressure waves that are linearly mixed and recoded on a linear array of receivers. Independent components are estimated using a statistical BSS technique and used to estimate the time of arrival delay curves for each signal. A hyperbolic localisation algorithm for linear arrays is applied to estimate the source location, and the output is compared to a current Passive Acoustic Mapping (PAM) technique).

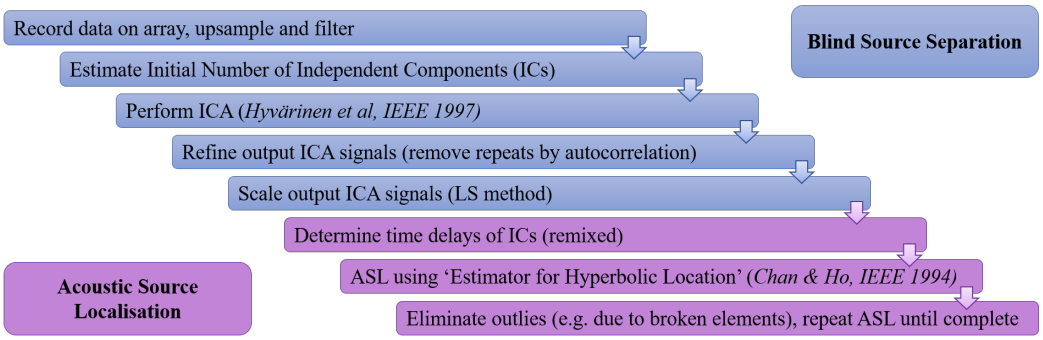


Figure 4.2: Flowchart of the proposed new beamforming algorithm.

$$\mathrm{MDL}(w) = -K(n-w)\ln\kappa(w) + 0.5m(2n-w)\ln K \tag{4.18}$$

where $\kappa(w)$ is the ratio of the geometric mean of the $n-w$ smallest PCA eigenvalues to their arithmetic mean, and is defined as:

$$\kappa(w) = \frac{(\lambda_{w+1}\lambda_{w+2}\ldots\lambda_n)^{\frac{1}{n-w}}}{\frac{1}{n-w}(\lambda_{w+1}+\lambda_{w+2}+\ldots+\lambda_n)} \tag{4.19}$$

The initial number of sources is then selected as the w that minimises the MDL criterion.

4.5.2 Step 2: Blind Source Separation by ICA

Next, the signals on the central 10 elements, in conjunction with the initial approximation of the number of sources, become the inputs to a BSS algorithm. The algorithm selected here is a fast fixed-point algorithm based on signal independence developed by Hyvärinen et al [175]. This ICA approach is selected because, as described in section 4.2, multiple bubbles could be treated as independent point sources. Furthermore, the signals generated by cavitating bubbles tend to be supergaussian, which means that fourth order HOS can be used to maximum effect in this application. Finally, ICA is chosen for source separation as it utilises higher order statistics, and can therefore make the separation without any further assumptions on the statistical structure of the signals, other than to say that the sources are independent and all but one have a non-Gaussian probability distribution.

The general principle and key equations of the ICA method used in this chapter are now discussed. Starting from the simplified model of multiple signals in equation 4.7, we aim to determine the mixing matrix W. Mathematically:

$$\mathbf{s} = \mathbf{A^{-1}x} = \mathbf{Wx} \tag{4.20}$$

As previously discussed, the independence criterion is stronger than the uncorrelatedness criterion, however methods that transform the variables into zero mean, uncorrelated variables on orthogonal axes are a useful preprocessing step in ICA [115][155]. Thus the first step is to centre the variables by equation:

$$\mathbf{x} = \mathbf{x}' - E\{\mathbf{x}'\} \tag{4.21}$$

where E denotes the expectation operator, $\mathbf{x}'$ is the original signal, and $\mathbf{x}$ is the zero mean output. It should be noted that this step also forces the output independent components to have zero mean, but does not affect the mixing matrix since:

$$E\{\mathbf{s}\} = \mathbf{A^{-1}}E\{\mathbf{x}\} \tag{4.22}$$

The variables are then whitened using an eigenvalue decomposition (similar to that used in PCA) in order to remove correlations [115]. Equation 4.23 gives the eigenvectors in the orthogonal matrix $\mathbf{E}$, and the eigenvalues along the diagonal of $\mathbf{D}$.

$$E\{\mathbf{xx^T}\} = \mathbf{EDE^T} \tag{4.23}$$

The whitening matrix, V can then be found by:

$$\mathbf{V} = \mathbf{ED^{-1/2}E^T} \tag{4.24}$$

where $\mathbf{D}^{-1/2} = \mathrm{diag}(d_1^{-1/2}, \ldots, d_n^{-1/2})$.

Ultimately, the whitened variables are given by $\mathbf{z} = \mathbf{Vx}$. In the case of ICA, this becomes

$$\mathbf{z} = \mathbf{V}\mathbf{x} = \mathbf{V}\tilde{\mathbf{A}}\mathbf{s} \tag{4.25}$$

These whitened variables are both uncorrelated and also have unit variance, which implies:

$$E\{\mathbf{z}\mathbf{z}^{\mathbf{T}}\} = \tilde{\mathbf{A}}E\{\mathbf{s}\mathbf{s}^{\mathbf{T}}\}\tilde{\mathbf{A}}^T = \tilde{\mathbf{A}}\tilde{\mathbf{A}}^T = \mathbf{I} \tag{4.26}$$

The whitening process (and other PCA processes) can only separate signals up to an orthogonal transformation [178], i.e. if an orthogonal transformation is performed on input signals, both the input and output signals will satisfy the criterion for being considered white. Since many orthogonal transformations exist, the correct 'independent' signals cannot be determined using the whiteness criterion alone [178]. However, as can be seen from equation 4.26, if applied as a pre-processing step for ICA, then the new mixing matrix, $\tilde{\mathbf{A}}$ is orthogonal, which reduces the number of possible mixing matrices significantly.

As previously discussed in Section 4.4.2, Kurtosis, the fourth order cumulant of the signal, can be used as a proxy for Gaussianty, and thus independence. It is defined for the purposes of ICA in [115]:

$$kurt(y) = E\{y^4\} - 3(E\{y^2\})^2 \tag{4.27}$$

Given the pre-processed signals have unit variance, ($E\{y^2\} = 1$), equation 4.27 becomes:

$$kurt(y) = E\{y^4\} - 3 \tag{4.28}$$

Kurtosis is linear, meaning that $\text{kurt}(x_1 + x_2) = \text{kurt}(x_1) + \text{kurt}(x_2)$ and also $\text{kurt}(\alpha x_1) = \alpha^4\text{kurt}(x_1)$.

In order to determine the independent components, the coefficients in the weighting matrix, $\mathbf{W}$, are varied such that they maximise the absolute value of Kurtosis.

Looking first at an individual component: $y = \mathbf{b^T x} = \mathbf{b^T AS} = \mathbf{q^T s} = \mathbf{q_1 s_1} + \mathbf{q_2 s_2}$, then from the additive property of Kurtosis:

$$\text{kurt}(y) = \text{kurt}(q_1 s_1) + \text{kurt}(q_2 s_2) = q_1^4 \text{kurt}(s_1) + q_2^4 \text{kurt}(s_2) \tag{4.29}$$

Due to the unit variance, the optimisation problem is to determine the maximum of $|kurt(y)|$ that lies on the unit circle.

For whitened data $\mathbf{z}$, $\mathbf{q} = (\mathbf{VA})^\mathbf{T}\mathbf{w}$, and thus:

$$||\mathbf{q}||^2 = (\mathbf{w^T VA})(\mathbf{A^T V^T w}) = ||\mathbf{w}||^2 \tag{4.30}$$

In this case the fast fixed-point algorithm designed by Hyvärinen and Oja [179] is used to determine the maximum. It is based on the theory of gradient descent algorithms, and it is thus instructive to recount the gradient descent approach presented in [179] first. The theory is to start with a vector, $\mathbf{w}$, and then compute the direction in which the absolute value of kurtosis of $\mathbf{y} = \mathbf{w^T z}$ is growing most strongly based on the available sample. Once determined, the vector $\mathbf{w}$ should be moved in that direction. Expressed mathematically, the gradient algorithm can be given as

$$\frac{\partial |\text{kurt}(\mathbf{w^T x})|}{\partial \mathbf{w}} = 4\text{sign}(\text{kurt}(\mathbf{w^T z}))[E\{\mathbf{z}(\mathbf{w^T z})^3\} - 3\mathbf{w}||\mathbf{w}||^2] \tag{4.31}$$

It can be further simplified by realising that the last term only modifies the scale of the vector, not the direction, and the update rule becomes:

$$\triangle \mathbf{w} \propto \text{sign}(\text{kurt}(\mathbf{w^T z}))E\{\mathbf{z}(\mathbf{w^T z})^3\} \tag{4.32}$$

$$\mathbf{w} \leftarrow \frac{\mathbf{w}}{||\mathbf{w}||} \tag{4.33}$$

Implementation of a gradient descent method can be slow, and thus an alternative fixed-point iterative algorithm is ultimately used as described in [179]:

$$\mathbf{w} \propto \left[E\{\mathbf{z}(\mathbf{w^T z})^3\} - 3||\mathbf{w}||^2\mathbf{w}\right] \tag{4.34}$$

which implies an update rule as follows:

$$\mathbf{w} \leftarrow E\{\mathbf{z}(\mathbf{w}^{\mathbf{T}}\mathbf{z})^3\} - 3||\mathbf{w}|| \tag{4.35}$$

This fixed point algorithm was developed by Hyvärinen and Oja [179] and is used as the BSS technique for the remainder of this chapter.

4.5.3 Step 3: Compensating for Ambiguities arising from ICA

Although the MDL criterion mentioned previously provides a good initial estimate of the number of sources, it is still necessary to examine the output of the ICA algorithm to remove signals that are repeats of each other. This is done by comparing the signal envelopes in order to remove similar signals, in a similar manner to that described by Sawada *et al.* [180].

ICA algorithms have two main ambiguities. First, the correct signal scaling cannot be recovered, since if the magnitude of a source is multiplied by a scalar (positive or negative), so too can the magnitude of the corresponding column of the weighting matrix:

$$\mathbf{x} = \sum \left(\frac{1}{\lambda_i}\mathbf{a}_i\right)(s_i\lambda_i) \tag{4.36}$$

In addition, the order of the output signals is not consistent and cannot be ranked since the order of columns in the mixing matrix and source signal matrix can simply be swapped. Mathematically, this is given as:

$$\mathbf{x} = \mathbf{A}\mathbf{P}^{-\mathbf{1}}\mathbf{P}\mathbf{s} \tag{4.37}$$

where P is a permutation matrix.

In the case of the proposed algorithm, only the shape and scale of the recovered ICs are important as the ICs are ultimately compared with the original received signals on the array elements in the time domain.

In order to correctly rescale the output ICs, the power of the output ICs is matched to the input mixed signal data using power-recovery scaling as described in [180]. The scaling matrix is given by:

$$\mathbf{\Lambda} = \sqrt{\text{diag}[(\mathbf{W}\mathbf{W}^{\mathbf{T}})^{-1}]} \tag{4.38}$$

and hence the new signals are given by:

$$\mathbf{s} = \mathbf{\Lambda}\mathbf{W}\mathbf{x} \tag{4.39}$$

4.5.4 Step 4: Position Estimation using TDOA

Once the signals have been correctly identified and scaled, they are mixed with different time delays and compared to the original received signal on each element by cross correlation. In this way, the relative time delay between receiver pairs for each signal can be determined. The final stage is then to use the time delays for localisation.

The criteria for selecting an ASL algorithm are that it must be an indirect method that:

1. Works with a linear array of receivers
2. Functions well in the overdetermined case (more sensors than sources)
3. Approaches the best localisation performance in a computationally efficient way

Thus the popular hyperbolic estimator, proposed by Chan and Ho [140], is implemented. The algorithm is recounted here for convenience. First, the received signal, x_i for $i = 1, 2, 3, ..., N$ receivers is given by:

$$x_i(t) = s(t - d_i) + \eta_i(t) \tag{4.40}$$

where s is the signal radiating from the source, d_i is the time delay associated with receiver i and $\eta_i(k)$ is additive noise.

The relative time differences between different elements are then given by:

$$d_{i,j} = d_{i,1} - d_{j,1}, \quad \text{where } i, j = 2, 3, \ldots, M \tag{4.41}$$

or in vector form:

$$\mathbf{d} = [d_{2,1}, d_{3,1}, \ldots, d_{M,1}]^T \tag{4.42}$$

If the source is at position (x_s, y_s), and the sensors at positions (x_i, y_i), then the squared distance is given by:

$$\begin{aligned} r_i^2 &= (x_i - x_s)^2 + (y_i - y_s)^2 \\ &= K_i - 2x_i x_s - 2y_i y_s + x_s^2 + y_s^2, \ \ for\ i = 1, 2, \ldots, M \\ K_i &= x_i^2 + y_i^2 \end{aligned} \tag{4.43}$$

Given a propagation speed of c, then:

$$r_{i,1} = cd_{i,1} = r_i - r_1 \tag{4.44}$$

As discussed in section 4.3.3, there are methods to linearise this equation, for example by using a Taylor Series expansion, but convergence is not guaranteed and a good initial guess needs to be made in order for this algorithm to produce real outputs.

Transforming 4.43 using 4.44:

$$r_{i,1}^2 + 2r_{i,1}r_1 + r_1^2 = K_i - 2x_i x_s - 2y_i y_s + x_s^2 + y_s^2 \tag{4.45}$$

Setting $i = 1$ and subtracting equation 4.43 from equation 4.45 gives:

$$r_i^2 + 2r_{i,1}r_1 = -2x_{i,1}x_s - 2y_{i,1}y_s + K_i - K_1 \tag{4.46}$$

For a linear array, $y_i = ax_i + b, i = 1, 2, \ldots, M$, where a and b are constants. Rewriting 4.46 as:

$$-2x_{i,1}(x_s + ay_s) - 2r_{i,1}r_1 = r_{i,1}^2 - K_i + K_1 \tag{4.47}$$

In a system of four or more sensors, the system is overdetermined, and it is possible, especially in the presence of noise, that the hyperbolas will not all intersect at the same points. Therefore an error vector needs to be defined to determine how to select the source point. Define the unknowns together in matrices $\mathbf{z_l}$ and $\mathbf{G_l}$, and the knowns in $\mathbf{h}$:

$$\mathbf{z_l} = \begin{bmatrix} x_s + ay_s \\ r_1 \end{bmatrix}, \mathbf{G_l} = -\begin{bmatrix} x_{2,1} & r_{2,1} \\ x_{3,1} & r_{3,1} \\ & \vdots \\ x_{M,1} & r_{M,1} \end{bmatrix}, \mathbf{h} = \frac{1}{2}\begin{bmatrix} r_{2,1}^2 - K_2 + K_1 \\ r_{3,1}^2 - K_3 + K_1 \\ \vdots \\ r_{M,1}^2 - K_M + K_1 \end{bmatrix} \tag{4.48}$$

An error vector can the be defined as:

$$\psi = \mathbf{h_l} - \mathbf{G_l}\mathbf{z_l^0} \tag{4.49}$$

where $\mathbf{z_l^0}$ represents the unknowns. Re-writing r by splitting out the noise gives $r_i^0 = r_{i,1}^0 + r_1^0$, and as a result, ψ can be written as:

$$\psi = c\mathbf{B}\mathbf{n} + 0.5c^2\mathbf{n}\cdot\mathbf{n} \tag{4.50}$$

where $\mathbf{B} = \text{diag}\{r_2^0, r_3^0, \ldots, r_M^0\}$.

In practice, $cn_{i,1} \ll r_i^0$ and Ψ becomes a random vector with a covariance matrix given by:

$$\mathbf{\Psi} = \mathbf{E}[\Psi\Psi^T] = c^2\mathbf{B}\mathbf{Q}\mathbf{B} \tag{4.51}$$

Now, equation 4.45 is linear in r_1 and $x_s = w - ay_s$, so a least squares approach can be used to solve the equation as follows:

$$\mathbf{z} = (\mathbf{G_l^T}\mathbf{\Psi^{-1}}\mathbf{G_l})^{-1}\mathbf{G_l^T}\mathbf{\Psi^{-1}}\mathbf{h} \tag{4.52}$$

r_1 and $x = w - ay_s$ can be substituted into 4.43 at $i = 1$ to solve for a quadratic in y.

If the array is on the x-axis and if (x_1, y_1) is at the origin then $a = b = K_1 = 0$.

4.5.5 Step 5: Application of Error Tolerances

In practice, the matrix Ψ is not known in advance, but if we assume that the signal and noises of the observed samples are white random processes, and that the Signal to Noise Ratio (SNR) of all sensor inputs are identical, then the covariance matrix, Q is given as follows:

$$\mathbf{\Psi} \approx \mathbf{Q} = \sigma_{\mathrm{t}}^2 \begin{bmatrix} 1 & 0.5 & \dots & 0.5 \\ 0.5 & 1 & \dots & 0.5 \\ \vdots & \vdots & \ddots & \vdots \\ 0.5 & 0.5 & \dots & 1 \end{bmatrix} \tag{4.53}$$

where σ_{t}^2 is the TDOA variance.

Although this approach appears to be sufficient to localise sources when there are no outliers in the TDOA matrix, the algorithm performance deteriorates significantly if there are multiple outliers in the TDOA matrix. This is often the case in the proposed algorithm, given that the signals have first been separated using a statistical BSS technique, and given that in the real world situation, array elements may have reduced sensitivity or may be completely broken and only register noise.

Therefore an additional step is necessary to remove these outliers. In this case, it suffices to use an iterative approach. Once a source position is estimated, the delays to each element are calculated. The element with the maximum error in the delay is then removed, and the process is repeated until the difference between the estimated and actual time delay for all elements falls below a pre-defined maximum error, or until more than a predefined proportion of elements have been eliminated. Furthermore, points with a total error or average error above a certain level may be excluded in a similar manner.

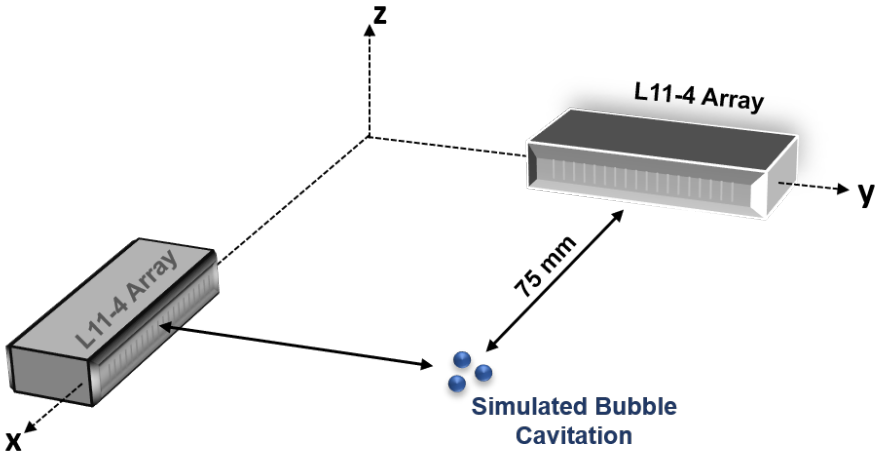


Figure 4.3: Setup for bubble simulations. Two linear arrays are placed 75mm away from 1 - 3 cavitating bubbles. The bubbles are modelled using a Keller-Miksis equation with a 0.5 MHz, 1 MPa driving HIFU excitation.

4.6 Simulation Results

In order to test the algorithm, both simulation and experimental results have been obtained. The setup for the simulation is shown in figure 4.3. The bubble simulation code and the simulated mixed bubble signal datasets used in this chapter were provided by Dr Erasmia Lyka.

4.6.1 Simulation Parameters

In simulations, groups of one, two or three bubbles were simulated using the Keller-Miksis single-bubble model, given in equation 4.54.

$$\left(1-\frac{\dot{R}}{c}\right)R\ddot{R}+\left(\frac{3}{2}-\frac{\dot{R}}{2c}\right)\dot{R}^2=\frac{1}{\rho}\left(1+\frac{\dot{R}}{c}\right)p_w+\frac{R}{\rho c}\frac{dp_w}{dt} \tag{4.54}$$

where R is the instantaneous bubble radius and c is the speed of sound in the medium. The pressure at the bubble wall, p_w, is:

$$p_w=\left(P_0+\frac{2\sigma}{R_0}\right)\left(\frac{R_0}{R}\right)^{3\kappa}-\frac{2\sigma}{R}-\frac{4\eta\dot{R}}{R}-P_0-P_a\sin(\omega t) \tag{4.55}$$

where σ is the surface tension between the gas-water interface, R_0 is the equilib-

Table 4.1: Bubble simulation parameters

Excitation frequency	0.5 MHz
Number of Excitation Cycles	20
Excitation Pressure	1.0 MPa
Initial Bubble Radius Range	0.6 to 1.1 µm
Bubble Position Range	Within 1.5 mm radius circle at origin
SNR (where noise is added)	20 - 25 dB
Number of Receiver Arrays	Two Linear Arrays (4 - 11 MHz)
Number of Elements per Array	128
Element pitch	0.3 mm
Sampling Frequency	157 MHz

rium radius, κ is the polytropic exponent, and P_a is the HIFU excitation pressure amplitude. Finally, the pressure at a distance r from the bubble, P_r, can be computed as follows:

$$P_r = \rho \frac{R^2 \ddot{R} + 2R\dot{R}^2}{r} \tag{4.56}$$

The Keller-Miksis equation is selected for this work as it is specifically derived for inertial bubble dynamics. Even in the case of a bubble cloud in which bubbles are located very near to each other, the model might still be a good approximation since bubbles near to each other tend to act in phase [181]. A limitation in using this model is that bubble-bubble interactions are neglected, however the utility of the proposed technique in comparison to PAM can still be shown. Should the independence criterion not be met in real life scenarios, then a more complex source separation technique that is able to relax the independence assumption can be used [115].

The simulated bubbles are located near the origin, with dual arrays positioned 75 mm away and perpendicular to each other as shown in figure 4.3. Simulated signals are then advanced to the element positions and are summed at the point of the receiver. The parameters of the simulation are given in table 4.1.

4.6.2 Single Source

In the case of a single source, the results for both no noise and added noise are shown in figures 4.4 to 4.7. In these figures, the BSS-ASL output is generated using only the elements on either Array 1 or only the elements on Array 2. The PAM maps are generated by either Array 1 or 2 individually, or by both arrays together (dual array PAM). The overlay of the BSS-ASL output on the PAM maps is also shown. It is clear from these figures that the BSS-ASL algorithm performs well, and the maximum localisation error for a single source is less than 0.1 mm.

Good performance in the case of a single bubble is expected in the noise free environment as there is little chance of the ICA stage failing to identify the source signal in order to generate a time-delay curve. Even if the ICA algorithm did separate the signal from a single source into multiple sources, the time-delay curves for all of those identified signals should be the same. In reality, the algorithm does not always identify all sources on every run, however over enough iterations the algorithm is able to localise almost all sources. In addition, although the MDL number is useful to give a general estimate of the number of sources, in most cases it over estimates the sources present, and hence the removal of auto- and cross-correlated sources is necessary.

In the presence of noise, this performance may decrease as it is again possible that the ICA algorithm may fail to identify the signal out of the noise. In addition, if an extremely noisy signal was output as the only IC, then it is possible that an accurate time-delay curve may not be obtained. Therefore, a single bubble was simulated with noise added to the simulated bubble signal at the sensor. The maximum noise level was approximately 10% of that of the maximum signal strength. It is noted that the performance of the PAM beamformer in the presence of noise seems to be improved compared to the noiseless case. This is due to the fact that selection of the signal element weights in the adaptive PAM beamforming algorithm used is optimised for a noisy signal input.

The results for a single bubble in a noisy environment are shown in figures 4.6 and 4.7. Again, the BSS-ASL algorithm performs well, using either Array 1 (figure 4.6) or Array 2 (figure 4.7). This demonstrates that additive sensor noise should not be a problem in the real world environment.

Although these results demonstrate good localisation performance, this level of localisation accuracy could also be achieved with any existing ASL algorithms, or with a super-resolution algorithm applied to a PAM map generated by existing beamforming methods. This is because there is only a single source present in the PSF of the system, and thus it is necessary to test the algorithm on multiple sources.

4.6.3 Multiple Sources

In the case of multiple sources the BSS stage of the algorithm must first correctly separate the signals. Even if the separated signals are not exactly identical to the original signals, they may still represent the original signals accurately enough for adequate performance.

The results for three bubbles for no noise and additive noise cases are given in figures 4.8 to 4.11. Results are given for the BSS-ASL output from both Array 1 and Array 2 to demonstrate the differences between the array orientation. As the BSS stage relies on a statistical technique, the performance differences cannot only be attributed to array orientation differences, but are rather a combination of array orientation, bubble location, and statistics of the recorded signals.

Even so, there is a clear elongation in the axial direction evident in the results shown in figures 4.8 to 4.9, similar to that seen in the single array PAM images.

Figures showing the output of the BSS-ASL algorithm for a single run are shown in figure 4.12. The three simulated signals are shown in the top row, and the output after running ICA and performing the scaling is shown in the second row. Here it can be seen that the recovery for each signal is not exact, but from the delay curves shown in the third row, even the approximated signals provide good enough estimates of the delays. The pink circles in the third row of figure 4.12 demonstrate that the

Single Bubble in the Noiseless Case - Array 1 BSS-ASL Reconstruction

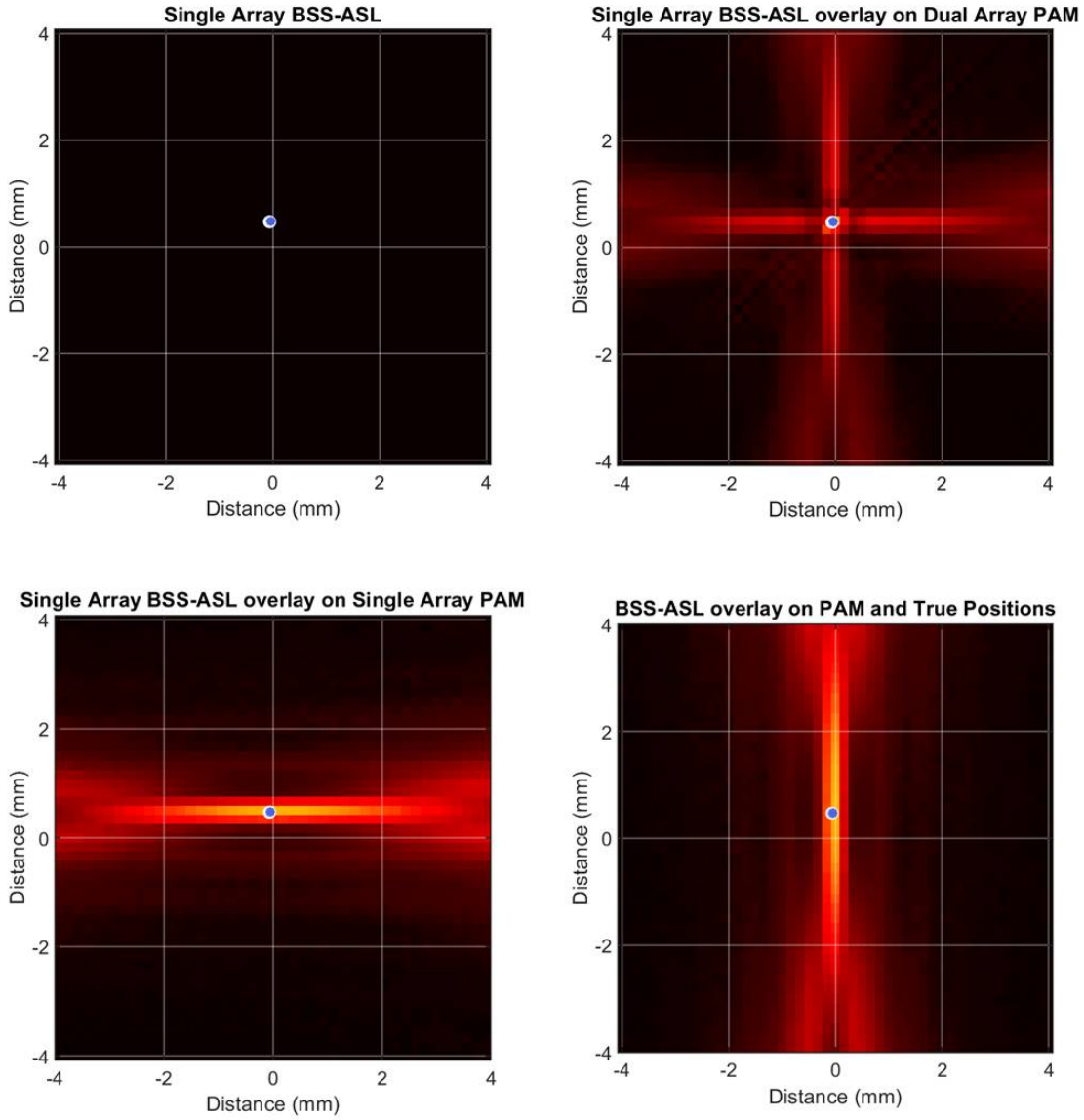


Figure 4.4: Comparison of PAM and BSS-ASL algorithm for a single simulated bubble. True bubble location is shown by blue asterisk, white dots represent the output from multiple iterations of the BSS-ASL algorithm using only signals received on Array 1, red and yellow map represents energy from RCB-PAM beamforming using both arrays (top right), only using Array 1 (bottom left) or only using Array 2 (bottom right). The BSS-ASL algorithm is able to accurately locate the bubble using data from a single array.

Single Bubble in the Noiseless Case - Array 2 BSS-ASL Reconstruction

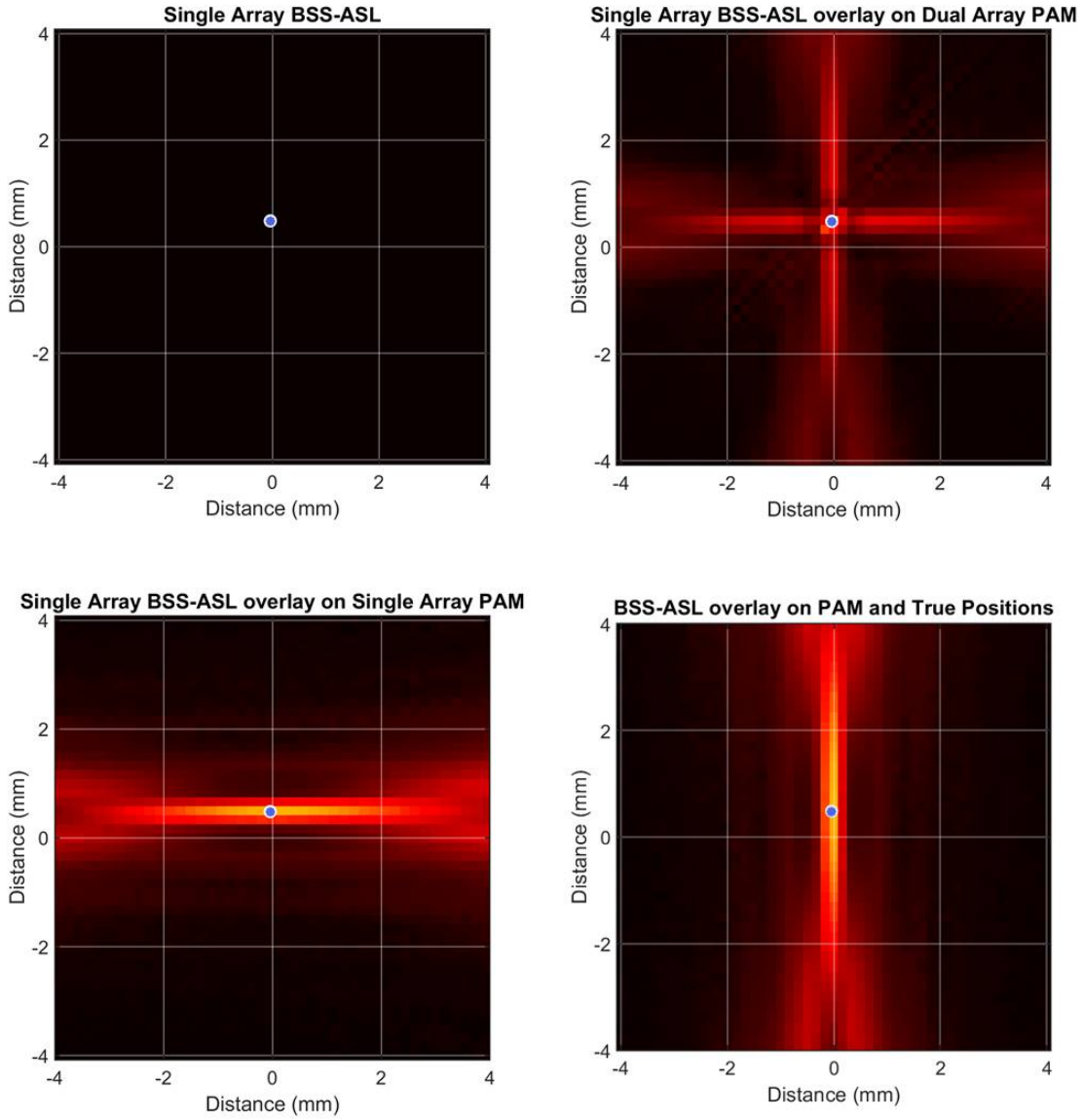


Figure 4.5: Comparison of PAM and BSS-ASL algorithm for a single simulated bubble using data from the perpendicular array (Array 2), shown for comparison to the BSS-ASL output from Array 1 in the previous figure. True bubble location shown by blue asterisk, white dots represent outputs from multiple iterations of the BSS-ASL algorithm using only signals received on Array 2, red and yellow map represents energy from RCB-PAM beamforming using both arrays (top right), only using Array 1 (bottom left) or only using Array 2 (bottom right). Using the perpendicular array, the BSS-ASL algorithm is able to accurately locate the bubble using data from a single array.

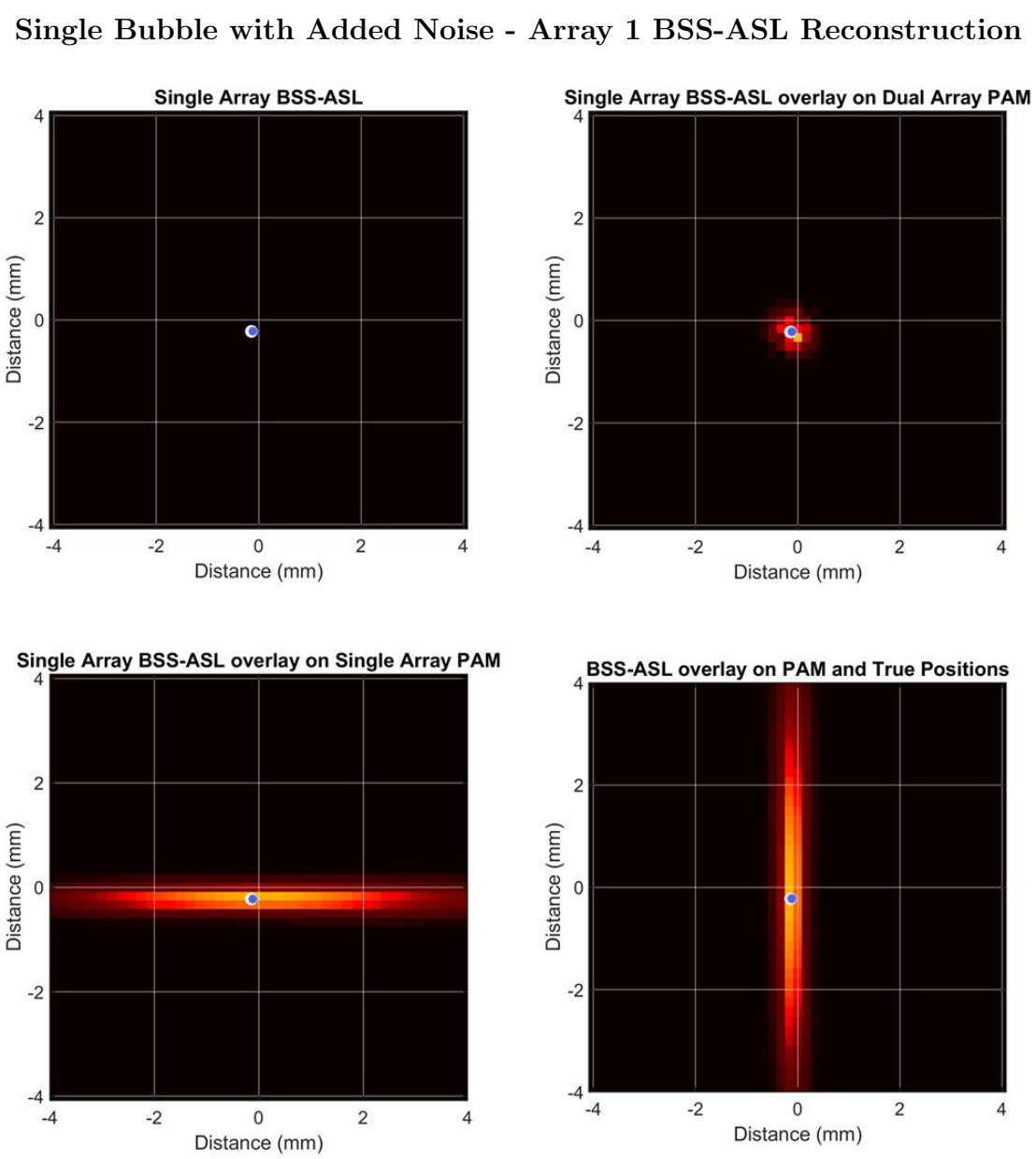


Figure 4.6: Comparison of PAM and BSS-ASL algorithm for a single simulated bubble with added noise. True bubble location is shown by blue asterisk, white dots represent the output from multiple iterations of the BSS-ASL algorithm using only signals received on Array 1, red and yellow map represents energy from RCB-PAM beamforming using both arrays (top right), only using Array 1 (bottom left) or only using Array 2 (bottom right). Even in the presence of added noise on the received signals, the BSS-ASL algorithm is still able to accurately locate the bubble using data from a single array.

Single Bubble with Added Noise - Array 2 BSS-ASL Reconstruction

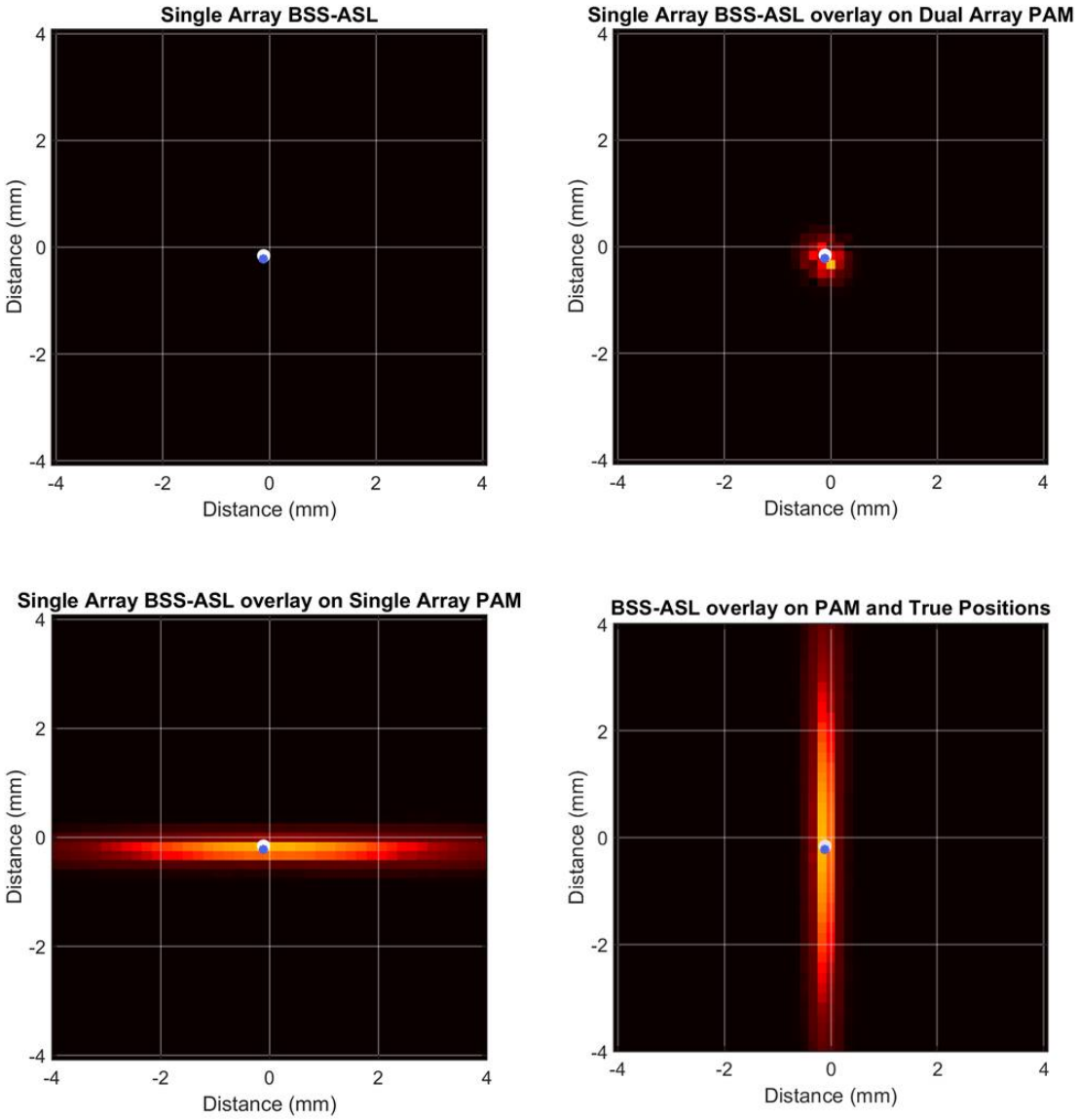


Figure 4.7: Comparison of PAM and BSS-ASL algorithm for a single simulated bubble with added noise, using data from the perpendicular array (Array 2), and shown for comparison to the BSS-ASL output from Array 1 in the previous figure. True bubble location is shown by blue asterisk, white dots represent the output from multiple iterations of the BSS-ASL algorithm using only signals received on Array 2, red and yellow map represents energy from RCB-PAM beamforming using both arrays (top right), only using Array 1 (bottom left) or only using Array 2 (bottom right). Again, in presence of added noise on the received signals, the BSS-ASL algorithm is still able to accurately locate the bubble using data from a single array.

Multiple Bubbles in the Noiseless Case - Array 1 BSS-ASL Reconstruction

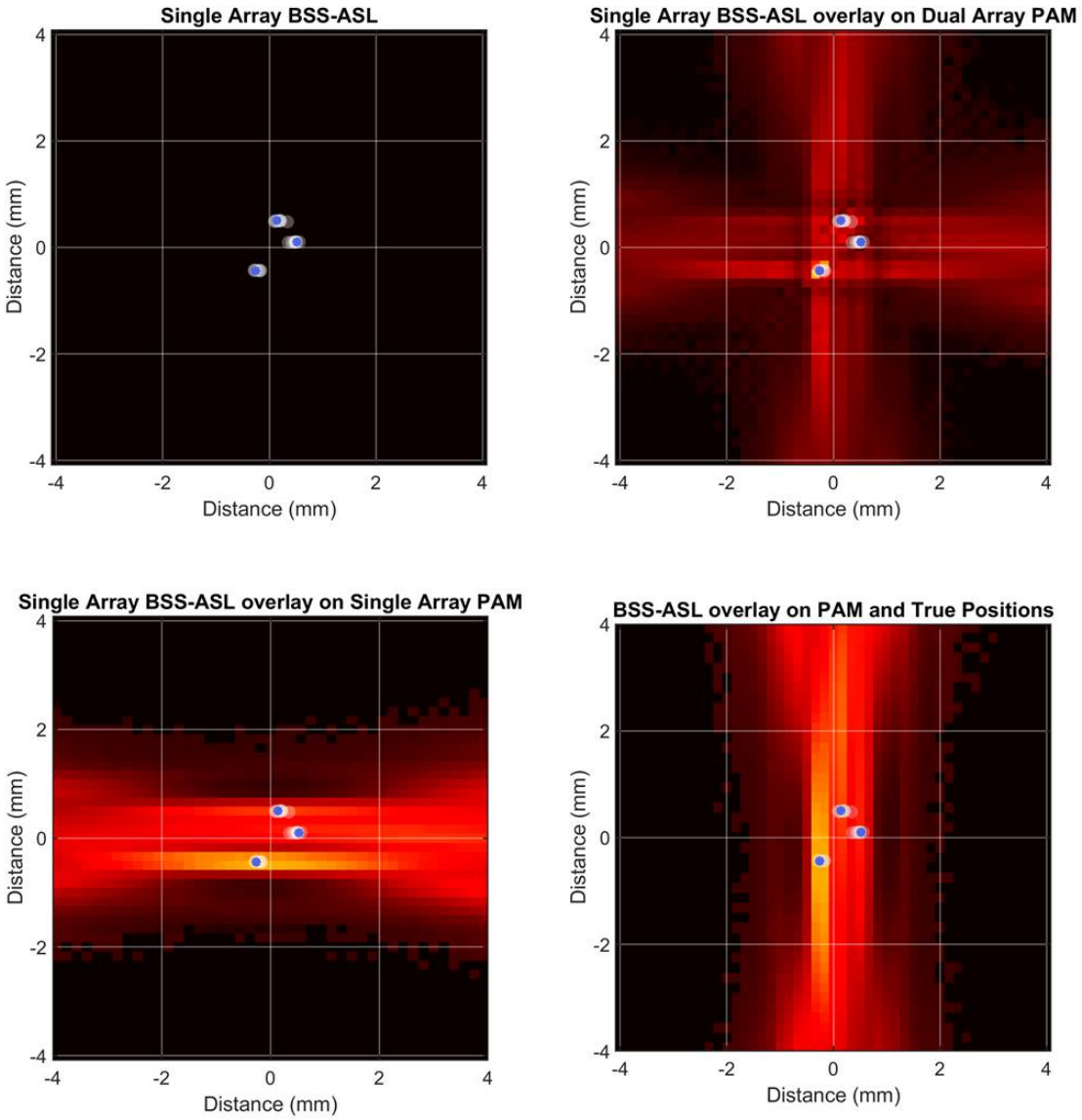


Figure 4.8: Comparison of PAM and BSS-ASL algorithm for three simulated bubbles in the noiseless case. True bubble location is shown by blue asterisk, white dots represent the output from multiple iterations of the BSS-ASL algorithm using only signals received on Array 2, red and yellow map represents energy from RCB-PAM beamforming using both arrays (top right), only using Array 1 (bottom left) or only using Array 2 (bottom right). In the noiseless case, the BSS-ASL algorithm is able to accurately locate all three bubbles using data from a single array. Crucially, the image from the corresponding PAM reconstruction on Array 1 cannot distinguish the three sources.

Multiple Bubbles in the Noiseless Case - Array 2 BSS-ASL Reconstruction

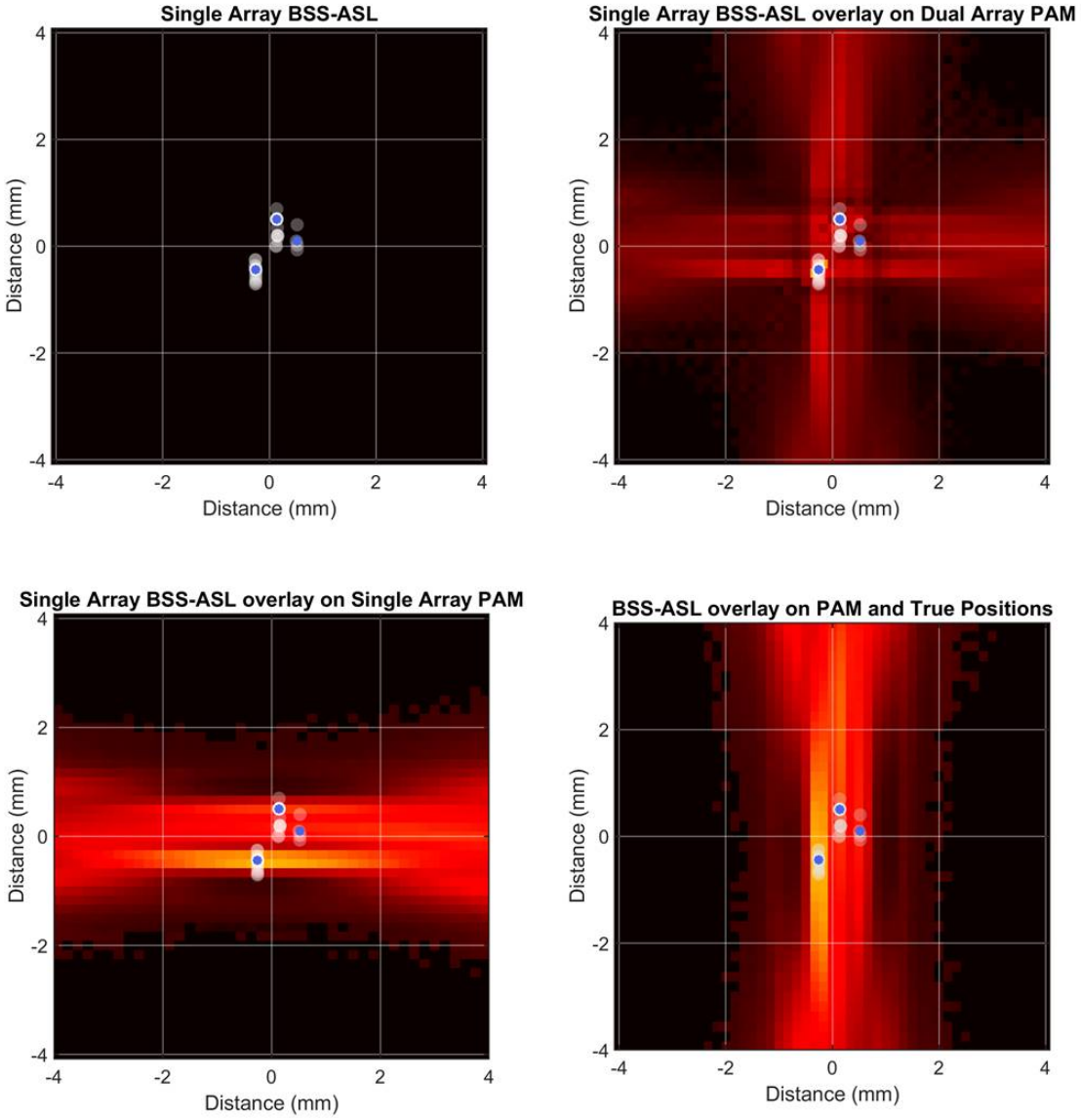


Figure 4.9: Comparison of PAM and BSS-ASL algorithm for three simulated bubbles in the noiseless case, reconstructed using Array 2 data, and shown for comparison to Array 1 BSS-ASL reconstruction. True bubble location is shown by blue asterisk, white dots represent the output from multiple iterations of the BSS-ASL algorithm using only signals received on Array 2, red and yellow map represents energy from RCB-PAM beamforming using both arrays (top right), only using Array 1 (bottom left) or only using Array 2 (bottom right). In the noiseless case, the BSS-ASL algorithm is able to accurately locate all three bubbles using data from a single array, and again outperforms the corresponding PAM map in source identification.

simple iterative approach to exclude points with the maximum error is effective in removing outliers in the time delay curve. Finally, the localisation of points can be seen in the final row of the figure. Here, the importance of multiple runs can be seen, especially in column 2 of the figure where the final localisation is not completely accurate, despite the delay curve being relatively good.

In terms of resolution limits, this will also depend in part on the accuracy of the BSS stage, along with the physical location of the bubbles. For example, figure 4.16 shows the BSS-ASL output for a different set of three bubbles in the presence of noise. In this case, all three bubbles have approximately the same transverse axis location, but all have different axial locations, and the PAM image generated by Array 2 fails to distinguish these sources as separate. The BSS-ASL algorithm on the other hand does detect three separate sources, and localises them with a relatively high degree of accuracy. The outputs from the different stages of the BSS-ASL algorithm for this case are shown in figure 4.13. Interestingly, even though the third IC is recovered with a high level of noise, the algorithm is still able to track the time delays of this signal across the elements, and a relatively accurate source location is still achieved.

However, in this case, because two of the three sources are located close together in the axial direction, some of the BSS-ASL output locations fall in between two true source locations, and therefore it is not clear that two separate sources exist. If the error tolerance of the output of the BSS-ASL algorithm is decreased, then some erroneous output locations are removed, and the result for this case is shown in figure 4.14. Even with the introduction of a maximum allowable error however, two separate sources are still not clearly distinguishable. Therefore another option is to change the elements used in the position estimator. For example, if the central elements of the array are not passed to the estimator, then the separation between the two sources does become evident, as shown in figure 4.15. This improved separation performance is most likely because the difference in time of arrival between consecutive elements is greater on the edges of the array, and thus the localisation is also more accurate. In fact, this type of element suppression is similar to that found in the

Multiple Bubbles with added Noise - Array 1 BSS-ASL Reconstruction

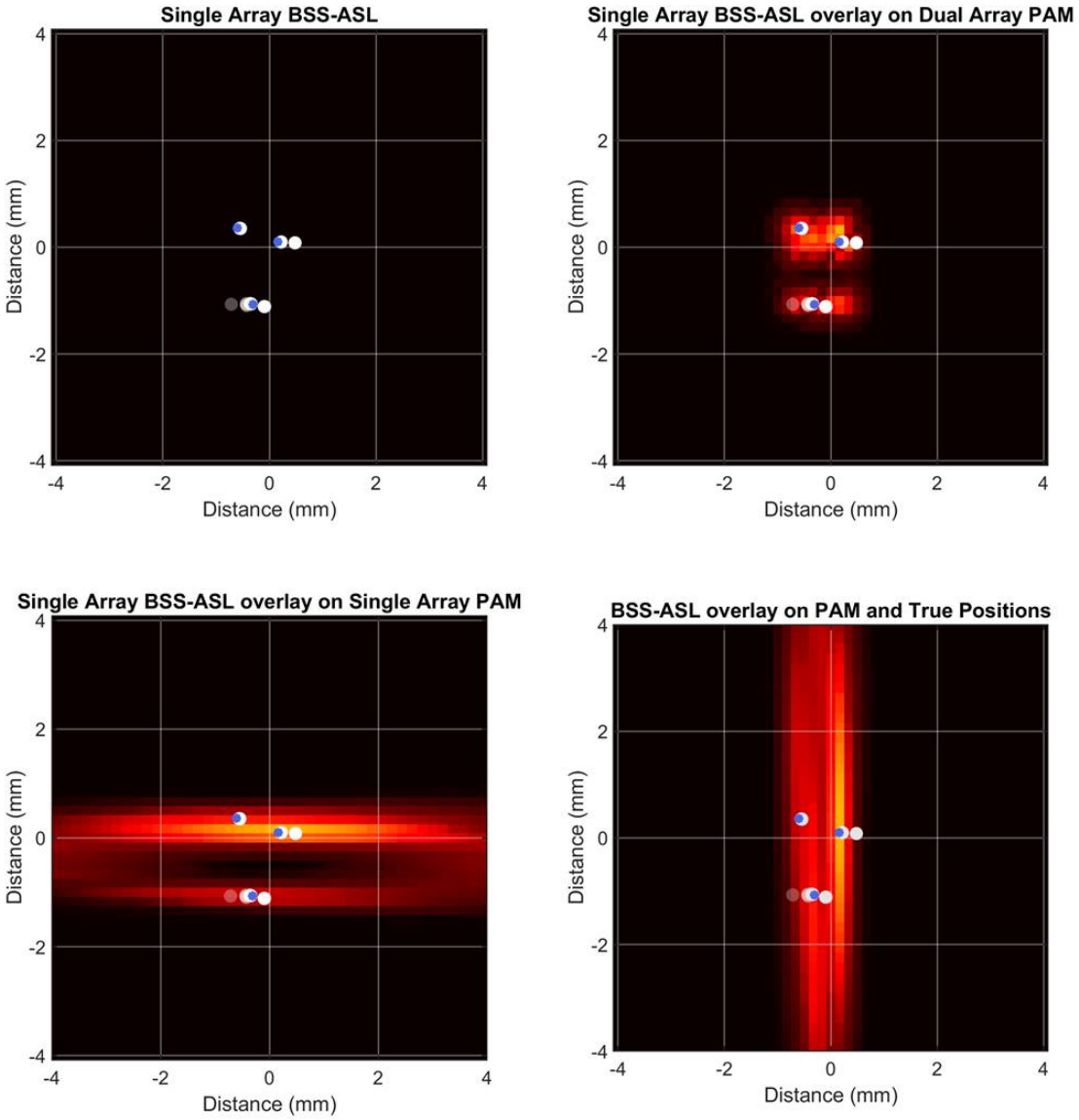


Figure 4.10: Comparison of PAM and BSS-ASL algorithm for three simulated bubbles with added noise, reconstructed using Array 1 data, and shown for comparison to Array 1 BSS-ASL reconstruction. True bubble location is shown by blue asterisk, white dots represent the output from multiple iterations of the BSS-ASL algorithm using only signals received on Array 1, red and yellow map represents energy from RCB-PAM beamforming using both arrays (top right), only using Array 1 (bottom left) or only using Array 2 (bottom right). In the noisy case, the BSS-ASL algorithm is able to accurately locate all three bubbles using data from a single array, and outperforms the corresponding PAM map in source identification.

Multiple Bubbles with added Noise - Array 2 BSS-ASL Reconstruction

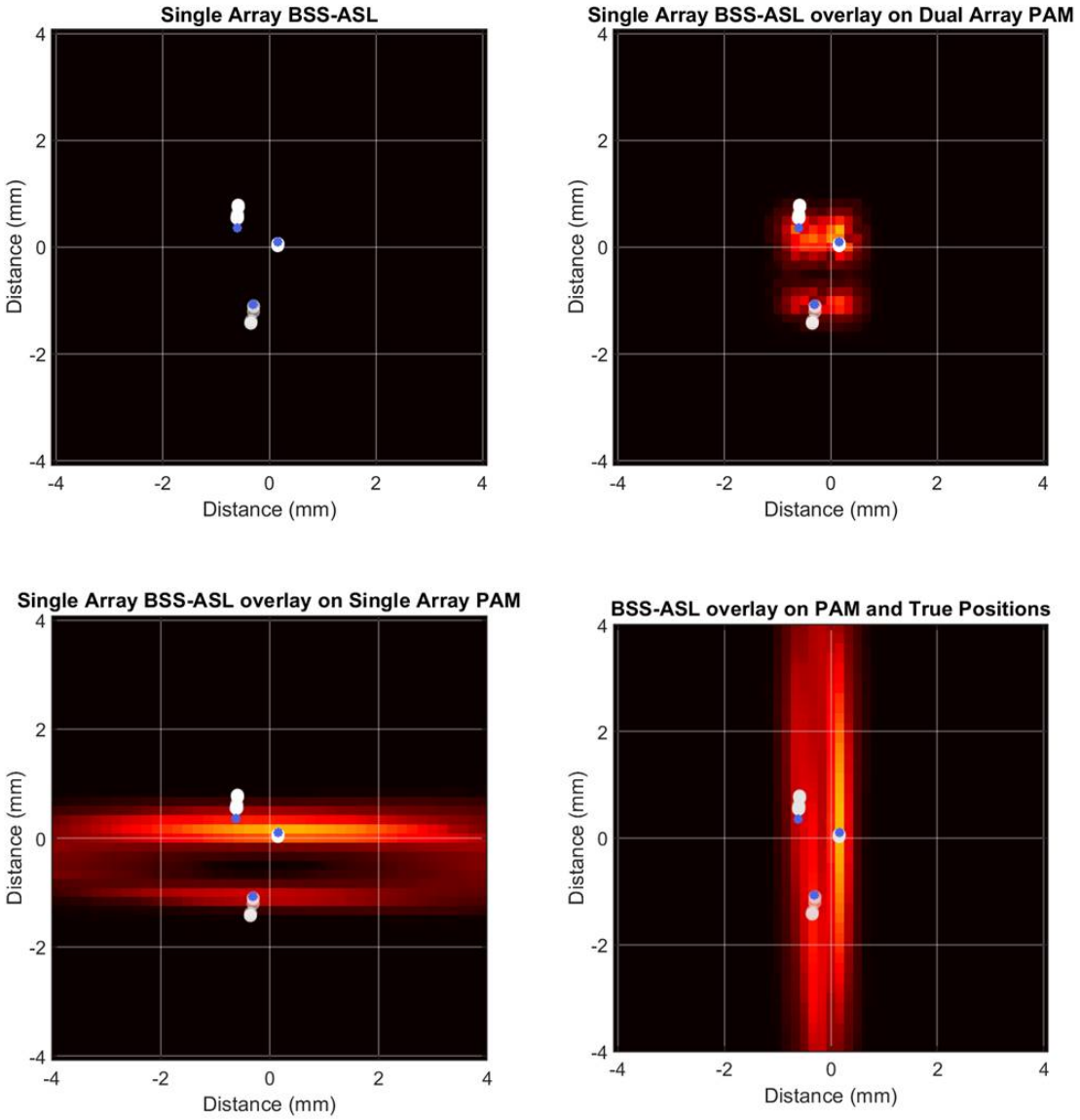


Figure 4.11: Comparison of PAM and BSS-ASL algorithm for three simulated bubbles with added noise, reconstructed using Array 2 data, and shown for comparison to Array 1 BSS-ASL reconstruction. True bubble location is shown by blue asterisk, white dots represent the output from multiple iterations of the BSS-ASL algorithm using only signals received on Array 1, red and yellow map represents energy from RCB-PAM beamforming using both arrays (top right), only using Array 1 (bottom left) or only using Array 2 (bottom right). In the noisy case, the BSS-ASL algorithm using Array 2 is able to accurately locate all three bubbles, and outperforms the corresponding PAM map in source identification.

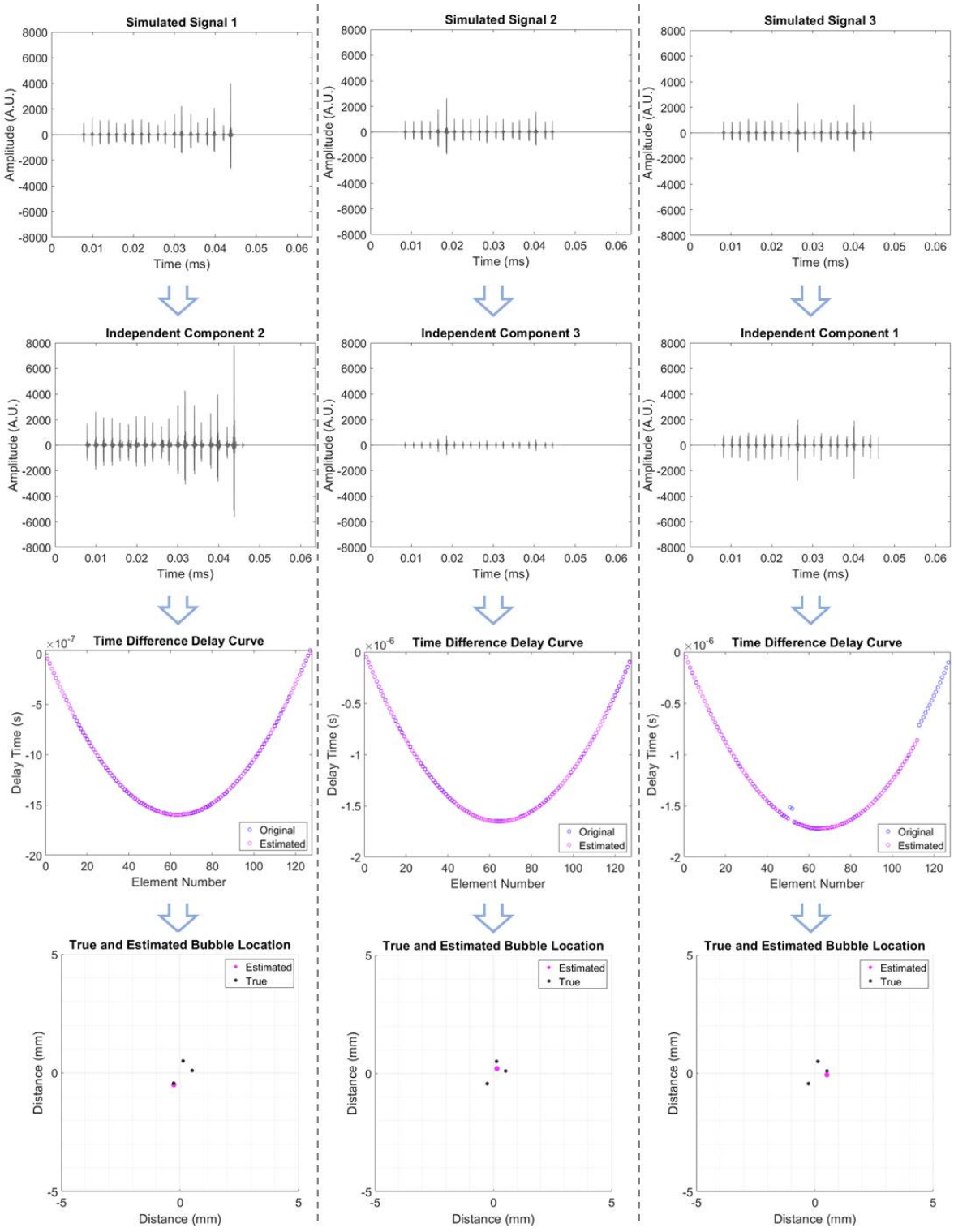


Figure 4.12: Output for each stage of the BSS-ASL algorithm for three bubbles with no noise. Top row: simulated signals. Second row: Recovered ICs. Third row: Time delays on each element (blue) and time delays calculated from estimated source position (pink). Bottom row: Recovered source position (pink) relative to true position (black).

adaptive beamformers used in PAM. Although this technique is not explored further in this thesis, it does suggest a possible future method for improving the performance of the BSS-ASL algorithm. The final resulting image, overlaid with the PAM maps for the corresponding bubbles, is presented in figure 4.16.

Statistics for evaluating groups of randomly selected bubbles are given in table 4.2 and shown in figures 4.17 and 4.18. In these cases, the mixed signals are created as the summation of signals from three randomly generated bubbles. Ten unique sets of bubbles are evaluated. In each case, the BSS-ASL algorithm is run 100 times, and the central elements of the array are excluded in the position estimation stage of the algorithm.

From the figures, it can be seen that the algorithm generally tends to identify the correct number of sources overall, but from the statistics in table 4.2 it is also clear that the initial estimate of the number of sources using the MDL criterion is high. In practice, the ICA algorithm tends to output ICs that are 'repeats' of other ICs, or it tends to output signals that are very similar to the overall mixed signal. The need for the elimination of highly correlated signals is therefore clear. It is also clear from the statistics of the number of sources finally identified at the end of each run that the algorithm (after performing ICA and removing highly correlated sources) does not identify the correct number of sources on every single run. This type of inconsistent behaviour in source identification is expected since the BSS stage relies on a statistical technique. However it is interesting to note that even though not all sources are identified 100% of the time, the TDOA and position estimation stages of the algorithm still work relatively well. These statistics demonstrate the clear need to run the algorithm multiple times and collect and display the output of all runs in order to accurately locate cavitation sources.

In terms of localisation performance, the distances to each source given in table 4.2 show that the average distance to any one source is less than 0.3 mm, but that the maximum distance can be up to 0.7 mm, as in the case of Set 3. This level of performance for a single array is better than the localisation that can be achieved

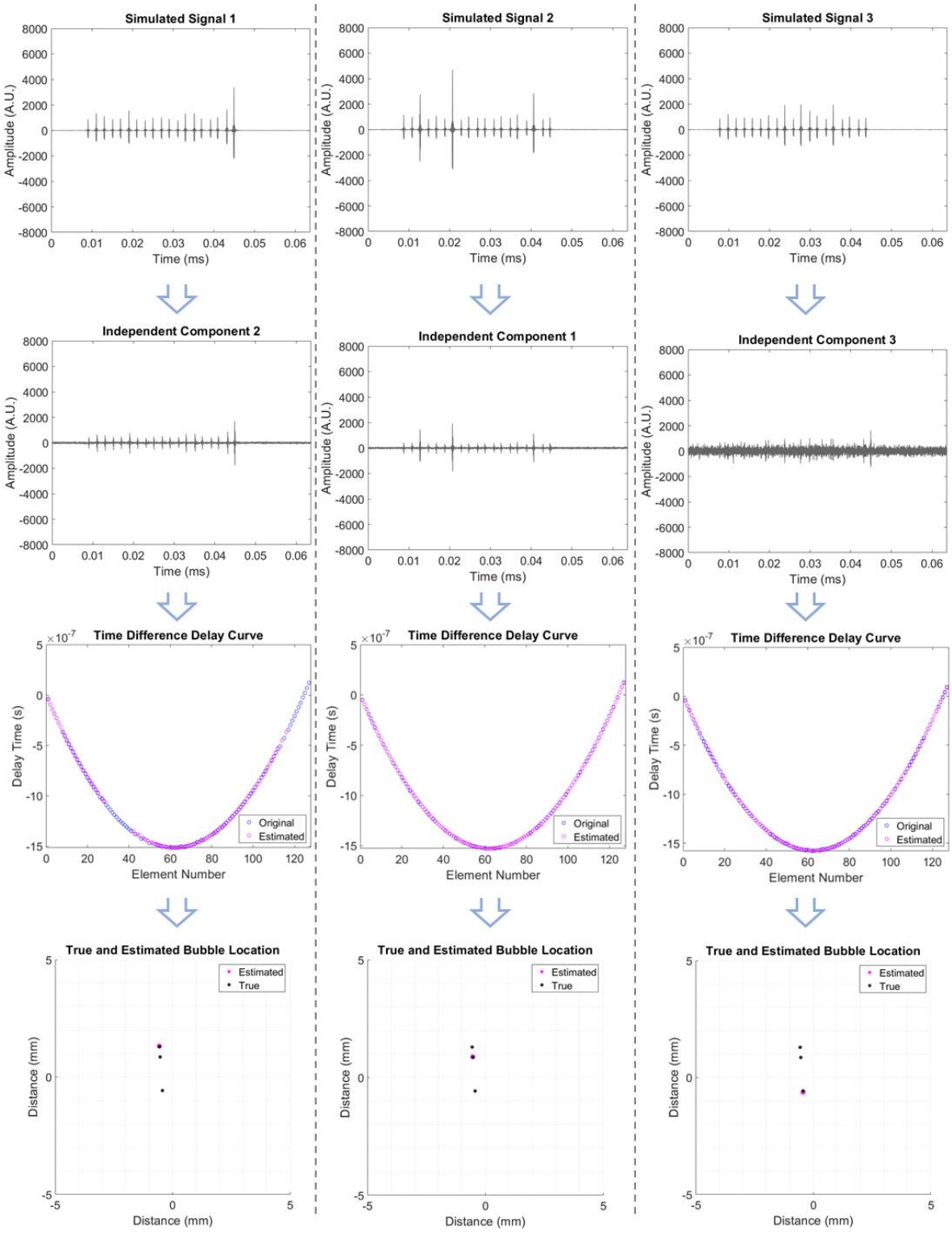


Figure 4.13: Output for each stage of the BSS-ASL algorithm for three bubbles with noise. Top row: simulated signals. Second row: Recovered ICs. Third row: Time delays on each element (blue) and time delays calculated from estimated source position (pink). Bottom row: Recovered source position (pink) relative to true position (black).

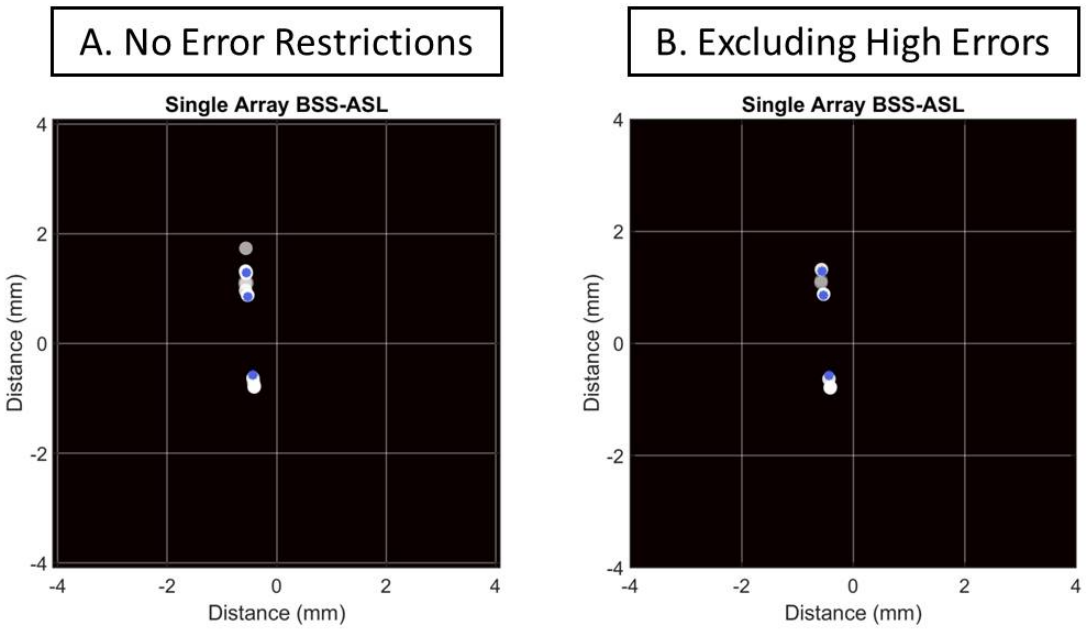


Figure 4.14: BSS-ASL output for three simulated bubbles. True bubble locations shown by blue asterisks, BSS-ASL outputs showns by white dots. Left: All outputs included. Right: Outputs with high average time estimation errors excluded.

with single array PAM, but in the worst case, is not as good as the accuracy with with sources can be located using dual array PAM.

4.7 Experimental Results

Although the simulation section shows good results and is a useful indication of whether the algorithm is worth investigating, there are several factors that may prohibit the use of the algorithm in a real-world setting. First, simulated signals are created independently, and the dynamic interactions between cavitating bubbles cannot be captured in the simulation. Interactions between bubbles serve to reduce the independence of each source, and therefore may cause the BSS algorithm to fail, as it is primarily based on the independence of sources. Second, the level of noise present in an experimental situation may cause interference with the ICA algorithm, but further may reduce the ability of the algorithm to obtain accurate time delays for each signal as this part of the algorithm is based on correlation. Finally, even in an experiment

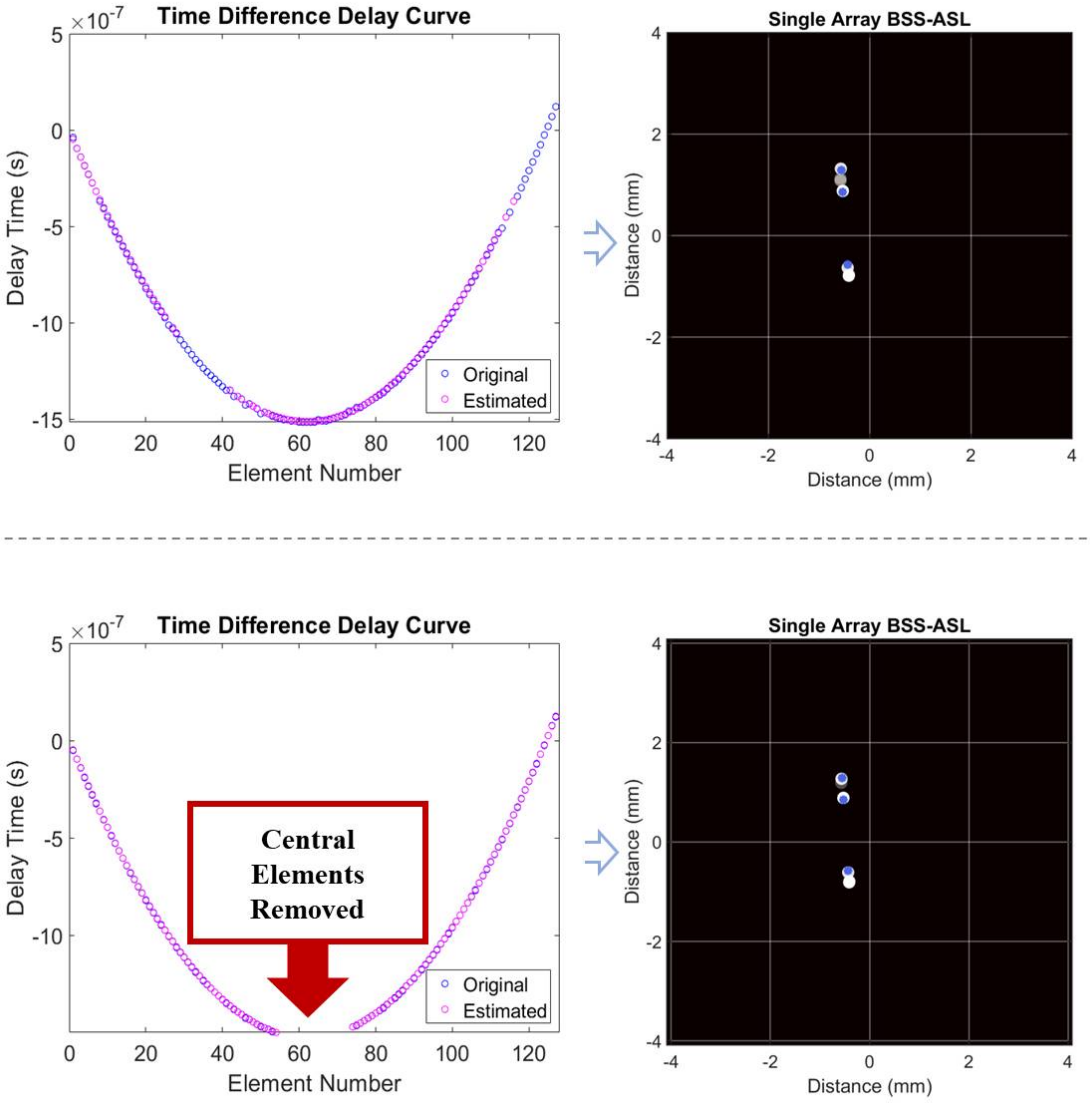


Figure 4.15: Representative TDOA curves (left) for all elements (top) and with the central 20 elements removed (bottom). BSS-ASL output (right) generated from Array 2 data using all elements for position estimation (top) or using the outer elements for position estimation (bottom).

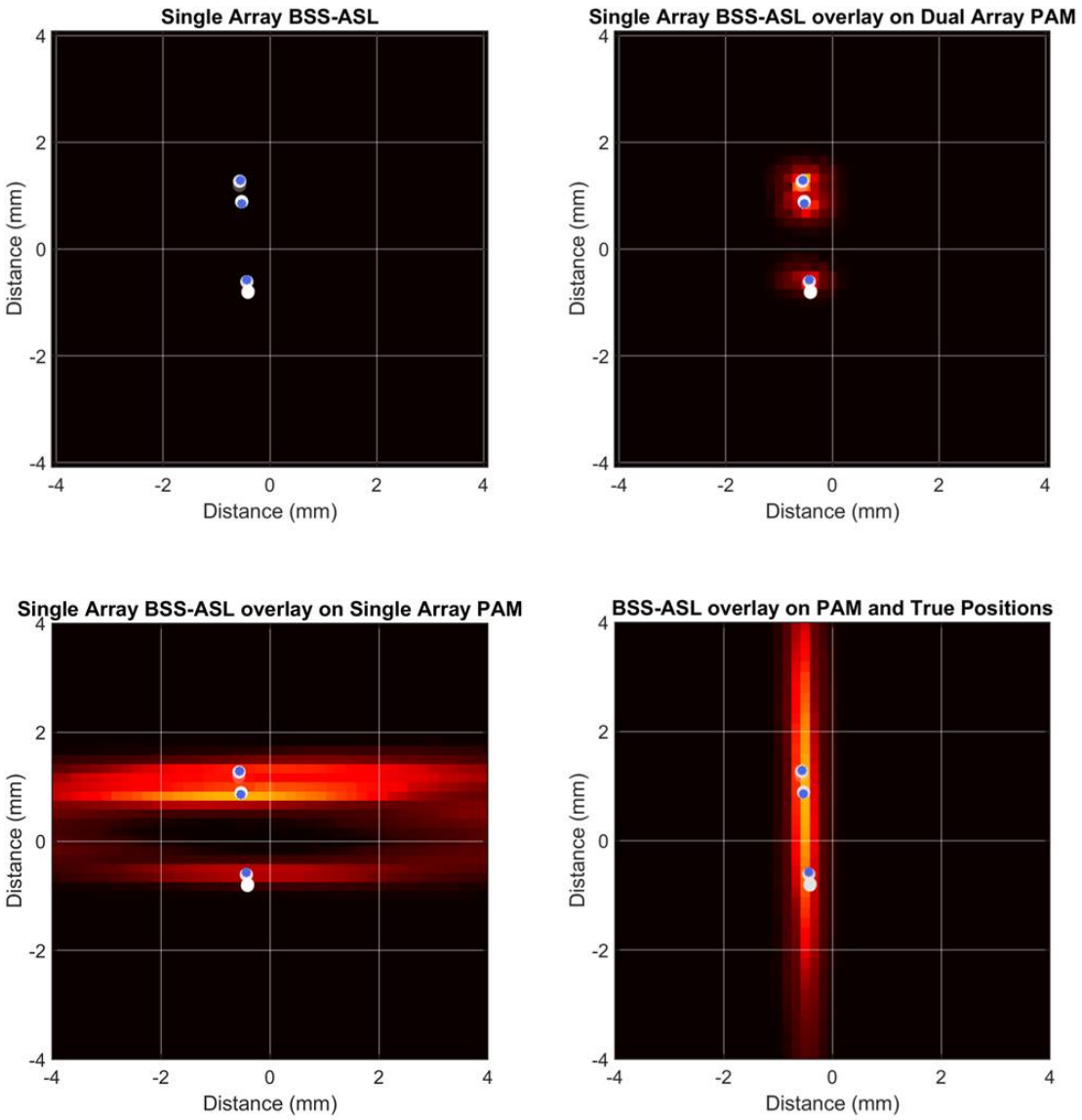


Figure 4.16: Three simulated bubbles arranged in a linear manner. True bubble locations shown by blue asterisks, white dots represent BSS-ASL algorithm output generated from Array 2, red and yellow background represents RCB-PAM beamformed using both arrays (top right), only using Array 1 (bottom left) or only using Array 2 (bottom right). Even in the case of three sources that all fall within the PSF of single array PAM, the BSS-ASL algorithm with error corrections can still localise the three sources.

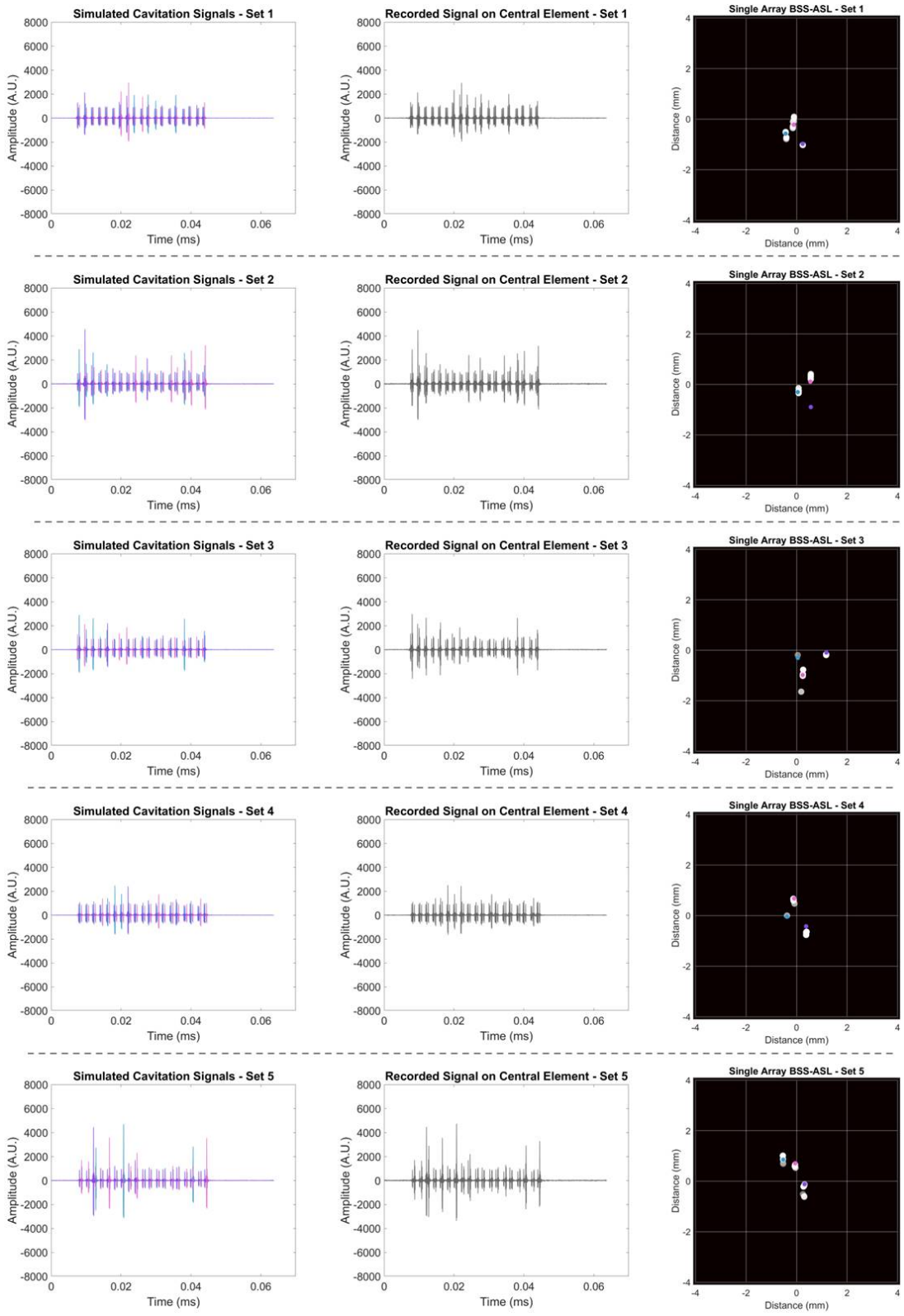


Figure 4.17: Sets 1 - 5 (of 10 total) of BSS-ASL output for 100 iterations of randomly positioned bubbles. Left Column: Simulated bubble signals. Centre Column: Signal recorded on central array element. Right Column: BSS-ASL output for a single array, overlaid on the true source positions.

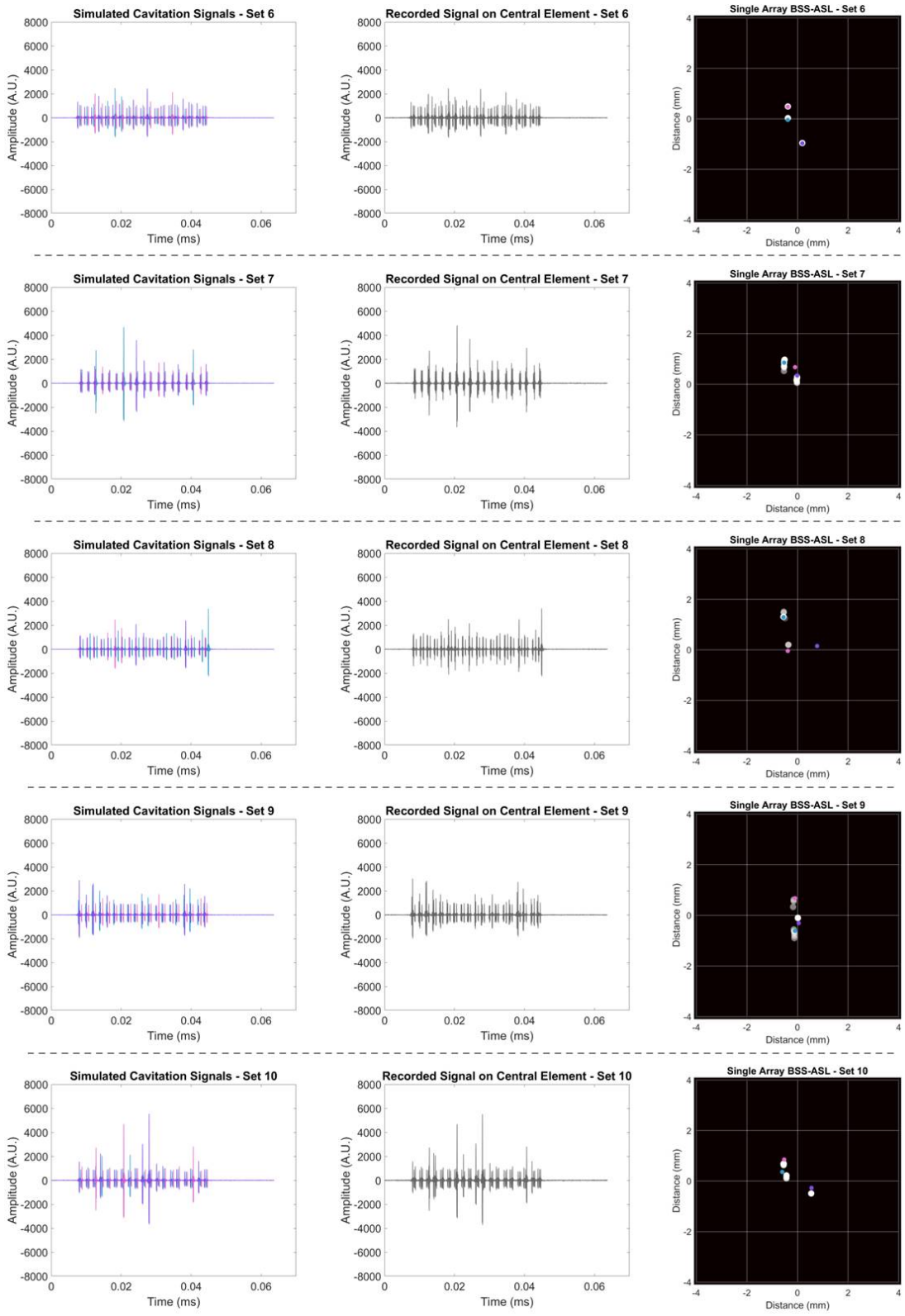


Figure 4.18: Sets 6 - 10 (of 10 total) of BSS-ASL output for 100 iterations of randomly positioned bubbles. Left Column: Simulated bubble signals. Centre Column: Signal recorded on central array element. Right Column: BSS-ASL output for a single array, overlaid on the true source positions.

Table 4.2: Quantification of simulation results for 10 sets of three randomly positioned bubbles. Distances from estimated to true locations for each source given as averages in mm, distance overall is a weighted average, maximum distance is taken from the BSS-ASL output point that is furtherest away from any given source.

Set	MDL No.	Sep. sources Evident	% runs showing 1 source	% runs showing 2 sources	% runs showing 3 sources	Dist to 1st source (mm)	Dist to 2nd source (mm)	Dist to 3rd source (mm)	Avg dist to all Sources (mm)	Max dist to any source (mm)
1	6	3	0	33	42	0.104	0.173	0.042	0.118	0.318
2	7	2	0	0	33	0.075	0.208	N/A	0.144	0.323
3	7	4	69	29	2	0.114	0.082	0.072	0.080	0.663
4	4	3	30	70	0	0.043	0.079	0.277	0.225	0.342
5	5	4	0	16	38	0.104	0.111	0.213	0.143	0.495
6	5	3	0	55	45	0.072	0.010	0.007	0.016	0.072
7	5	2	0	0	100	0.103	N/A	0.151	0.132	0.332
8	6	2	2	23	47	0.028	0.243	N/A	0.040	0.241
9	6	3	0	0	15	0.130	0.189	0.204	0.174	0.335
10	5	3	0	42	58	0.248	0.185	0.219	0.200	0.300

where the propagation medium is relatively uniform, all or part of the signal from some cavitating sources may be blocked by other cavitating sources, thereby reducing the number of usable signals recorded on elements. This is especially a problem if the signals are prevented from reaching the central array elements (on which ICA is performed).

In order to test whether the algorithm may be applicable to real-world situations, an experiment using a 3% agarose phantom was designed. The setup is shown in figure 4.19.

Figures 4.20 and 4.20 show the results of the algorithm applied to experimental data. The output shows good agreement with the location of sources, determined from high resolution dual array RCB-PAM. For a single cavitation source, the BSS-ASL output is more disperse than for a single source in the simulation data, which is most likely due to higher levels of noise in the data, as well as due to small differences in the assumed versus the true element positions. In the case of multiple sources, the

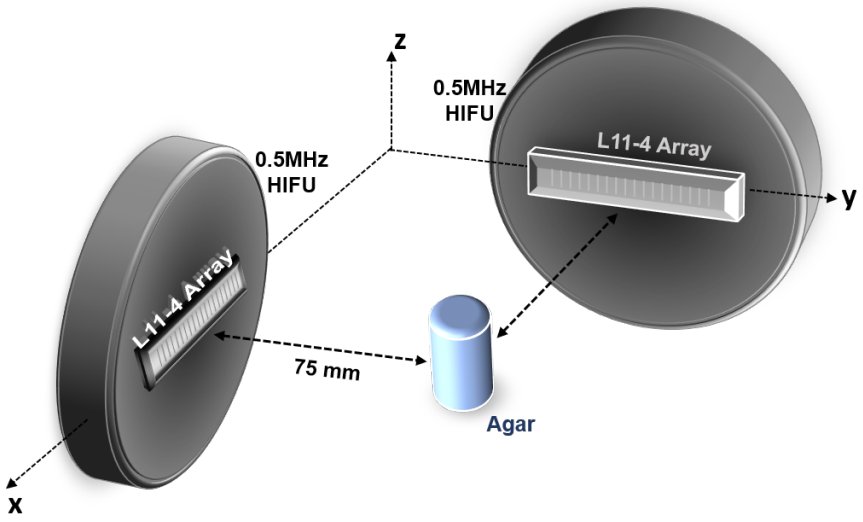


Figure 4.19: The setup for experiments. Two linear arrays are placed perpendicular to each other, with each co-axially aligned with a 0.5 MHz HIFU transducer (H107 Model, Sonic Concepts). An agarose phantom is placed at the focus of the HIFU transducer (approximately 75 mm away from each linear array).

BSS-ASL algorithm correctly identifies the location of the sources, but once again displays greater dispersion than in the simulation case, with the greatest distance from a BSS-ASL output to the true source location of approximately 1 mm in this experimental setup. Even though the output in the experimental case is less precise than in the simulation case, the BSS-ASL algorithm is able to identify and localise multiple sources that were previously indistinguishable with single array RCB-PAM in the same orientation.

4.8 Discussion

From the results presented it can be seen that the proposed approach to source localisation shows promise for the simulations and experimental situations presented. However there are still some significant limitations that need to be addressed before the algorithm can be used on *in vivo* data, and other improvements could also be

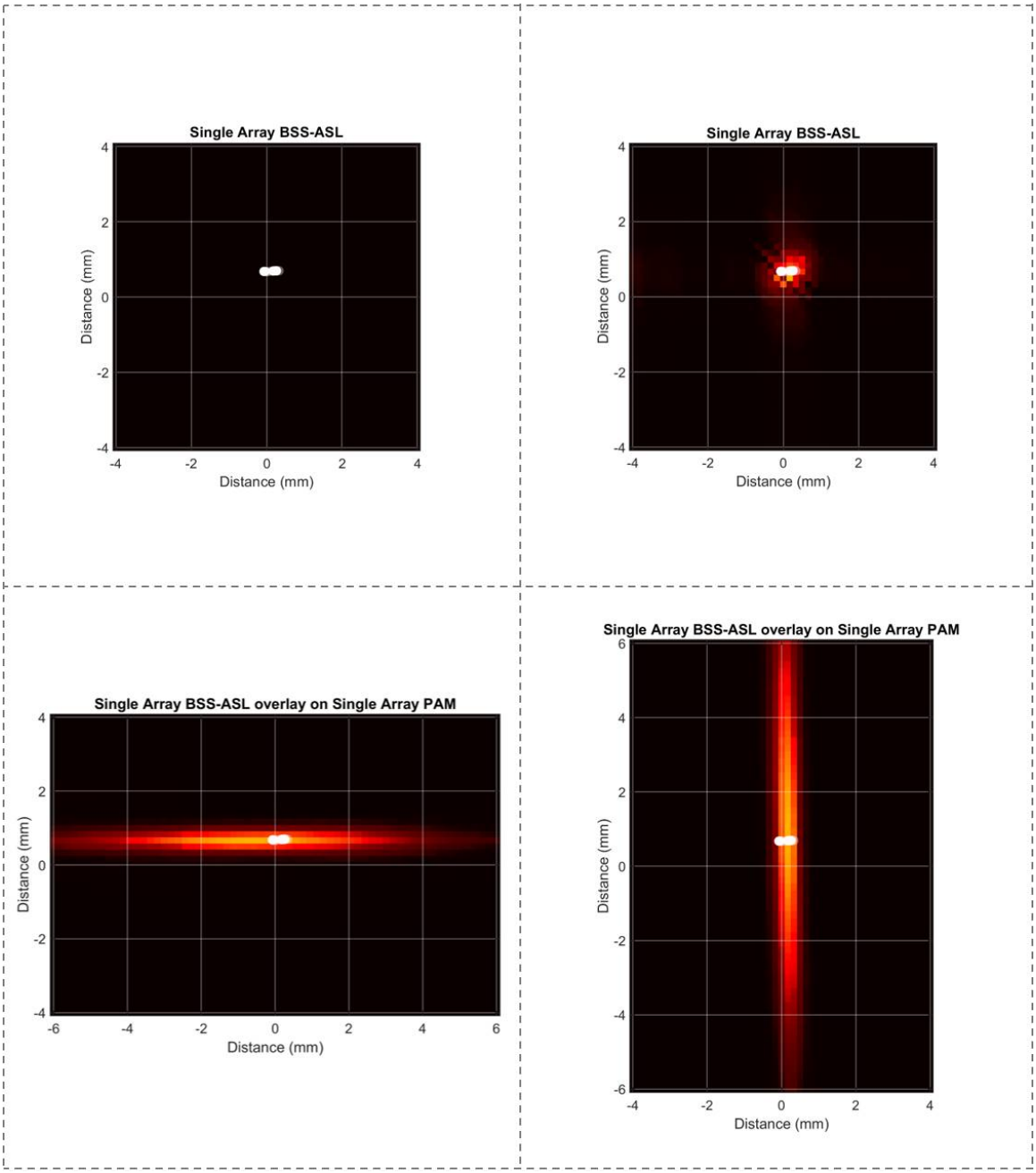


Figure 4.20: Experiment showing one distinct cavitation source, as identified by dual array PAM. White dots represent BSS-ASL algorithm output (generated from Array 1), red and yellow background represents PAM beamformed using both arrays (top right), only using Array 1 (bottom left) or only using Array 2 (bottom right).

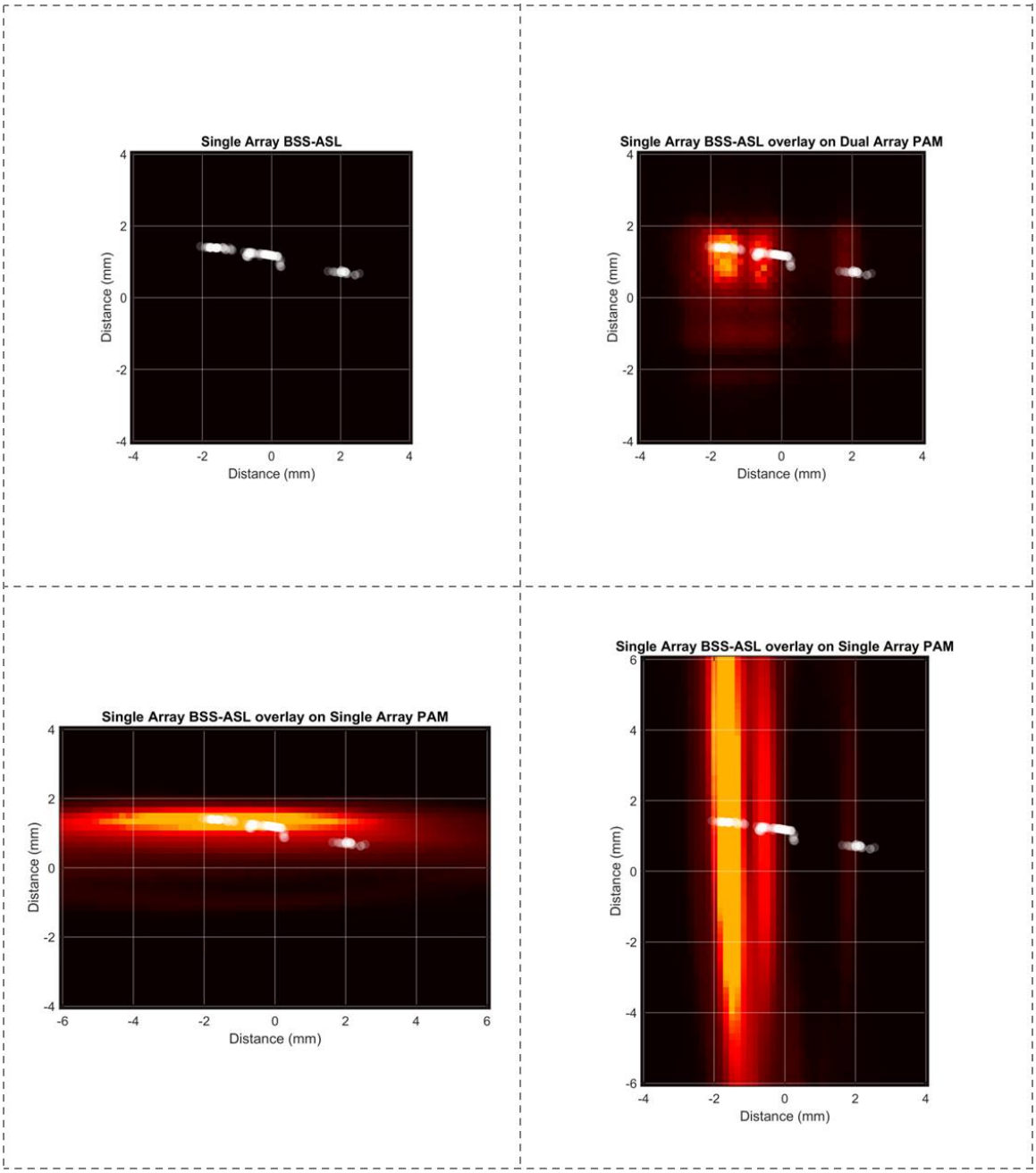


Figure 4.21: Experiment showing three distinct cavitation sources, as identified by dual array PAM. White dots represent BSS-ASL algorithm output (generated from Array 1), red and yellow background represents PAM beamformed using both arrays (top right), only using Array 1 (bottom left) or only using Array 2 (bottom right).

useful in terms of improving speed of execution.

4.8.1 Limitations

At present, the proposed approach has three significant limitations due to the choice of algorithms used in each stage and due to complexities that may arise in practical applications.

4.8.1.1 Choice of ICA Approach

At present, the BSS portion of the algorithm utilises a fairly basic ICA approach, which was selected for this work due to ease of implementation and fast execution time. However there are a number of more advanced ICA algorithms that have the potential to create significant improvements to the BSS-ASL approach. Specifically, the present *fastICA* algorithm is an instantaneous ICA approach, meaning that received signals should arrive approximately at the same time on each receiver. This condition limits the set of elements on which ICA can be performed to the central section of a linear array (for the typical distances used in focussed ultrasound treatments). Thus, although the ICA algorithm can theoretically separate as many signals as there are receivers, the maximum number of sources that can be recovered is in practice limited to the number of elements on which signals arrive simultaneously. For the cases presented in this work, with receivers located approximately 75 mm away from the sources, the number of elements that can be used has been experimentally determined to be 10 to 12.

The maximum number of sources that can be identified can be increased by performing convolutive ICA, which accounts for time delays and multipath signals. Most convolutive ICA approaches are performed in the frequency domain on distinct frequency bins. Although performing ICA in the frequency domain removes the time delay issue, it introduces a problem in the subsequent reconstruction of the signals. As discussed in section 4.5.3, one of the ambiguities in ICA is a permutation ambiguity. This ambiguity creates a significant challenge when trying to align the ICA

output from different frequency bins in order to reconstruct the original signal. Several approaches have been proposed to overcome this, including a merged time-frequency approach [182][115][183], but these approaches are typically computationally complex. Nonetheless, this type of convolutive ICA approach would likely provide significant benefit in terms of signal separation, especially if there is a large number of sources, or if the sources are spread out across fairly large distances.

In the case where additional knowledge about source signal characteristics is known in advance, other BSS models may prove more effective or more computationally efficient than ICA at source separation. Some example models that can be used when additional assumptions are placed on the signals include Second Order Blind Deconvolution methods, for example, those mentioned in Section 4.4.1.

4.8.1.2 Performance in Variable Speed of Sound Conditions

The algorithm has been tested in simulations and experiments where the speed of sound through the media has been relatively constant. However, this is not true when non-homogeneous media is present, for example, in an *in vivo* situation where different layers of tissue have different sound speeds. Two types of errors may occur in this situation. First, if the average speed of sound on the path between each receiver and the source is the same, but different to the overall assumed speed of sound, then the source position will be estimated incorrectly in the axial direction. Second, if the average speed of sound on the path between each receiver and the source is different, then the hyperbolas created between receiver pairs based on the TDOA will not intersect at all, and the error in the position estimate may be large in both the axial and transverse directions.

Before applying the algorithm to an *in vivo* experiment, it is therefore necessary to verify that the algorithm can still suitably localise bubbles in the presence of non-homogeneous media. If performance is significantly decreased then it may be possible to correct for time delay errors by using a layered speed of sound propagation model derived from the depth and composition of tissue layers observed on B-Mode images,

such as a version of the method proposed in [184].

4.8.1.3 Required Level of Independence

The simulation results presented here were generated from the Keller-Miksis model with no explicit bubble-bubble interaction term included. Whilst this simplified model has proven useful for comparing the performance of existing PAM techniques with the proposed algorithm as a proof-of-concept for the algorithm, it does not accurately model reality for a large number of scenarios. Thus a larger simulation study utilising a more computationally complex model that more accurately captures real bubble interactions should be completed.

The results presented from experimental data only utilise dual array PAM to determine the 'true' bubble locations. In practice, there may be multiple bubbles located very close together that appear on PAM maps as a single source. Thus ideally, an optical verification technique should be used to confirm the accuracy of the localisation algorithm, for example, by using a high speed camera with a known nucleation point for the bubbles.

Furthermore, the limitations of when bubbles act as independent sources could also be investigated with an optical technique. As shown by [181], bubbles close together in 'bubble clouds' demonstrate strong bubble-bubble interactions, and may act in phase. This serves to strongly limit the independence of the bubbles, and thus individual sources might not be separable by ICA. However as previously mentioned in section 4.2, the exact level of independence required to allow the algorithm to succeed has not yet been determined, and thus even bubbles that are located close together but act as semi-independent sources might still be separable by ICA. Therefore an important part of future work on this topic should include an investigation into the limit of when the ICA signal separation will fail due to a lack of independence.

4.8.1.4 Geometric Limitations

The method of localisation proposed relies on the idea that there exists relative time delays between receivers, and that the difference in time delays between receiver pairs is not equal. The further away a source is located from the arrays, the more constant the difference in time delays between receivers becomes, and the more difficult it is to estimate the true axial position of the source. In some cases for a distant source, a Direction of Arrival estimate may be made, but true source location cannot be determined.

In addition, the simulations and experiments up to this point have assumed only a 2D plane geometry, when in reality source localisation should be performed in three dimensions. This would require the addition of another array, or another set of elements located in the elevational plane. In a 3D geometry the hyperbolic TDOA position estimator can still be used to determine source location with some slight modifications.

4.8.2 Other Algorithm Improvements

In addition to overcoming the limitations discussed in the previous section, other improvements can also be made to improve performance and decrease computational time.

4.8.2.1 Determination of the Time Delays

In the current version of the algorithm, the time delays for each signal on each element are determined in the time domain by performing cross correlations between re-mixed ICA output signals (with known time delays between them) and the signals received on each element. Although this process is currently parallelised, it is still the most time consuming aspect of the current implementation. Identifying which mixed signal is most correlated with the received signal could be performed in the frequency domain, thereby providing a significant reduction in processing time.

4.8.2.2 Selection and Weighting of Received Signals

Although the hyperbolic location estimator performs relatively well with only a simple method of excluding far outliers, there are also more advanced methods that can be used to improve error rejection. As presented in the results section, the use of elements on the outer edges of the array improves position estimation of sources due to the larger received signal time delays between elements. Thus a more robust implementation of the position estimation will likely provide significant improvements to the accuracy of the algorithm. Once such approach would be to vary the weights in the covariance matrix, Q, in such a manner as to reduce the output variance in a process akin to selecting weights to reduce output variance in adaptive PAM algorithms.

4.8.3 Applications

At present, the proposed algorithm is most suitable for *in vitro* experimentation where the localisation of sources is more important than the energy in an overall region. One such application would be in studying the effects of cavitation on *ex vivo* tissue samples or on *in vitro* cells. In these cases, the accurate localisation of cavitation activity is important in order to assess and correlate any effects seen in the sample with the location of collapsing bubbles.

This type of approach to cavitation localisation may also be used to aid super-resolution imaging. In particular, the estimation of the number of sources and separation procedure may be of assistance in discerning between frames that contain multiple sources and those that do not, thereby enabling the automated selection of suitable frames for super-resolution imaging algorithms. In addition, if an estimate of source location can be determined as a first stage procedure, then it may be possible to deconvolve the PSF of the imaging system in several different overlapping locations of the image in order to recover multiple sources using existing super-resolution techniques.

Finally, the proposed technique may be applicable in cases where accurate localisation is required, but where geometric constraints mean that only a single linear array can be used for cavitation monitoring. This is likely to be the case in clinical settings, and even in some small animal *in vivo* settings. However, as discussed in the limitations section, further improvements and verifications would need to be implemented before the algorithm can be used in an *in vivo* setting.

4.9 Conclusion

In this chapter, a new approach to multi-source cavitation localisation has been presented. The algorithm has two main stages, first to separate and recover signals arising from independent sources, and second, to estimate the time delays of these signals arriving on a receiver in order to localise the source using a TDOA localisation approach. The first part of the algorithm uses a BSS technique known as ICA, which relies on HOS to recover signals. The second part uses a generalised cross correlation approach followed by a localisation estimate using a simple hyperbolic estimator. The algorithm has been tested on noise-free and noisy simulation data, and on experimental data. The BSS-ASL algorithm output for simulations shows good localisation performance, with the ability to localise bubbles to less than 0.3mm on average, with a maximum distance being approximately 0.7mm. In the experimental case, the proposed algorithm, using data from only a single array, shows good agreement with current high resolution PAM techniques that use two perpendicular arrays. The current algorithm is limited in the number of sources that can be separated, and is also limited to a linear array geometry. Future work will aim to address these limitations by using more advanced ICA algorithms, and by extending the possible array geometries to include arbitrary element configurations. Although further testing is necessary to determine the physical limitations of this approach, the proposed algorithm could currently be used in *in vitro* experiments, and may one day be applied for the purpose of high resolution cavitation monitoring in *in vivo* environments.

Chapter 5

Conclusions and Future Work

In many solid tumours, vascularity plays a significant role in tumour progression and response to treatment. The level of vascularity, coupled with the ability of drugs and cells to move between the bloodstream and tumour tissue, can be a source of variability in tumour response to cancer treatments.

As discussed in the introduction, the permeability of vasculature in tumours is highly dependent on the rate of growth of tumours, and the typically rapid angiogenesis required leaves vessel walls extremely underdeveloped. Thus large gaps in the endothelial walls exist enabling large molecules to extravasate passively, or with the assistance of active methods such as focussed ultrasound.

As larger, more complex therapeutics are increasingly deployed in first-line therapies, knowledge of the critical property of vascular permeability to this size range of molecules would be helpful in determining whether drug transport from the bloodstream into tumour tissue is likely. While the transport of therapeutics will depend on factors other than size alone, a global assessment of tumour permeability to nanoparticles could nevertheless provide a useful guide as to the suitability of particular tumours for treatment with nanomedicines or other macromolecular drugs.

The present methods available to assess tumour permeability discussed in the introduction all have significant drawbacks, such as cost and portability, and furthermore are not used to assess permeability of tumour vasculature to large molecules (in the order of hundreds of nanometers).

Developments in the field of non-invasive ultrasound therapy for drug delivery have enabled the creation of solid nanoscale cavitation nuclei, which are able to cross the vascular wall into the tumour tissue itself, and remain stable *in vivo*. The implementation of a non-invasive method of spatio-temporal cavitation monitoring, passive acoustic mapping, has also been a significant development. The aim of the work presented in this thesis was to ascertain whether tumour vessel permeability to large molecules could be assessed using nanoscale cavitation nuclei in conjunction with passive acoustic mapping and source localisation techniques.

In order to address this question, a body of *in vitro* work was performed to assess whether nanoscale cavitation nuclei, once extravasated under ultrasound excitation, could be re-excited using ultrasound. This type of re-excitation regime has not been explored previously. As a secondary aim, the work in the *in vitro* chapter also explored the type of passive acoustic mapping techniques currently available. High resolution mapping of leaky vasculature can provide crucial spatial information regarding tumour composition (for example, leaky versus necrotic regions). Thus the comparison of beamformers was of critical importance in this controlled *in vitro* environment.

The *in vitro* chapter detailed the characterisation of a dual High Intensity Focussed Ultrasound (HIFU) transducer setup, along with a dual linear array setup to improve resolution in PAM. Using this setup, results showed that cavitation nuclei could indeed be re-excited and mapped using PAM, even following ultrasound enhanced extravasation into an agarose gel phantom. This key concept formed the basis of the *in vivo* work presented, and the *in vitro* design was also carried forward into the *in vivo* experiments.

Another key result from the *in vitro* work highlighted the importance of the analysis of nanocup size when considering the choice of acoustic excitation parameters, and set the stage for this discussion to continue into the *in vivo* chapter. In particular, the sonication regime required to re-excite extravasated nanocups should start at the extravasation pressure used on the initial sonication, and should then be increased in order to ensure that smaller size nanocups (which are generally more likely

to extravasate, and which have a higher inertial cavitation threshold) are also re-excited. The discussion of the key relationship between sonication pressure, recorded PAM signal, and size of the cavitation nuclei, which starts in this *in vitro* chapter, is critically important in the subsequent *in vivo* work.

In relation to passive localisation of sources, another useful result from the *in vitro* chapter showed that the best PAM resolution was achieved with adaptive beamformers in conjunction with the largest possible aperture array (two arrays perpendicular to each other). However, when reduced to a single array, an interesting result showed that the best source localisation was achieved with a beamformer based on examining the Higher Order Statistics (HOS) of the signal. Such behaviour illustrated the significant benefit of considering the HOS of signals, especially when reduced to a single array, as may be the case, for example, in a clinical setting. The concept of leveraging the HOS of signals to improve source localisation was carried through from the *in vitro* chapter into the penultimate chapter of this thesis, which focussed solely on improving source localisation based on the HOS of signals.

Chapter 3 then detailed the translation of the concepts tested *in vitro* to an *in vivo* setting. Three key experiments were performed to investigate various aspects of tumour vasculature assessment *in vivo*. The first experiment aimed to replicate the concepts proven *in vitro* as closely as possible. Despite a similar protocol to the *in vitro* work, the complex *in vivo* tumour environment added multiple new variables that resulted in different outcomes to those expected from the *in vitro* work, and the remainder of the chapter was dedicated to investigating these interesting findings.

Principal among them was the result that for mice with bi-lateral tumours, where one tumour had been exposed to an initial sonication ('treated tumour'), the second sonication yielded a higher level of cavitation in the tumour that had not received the initial sonication ('untreated tumour') than in the side that had received the initial sonication. This result was surprising since it was expected that a greater level of extravasation would occur under active ultrasound delivery conditions in the treated tumour. To assess a possible cause of this result, a comparison was drawn between

the probability of cavitation in the experiment and the probability of cavitation for different size nanocups drawn from data published in literature by Kwan *et al.* [82]. This comparison indicated that size range of nanocups that were being excited on the second sonication was approximately 100 - 300 nm, which is less than the mean of the distribution of cups initially injected (200 - 800 nm). This indicated the possibility that the ultrasound exposure at 5% duty cycle has a mechanical effect on the cavitation nuclei that served to increase the ability of the nuclei to passively accumulate in the untreated tumour. For example, a 5% duty cycle treatment could cause fractionation of the cavitation nuclei, resulting in a shift in the size distribution of the cavitation agents that remain in circulation. This effect alone would not serve to explain the phenomenon, but may be a contributing factor. Other biological effects, such as inflammation, and potentially a reduced level of permeability to large molecules on the treated side tumour, may also be contributing factors. A follow-up study to assess this is discussed in Future Work (section 5.1).

Another possible explanation for the low level of cavitation in the treated side versus the untreated side is that exposure of a tumour to ultrasound treatment could alter the structure of the tumour vasculature, and hence ultimately, alter the permeability of the tumour to cavitation nuclei. To investigate this possibility further, a study was designed using AngioSense: a small, fluorescent molecule that circulates in the blood vessels and accumulates in regions that have leaky vasculature at 24 hours post injection. The protocol in this study was similar to that of the previous study and the *in vitro* work. Quantitative fluorescence measurements of AngioSense in the tumour region indicated that neither a reduction, nor an enhancement in permeability was present on the treated side at 24 hours for this small molecule. Crucially though, the cavitation data from this study showed the same results as the cavitation data in the previous study, thereby confirming that passive accumulation is a worthwhile topic to investigate.

Thus a final *in vivo* experiment was performed in order to assess the passive accumulation of nanoscale cavitation nuclei at different developmental stages within a

single tumour line, as well as between tumour lines with different stromal composition. Radiopaque resin perfusions were used to assess the ground truth of the location of vessels within the tumours. Results indicated that for a murine colorectal tumour line, passive accumulation appeared to be present, as evidenced by cavitation within the tumour region at a time well after the nanocups should have been cleared from the vasculature. In addition, when grouped by developmental stage, differences in cavitation levels showed that passive accumulation could be detected in tumours when compared to controls for the normal tumour treatment size.

Furthermore, a comparison between passive accumulation in different tumour lines showed no difference in the cavitation levels between the treatment and control groups for a human pancreatic cell line for the size range tested. Although cavitation on the treated side of the murine colorectal tumours seemed to trend higher than the control for the same size range and tumour line, the difference was not significant. On examination of individual tumour points, a high variability within groups was evident, showing that some tumours did appear to have passive accumulation based on cavitation data, whilst others did not. Further analysis of the micro-CT scans of three of the tumours indicated that all had vessels both surrounding and passing through the tumours, but no other clear differences were present. Further analysis on this data is the subject of future work, discussed in section 5.1.

Another outcome of the passive accumulation study was to assess whether a high resolution dual array setup could be used to map regions of extravasation in a tumour in three dimensions. To evaluate this, PAM maps overlaid on B-Mode images were generated for a series of layers of the tumour, and were then overlaid on a micro-CT image digitally sectioned into the same layers. Results of the final B-Mode/PAM/Micro-CT overlay showed good agreement between tumour vasculature and PAM activity. Whilst the possibility of nanocups still being in circulation exists, if the results seen in the PAM overlay are due to passive accumulation, then a 3D mapping procedure such as the one presented could prove useful in determining regions of cavitation. However, the high resolution dual array setup may not always

be possible in a clinical setting.

Thus in order to overcome the challenge of localising particles using only a single array, a new approach to source localisation based on HOS is presented in Chapter 4. While usual PAM approaches aim to create a map of cavitation energy over a given region, the proposed approach uses a combination of Blind Source Separation (BSS) and Acoustic Source Localisation (ASL) techniques to first recover the signals arising from individual sources before determining the relative time delays between the signals on different elements of a linear array. The BSS approach assumes signal independence, and relies on a surrogate measure of Gaussianity to obtain separated signals. Cross correlation is then used to ascertain the relative time delays between elements, and finally, a simple estimator for hyperbolic location is used to estimate the source position. Simulation results for this approach show good performance for the identification of multiple sources which, crucially, are not usually separable with a single array even using the most advanced PAM algorithms currently available.

The performance of the proposed algorithm on real data is also demonstrated by analysis of simple *in vitro* experimental data. In this case, the single array BSS-ASL output is compared to a high resolution dual array PAM setup, and is able to correctly localise multiple bubbles which again are not usually separable by single array PAM in isolation.

While the algorithm presented shows promise for multi-source localisation, further work is still required before the algorithm can be applied to *in vivo* data, as detailed in Future Work (section 5.1).

Overall, the work in this thesis makes several contributions to the original objective stated: to ascertain whether tumour vessel permeability to large molecules in tumours can be assessed using nanoscale cavitation nuclei in conjunction with passive acoustic mapping and localisation techniques on a clinically relevant scale. Each chapter presented in this thesis contributes to a slightly different aspect of the overall thesis goal. However, some of the results obtained during the course of this work have raised interesting new questions and possibilities. Therefore recommendations for possible

avenues to explore related to this topic are discussed in the next section.

5.1 Future Work

Optimisations and further work can be completed both on the *in vivo* processes, as well as on the passive source mapping and localisation algorithms.

From an *in vivo* perspective, one of the most interesting results from the initial *in vivo* experiment in Chapter 3 was that cavitation levels in an untreated tumour were higher than cavitation levels in a treated tumour following treatment by focussed ultrasound with a 5% duty cycle, with injected nanocscale cavitation nuclei present. One hypothesis for the lower treated tumour cavitation levels is that stabilised nanobubbles are created *in vivo* as a result of a 5% DC cavitation treatment. In order to assess this, a series of *in vitro* experiments would need to be conducted to assess the effect that biological components, such as plasma proteins, may have on gas fragments generated as a result of a 5% DC sonication. In addition, this experiment should also include a comparison of the effects caused by ultrasound excitation at different duty cycles and at different amplitudes in excess of the inertial cavitation threshold of the nanocups. Thereafter, another *in vivo* experiment, with a protocol similar to that of the original experiment performed in Chapter 3 should be completed, but larger animal cohorts and full control groups should be used to assess the *in vivo* effects.

In addition to an investigation into the cause of differences in cavitation data, a further investigation of the effect of cavitation on tumour vasculature should be explored, with specific focus on the effect on permeability of vessels to medium and large molecules (100 - 800 nm in size) following ultrasound treatment. This type of study would be helpful in determining changes to tumour vasculature, as well as assessing whether the size of gaps in tumour vessels is altered as a result of the cavitation of nuclei in the order of 300 - 800 nm. This could be achieved by creating fluorescently labelled nanocups with different fluorescent labels in the size range 100 -

300 nm and 300 - 800 nm, thus enabling a comparison of the relative contributions of these populations to cavitation activity post-extravasation.

Finally, further quantitative analysis of the micro-CT data acquired in the final *in vivo* experiment presented in this thesis may yield interesting results that could be correlated with the level of passive accumulation in tumours. For example, metrics such as average inter-vessel distance, or average vessel mass or diameter could prove interesting parameters for assessment. These metrics could then be correlated to spatial variations in the PAM images on a frame-by-frame basis, particularly if it were possible to achieve improved co-registration of the ultrasound array with the CT data.

In terms of source imaging and localisation, several improvements could be useful for both existing HOS based PAM algorithms and for the proposed BSS-ASL algorithm. One of the largest areas of improvement for the adaptive HOS statistics PAM beamformer would be to perform part of the computation on commercially available, purpose built hardware, or to investigate the use of data minimisation strategies to achieve similar performance at lower computational cost.

In the case of the new BSS-ASL algorithm, several improvements are required to overcome key limitations and improve performance sufficiently before the algorithm can be applied to *in vivo* data. First, an evaluation of the effect of layers of tissue (with different speeds of sound) on the performance of the beamformer needs to be tested in order to determine whether the performance of the algorithm remains sufficient for the purpose of mapping cavitation nuclei. Should the performance degradation be severe, then a model that estimates the speed of sound for each element path should be calculated, ideally from a B-Mode image if possible, in order to streamline the imaging process.

In addition, another significant improvement to the BSS part of the algorithm would be to employ a convolutive BSS model. Whilst this would bring a new set of unique challenges, ultimately, a convolutive model would significantly broaden the range of applications of the algorithm as it would remove the restriction that signals

must arrive simultaneously on receivers. Thus the entire array, rather than just the central elements could be used for processing signals which need to be separated.

Furthermore, to decrease computation time, the cross correlations between elements to determine the signal time delays could be performed in the frequency domain rather than the time domain. This would reduce the computation to a series of Fourier transforms and multiplications, which are significantly faster than performing time domain cross-correlation operations.

Finally, another significant area of work relating to the BSS-ASL algorithm is the verification of the location of cavitation nuclei using an optical method, rather than dual array PAM. An optical method could test whether individual bubbles near to each other are correctly captured on the BSS-ASL algorithm, and may also be used to determine the limits of independence required between bubbles for the BSS algorithm to successfully separate the signals.

The possible directions for future work are numerous, but the areas discussed in this chapter could add significant value to the project if researched further. In time, it may be possible to generate a high resolution spatial map of passive accumulation in tumours, in order to assess tumour vessel leakiness. Such information would be of significant benefit to clinicians as it could aid them with decisions about the approach to tumour treatment, therefore increasing the effectiveness of the selected therapies and potentially decreasing overall treatment costs.

Ultimately, the true benefit of improved diagnostic capabilities is for the cancer patient - an objective that is likely to be worth pursuing well into the future.

Bibliography

[1] M. J. Thun, J. O. DeLancey, M. M. Center, A. Jemal, and E. M. Ward, "The global burden of cancer: Priorities for prevention," *Carcinogenesis*, vol. 31, no. 1, pp. 100–110, 2009.

[2] G. L. G. Miklos, "The Human Cancer Genome Project - One more misstep in the war on cancer," *Nat. Biotechnol.*, vol. 23, no. 5, pp. 535–537, 2005.

[3] J. Ferlay, H. R. Shin, F. Bray, D. Forman, C. Mathers, and D. M. Parkin, "Estimates of worldwide burden of cancer in 2008: GLOBOCAN 2008," *Int. J. Cancer*, vol. 127, no. 12, pp. 2893–2917, 2010.

[4] S. Azzi, J. K. Hebda, and J. Gavard, "Vascular permeability and drug delivery in cancers.," *Front. Oncol.*, vol. 3, no. August, p. 211, 2013.

[5] J. P. B. O'Connor, P. S. Tofts, K. A. Miles, L. M. Parkes, G. Thompson, and A. Jackson, "Dynamic contrast-enhanced imaging techniques: CT and MRI," *Br. J. Radiol.*, vol. 84, no. SPEC. ISSUE 2, 2011.

[6] C. Cuenod and D. Balvay, "Perfusion and vascular permeability: Basic concepts and measurement in DCE-CT and DCE-MRI," *Diagn. Interv. Imaging*, vol. 94, no. 12, pp. 1187–1204, 2013.

[7] P. K. Singh, J. Doley, G. Ravi Kumar, A. P. Sahoo, and A. K. Tiwari, "Oncolytic viruses & their specific targeting to tumour cells," *Indian J. Med. Res.*, vol. 136, no. 4, pp. 571–584, 2012.

[8] J. R. Lindner, "Microbubbles in medical imaging: current applications and future directions.," *Nat. Rev. Drug Discov.*, vol. 3, no. 6, pp. 527–32, 2004.

[9] J. J. Kwan, R. Myers, C. M. Coviello, S. M. Graham, A. R. Shah, E. Stride, R. C. Carlisle, and C. C. Coussios, "Ultrasound-Propelled Nanocups for Drug Delivery," *Small*, vol. 11, no. 39, pp. 5305–5314, 2015.

[10] R. E. Apfel, "Acoustic cavitation prediction," *J. Acoust. Soc. Am.*, vol. 69, no. 6, pp. 1624–1633, 1981.

[11] E. Stride and C. Coussios, "Nucleation, mapping and control of cavitation for drug delivery," *Nat. Rev. Phys.*, vol. 1, no. 8, pp. 495–509, 2019.

[12] G. C. Carter, "Time Delay Estimation for Passive Sonar Signal Processing," *IEEE Trans. Acoust.*, vol. 29, no. 3, pp. 463–470, 1981.

[13] C. H. Farny and R. G. Holt, "Monitoring the development of HIFU-induced cavitation activity," *AIP Conf. Proc.*, vol. 829, no. May, pp. 348–352, 2006.

[14] M. Gyöngy, M. Arora, J. A. Noble, and C. C. Coussios, "Use of Passive Arrays for Characterization and Mapping of Cavitation Activity during HIFU Exposure," in *IEEE Int. Ultrason. Symp.*, pp. 871–874, 2008.

[15] J. W. Baish, T. Stylianopoulos, R. M. Lanning, W. S. Kamoun, D. Fukumura, L. L. Munn, and R. K. Jain, "Scaling rules for diffusive drug delivery in tumor and normal tissues.," *Proc. Natl. Acad. Sci. U. S. A.*, vol. 108, no. 5, pp. 1799–1803, 2011.

[16] A. I. Minchinton and I. F. Tannock, "Drug penetration in solid tumours," *Nat. Rev. Cancer*, vol. 6, no. 8, pp. 583–592, 2006.

[17] V. P. Chauhan and R. K. Jain, "Strategies for advancing cancer nanomedicine.," *Nat. Mater.*, vol. 12, no. 11, pp. 958–62, 2013.

[18] T. H. Maugh, "Chalones: Chemical Regulation of Cell Division," *Science (80-.).*, vol. 176, no. 4042, pp. 1407–1408, 1972.

[19] P. a. Netti, D. a. Berk, M. a. Swartz, a. J. Grodzinsky, and R. K. Jain, "Role of extracellular matrix assembly in interstitial transport in solid tumors," *Cancer Res.*, vol. 60, pp. 2497–2503, 2000.

[20] H. Maeda, "Macromolecular therapeutics in cancer treatment: The EPR effect and beyond," *J. Control. Release*, vol. 164, no. 2, pp. 138–144, 2012.

[21] Y. Matsumura and H. Maeda, "A new concept for macromolecular therapeutics in cnacer chemotherapy: mechanism of tumoritropic accumulatio of proteins and the antitumor agents Smancs," *Cancer Res.*, vol. 46, no. December, pp. 6387– 6392, 1986.

[22] D. Peer, J. M. Karp, S. Hong, O. C. Farokhzad, R. Margalit, and R. Langer, "Nanocarriers as an emerging platform for cancer therapy.," *Nat. Nanotechnol.*, vol. 2, no. 12, pp. 751–760, 2007.

[23] U. Prabhakar, H. Maeda, R. K. Jain, E. M. Sevick-Muraca, W. Zamboni, O. C. Farokhzad, S. T. Barry, A. Gabizon, P. Grodzinski, and D. C. Blakey, "Challenges and key considerations of the enhanced permeability and retention effect for nanomedicine drug delivery in oncology," *Cancer Res.*, vol. 73, no. 8, pp. 2412–2417, 2013.

[24] E. E. Uzgiris, "Tumor microvasculature: endothelial leakiness and endothelial pore size distribution in a breast cancer model.," *Breast Cancer (Auckl).*, vol. 1, pp. 83–90, 2008.

[25] S. K. Hobbs, W. L. Monsky, F. Yuan, W. G. Roberts, V. P. Torchilin, R. K. Jain, W. G. Robertsii, and L. Griffitht, "Regulation of Transport Pathways in Tumor Vessels : Role of Tumor Type and Microenvironment," *Proc. Natl. Acad. Sci. U. S. A.*, vol. 95, 1998.

[26] M. Dellian, F. Yuan, V. S. Trubetskoy, V. P. Torchilin, and R. K. Jain, "Vascular permeability in a human tumour xenograft: molecular charge dependence.," *Br. J. Cancer*, vol. 82, no. 9, pp. 1513–1518, 2000.

[27] J. V. Frangioni, "New technologies for human cancer imaging," *J. Clin. Oncol.*, vol. 26, no. 24, pp. 4012–4021, 2008.

[28] D. M. McDonald and P. L. Choyke, "Imaging of angiogenesis: from microscope to clinic.," *Nat. Med.*, vol. 9, no. 6, pp. 713–725, 2003.

[29] R. Acharya, J. Stevens, R. Wasserman, and C. Hinojosa, "Biomedical Imaging Modalities: A Tutorial," *Comput. Med. Imaging Graph.*, vol. 19, no. I, pp. 3–25, 1995.

[30] D. F. Van Wijk, A. C. Strang, R. Duivenvoorden, D. J. F. Enklaar, R. J. Van Der Geest, J. J. Kastelein, E. De Groot, E. S. Stroes, and A. J. Nederveen, "Increasing spatial resolution of 3T MRI scanning improves reproducibility of carotid arterial wall dimension measurements," *Magn. Reson. Mater. Physics, Biol. Med.*, vol. 27, no. 3, pp. 219–226, 2014.

[31] D. Stucht, K. A. Danishad, P. Schulze, F. Godenschweger, M. Zaitsev, and O. Speck, "Highest resolution in vivo human brain MRI using prospective motion correction," *PLoS One*, vol. 10, no. 7, pp. 1–17, 2015.

[32] J. Budde, G. Shajan, K. Scheffler, and R. Pohmann, "Ultra-high resolution imaging of the human brain using acquisition-weighted imaging at 9.4T," *Neuroimage*, 2014.

[33] A. Jasanoff, "MRI contrast agents for functional molecular imaging of brain activity," *Curr. Opin. Neurobiol.*, vol. 17, no. 5, pp. 593–600, 2007.

[34] E. Karathanasis, L. Chan, L. Karumbaiah, K. McNeeley, C. J. D'Orsi, A. V. Annapragada, I. Sechopoulos, and R. V. Bellamkonda, "Tumor vascular per-

meability to a nanoprobe correlates to tumor-specific expression levels of angiogenic markers," *PLoS One*, vol. 4, no. 6, 2009.

[35] M. K. Kalra, M. M. Maher, T. L. Toth, L. M. Hamberg, M. a. Blake, J.-A. Shepard, and S. Saini, "Strategies for CT radiation dose optimization.," *Radiology*, vol. 230, no. 3, pp. 619–628, 2004.

[36] N. Ahmed, K. Niyaz, A. Borakati, F. Marafi, R. Birk, and S. Usmani, "Hybrid SPECT/CT imaging in the management of differentiated thyroid carcinoma," *Asian Pacific J. Cancer Prev.*, vol. 19, no. 2, pp. 303–308, 2018.

[37] M. M. Khalil, J. L. Tremoleda, T. B. Bayomy, and W. Gsell, "Molecular SPECT Imaging: An Overview," *Int. J. Mol. Imaging*, vol. 2011, pp. 1–15, 2011.

[38] E. Lopci, I. Grassi, A. Chiti, C. Nanni, G. Cicoria, L. Toschi, C. Fonti, F. Lodi, S. Mattioli, and S. Fanti, "PET radiopharmaceuticals for imaging of tumor hypoxia: a review of the evidence.," *Am J Nucl Med Mol Imaging*, vol. 4, no. 4, pp. 365–84, 2014.

[39] M. Solomon, Y. Liu, M. Y. Berezin, and S. Achilefu, "Optical imaging in cancer research: Basic principles, tumor detection, and therapeutic monitoring," *Med. Princ. Pract.*, vol. 20, no. 5, pp. 397–415, 2011.

[40] L. V. Wang, "Prospects of photoacoustic tomography," *Med. Phys.*, vol. 35, no. 12, pp. 5758–5767, 2008.

[41] S. Hu and L. V. Wang, "Photoacoustic imaging and characterization of the microvasculature," *J. Biomed. Opt.*, vol. 15, no. 1, p. 011101, 2010.

[42] C. Harvey, J. Pilcher, R. Eckersley, M. Blomley, and D. Cosgrove, "Advances in ultrasound," *Clin. Radiol.*, vol. 57, pp. 157–177, 2001.

[43] N. Reznik, R. Williams, and P. N. Burns, "Investigation of Vaporized Submicron Perfluorocarbon Droplets as an Ultrasound Contrast Agent," *Ultrasound Med. Biol.*, vol. 37, no. 8, pp. 1271–1279, 2011.

[44] T. O. Matsunaga, P. S. Sheeran, S. Luois, J. E. Streeter, L. B. Mullin, B. Banerjee, and P. A. Dayton, "Phase-Change nanoparticles using highly volatile perfluorocarbons: Toward a platform for extravascular ultrasound imaging," *Theranostics*, vol. 2, no. 12, pp. 1185–1198, 2012.

[45] P. Sheeran, J. Streeter, L. Mullin, T. Matsunaga, and P. Dayton, "Toward Ultrasound Molecular Imaging with Phase-Change Contrast Agents: An In-Vitro Proof-of-Principle," *Ultrasound Med. Biol.*, vol. 39, 2013.

[46] J. Y. Lee, D. Carugo, C. Crake, J. Owen, M. De Saint Victor, A. Seth, C. Coussios, and E. Stride, "Nanoparticle-Loaded Protein-Polymer Nanodroplets for Improved Stability and Conversion Efficiency in Ultrasound Imaging and Drug Delivery," *Adv. Mater.*, vol. 27, no. 37, pp. 5484–5492, 2015.

[47] L. Zhu, H. Zhao, Z. Zhou, Y. Xia, Z. Wang, H. Ran, P. Li, and J. Ren, "Peptide-Functionalized Phase-Transformation Nanoparticles for Low Intensity Focused Ultrasound-Assisted Tumor Imaging and Therapy," *Nano Lett.*, vol. 18, no. 3, pp. 1831–1841, 2018.

[48] G. Zhang, S. Harput, S. Lin, K. Christensen-Jeffries, C. H. Leow, J. Brown, C. Dunsby, R. J. Eckersley, and M. X. Tang, "Acoustic wave sparsely activated localization microscopy (AWSALM): Super-resolution ultrasound imaging using acoustic activation and deactivation of nanodroplets," *Appl. Phys. Lett.*, vol. 113, no. 1, 2018.

[49] P. S. Sheeran and P. A. Dayton, "Improving the Performance of Phase-Change Perfluorocarbon Droplets for Medical Ultrasonography: Current Progress, Challenges, and Prospects," *Scientifica (Cairo).*, vol. 2014, pp. 1–24, 2014.

[50] H. S. Min, S. Son, T. W. Lee, H. Koo, H. Y. Yoon, J. H. Na, Y. Choi, J. H. Park, J. Lee, M. H. Han, R. W. Park, I. S. Kim, S. Y. Jeong, K. Rhee, S. H. Kim, I. C. Kwon, and K. Kim, "Liver-specific and echogenic hyaluronic acid nanoparticles facilitating liver cancer discrimination," *Adv. Funct. Mater.*, vol. 23, no. 44, pp. 5518–5529, 2013.

[51] H. Feigenbaum, J. M. Stone, A. Don, and W. K. Nasser, "Identification of Ultrasound Echoes from the Left Ventricle by Use of Intracardiac Injections of Indocyanine Green," *Circulation*, vol. 41, no. 4, 1970.

[52] P. A. Dijkmans, L. J. M. Juffermans, R. J. P. Musters, A. V. Wamel, F. J. Cate, W. V. Gilst, C. A. Visser, N. D. Jong, and O. Kamp, "Microbubbles and ultrasound : from diagnosis to therapy," *Echocardiography*, vol. 5, no. November, pp. 245–256, 2004.

[53] J. E. Kennedy, F. Wu, G. R. Ter Haar, F. V. Gleeson, R. R. Phillips, M. R. Middleton, and D. Cranston, "High-intensity focused ultrasound for the treatment of liver tumours," *Ultrasonics*, vol. 42, no. 1-9, pp. 931–935, 2004.

[54] S. Datta, C. C. Coussios, L. E. McAdory, J. Tan, T. Porter, G. De Courten-Myers, and C. K. Holland, "Correlation of cavitation with ultrasound enhancement of thrombolysis," *Ultrasound Med. Biol.*, vol. 32, no. 8, pp. 1257–1267, 2006.

[55] R. Carlisle, J. Choi, M. Bazan-Peregrino, R. Laga, V. Subr, L. Kostka, K. Ulbrich, C.-C. Coussios, and L. W. Seymour, "Enhanced Tumor Uptake and Penetration of Virotherapy Using Polymer Stealthing and Focused Ultrasound," *JNCI J. Natl. Cancer Inst.*, vol. 105, no. 22, pp. 1701–1710, 2013.

[56] K. Hynynen, N. McDannold, N. A. Sheikov, F. A. Jolesz, and N. Vykhodtseva, "Local and reversible blood-brain barrier disruption by noninvasive fo-

cused ultrasound at frequencies suitable for trans-skull sonications," *Neuroimage*, vol. 24, no. 1, pp. 12–20, 2005.

[57] S. Mitragotri, D. Blankschtein, and R. Langer, "Ultrasound-mediated transdermal protein delivery," *Science (80-.).*, vol. 269, no. 5225, pp. 850–853, 1995.

[58] C. C. Coussios and R. A. Roy, "Applications of Acoustics and Cavitation to Noninvasive Therapy and Drug Delivery," *Annu. Rev. Fluid Mech.*, vol. 40, no. 1, pp. 395–420, 2008.

[59] M. Gyöngy and C. C. Coussios, "Passive cavitation mapping for localization and tracking of bubble dynamics," *J. Acoust. Soc. Am.*, vol. 128, no. 4, pp. EL175–EL180, 2010.

[60] F. Caupin and E. Herbert, "Cavitation in water: a review," *Comptes Rendus Phys.*, vol. 7, no. 9-10, pp. 1000–1017, 2006.

[61] K. B. Bader, E. Vlaisavljevich, and A. D. Maxwell, "For Whom the Bubble Grows: Physical Principles of Bubble Nucleation and Dynamics in Histotripsy Ultrasound Therapy," *Ultrasound Med. Biol.*, vol. 45, no. 5, pp. 1056–1080, 2019.

[62] T. G. Leighton, "Chapter 9 - Principles of Cavitation," in *Ultrasound Food Process.* (Povey, M.J.W. and T. Mason, eds.), pp. 151–182, 1997.

[63] R. Apfel and C. Holland, "Gauging The Likelihood of Cavitation from Short-Pulse, Low-Duty Cycle Diagnostic Ultrasound," *Ultrasound Med. Biol.*, vol. 17, no. 2, pp. 179–185, 1991.

[64] P. R. Birkin, D. G. Offin, and T. G. Leighton, "Experimental and theoretical characterisation of sonochemical cells.," *Phys. Chem. Chem. Phys.*, vol. 7, pp. 530–537, 2005.

[65] S. Meairs and A. Alonso, "Ultrasound, microbubbles and the blood-brain barrier," *Prog. Biophys. Mol. Biol.*, vol. 93, no. 1-3, pp. 354–362, 2007.

[66] M. Gyöngy, M. Arora, J. a. Noble, and C. C. Coussios, "Use of passive arrays for characterization and mapping of cavitation activity during hifu exposure," *Proc. - IEEE Ultrason. Symp.*, pp. 871–874, 2008.

[67] C. C. Church, "Spontaneous homogeneous nucleation, intertial cavitation and the safety of diagnostic ultrasound," *Untrasound Med. Biol.*, vol. 28, no. 10, pp. 1349–1364, 2002.

[68] S. Vaezy, X. Shi, R. W. Martin, E. Chi, P. I. Nelson, M. R. Bailey, and L. A. Crum, "Real-time visualization of high-intensity focused ultrasound treatment using ultrasound imaging," *Ultrasound Med Biol*, vol. 27, no. 1, pp. 33–42, 2001.

[69] K. Hynynen, O. Pomeroy, D. N. Smith, P. E. Huber, N. J. McDannold, J. Kettenbach, J. Baum, S. Singer, and F. A. Jolesz, "MR Imaging-guided Focused Ultrasound Surgery of Fibroadenomas in the Breast: A Feasibility Study," *Radiology*, vol. 219, no. 1, pp. 176–185, 2001.

[70] A. A. Atchley, L. A. Frizzell, R. E. Apfel, C. K. Holland, S. Madanshetty, and R. A. Roy, "Thresholds for cavitation produced in water by pulsed ultrasound," *Ultrasonics*, vol. 26, no. 5, pp. 280–285, 1988.

[71] C. H. Farny, R. G. Holt, and R. A. Roy, "Temporal and Spatial Detection of HIFU-Induced Inertial and Hot-Vapor Cavitation with a Diagnostic Ultrasound System," *Ultrasound Med. Biol.*, vol. 35, no. 4, pp. 603–615, 2009.

[72] V. A. Salgaonkar, S. Datta, C. K. Holland, and T. D. Mast, "Passive cavitation imaging with ultrasound arrays," *J. Acoust. Soc. Am.*, vol. 126, no. 6, pp. 3071–3083, 2009.

[73] K. J. Haworth, T. D. Mast, K. Radhakrishnan, M. T. Burgess, J. A. Kopechek, S.-L. Huang, D. D. McPherson, and C. K. Holland, "Passive imaging with

pulsed ultrasound insonations," *J. Acoust. Soc. Am.*, vol. 132, no. 1, pp. 544–553, 2012.

[74] C. M. Coviello, R. J. Kozick, A. Hurrell, P. Smith, and C. C. Coussios, "Thin-film sparse boundary array design for passive acoustic mapping during ultrasound therapy," *IEEE Trans. Ultrason. Ferroelectr. Freq. Control*, vol. 59, no. 10, pp. 2322–2330, 2012.

[75] C. Coviello, R. Kozick, J. Choi, M. Gyongy, C. Jensen, P. P. Smith, and C.-C. Coussios, "Passive acoustic mapping utilizing optimal beamforming in ultrasound therapy monitoring," *JASA*, 2014.

[76] C. D. Arvanitis, C. Crake, N. McDannold, and G. T. Clement, "Passive Acoustic Mapping with the Angular spectrum method," *IEEE Trans. Med. Imaging*, vol. 36, no. 4, pp. 983–993, 2016.

[77] S. Lu, R. Li, X. Yu, D. Wang, and M. Wan, "Delay multiply and sum beamforming method applied to enhance linear-array passive acoustic mapping of ultrasound cavitation," *Med. Phys.*, 2019.

[78] E. Lyka, C. M. Coviello, C. Paverd, M. D. Gray, and C. C. Coussios, "Passive Acoustic Mapping Using Data-Adaptive Beamforming Based on Higher Order Statistics," *IEEE Trans. Med. Imaging*, vol. 37, no. 12, pp. 2582–2592, 2018.

[79] M. D. Gray, E. Lyka, and C. C. Coussios, "Diffraction Effects and Compensation in Passive Acoustic Mapping," *IEEE Trans. Ultrason. Ferroelectr. Freq. Control*, vol. 65, no. 2, pp. 258–268, 2018.

[80] Miklós Gyöngy, *Passive cavitation mapping for monitoring ultrasound therapy.* PhD thesis, 2010.

[81] S. Sirsi and M. Borden, "Microbubble Compositions, Properties and Biomedical Applications," *Bubble Sci Eng Tech*, vol. 71, pp. 165–169, 2009.

[82] J. J. Kwan, S. Graham, R. Myers, R. Carlisle, E. Stride, and C. Coussios, "Ultrasound-induced inertial cavitation from gas-stabilizing nanoparticles," *Phys. Rev. E*, vol. 023019, no. August, pp. 1–5, 2015.

[83] J. Kwan, G. Lajoinie, N. de Jong, E. Stride, M. Versluis, and C. Coussios, "Ultra High Speed Dynamics of Micron Sized Inertial Cavitation from Nanoparticles,"

[84] G. Lemperle, "Biocompatibility of Injectable Microspheres," *Biomed. J. Sci. Tech. Res.*, vol. 2, no. 1, 2018.

[85] M. Bazan-Peregrino, C. D. Arvanitis, B. Rifai, L. W. Seymour, and C. C. Coussios, "Ultrasound-induced cavitation enhances the delivery and therapeutic efficacy of an oncolytic virus in an in vitro model," *J. Control. Release*, vol. 157, no. 2, pp. 235–242, 2012.

[86] M. Bazan-Peregrino, B. Rifai, R. C. Carlisle, J. Choi, C. D. Arvanitis, L. W. Seymour, and C. C. Coussios, "Cavitation-enhanced delivery of a replicating oncolytic adenovirus to tumors using focused ultrasound," *J. Control. Release*, vol. 169, no. 1-2, pp. 40–47, 2013.

[87] S. Bhatnagar, J. J. Kwan, A. R. Shah, C.-c. Coussios, and R. C. Carlisle, "Exploitation of sub-micron cavitation nuclei to enhance ultrasound-mediated transdermal transport and penetration of vaccines," *J. Control. Release*, vol. 238, pp. 22–30, 2016.

[88] K. Zell, J. I. Sperl, M. W. Vogel, R. Niessner, and C. Haisch, "Acoustical properties of selected tissue phantom materials for ultrasound imaging.," *Phys. Med. Biol.*, vol. 52, no. 20, pp. N475–84, 2007.

[89] J. Narayanan, J.-Y. Xiong, and X.-Y. Liu, "Determination of agarose gel pore size: Absorbance measurements vis a vis other techniques," *J. Phys. Conf. Ser.*, vol. 28, no. 1, pp. 83–86, 2006.

[90] P. S. Sheeran, J. D. Rojas, C. Puett, J. Hjelmquist, C. B. Arena, and P. a. Dayton, "Contrast-enhanced ultrasound imaging and in vivo circulatory kinetics with low-boiling-point nanoscale phase-change perfluorocarbon agents," *Ultrasound Med. Biol.*, vol. 41, no. 3, pp. 814–831, 2015.

[91] R. Myers, *Ultrasound - enhanced delivery of therapeutic agent s to tumours using submicron cavitation nuclei*. PhD thesis, 2015.

[92] T. Ridler and S. Calvard, "Picture Thresholding Using," *IEEE Trans. Syst. Man Cybern.*, vol. smc-8, no. 8, pp. 630–632, 1978.

[93] X. Jiang, W. J. Zeng, A. Yasotharan, H. C. So, and T. Kirubarajan, "Robust beamforming by linear programming," *IEEE Trans. Signal Process.*, vol. 62, no. 7, pp. 1834–1849, 2014.

[94] J. Keller and M. Miksis, "Bubble Oscillations of Large Amplitude," *J. Acoust. Soc. Am.*, pp. 461–468, 1980.

[95] J. R. T. Collin and C. C. Coussios, "Quantitative observations of cavitation activity in a viscoelastic medium," *J. Acoust. Soc. Am.*, vol. 130, no. 5, pp. 3289–3296, 2011.

[96] H. Lea-Banks, B. Teo, E. Stride, and C. C. Coussios, "The effect of particle density on ultrasound-mediated transport of nanoparticles," *Phys. Med. Biol.*, vol. 61, pp. 7906–7918, oct 2016.

[97] C. Mannaris, L. Bau, M. Grundy, M. Gray, H. Lea-Banks, A. Seth, B. Teo, R. Carlisle, E. Stride, and C. C. Coussios, "Microbubbles, Nanodroplets and Gas-Stabilizing Solid Particles for Ultrasound-Mediated Extravasation of Unencapsulated Drugs: An Exposure Parameter Optimization Study," *Ultrasound Med. Biol.*, vol. 45, no. 4, pp. 954–967, 2019.

[98] V. P. Chauhan, T. Stylianopoulos, J. D. Martin, Z. PopoviÄ, O. Chen, W. S. Kamoun, M. G. Bawendi, D. Fukumura, and R. K. Jain, "Normalization of

tumour blood vessels improves the delivery of nanomedicines in a size-dependent manner," *Nat. Nanotechnol.*, vol. 7, no. 6, pp. 383–388, 2012.

[99] M. R. Junttila and F. J. De Sauvage, "Influence of tumour micro-environment heterogeneity on therapeutic response," *Nature*, vol. 501, no. 7467, pp. 346–354, 2013.

[100] A. Jackson, J. P. B. O'Connor, G. J. M. Parker, and G. C. Jayson, "Imaging tumor vascular heterogeneity and angiogenesis using dynamic contrast-enhanced magnetic resonance imaging," *Clin. Cancer Res.*, vol. 13, no. 12, pp. 3449–3459, 2007.

[101] F. Yuan, M. Dellian, D. Fukumura, M. Leunig, D. A. Berk, V. P. Torchilin, and R. K. Jain, "Vascular Permeability in a Human Tumor Xenograft: Molecular Size Dependence and Cutoff Size1," *Cancer Res.*, pp. 3752–3757, 1995.

[102] F. Yuan, M. Leunig, S. K. Huang, D. a. Berk, D. Papahadjopoulos, and R. K. Jam, "Mirovascular Permeability and Interstitial Penetration of Sterically Stabilized (Stealth) Liposomes in a Human Tumor Xenograft," *Cancer Res.*, no. n 12, pp. 3352–3356, 1994.

[103] W. L. Monsky, D. Fukumura, T. Gohongi, F. Yuan, and R. K. Jain, "Augmentation of Transvascular Transport of Macromolecules and Nanoparticles in Tumors Using Vascular Endothelial Growth Factor Augmentation of Transvascular Transport of Macromolecules and Nanoparticles in Tumors Using Vascular Endothelial Growth Factor 1," *Cancer Res.*, pp. 4129–4135, 1999.

[104] H. Hashizume, P. Baluk, S. Morikawa, J. W. McLean, G. Thurston, S. Roberge, R. K. Jain, and D. M. McDonald, "Openings between defective endothelial cells explain tumor vessel leakiness," *Am. J. Pathol.*, vol. 156, no. 4, pp. 1363–1380, 2000.

[105] J. Folkman, "Tumor Angiogenesis Factor," *Cancer Res.*, no. AUGUST, pp. 2109–2113, 1974.

[106] J. Folkman, "Angiogenesis in cancer, vascular rheumatoid and other disease," *Nat. Med.*, vol. 1, no. 5, pp. 1–6, 1995.

[107] S. R. Gordon, R. L. Maute, B. W. Dulken, G. Hutter, B. M. George, M. N. McCracken, R. Gupta, J. M. Tsai, R. Sinha, D. Corey, A. M. Ring, A. J. Connolly, and I. L. Weissman, "PD-1 expression by tumour-associated macrophages inhibits phagocytosis and tumour immunity," *Nature*, vol. 545, no. 7655, pp. 495–499, 2017.

[108] R. Myers, C. Coviello, P. Erbs, J. Foloppe, C. Rowe, J. Kwan, C. Crake, S. Finn, E. Jackson, J.-m. Balloul, C. Story, C. Coussios, and R. Carlisle, "Polymeric Cups for Cavitation-mediated Delivery of Oncolytic Vaccinia Virus," *Mol. Ther.*, vol. 24, no. 9, pp. 1627–1633, 2016.

[109] M. Konerding, A. Miodonski, and A. Lametschwandtner, "Microvasculature Corrosion Casting in the Study of Tumour Vascularit: A Review," *Scanning Microsc.*, vol. 9, no. 4, pp. 1233–1243, 1995.

[110] F. D. Verli, T. R. Rossi-Schneider, F. L. Schneider, L. S. Yurgel, and M. A. L. De Souza, "Vascular corrosion casting technique steps," *Scanning*, vol. 29, no. 3, pp. 128–132, 2007.

[111] J. Forster, W. Harriss-Phillips, M. Douglass, and E. Bezak, "A review of the development of tumor vasculature and its effects on the tumor microenvironment," *Hypoxia*, vol. Volume 5, pp. 21–32, 2017.

[112] A. Falanga and M. Marchetti, "Hemostatic biomarkers in cancer progression," *Thromb. Res.*, vol. 164, no. December 2017, pp. S54–S61, 2018.

[113] K. R. Sahana, P. Akila, V. Prashant, B. S. Chandra, and M. N. Suma, "Quantitation of vascular endothelial growth factor and interleukin-6 in different stages of breast cancer," *Reports Biochem. Mol. Biol.*, vol. 6, no. 1, pp. 32–38, 2017.

[114] K. Yasui, T. Tuziuti, J. Lee, T. Kozuka, A. Towata, and Y. Iida, "Ultrasonics Sonochemistry Numerical simulations of acoustic cavitation noise with the temporal fluctuation in the number of bubbles," vol. 17, pp. 460–472, 2010.

[115] A. Hyvärinen, J. Karhunen, and E. Oja, "Independent Component Analysis," *Appl. Comput. Harmon. Anal.*, vol. 21, no. 1, pp. 135–144, 2001.

[116] N. Madhu and R. Martin, "Acoustic source localization using microphone arrays," in *Adv. Digit. Speech Transm.* (R. Martin, U. Heute, and C. Antweiler, eds.), 2008.

[117] S. A. Vorobyov, *Adaptive and Robust Beamforming*, vol. 3. Elsevier Ltd, 2014.

[118] S. Lu, A. Shi, B. Jing, X. Du, and M. Wan, "Real-time monitoring of controllable cavitation erosion in a vessel phantom with passive acoustic mapping," *Ultrason. Sonochem.*, vol. 39, no. April, pp. 291–300, 2017.

[119] K. J. Haworth, K. B. Bader, K. T. Rich, C. K. Holland, and T. D. Mast, "Quantitative frequency-domain passive cavitation imaging," *IEEE Trans. Ultrason. Ferroelectr. Freq. Control*, vol. 64, no. 1, pp. 177–191, 2017.

[120] S. H. Abadi, K. J. Haworth, K. P. Mercado-Shekhar, and D. R. Dowling, "Frequency-sum beamforming for passive cavitation imaging," *J. Acoust. Soc. Am.*, vol. 144, no. 1, pp. 198–209, 2018.

[121] S. J. Norton and I. J. Won, "Time Exposure Acoustics," *IEEE Trans. Geosci. Remote Sens.*, vol. 38, no. 3, pp. 1337–1343, 2000.

[122] P. Boulos, F. Varray, A. Poizat, A. Ramalli, B. Gilles, J. C. Bera, and C. Cachard, "Weighting the passive acoustic mapping technique with the phase

coherence factor for passive ultrasound imaging of ultrasound-induced cavitation," *IEEE Trans. Ultrason. Ferroelectr. Freq. Control*, vol. 65, no. 12, pp. 2301–2310, 2018.

[123] M. D. Gray and C. C. Coussios, "Broadband Ultrasonic Attenuation Estimation and Compensation with Passive Acoustic Mapping," *IEEE Trans. Ultrason. Ferroelectr. Freq. Control*, vol. 65, no. 11, pp. 1997–2011, 2018.

[124] J. H. DiBiase, H. F. Silverman, and M. S. Brandstein, "Robust Localization in Reverberant Rooms," pp. 157–180, 2001.

[125] C. Errico, J. Pierre, S. Pezet, Y. Desailly, Z. Lenkei, O. Couture, and M. Tanter, "deep super-resolution vascular imaging," *Nature*, vol. 527, no. 7579, pp. 499–502, 2015.

[126] K. Christensen-jeffries, J. Brown, S. Member, P. Aljabar, M. Tang, C. Dunsby, R. J. Eckersley, and S. Member, "Super-Resolved Velocity Mapping Using Microbubbles," *IEEE Trans. Ultrason. Ferroelectr. Freq. Control*, vol. 64, no. 10, pp. 1478–1486, 2017.

[127] K. Diamantis, A. H. Greenaway, T. Anderson, J. A. Jensen, P. A. Dalgarno, and V. Sboros, "Super-resolution axial localization of ultrasound scatter using multi-focal imaging," *IEEE Trans. Biomed. Eng.*, vol. 65, no. 8, pp. 1840–1851, 2018.

[128] M. A. O'Reilly and K. Hynynen, "A super-resolution ultrasound method for brain vascular mapping," *Med. Phys.*, vol. 40, no. 11, p. 110701, 2013.

[129] I. K. Holfort, F. Gran, and J. A. Jøensen, "Broadband minimum variance beamforming for ultrasound imaging," *IEEE Trans. Ultrason. Ferroelectr. Freq. Control*, vol. 56, no. 2, pp. 314–325, 2009.

[130] P. Milanfar, *Super-Resolution Imaging.* CRC Press, 1st ed., 2010.

[131] R. Schmidt, *A Signal Subspace Approach to Multiple Emitter Location and Spectral Estimation*. PhD thesis, Stanford University, 1981.

[132] R. Roy and T. Kailath, "ESPRIT-estimation of signal parameters via rotational invariance techniques," *IEEE Trans. Acoust.*, vol. 37, no. 7, pp. 984–995, 1989.

[133] M. A. T. Wax, T.-j. Shan, and T. Kailath, "Spatio-Temporal Spectral Analysis by Eigenstructure Methods," *IEEE Trans. Acoust. Speech Signal Process.*, no. 4, 1984.

[134] G. Su and M. Morf, "The Signal Subspace Approach for Multiple Wide-Band Emitter Location," *IEEE Trans. Acoust. Speech Signal Process.*, no. 6, pp. 1502–1522, 1983.

[135] T. G. Dvorkind and S. Gannot, "Time Difference of Arrival Estimation of Speech Source in a Noisy and Reverberant Environment," *Signal Processing*, no. October, 2003.

[136] A. Brutti, M. Omologo, P. Svaizer, I. Trentino, and V. Sommarive, "Oriented global coherence field for the estimation of the head orientation in smart rooms equipped with distributed microphone arrays," in *INTERSPEECH*, pp. 2337–2340, 2005.

[137] J. Chen, Y. Huang, and J. Benesty, "An adaptive blind SIMO identification approach to joint multichannel time delay estimation," *ICASSP, IEEE Int. Conf. Acoust. Speech Signal Process. - Proc.*, vol. 4, 2004.

[138] W. Foy, "Position Location Solutions by Taylor-Series Estimation," *IEEE Trans. Aerosp. Electron. Syst.*, no. 2, pp. 187–194, 1976.

[139] H. Schau and A. Robinson, "Passive Source Localization Employing Intersecting Spherical Surfaces from Time-of-Arrival Differences," *IEEE Trans. Acoust. Speech Signal Process.*, no. 8, 1987.

[140] Y. T. Chan and K. C. Ho, "A Simple and Efficient Estimator for Hyperbolic Location," *IEEE Trans. Signal Process.*, vol. 42, no. 8, pp. 1905–1915, 1994.

[141] Y. Huang, J. Benesty, G. W. Elko, and R. M. Mersereau, "Real-time passive source localization: A practical linear-correction least-squares approach," *IEEE Trans. Speech Audio Process.*, vol. 9, no. 8, pp. 943–956, 2001.

[142] J. C. Chen, R. E. Hudson, and K. Yao, "Maximum-likelihood source localization and unknown sensor location estimation for wideband signals in the near-field," *IEEE Trans. Signal Process.*, vol. 50, no. 8, pp. 1843–1854, 2002.

[143] C. Jutten, "Source separation: From Dusk till Dawn," in *2nd Intl Worskshop ICA*, pp. 15–26, 2000.

[144] G. Bienvenu and L. Kopp, "Optimality of High Resolution Array Processing Using the Eigensystem Approach," *IEEE Trans. Acoust. Speech Signal Process.*, vol. 31, no. 5, 1983.

[145] J. Herault, C. Jutten, and B. Ans, "Circuits neuronaux à synapses modifiables: décodage de messages composites para apprentissage non supervise," in *C.R. l'Academie des Sci.*, pp. 525–528, 1984.

[146] J. Herault, C. Jutten, and B. Ans, "Detection de grandeurs primitives dans un message composite par une architecture de calcul neuromimetique en apprentissage non supervise.," *Actes du Xeme Colloq. GRETSI*, pp. 1017–1022, 1985.

[147] J. Herault and C. Jutten, "Space or time adaptive signal processing by neural network models," in *AIP Conf. Proc.*, vol. 151, 1986.

[148] J.-F. Cardoso, "Blind Identificaiton of Independent Sginals.pdf," in *Work. High. Order Spectr. Anal.*, 1989.

[149] P. Comon, "Separation of Stochastic Processes," in *Work. High. Order Spectr. Anal.*, 1989.

[150] J.-L. Lacoume and P. Ruiz, "Sources Identificaiton: A Solution Based On Cumulants," in *IEEE ASSP Work.*, 1988.

[151] G. Burel, "Blind Separation of Sources : A Nonlinear Neural Algorithm," vol. 5, pp. 937–947, 1992.

[152] A. Cichocki, R. Unbehauen, and E. Rummert, "Robust learning algorithm for blind separation of signals .," *IEEE Electron. Lett.*, vol. 30, no. 17, pp. 1386–1387, 1994.

[153] A. Cichocki and R. Unbehauen, "Robust Neural Networks with On-Line Learning for Blind Identification and Blind Separation of Sources," *IEEE Trans. Circuits Syst.*, vol. 43, no. 11, pp. 894–906, 1996.

[154] A. J. Bell and T. J. Sejnowski, "An information-maximisation approach to blind separation and blind deconvolution," Tech. Rep. February 1995, 1995.

[155] S. Choi, A. Cichocki, H.-M. Park, and S.-Y. Lee, "Blind Source Separation and Independent Component Analysis : A Review," *Neural Informait. Process.*, vol. 6, no. 1, pp. 1–57, 2005.

[156] A. Hyvärinen, "Independent component analysis : recent advances Subject Areas :," *Phil. Trans. R. Soc. A*, 2012.

[157] M. S. Pedersen, J. Larsen, U. Kjems, and L. C. Parra, "A Survey of Convolutive Blind Source Separation Methods," *Speech Commun.*, pp. 1–34, 2007.

[158] P. Comon and C. Jutten, *Handbook of Blind Source Separation: Independent Component Analysis and Applications*. 2010.

[159] D. W. E. Schobben and P. C. W. Sommen, "On the indeterminacies of convolutive blind signal separation based on second order statistics," *ISSPA 1999 - Proc. 5th Int. Symp. Signal Process. Its Appl.*, vol. 1, no. 2, pp. 215–218, 1999.

[160] E. Weinstein, M. Feder, and A. Oppenheim, "Multi-Channel Signal Separation by Decorrelation," *IEEE Trans. Acoust. Speech Audio Process.*, vol. 1, no. 4, pp. 405–413, 1993.

[161] A. Souloumiac, "Blind Source Detection and Separation Using Second Order Non-Stationarity," in *Int. Conf. Acoust. Speech, Signal Process.*, 1995.

[162] H.-c. Wu and J. C. Principe, "Simultaneous Diagonalization in the Frequency Domain (SDIF) for Source Separation," in *ICA'99*, no. 1, pp. 1–6.

[163] S. Schell and W. Gardner, "Maximum likelihood and common factor analysis-based blind adaptive spatial filtering for cyclostationary signals," pp. 292–295 vol.4, 2002.

[164] I. Bradaric, A. P. Petropulu, and K. I. Diamantaras, "On blind identifiability of FIR-MIMO systems with cyclostationary inputs using second order statistics," *IEEE Trans. Signal Process.*, vol. 51, no. 2, pp. 434–441, 2003.

[165] K. Abed-Meraim, Y. Xiang, and Y. Hua, "Blind source separation using second-order cyclostationary statistics," *IDC 1999 - 1999 Information, Decis. Control. Data Inf. Fusion Symp. Signal Process. Commun. Symp. Decis. Control Symp. Proc.*, vol. 49, no. 4, pp. 321–326, 1999.

[166] L. Tong, V. Soon, Y. Huang, and R. Liu, "AMUSE A New Blind Identification Algorithm," *Proc. IEEE ISCAS*, vol. 3, 1990.

[167] A. Belouchrani, K. Abed-Meraim, J. F. Cardoso, and E. Moulines, "A blind source separation technique using second-order statistics," *IEEE Trans. Signal Process.*, vol. 45, no. 2, pp. 434–444, 1997.

[168] T. Lee, M. Lewicki, M. Girolami, and T. Sejnowski, "Blind source separation of more sources than mixtures using overcomplete representations," *Pattern Recognit. Lett.*, vol. 26, no. 16, pp. 2491–2499, 1999.

[169] F. Abrard, Y. Deville, and P. White, "From blind source separation to blind source cancellation in the underdetermined case: a new approach based on time-frequency analysis," *Proc. Int. Conf. Indep. Compon. Anal. Blind Source Sep.*, no. 2, pp. 734–739, 2001.

[170] S. Gribonval, Rémi;Lesage, "A survey of Sparse Component Analysis for Blind Source Separation: principles, perspectives, and new challenges," *Eur. Symp. Artif. Neural Networks*, no. April, pp. 323–330, 2006.

[171] A. Jourjine, F. Hall, and W. Road, "Blind Separation of Disjoint Orthogonal Signals: Demixing N Sources from 2 Mixtures," in *ICASSP, IEEE Int. Conf. Acoust. Speech Signal Process. - Proc.*, pp. 2985–2988, 2000.

[172] D. D. Lee and H. S. Seung, "Learning the parts of objects by non-negative matrix factorization," *Nature*, vol. 401, no. 6755, pp. 788–791, 1999.

[173] B. Wang and M. Plumbley, "Musical audio stream separation by non-negative matrix factorization," *Proc. UK Digit. Music Res. Netw. (DMRN 2005) Summer Conf.*, pp. 23–4, 2005.

[174] T. Virtanen, A. T. Cemgil, and S. Godsill, "Bayesian extensions to non-negative matrix factorisation for audio signal modelling," *ICASSP, IEEE Int. Conf. Acoust. Speech Signal Process. - Proc.*, no. 2, pp. 1825–1828, 2008.

[175] A. Hyvarinen, "A family of fixed-point algorithms for independent component analysis," *1997 IEEE Int. Conf. Acoust. Speech, Signal Process.*, vol. 5, no. 3, pp. 3917–3920, 1997.

[176] J. Karhunen, A. Cichocki, W. Kasprzak, and P. Pajunen, "On neural blind separation with noise suppression and redundancy reduction.," *Int. J. Neural Syst.*, vol. 8, no. 2, pp. 219–237, 1997.

[177] M. Wax and T. Kailath, "Detection of Signals by Information Theoretic Criteria," *IEEE Trans. Acoust. Speech Signal Process.*, vol. 33, no. 2, 1985.

[178] J. Cordoso, "Blind Signal Separation : Statistical Principles," *Proc IEEE*, vol. 86, no. 10, pp. 2009–2025, 1998.

[179] A. Hyvarinen and E. Oja, "A Fast Fixed-Point Algorithm for Independent Component Analysis," *Neural Comput.*, vol. 9, no. 7, 1997.

[180] H. Sawada, R. Mukai, S. Araki, and S. Makino, "Estimating the number of sources using independent component analysis," *Acoust. Sci. Technol.*, vol. 26, no. 5, pp. 450–452, 2005.

[181] K. Johansen, J. H. Song, and P. Prentice, "Validity of the Keller-Miksis equation for 'non-stable' cavitation and the acoustic emissions generated," *IEEE Int. Ultrason. Symp. IUS*, pp. 1–4, 2017.

[182] Z. Chen and L. CChan, "A novel hybrid approach to the permutation problem of frequency domain blind source separation," in *Lect. Notes Comput. Sci. (including Subser. Lect. Notes Artif. Intell. Lect. Notes Bioinformatics)*, vol. 3195, pp. 532–539, 2004.

[183] C. Puntonet and A. Prieto, eds., *Independent Component Analysis and Blind Signal Separation*. Springer-Verlag, 2004.

[184] M. Jakovljevic, S. Hsieh, R. Ali, G. Chau Loo Kung, D. Hyun, and J. J. Dahl, "Local speed of sound estimation in tissue using pulse-echo ultrasound: Model-based approach," *J. Acoust. Soc. Am.*, vol. 144, no. 1, pp. 254–266, 2018.

Appendix A

Full *In Vitro* Experimental Results

This appendix presents the full set of images for the *in vitro* agarose flow channel experiments described in Chapter 2 of this thesis.

In the following figures, green represents the microscopy region of interest (indicating the presence of extravasated fluorescent nanocups), magenta indicates the thresholded Passive Acoustic Mapping (PAM) image (indicating the presence of cavitation in that area), white indicates areas of overlap between PAM signal and the microscopy region of interest, the red circle shows the location of the channel, the red arrows indicate the direction of ultrasound, and the white arrows indicate the axial direction of view of the linear arrays used during the PAM reconstruction.

Results for three PAM beamformers are shown. PAM is performed using data from either a single linear array (Single Array 1 or Single Array 2), or using data from both arrays simultaneously (Dual Array).

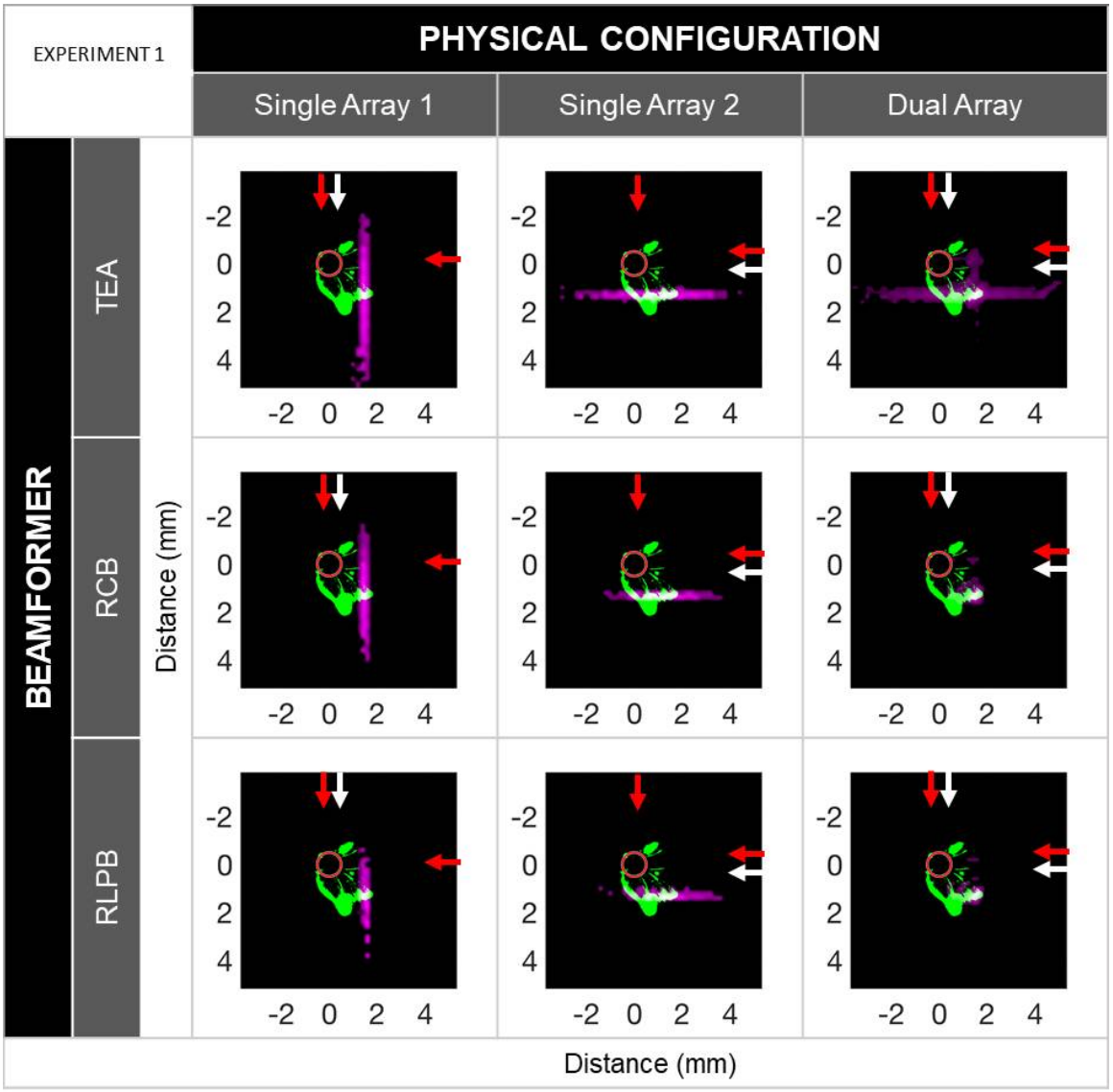


Figure A.1: Results for three beamformers for single and dual array configuration for Experiment 1 of 10. Green represents the microscopy region of interest (indicating the presence of extravasated fluorescent nanocups), magenta indicates the thresholded PAM image (indicating the presence of cavitation in that area), white indicates areas of overlap between PAM signal and the microscopy region of interest, the red circle shows the location of the channel, the red arrows indicate the direction of ultrasound, and the white arrows indicate the axial direction of view of the linear arrays used during the PAM reconstruction

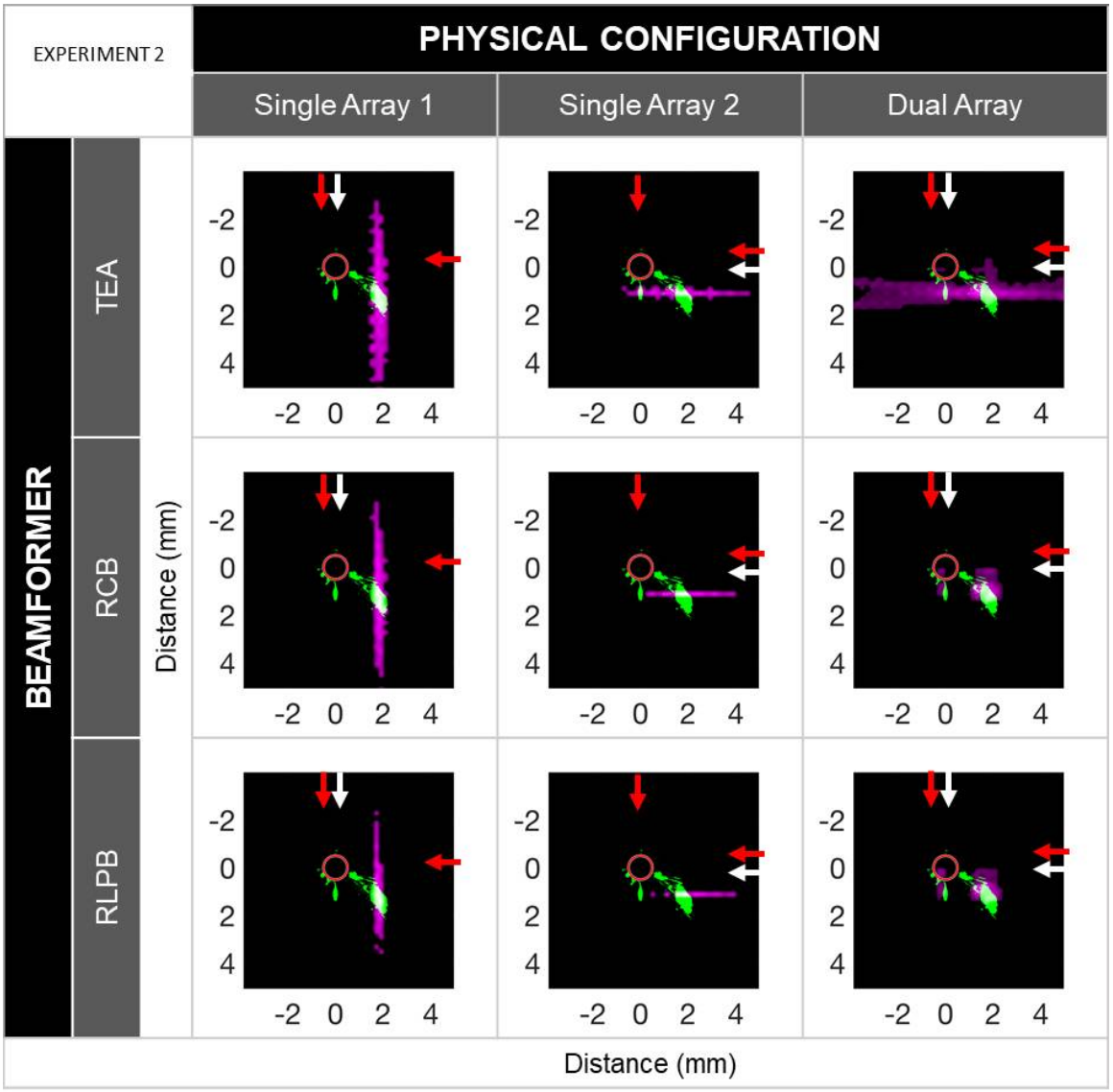


Figure A.2: Results for three beamformers for single and dual array configuration for Experiment 2 of 10. Green represents the microscopy region of interest (indicating the presence of extravasated fluorescent nanocups), magenta indicates the thresholded PAM image (indicating the presence of cavitation in that area), white indicates areas of overlap between PAM signal and the microscopy region of interest, the red circle shows the location of the channel, the red arrows indicate the direction of ultrasound, and the white arrows indicate the axial direction of view of the linear arrays used during the PAM reconstruction

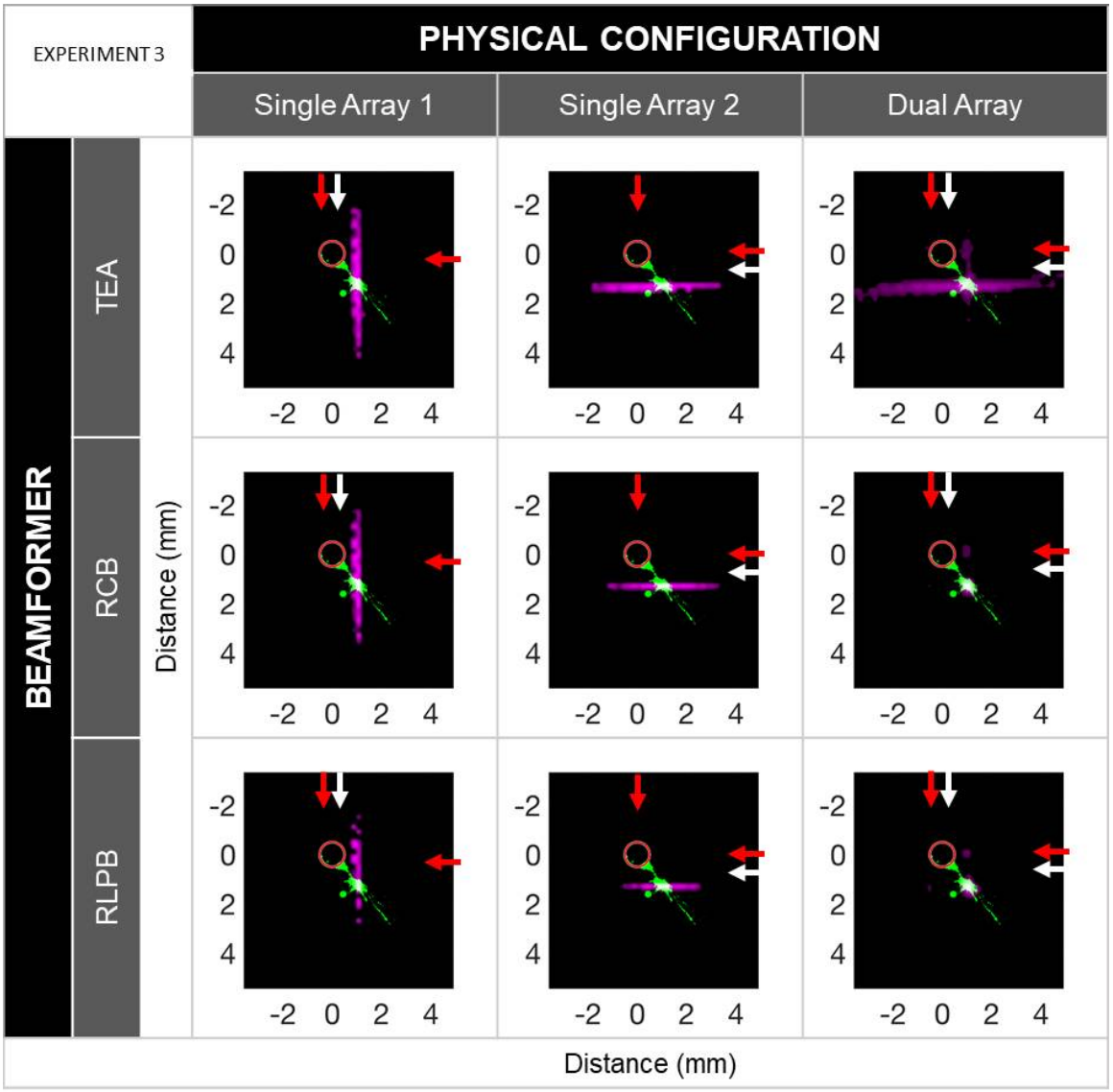


Figure A.3: Results for three beamformers for single and dual array configuration for Experiment 3 of 10. Green represents the microscopy region of interest (indicating the presence of extravasated fluorescent nanocups), magenta indicates the thresholded PAM image (indicating the presence of cavitation in that area), white indicates areas of overlap between PAM signal and the microscopy region of interest, the red circle shows the location of the channel, the red arrows indicate the direction of ultrasound, and the white arrows indicate the axial direction of view of the linear arrays used during the PAM reconstruction

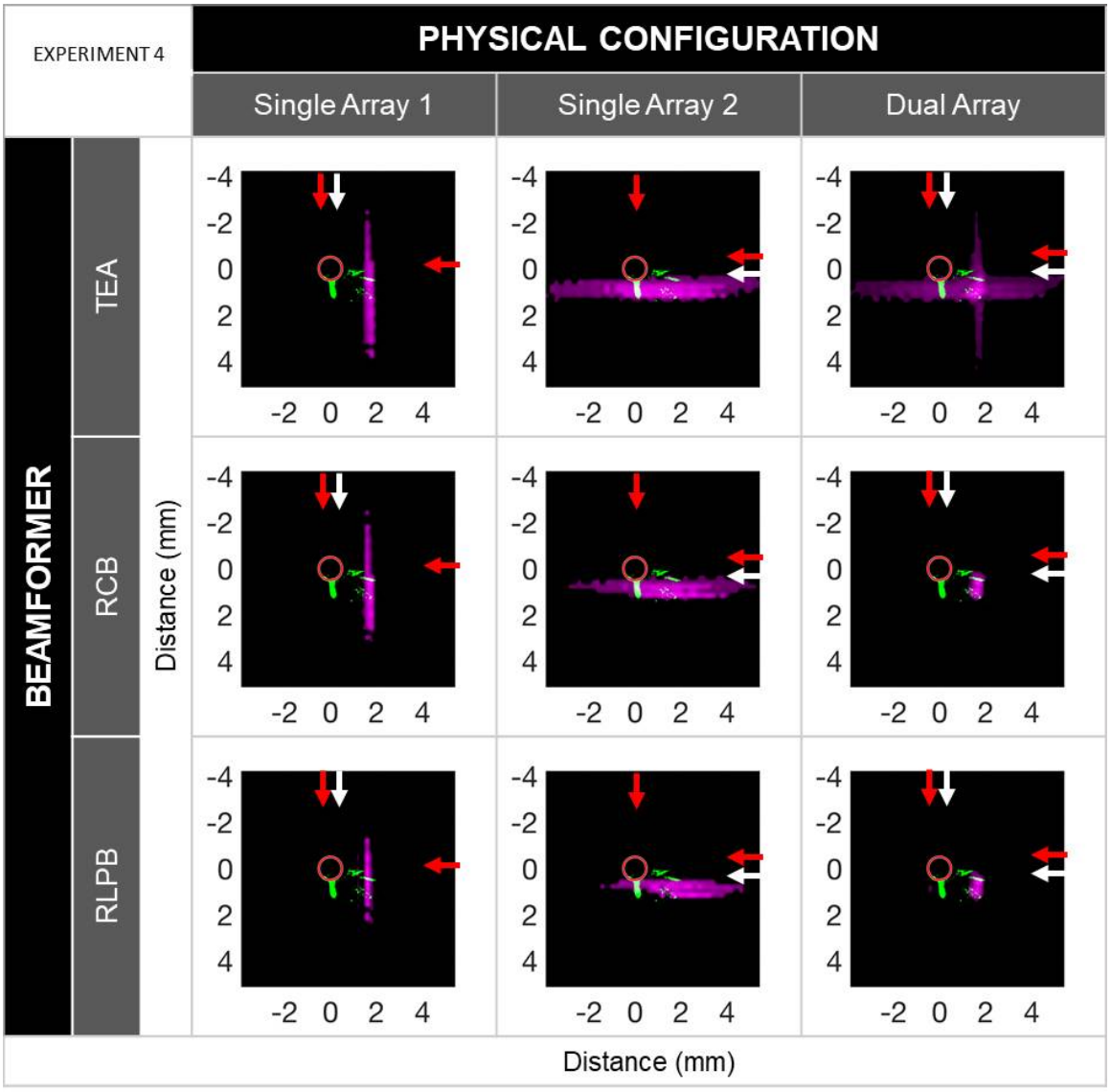


Figure A.4: Results for three beamformers for single and dual array configuration for Experiment 4 of 10. Green represents the microscopy region of interest (indicating the presence of extravasated fluorescent nanocups), magenta indicates the thresholded PAM image (indicating the presence of cavitation in that area), white indicates areas of overlap between PAM signal and the microscopy region of interest, the red circle shows the location of the channel, the red arrows indicate the direction of ultrasound, and the white arrows indicate the axial direction of view of the linear arrays used during the PAM reconstruction

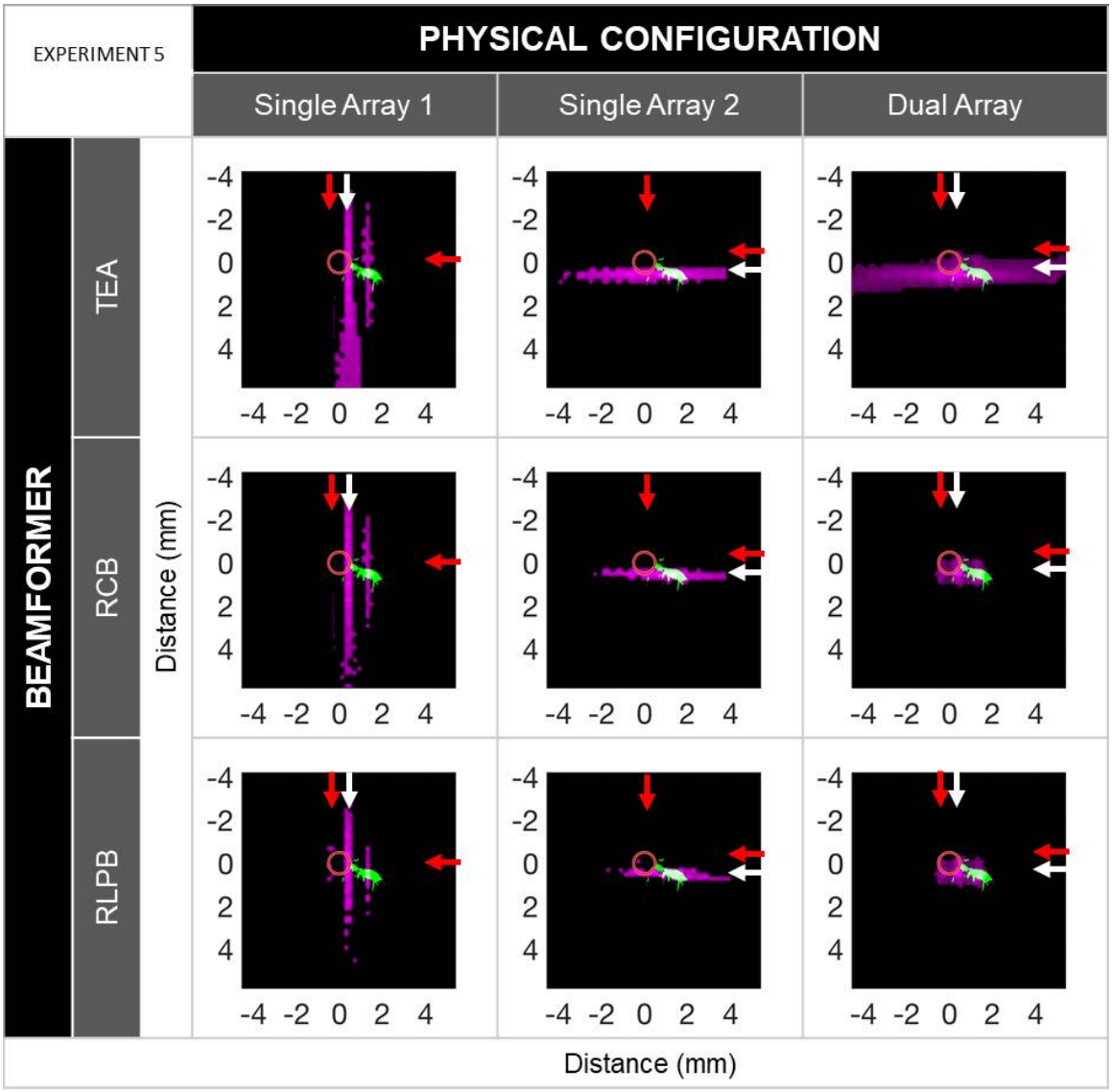


Figure A.5: Results for three beamformers for single and dual array configuration for Experiment 5 of 10. Green represents the microscopy region of interest (indicating the presence of extravasated fluorescent nanocups), magenta indicates the thresholded PAM image (indicating the presence of cavitation in that area), white indicates areas of overlap between PAM signal and the microscopy region of interest, the red circle shows the location of the channel, the red arrows indicate the direction of ultrasound, and the white arrows indicate the axial direction of view of the linear arrays used during the PAM reconstruction

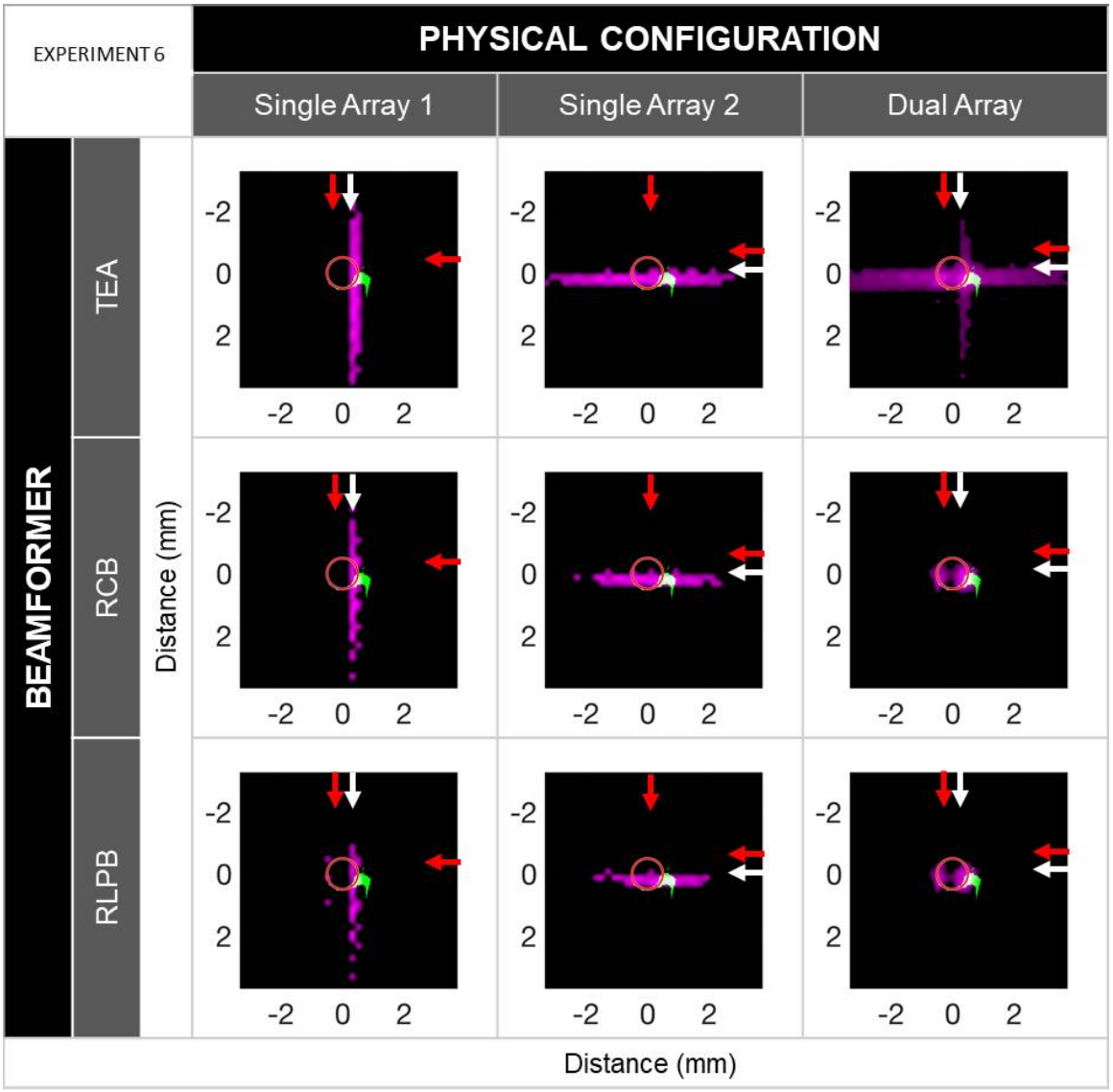


Figure A.6: Results for three beamformers for single and dual array configuration for Experiment 6 of 10. Green represents the microscopy region of interest (indicating the presence of extravasated fluorescent nanocups), magenta indicates the thresholded PAM image (indicating the presence of cavitation in that area), white indicates areas of overlap between PAM signal and the microscopy region of interest, the red circle shows the location of the channel, the red arrows indicate the direction of ultrasound, and the white arrows indicate the axial direction of view of the linear arrays used during the PAM reconstruction

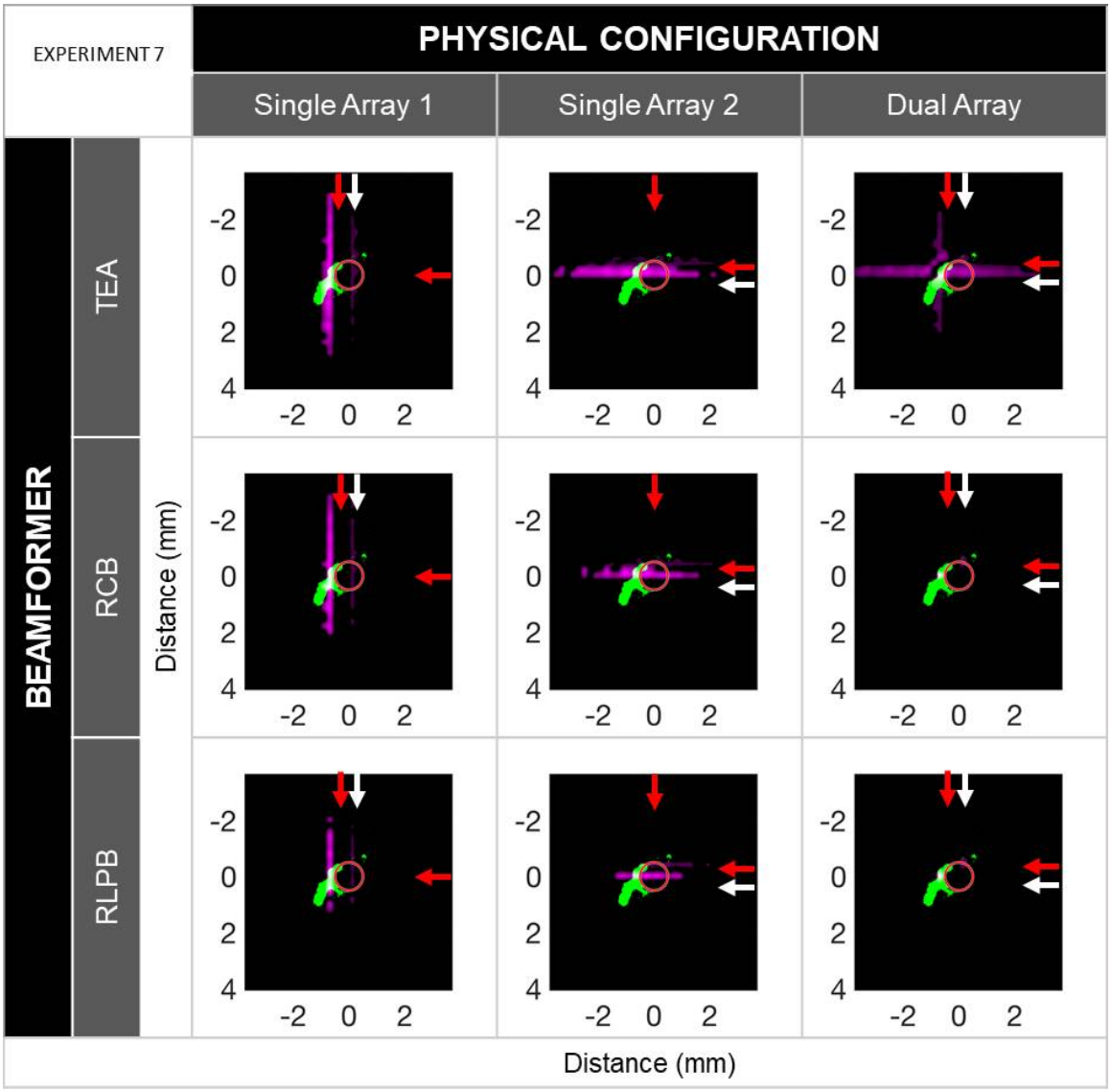


Figure A.7: Results for three beamformers for single and dual array configuration for Experiment 7 of 10. Green represents the microscopy region of interest (indicating the presence of extravasated fluorescent nanocups), magenta indicates the thresholded PAM image (indicating the presence of cavitation in that area), white indicates areas of overlap between PAM signal and the microscopy region of interest, the red circle shows the location of the channel, the red arrows indicate the direction of ultrasound, and the white arrows indicate the axial direction of view of the linear arrays used during the PAM reconstruction

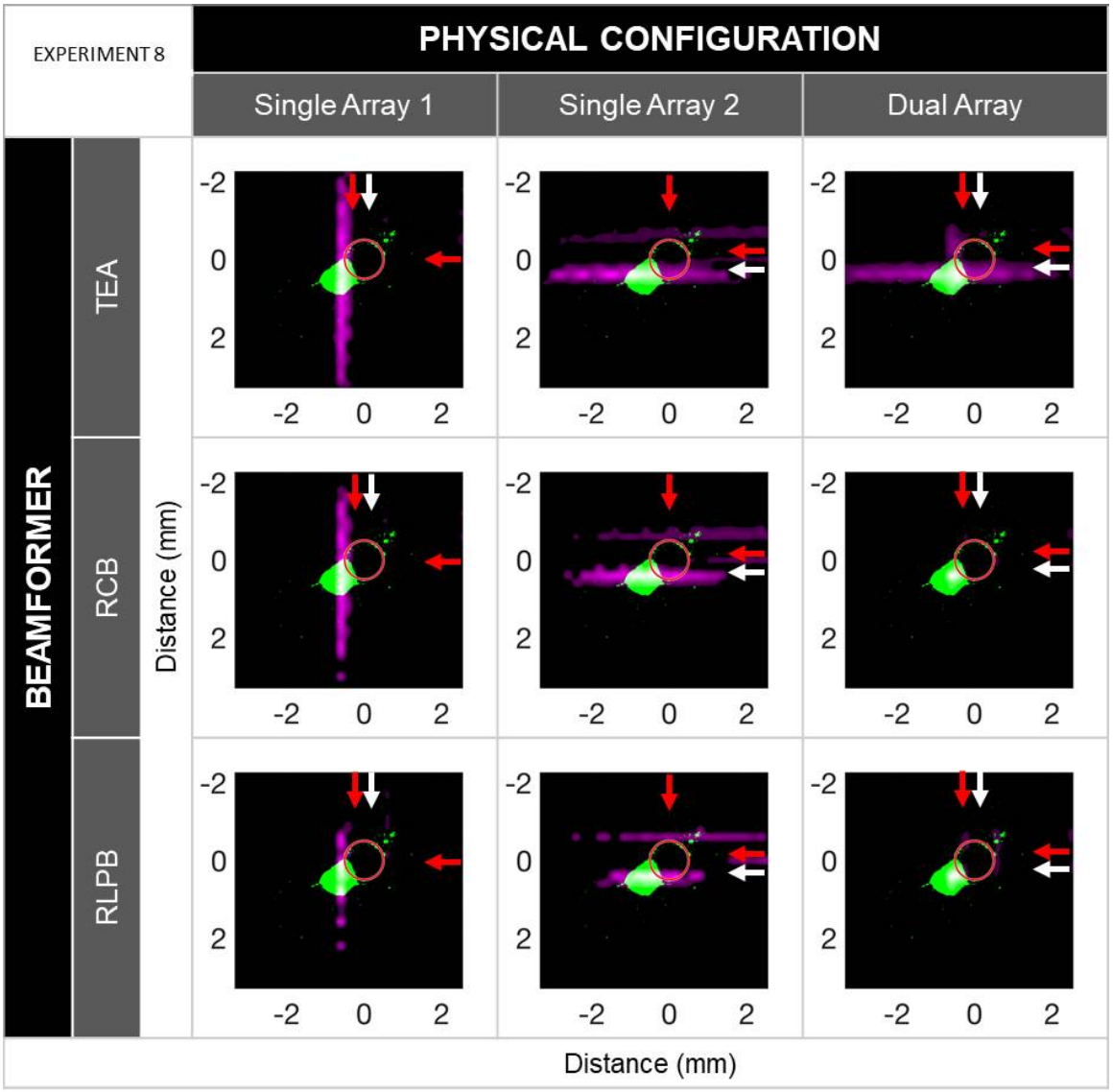


Figure A.8: Results for three beamformers for single and dual array configuration for Experiment 8 of 10. Green represents the microscopy region of interest (indicating the presence of extravasated fluorescent nanocups), magenta indicates the thresholded PAM image (indicating the presence of cavitation in that area), white indicates areas of overlap between PAM signal and the microscopy region of interest, the red circle shows the location of the channel, the red arrows indicate the direction of ultrasound, and the white arrows indicate the axial direction of view of the linear arrays used during the PAM reconstruction

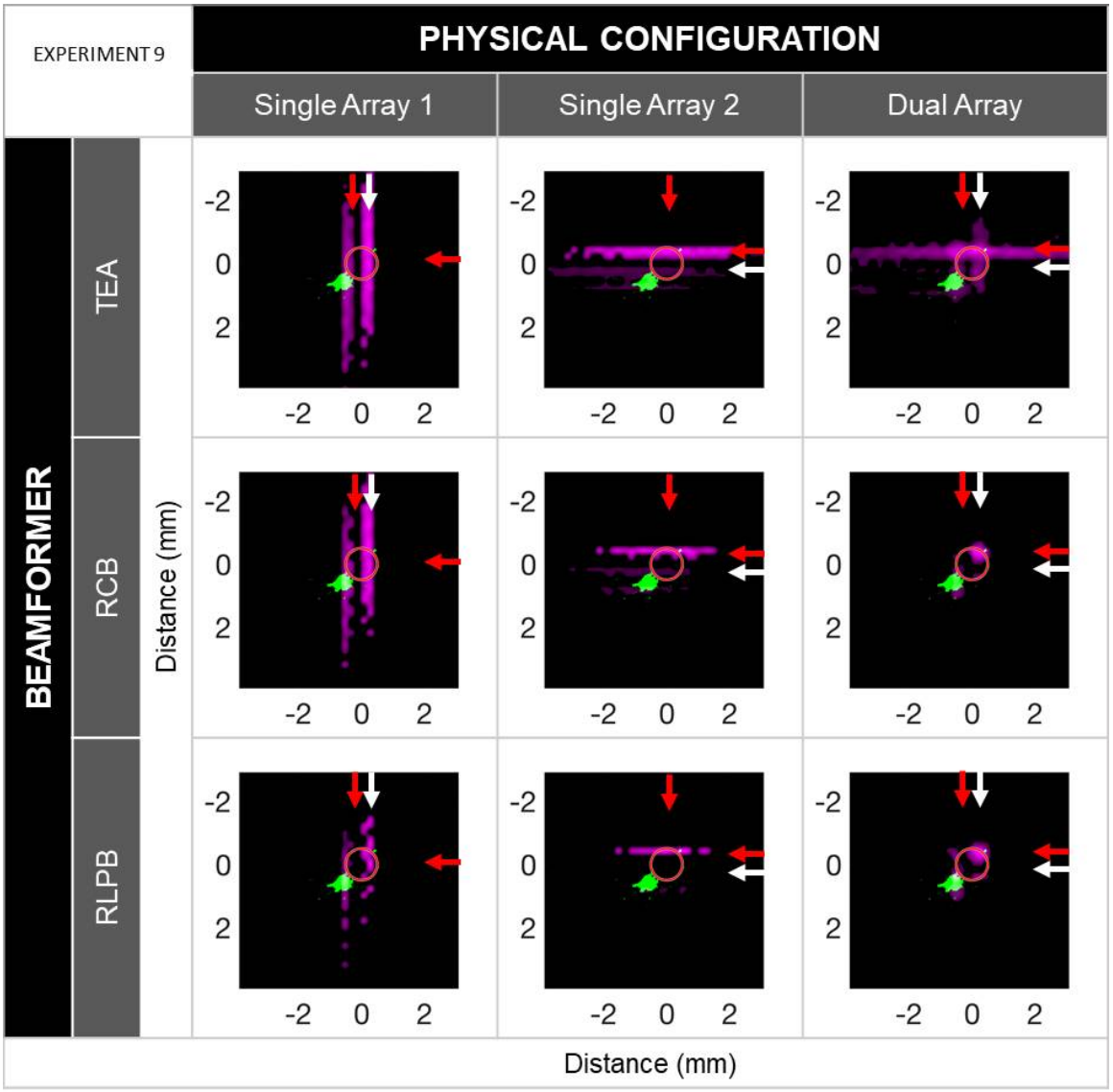


Figure A.9: Results for three beamformers for single and dual array configuration for Experiment 9 of 10. Green represents the microscopy region of interest (indicating the presence of extravasated fluorescent nanocups), magenta indicates the thresholded PAM image (indicating the presence of cavitation in that area), white indicates areas of overlap between PAM signal and the microscopy region of interest, the red circle shows the location of the channel, the red arrows indicate the direction of ultrasound, and the white arrows indicate the axial direction of view of the linear arrays used during the PAM reconstruction

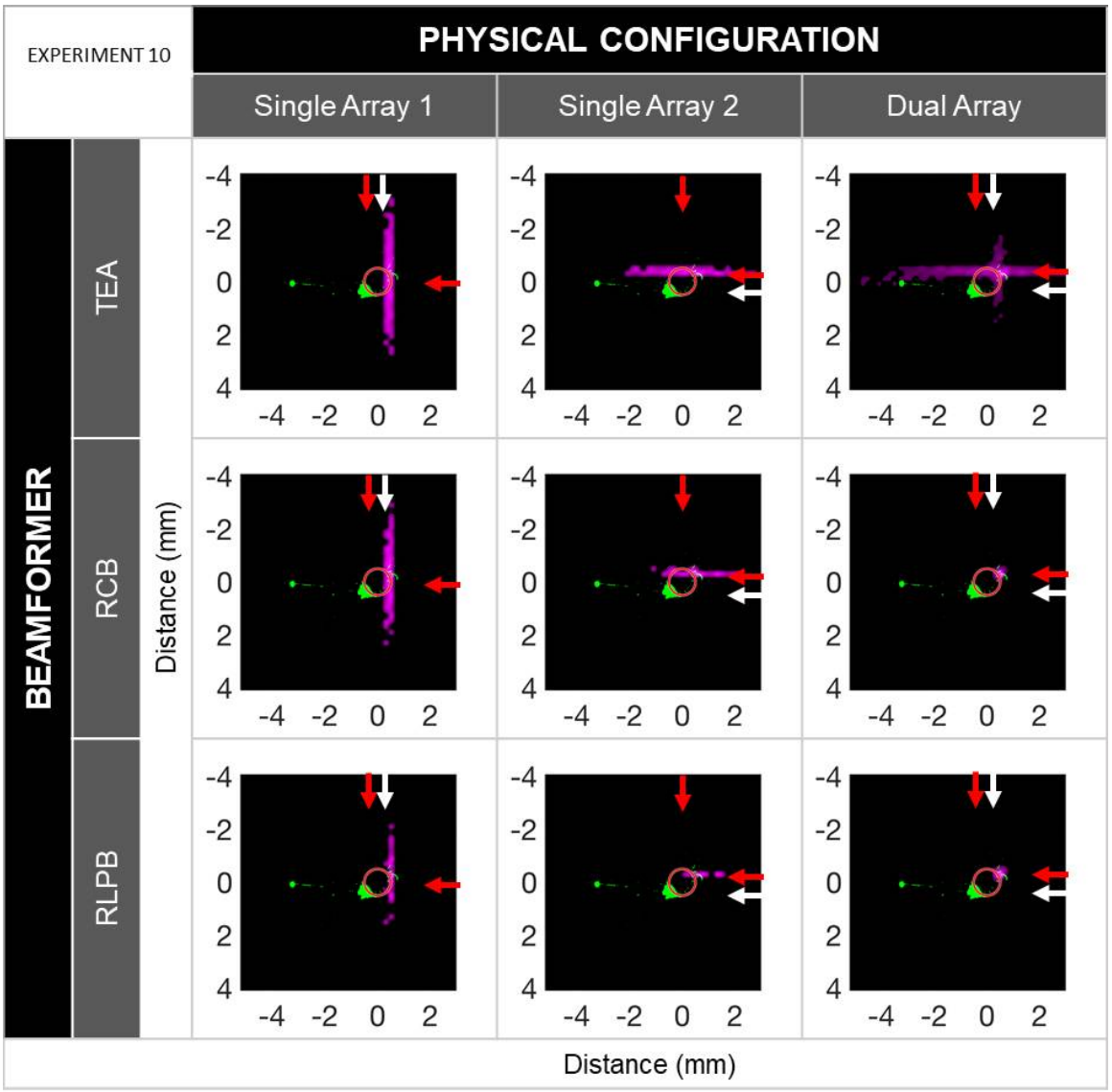


Figure A.10: Results for three beamformers for single and dual array configuration for Experiment 10 of 10. Green represents the microscopy region of interest (indicating the presence of extravasated fluorescent nanocups), magenta indicates the thresholded PAM image (indicating the presence of cavitation in that area), white indicates areas of overlap between PAM signal and the microscopy region of interest, the red circle shows the location of the channel, the red arrows indicate the direction of ultrasound, and the white arrows indicate the axial direction of view of the linear arrays used during the PAM reconstruction